

CHLORITE STABILITY IN THE SUBDUCTION ZONE

Implications for water transport to the deep mantle,
slab diapirs and mantle melting

Shayne Lawrence Lakey

A thesis submitted for the degree of Doctor of Philosophy

of The Australian National University

March 2019



© Copyright by Shayne Lawrence Lakey, 2019

Declaration

The work presented herein is an account of research performed during the academic programme towards the degree of Doctor of Philosophy at the Australian National University.

I certify that this thesis does not contain any material previously submitted for a degree or diploma at any university, nor does it contain any material previously published or written by another person, except where due reference is made in the text.

Shayne Lawrence Lakey

ABSTRACT

Hydrous minerals subducted at convergent margins provide the bulk of water to arc magmas. At temperatures beyond serpentinite stability, chlorite becomes the main water-bearing contributor in the subduction zone. The maximum stability field of chlorite is not well constrained, and the experimental studies which have been conducted have involved synthesis experiments using chlorite of clinocllore composition which may not adequately represent the variety of behaviour of naturally-occurring chlorite in a subduction setting.

This thesis provides new data which successfully determined the upper stability field of chlorite in a range of subduction lithologies. Piston cylinder experiments were conducted over a range of pressures (1.0 GPa-6.3 GPa) and temperatures (500°C-1150°C) which were analysed using field emission scanning electron microscopy (FE-SEM), Raman and X-Ray Diffraction (XRD). Only natural mineral samples were used. Results confirmed those of previous research below ~4.0 GPa, when adjusted for compositional differences, but at higher P,T conditions, some unexpected findings were revealed.

Series 1 experiments (Chapter 3) examined chlorite stability in ultramafic chlorite schists (Mg#=0.94) examining two terminal chlorite reactions Reaction 1: chlorite = orthopyroxene + olivine + spinel + H₂O and Reaction 2: chlorite = garnet + olivine + spinel + H₂O. Series 2 experiments (Chapter 4) explored chlorite stability in a fertile chlorite peridotite (Mg#=0.94) exploring two reactions reported in previous studies: Reaction 3: chlorite + clinopyroxene = garnet + olivine + H₂O ± spinel, and Reaction 4: chlorite + orthopyroxene = garnet + olivine + H₂O ± spinel. Series 3 experiments (Chapter 5) were completed in two parts. The first examined two samples of mafic chlorite schist (Mg#=0.50 and 0.68) to test the feasibility of chlorite schist forming mélange diapirs (Marschall and Schumacher, 2012) to transport fluid through the mantle wedge. The second part used chlorite schist (Mg#=0.94) to locate the wet peridotite solidus, the subject of much debate.

Results of Series 1 and 2 experiments showed chlorite possessed a maximum pressure stability of 6.2 GPa in both chlorite schist and chlorite peridotite with the former lithology also possessing ~40°C higher thermal stability. This represented enhanced stability some 40 kms deeper than determined by previous research and places stable chlorite within the upper mantle.

The high-pressure breakdown of chlorite produced some unexpected phases. Chlorite schist reacted to garnet, olivine, water and 11.5Å-phase (12.1 wt% water) whilst the transformation of chlorite peridotite formed olivine, water and Mg-sursassite (7.2 wt% water). Both hydrous minerals are stable to high P,T conditions and so in a cooler subduction settings, these phases could transport significant quantities of water to the deeper mantle. Results of Series 3 experiments showed mafic chlorite schist

attained a maximum stability at 3.0 GPa of 780°C and 765°C respectively. Upon chlorite breakdown, mafic schist transformed to a garnet peridotite, a denser rock than average peridotite, which disproved the feasibility of the diapir model. The location of the wet peridotite solidus was determined to be >1100°C which disputed the existence of chlorite melting in hydrous peridotites.

ACKNOWLEDGEMENTS

The completion of this thesis marks the end of a ten-year long personal challenge which started out as a mid-life change-of-direction to take up the study of earth sciences and eventually this PhD.

I owe an enormous debt of gratitude to Joerg Hermann. On a personal level, he agreed to take me on as a mature-age student with a background in the Humanities. I appreciated his calm demeanour, patience and ever-present upbeat personality. He willingly gave his time, even when I had the most basic of questions. As a supervisor, I was impressed by his fierce intellect, his prompt written feedback and his attention to detail. Without Joerg's supervision, I doubt I would ever have completed this PhD.

My appreciation is also extended to the other members of my supervisory panel. Thanks to Alberto Padron-Navarta (University of Montpellier) who taught me to use PerpleX and the mysteries of phase projections, to Greg Yaxley's for his willingness to act as my co-supervisor following Joerg's permanent relocation to Switzerland, and for the sage advice provided by Hugh O'Neil and Richard Arculus.

There was a surprising amount of technical expertise and workshop skills required in completing this PhD. Many thanks to Dave Clark and Dean Scott, the technical staff who managed the petrology labs, who provided my initial training in laboratory techniques. Thanks also to my fellow petrology lab users who willingly shared their own skills and experiences, all of which helped to build my own confidence in laboratory work. Thanks to each of the following people for training and assistance on various aspects of analytical equipment: Huijuan Li (SEM), Ulli Troitzsch and Lasse Noren (XRD devices), Frank Brink and Hua Chen (FE-SEM), Bob Rapp (microprobe), Antony Burnham (Raman).

Navigating the numerous administrative requirements in a PhD was made easy with the support of key admin staff. Josie Magro and Maree Coldrick were always a pleasure to deal with. Their meticulous planning and impeccable interpersonal skills meant that all requirements were met on time and with sound advice. Thanks very much to both of you. Thanks also to Duncan Bolt who provided prompt, efficient and friendly IT support when needed.

A strong sense of camaraderie was prevalent among the student body at RSES and this added to the positive PhD experience. No matter what disaster may have occurred in the lab or at the computer screen, a cup of tea, a chocolate biscuit (or two) and a chat at morning tea helped to lighten the mood and to refocus efforts. Thanks to all the regulars in J1. Thanks also to the class of 2013 – Eleanor, Mari, James, Rachel, Johanna and Kathryn. Our small group formed a special bond which I am sure will continue beyond the PhD. A special thanks to Kathryn for the many chats we managed in the J2 corridor, and for teaching me the basics of Adobe Illustrator. I seemed to move offices quite a lot whilst at ANU so thanks are extended to each of my fellow PhD candidates with whom I shared office

space: Chris, Patrick, Yang, Brendan, Paolo, Prokopiý as well as Stephan Klemme (University of Munster) whilst he was on sabbatical. Thanks to the members of the Tuesday night trivia team at the Fellow Bar. Although trivia was eventually cancelled due to too few participants, we know it was really because the RSES team was unbeatable!

Finally, and perhaps most importantly, thanks to family and friends who have endured my PhD 'adventure' especially Bernie who motivated me to embark on this PhD journey and has remained a rock of support.

This research is supported by an Australian Government Research Training Program (RTP) Scholarship.

LIST OF MINERALS AND THEIR ABBREVIATIONS

Antigorite	atg
Apatite	apa
Chlorite	chl
Clinochlore	cli
Clinopyroxene	cpx
Epidote	epi
Garnet	grt
Ilmenite	ilm
Magnesiokatophorite	kat
Olivine	ol
Omphacite	omp
Orthopyroxene	opx
Phase A	PhA
Phase-HAPY	hapy
Rutile	rut
Spinel	sp
Titanite	ttn
Tremolite	tre
Magnetite	mgt
Mg-sursassite	MgS
Wonesite	won
Water/Fluid	H ₂ O
11.5Å-phase	11.5Å
10Å-phase	10Å

TABLE OF CONTENTS

LIST OF FIGURES	xiv
LIST OF TABLES	xvii
CHAPTER 1 : INTRODUCTION.....	1
1.1 CHLORITE STABILITY	2
1.1.1 Chlorite stability at high pressure	2
1.1.2 Chlorite stability in varied lithologies and composition	2
1.1.3 Chlorite stability of ‘hybrid’ chlorite mélange	3
1.2 FLUID TRANSPORT MODELS THROUGH THE MANTLE WEDGE	4
1.2.1 ‘Free’ water released upon chlorite dehydration	4
1.2.2 Chlorite melts before it dehydrates.....	5
1.2.3 Chlorite retains ‘bound’ water and is transported in a diapir	5
1.3 PURPOSE OF THE STUDY.....	7
1.3.1 Study aims	7
1.3.2 Thesis outline.....	7
CHAPTER 2 : METHODOLOGY	9
2.1 SAMPLE PREPARATION	9
2.1.1 Sample selection.....	9
2.1.2 Sample processing	10
2.1.3 X-Ray Diffraction (XRD) analysis of natural minerals	10
2.1.4 Mineral separation	11
2.1.5 Preparation of starting mixes	12
2.1.6 starting mix analyses	12
2.2 EXPERIMENTAL PROCEDURE	12
2.2.1 Capsule production.....	13
2.2.2 Capsule assembly	13
2.2.3 Thermocouple production	15
2.2.4 Experimental run using HP and UHP Piston cylinder apparatus	15

2.2.5 Calibration of pressure and temperature on piston cylinder apparatus	17
2.3 POST-EXPERIMENT PROCEDURE	18
2.3.1 Constructing the mount	18
2.3.2 Polishing the mount	18
2.3.3 Performing chemical analyses	19
2.3.4 Mass balance.....	21
2.3.5 Performing Raman analyses	21
CHAPTER 3 : THE UPPER STABILITY LIMIT OF CHLORITE IN ULTRAMAFIC SCHISTS – IMPLICATIONS FOR WATER TRANSPORT INTO THE DEEP MANTLE	22
3.1 INTRODUCTION	22
3.1.1 Previous studies on chlorite in ultramafic schists.....	23
3.1.2 Starting material.....	25
3.2 RESULTS	27
3.2.1 Phase relations to 5.5 GPa.....	28
3.2.2 Phase textures to 5.5 GPa	28
3.2.3 Phase relations above 5.5 GPa	34
3.2.4 Phase textures above 5.5 GPa	39
3.2.5 Phase Composition.....	42
3.2.6 Element Partitioning.....	46
3.3 DISCUSSION.....	48
3.3.1 Attainment of equilibrium.....	48
3.3.2 Theoretical phase relations in the CrFMASH system	49
3.3.3 THEORETICAL PHASE RELATIONS – LOW-AL CHLORITE VERSUS CLINOCHLORE	52
3.3.4 Key terminal chlorite reactions determined by mass balance.....	54
3.3.5 Chlorite terminal reaction curves in ultramafic low-Al chlorite.....	55
3.3.6 Location of invariant points.....	56
3.3.7 Previous chlorite dehydration studies in the MASH system	58
3.3.8 The impact of Fe and Cr on chlorite stability.....	62
3.3.9 Delineation of Reaction 4/A6 and Reaction 2/A1/B2	65

3.3.10 The formation of other high-pressure hydrous minerals.....	67
3.3.11 Implications for bound water in ultramafic schists.....	68
3.4 CONCLUSIONS AND IMPLICATIONS	75
CHAPTER 4 : THE THERMAL STABILITY OF CHLORITE PERIDOTITE AT HIGH PRESSURE – IMPLICATIONS FOR WATER TRANSPORT IN THE MANTLE WEDGE AND THE DEEP MANTLE.....	77
4.1 INTRODUCTION	77
4.1.1 Previous Experiments on the stability of chlorite peridotite	78
4.2 STARTING MATERIAL.....	81
4.3 RESULTS.....	83
4.3.1 Phase relations	85
4.3.2 Progress of Reactions 3 and 4.....	88
4.3.3 Textural analysis	88
4.3.4 Compositional analysis	92
4.3.5 Element partitioning.....	99
4.4 DISCUSSION	101
4.4.1 Attainment of equilibrium	101
4.4.2 Theoretical phase relations in the CMASH system	102
4.4.3 Key chlorite reactions determined by mass balance	106
4.4.4 Chlorite reaction curves in chlorite peridotite	107
4.4.5 Location of invariant points	109
4.4.6 Previous studies of chlorite stability in chlorite peridotite	110
4.4.7 Absence of 10Å-phase in the current study.....	113
4.4.8 The impact of Ca on chlorite stability	114
4.4.9 Delineation of Reaction 3 and Reaction 4.....	116
4.4.10 Contrasting patterns of Cr-Al partitioning	119
4.4.11 Implications for bound water in chlorite peridotite	121
4.5 CONCLUSIONS AND IMPLICATIONS	130
CHAPTER 5: THE STABILITY OF MAFIC CHLORITE SCHISTS AT SUB-ARC PRESSURES – IMPLICATIONS FOR SLAB DIAPIRS AND MANTLE MELTING	132

5.1. INTRODUCTION	132
5.1.1. Mélange diapirs.....	132
5.1.2. The location of the wet peridotite solidus.....	133
5.2. STARTING MATERIAL.....	134
5.2.1. Description of SY3 starting material	134
5.2.2. Description of SY4 starting material	138
5.2.3. Description of high temperature starting material.....	141
5.3. RESULTS.....	141
5.3.1. Sample SY3 (Mg#=0.50).....	141
5.3.2. Sample SY3 (Mg#=0.50).....	141
5.3.3. Sample SY4 (Mg#=0.68).....	150
5.3.4. High temperature set (Mg#=0.94).....	159
5.4. DISCUSSION.....	165
5.4.1. Approach to equilibrium	166
5.4.2. Mafic chlorite schist from Syros, Greece	167
5.4.3. The onset of melting in garnet peridotite	175
5.5. CONCLUSIONS AND IMPLICATIONS.....	181
CHAPTER 6 : SUMMARY, IMPLICATIONS AND FUTURE RESEARCH.....	183
6.1 SUMMARY OF FINDINGS	184
6.1.1 Aim 1: To constrain the stability field of chlorite in chlorite schist, chlorite lherzolite and chlorite harzburgite.....	184
6.1.2 Aim 2: To investigate if chlorite breaks down into anhydrous or hydrous mineral assemblages.....	187
6.1.3 Aim 3: To examine the implications of chlorite stability upon slab diapir and mantle melting models	188
6.2 IMPLICATIONS OF INCREASED CHLORITE STABILITY FIELD AND WATER TRANSPORT	188
6.3 FUTURE RESEARCH DIRECTIONS.....	192
CHAPTER 7 : REFERENCE LIST	194

LIST OF FIGURES

FIGURE 1.1: Cross-section of a typical subduction zone. Cartoon is not to scale.	3
FIGURE 1.2: Three-dimensional representation of a mélange-diapir model.	6
FIGURE 2.1: Location of the components of the starting mixes.	9
FIGURE 2.2: A typical capsule assembly used in piston cylinder experimentation.	14
FIGURE 2.3: Piston cylinder devices in the ANU Experimental Petrology laboratories.	15
FIGURE 2.4: Experimental pressure log on the UHP 500t press at ANU laboratory.	17
FIGURE 2.5: Comparison of EDS vs WDS analyses of major oxides in chlorite, garnet and olivine.	20
FIGURE 2.6: Hitachi 4300 SE/N Schottky field-emission, scanning electron microscope (FE-SEM)	21
FIGURE 3.1: X-Ray Diffraction scan of Series 1 starting material.	25
FIGURE 3.2: Chemography of the Series 1 starting materials	27
FIGURE 3.3: Phase relations of ultramafic low-Al chlorite <5.5 GPa.	29
FIGURE 3.4: Representative FE-SEM BSE images of run products at 2.0 GPa and 3.0 GPa.	31
FIGURE 3.5: Representative FE-SEM BSE images of run products at 5.0 GPa and 6.0 GPa.	32
FIGURE 3.6: Phase relations of ultramafic low-Al chlorite >5.5 GPa.	34
FIGURE 3.8: Raman spectrum of the 11.5Å phase.....	35
FIGURE 3.7: XRD spectra of the 11.5Å-phase.	37
FIGURE 3.9: Representative FE-SEM BSE images of 11.5Å-phase.....	38
FIGURE 3.10: Compositional plots of 11.5Å-phase, olivine and garnet in Series 1	42
FIGURE 3.11: Compositional plots of spinel and orthopyroxene in Series 1	44
FIGURE 3.12: Element partitioning by selected phase in Series 1.	47
FIGURE 3.13: Chemography of low-Al chlorite in ternary compositional space.	50
FIGURE 3.14: Schreinemakers plot showing theoretical phase relations in low-Al chlorite at low pressure.	51
FIGURE 3.15: Schreinemakers plot showing theoretical phase relations of low-Al chlorite at high pressure	52
FIGURE 3.16: Schreinemakers analysis showing theoretical phase relations of clinocllore at high pressure	53

FIGURE 3.16: Phase relations in ultramafic, low-Al chlorite highlighting key Reactions 1, 2 and 4.	55
FIGURE 3.17: Key chlorite reactions – current study compared with previous studies.....	59
FIGURE 3.18: Delineation of Reaction 2/A1/B2 and Reaction 4/A6 in chlorite schist	66
FIGURE 3.19: Release of bound water from hydrous phases in Series 1 at 3.0 GPa and 6.0 GPa.	69
FIGURE 3.20: Slab surface temperature compared to chlorite, 11.5Å-phase and MgS stability fields.	70
FIGURE 3.21: Water sequestration in hydrous phases along three select geotherms.	72
FIGURE 3.22: Extension of the hydrous-anhydrous boundary in ultramafic chlorite schists.....	74
FIGURE 4.1: Chemography of the starting mix in Series 2	82
FIGURE 4.2: X-Ray Diffraction analyses of Series 2 starting mix.	84
FIGURE 4.3. Phase relations in ultramafic chlorite peridotite.	86
FIGURE 4.4. Changing phase relations of Reaction 3 (chl+cpx) and Reaction 4 (chl+opx).	87
FIGURE 4.5: Representative low-pressure phase textures from Series 2	89
FIGURE 4.6: Representative high-pressure phase textures from Series 2	90
FIGURE 4.7. Compositional plots for olivine and spinel in Series 2	94
FIGURE 4.8. Compositional plots for garnet and Mg-Sursassite in Series 2.....	96
FIGURE 4.9. Compositional plots for orthopyroxene and clinopyroxene in Series 2	97
FIGURE 4.10. Partitioning plots for select pairs in Series 2.....	100
FIGURE 4.11. Schreinemakers network in Series 2 at high pressure.	103
FIGURE 4.12. Schreinemakers network in Series 2 at low pressure	105
FIGURE 4.13: Phase relations in chlorite peridotite highlighting key Reactions 3 and 4.	108
FIGURE 4.14: Key chlorite reactions from current study compared with previous studies.	112
FIGURE 4.15: Reaction 4 curves from Series 1 and Series 2.	115
FIGURE 4.16: Arrangement of divariant fields in Reactions 3 and 4.....	117
FIGURE 4.17: X Cr in garnet and spinel vs pressure	120
FIGURE 4.18: Release of water from hydrous phases in chlorite peridotite.....	122
FIGURE 4.19: Model slab surface temperatures (SST) compared to Reactions 3 and 4.	124
FIGURE 4.20: Estimated water liberation from chlorite peridotite along three P,T paths	126
FIGURE 4.21: Subduction zone profile showing stability of ultramafic hydrous minerals.	127
FIGURE 4.22: Extension of the hydrous-anhydrous boundary in chlorite peridotite.....	129
FIGURE 5.1: Chemography of the SY3 starting mix and run products.	136
FIGURE 5.2: X-Ray Diffraction analysis of SY3 starting mix.....	137
FIGURE 5.3: Chemography of the SY4 starting mix and run products.	139
FIGURE 5.4: X-Ray Diffraction analysis of SY4 starting mix.....	140

FIGURE 5.5. Changing phase relations by temperature in SY3 experiments.	142
FIGURE 5.6. Relevant compositional plots for SY3 experimental set in Series 3.....	147
FIGURE 5.7. Relevant partitioning plots for SY3 bulk composition in Series 3 experiments ...	148
FIGURE 5.8: Phase abundance with increasing temperature in SY3 experimental set.	150
FIGURE 5.9. Changing phase relations by temperature in SY4 experiments.	151
FIGURE 5.10. Relevant compositional plots for SY4 bulk composition in Series 3	155
FIGURE 5.11. Relevant partitioning plots for SY4 bulk composition in Series 3 experiments .	157
FIGURE 5.12. Changing phase relations by temperature in SY4 experiments.	159
FIGURE 5.13. Changing phase relations and textures in high-temperature experiments.....	160
FIGURE 5.14. Relevant partitioning plots for high temperature set in Series 3 experiments .	164
FIGURE 5.15. Changing phase abundance with temperature in high-temperature experimental set.....	165
FIGURE 5.16. Maximum stability of chlorite of different Mg#.....	168
FIGURE 5.17. Water release from mafic chlorite schist by temperature.	172
FIGURE 5.18. The onset of melting in chlorite peridotite illustrated by phase textures.....	177
FIGURE 5.19. Mg# vs temperature - current study compared with Till et. al.	178
FIGURE 6.1: Comparison of bulk compositions used in this study.....	183
FIGURE 6.2: Comparison of phase relations in chlorite peridotite and chlorite schist	185

LIST OF TABLES

TABLE 1.1: Overview of the lithology, composition and chemistry in each region of the subduction zone.....	2
TABLE 2.1: A typical capsule assembly used in piston cylinder experimentation.....	12
TABLE 3.1: Compilation of studies involving ultramafic chlorite schist.	24
TABLE 3.2: Panel showing analyses of starting mix of Series 1.....	26
TABLE 3.3: Table of experimental conditions, run products and mass balance in Series 1.	28
TABLE 3.4: Representative analyses of run products in Series 1.	41
TABLE 3.5: Effect of Fe and Cr on chlorite stability in chlorite peridotite after Reaction 4/A6 ..	63
TABLE 3.6: Relevant high-pressure, hydrous minerals formed after chlorite breakdown	67
TABLE 4.1. Compilation of previous experiments on Reactions 3 and 4	79
TABLE 4.2: FE-SEM analysis of the starting mix.....	81
TABLE 4.3. Table of results for experimental Series 2.	85
TABLE 4.4. Table of representative phase analyses in Series 2	93
TABLE 4.5: Effect of Ca on chlorite stability.....	116
TABLE 5.1: FE-SEM analysis of the SY3 starting mix	135
TABLE 5.2: FE-SEM analysis of the SY4 starting mix	138
TABLE 5.3. Experimental conditions and run products in SY3 experimental set.	141
TABLE 5.4. Table of representative phase analyses for SY3 in in Series 3	145
TABLE 5.5. Summary of results for SY3 experimental set in Series 3.....	149
TABLE 5.6. Experimental conditions and run products for SY4 experimental set in Series 3 ..	150
TABLE 5.7. Table of representative phase analyses for SY4 in in Series 3	154
TABLE 5.8. Table of results for SY4 experiments in Series 3.	158
TABLE 5.9. Table of results for high temperature experiments in Series 3.....	159
TABLE 5.10. Table of representative phase analyses for high temperature set in Series 3	163
TABLE 5.11. Table of results for high temperature experiments in Series 3.....	165
TABLE 5.12. Density comparison of mafic chlorite schist and average peridotite at 3.0 GPa..	170

CHAPTER 1 : INTRODUCTION

The connection between subduction and arc volcanism at convergent margins is well known (Arculus and Johnson, 1978; Delany and Helgeson, 1978; Tatsumi, 1986; Schmidt and Poli, 1998). Dehydration of hydrous minerals within the subducting slab and in trapped sediments liberates water which percolates upwards, infiltrating the rocks in the overlying mantle wedge and incurs their partial melting. Melt accumulates eventually as the magma supply for arc volcanoes. At first glance, this process appears quite simple; in fact the transport of fluids from the slab to arc magma chambers involves a myriad of inter-related mechanisms (Schmidt and Poli, 2014); some well-understood, some theorised, others remaining a puzzle.

A variety of hydrous minerals liberate water within the subduction zone, but just three are credited with being the main water contributors. Ultramafic systems are dominated by antigorite and chlorite (Schmidt and Poli, 1998), each comprising ~ 13 wt% H₂O (Deer *et al.*, 1992), whilst lawsonite, which comprises ~11.5 wt% H₂O (Martin *et al.*, 2014), is significant in mafic systems.

There have been numerous studies of these hydrous minerals in natural rocks. Antigorite has been the subject of field (Peacock, 1987; Scambelluri *et al.*, 1995; Padron-Navarta *et al.*, 2008), geophysical (Cannat, 1993; Hyndman and Peacock, 2003; Rupke, 2004) and geochemical (Deschamps *et al.*, 2013; Spandler *et al.*, 2014) study. Chlorite has undergone broad-based study including crystallography (Jenkins and Chernosky, 1986; Bailey, 1988; Gemmi *et al.*, 2016), thermodynamic properties (Vidal *et al.*, 2001, 2005; Holland and Powell, 2011; Lanari *et al.*, 2014), geophysics (Tatsumi, 1986; Hacker *et al.*, 2003; Cagnioncle *et al.*, 2007), petrology (Evans and Trommsdorff, 1978; Poli and Schmidt, 2002), and chemical exchange mechanisms (Hunziker, 2003; Parra, 2005). Lawsonite is less-well studied but has undergone detailed field study (Ulmer, 2001; Zheng, 2009) and geochemical analysis (Martin *et al.*, 2014).

A different picture emerges with experimental studies of the same minerals. The stability fields of antigorite (Bromiley and Pawley, 2003; Padron-Navarta, Hermann, *et al.*, 2010a) and lawsonite (Pawley and Holloway, 1993; Schmidt and Poli, 1994) are well-constrained, complementing other studies and providing a comprehensive account of both minerals in a subduction setting. Chlorite, by contrast, has a clearly delineated stability field at low pressure, and without disregarding the importance and breadth of chlorite research, there remain key gaps in our knowledge of chlorite in the subduction zone. Four of these are covered below.

1.1 CHLORITE STABILITY

1.1.1 CHLORITE STABILITY AT HIGH PRESSURE

A significant gap exists with the pressure-temperature (P,T) stability field of chlorite at high pressure. Early experimental studies produced well-constrained chlorite stability to pressures relevant to the fore-arc (Yoder, 1952; Segnit, 1963; Fawcett and Yoder, 1966; Staudigel and Schreyer, 1977; Jenkins, 1981; Jenkins and Chernosky, 1986). More recent studies examined the high-pressure stability of chlorite within the sub-arc (Mysen and Boettcher, 1975; Pawley, 2003; Fumagalli and Poli, 2005; Grove *et al.*, 2006; Dvir *et al.*, 2011; Till *et al.*, 2012; Fumagalli *et al.*, 2014) and individual data points have also been determined as part of other studies (Bromiley and Pawley, 2002, 2003; Spandler *et al.*, 2014). Viewed together, there are few data at high pressure and therefore the maximum stability of chlorite remains poorly constrained.

1.1.2 CHLORITE STABILITY IN VARIED LITHOLOGIES AND COMPOSITION

A knowledge gap also exists with chlorite stability in chlorite of varied composition and in different lithologies. (Zanazzi *et al.*, 2009). In the subduction zone, chlorite forms metasomatically: chlorite schist and chlorite peridotite in the contact zone between the slab and the mantle wedge, and chlorite-rich veins and channels within the slab (Schmidt and Poli, 2014). The resulting chlorite lithologies reflect complex, semi-open chemical systems. Table 1.1 provides an overview of the compositional and chemical characteristics of the different lithologies in the subduction zone. Although the entire profile width may encompass as few as 20 kms, we see enormous variety of rock types and chemistry.

REGION	LITHOLOGY	COMPOSITION	Mg#
MANTLE WEDGE	Peridotite+Serpentinite+Chlorite	Ultramafic	X _{0.9}
	Chlorite	Ultramafic	X _{0.9}
	Serpentinite+Talc	Ultramafic	X _{0.9}
SUBDUCTION CHANNEL	Chlorite Schist	Hybrid mélange	X _{0.5-0.9}
	Metasediments	Sedimentary	X _{<0.5}
SLAB	Altered Oceanic Crust (AOC)	Mafic	X _{0.5-0.7}
	Gabbro+Serpentinite+Talc	Mafic	X _{0.5-0.7}
	Gabbro+Chlorite	Mafic	X _{0.5-0.7}
MANTLE	Peridotite+Serpentinite+Chlorite	Ultramafic	X _{0.9}

TABLE 1.1: Overview of the lithology, composition and chemistry in each region of the subduction zone

Numerous field studies have described chlorite within mafic (Evans and Trommsdorff, 1978; Miller *et al.*, 2009), ultramafic (Peacock, 1987; Smith, 1995) and hybrid mélange (Bebout, 1991; Sorensen and Grossman, 1993; Bebout and Barton, 2002; Mori *et al.*, 2014; Penniston-Dorland *et al.*, 2014; Bebout and Penniston-Dorland, 2016) lithologies. Similarly, geochemical studies (Manning, 2004; Fumagalli

and Poli, 2005; Marocchi *et al.*, 2007; Spandler *et al.*, 2008; Bulle *et al.*, 2010; Cooper *et al.*, 2012; Fumagalli *et al.*, 2014) have major, trace and isotopic character of the chlorite of varied composition. To date, however, experimental studies on chlorite stability, whilst acknowledging the field and geochemical evidence, have typically been synthesis experiments using pure end-member compositions which, by definition, are conducted within a closed chemical system using high free-energy starting materials (Fyfe and Mackenzie, 1969). Notwithstanding the importance of previous experimentation, a comprehensive understanding of chlorite stability requires its examination in varied lithologies and compositions.

1.1.3 CHLORITE STABILITY OF 'HYBRID' CHLORITE MÉLANGE

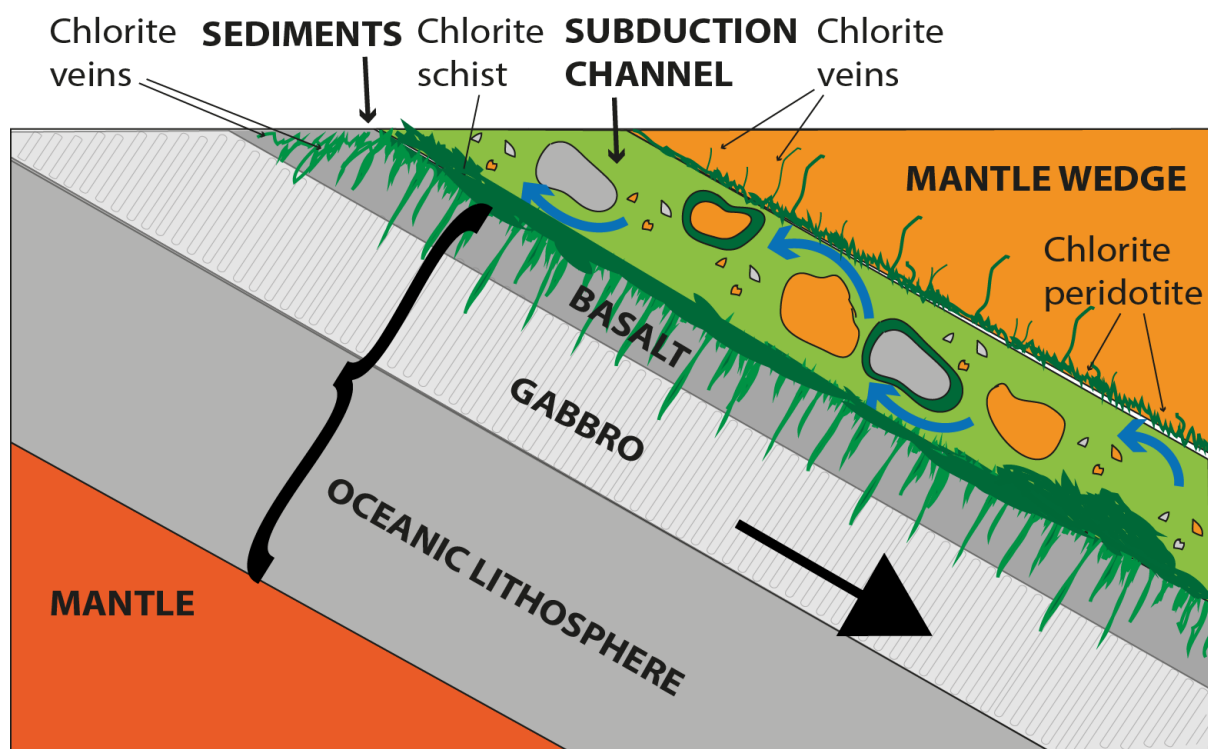


FIGURE 1.1: Cross-section of a typical subduction zone. *Cartoon is not to scale.*

The areas shaded in grey represent the slab components. Note the metasomatic rinds on the entrained rock fragments. It is thought that the subduction could explain the three-source signature of the fluids in arc magmas.

Another knowledge gap exists regarding ultramafic chlorite mélangé. Chlorite is formed in the subduction channel between the down-going slab and the hanging wall of the mantle wedge by the joint action of metasomatism and mechanical mixing of rocks from the slab, the mantle and sediments (Bebout and Penniston-Dorland, 2016). Figure 1.1 is a cartoon showing the juxtaposition of these contrasting lithologies.

The release of high-T, high-P fluids from the breakdown of hydrous minerals detaches fragments of rocks from the surface of the slab and the mantle wedge. As seen in Figure 1.1, these fragments

develop metasomatic rinds (Blanco-Quintero *et al.*, 2010) whilst the surface of the slab and the hanging wall of the mantle wedge are metasomatised creating mafic chlorite schist and chlorite peridotite respectively. Meanwhile, with the intermittent addition of fluid, the subduction channel is increasingly filled with chlorite-rich “hybrid” rocks (Spandler *et al.*, 2008; Marschall and Schumacher, 2012) which can form layers up to several tens of metres thick (Bebout and Barton, 2002; Spandler *et al.*, 2008; Miller *et al.*, 2009). The resulting lithology and geochemistry of these ultramafic chlorite schists are not found elsewhere on the planet, making them an important geological study. Unfortunately, to date, there have been no studies of the stability of chlorite in ultramafic chlorite mélangé although it is considered important to our understanding of subduction zone processes (Spandler *et al.*, 2008).

1.2 FLUID TRANSPORT MODELS THROUGH THE MANTLE WEDGE

Recent geochemical studies have shown that arc magma fluids possess three distinct ‘signatures’, indicating that they derive from a sediment source (Hermann and Spandler, 2008; Behn *et al.*, 2011; Plank, 2014), a slab source (Padron-Navarta, Tommasi, *et al.*, 2010b; Angiboust *et al.*, 2014; Bebout and Penniston-Dorland, 2016) and a mantle source (Ulmer, 2001; Tamura, 2003; England and Katz, 2010). The hybrid nature of chlorite mélangé outlined above provides a possible mechanism for this three-source signature to be contained within a single fluid (King *et al.*, 2006). Importantly, this would mean that chlorite mélangé possesses this three-part chemical signature prior to the commencement of fluid transport through the mantle. Can chlorite mélangé retain its three-component signature to an arc magma chamber?

Despite numerous studies on this topic, important questions remain. Do hydrous minerals dehydrate enabling ‘free’ water with its source signature to infiltrate the mantle? Is the fluid transported as part of a hydrous mineral melt? Does the water remain ‘bound’ in stable hydrous minerals until they melt within diapirs?

There are three general models that describe the transport of water through the subduction zone. These are described in turn below.

1.2.1 ‘FREE’ WATER RELEASED UPON CHLORITE DEHYDRATION

The commonly-held viewpoint is that hydrous minerals undergo metamorphic dehydration in the subduction zone, and release free water into the subduction channel (Poli and Schmidt, 2002; Abers, 2005; Fumagalli and Poli, 2005; Hermann *et al.*, 2006; Padron-Navarta, Tommasi, *et al.*, 2010; Wada *et al.*, 2012; Spandler and Pirard, 2013; Schmidt and Poli, 2014). This newly-liberated water performs

two immediate functions: it hydrates peridotite in the overlying mantle wedge which incurs its partial melting (Peacock, 1993; Schmadicke, 2000; Fumagalli and Poli, 2005; Padron-Navarta, Tommasi, *et al.*, 2010; Wada *et al.*, 2012; Scambelluri *et al.*, 2014; Schmidt and Poli, 2014), and it incurs the melting of proximal sediments (Spandler *et al.*, 2010; Tsuno and Dasgupta, 2012; Spandler and Pirard, 2013; Pirard and Hermann, 2015b; Turner and Langmuir, 2015). The melt from both sources rises buoyantly to eventually aggregate into reservoirs which feed arc volcanoes.

Within the subduction zone, the presence of low velocity anomalies which exhibit high electrical conductivity have been interpreted in several geophysical studies (Guillot *et al.*, 2001; Koyama *et al.*, 2004; Reynard *et al.*, 2011; Chantel *et al.*, 2012; Manthilake *et al.*, 2015) as free fluid liberated from hydrous minerals in subducting slabs. These results support the 'free water' model.

It is understood that volatiles have an important impact upon the partitioning of trace elements and large ion lithophile elements (LILE) between fluids and melts (Scambelluri *et al.*, 2004; John *et al.*, 2011; Li and Hermann, 2017). Some studies suggest that the role of sediment melt in element transport has been exaggerated (Keppler, 2017), and maintain that aqueous fluid rather than silicate melt is the main transport mechanism of LILE and trace elements due to the large, underestimated effect of chlorine on element partitioning (Kessel *et al.*, 2005a; Dalou *et al.*, 2012; Louvel *et al.*, 2014). Ongoing research will improve our understanding of this aspect of element partitioning.

1.2.2 CHLORITE MELTS BEFORE IT DEHYDRATES

A less prevalent view, and one tied inextricably to the location of the wet peridotite solidus (Mysen and Boettcher, 1975; Grove *et al.*, 2006, 2012; Till *et al.*, 2012; Nielsen and Marschall, 2017), is that at sub-arc conditions chlorite begins to melt before attaining maximum thermal stability. In this way, chlorite melt permeates the mantle wedge taking with it its entire complement of bound water. The infiltration of hydrous melt incurs further partial melting of mantle wedge peridotite, eventually collecting in a magma chamber in the upper crust.

1.2.3 CHLORITE RETAINS 'BOUND' WATER AND IS TRANSPORTED IN A DIAPIR

A third view (Cloos and Shreve, 1988; Castro and Gerya, 2008; Behn *et al.*, 2011; Hasenclever *et al.*, 2011; Marschall and Schumacher, 2012), strong among geophysicists, is that the hydrous minerals present in the subduction channel, being less dense than the peridotite in the hanging wall of the mantle wedge, trigger Rayleigh-Taylor instabilities (Castro and Gerya, 2008) and rise buoyantly as diapirs. These buoyant upwellings eventually aggregate into larger plume structures. A schematic of the mélange-diapir model is shown in Figure 1.2.

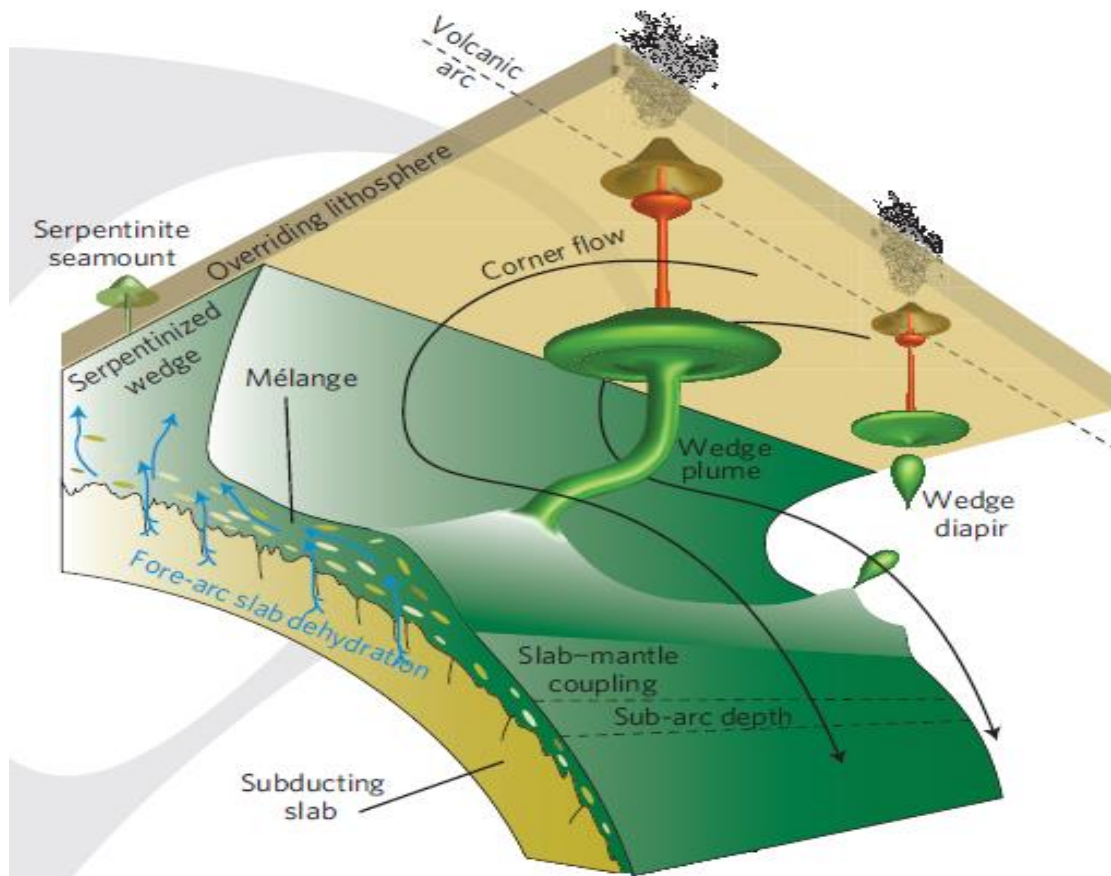


FIGURE 1.2: Three-dimensional representation of a mélangé-diapir model.

Note the diagonal movement of mélangé into the mantle wedge and the aggregation of diapirs into vertical plume conduits where melting takes place. Cartoon extracted from (Marschall and Schumacher, 2012).

The diapiric model has gained much traction recently. Tomographic (Gerya *et al.*, 2006; Castro and Gerya, 2008; Marschall and Schumacher, 2012), thermal (Peacock, 2004; Syracuse *et al.*, 2010) and numerical (Richard *et al.*, 2010) modelling reveals irregular structures interpreted as diapirs and/or plumes, even though 3D models are not yet well constrained (Behn *et al.*, 2011; Hasenclever *et al.*, 2011; Marschall and Schumacher, 2012). Diapirs provide a conduit for the rapid transport of material from the subduction channel through to the hottest part of the mantle wedge. This is assisted by the action of corner flow which forces the diapir to rise diagonally (Cagnioncle *et al.*, 2007) from the subduction channel into the mantle wedge (Marschall and Schumacher, 2012). The rapid ascent means that only the outermost layer of the plume structure will melt (Hall and Kincaid, 2001), so chlorite remains at below-solidus temperatures. This point is significant as it means all fluids contained within chlorite will be retained within the plume structure until the onset of melting, guaranteeing a large fluid injection into the arc magma source. Diapirs appear to form regularly spaced structures in the mantle wedge (Behn *et al.*, 2011) and could explain the regular spacing of arc volcanoes (Tatsumi, 2003; Wiens *et al.*, 2008). Diapiric and plume flow also allows around 5 Ma for ^{10}Be to complete its journey from sediments through the mantle wedge to arc volcanoes, which is

within an agreed geochemical timeframe (Marschall *et al.*, 2007; Behn *et al.*, 2011; Marschall and Schumacher, 2012). All three models have direct implications for fluid transport mechanisms within the subduction zone. Each offers contrasting insights into how these inter-related processes operate. Fundamental to each model is a set of assumptions governing the chlorite stability field which, as the above introduction has revealed, is at present poorly constrained and requires extensive investigation. This thesis seeks to address these inter-related questions.

1.3 PURPOSE OF THE STUDY

1.3.1 STUDY AIMS

The preceding introduction highlights significant knowledge gaps that exist regarding chlorite stability and this has implications for numerous subduction zone processes. The thesis aims to remedy this situation with a research program comprising three related aims:

To constrain the stability field of chlorite in chlorite schist, chlorite lherzolite and chlorite harzburgite.

To investigate if chlorite breaks down into anhydrous or hydrous mineral assemblages.

To examine the implications of chlorite stability upon slab diapir and mantle melting models

The research program will use a multi-faceted approach. A comprehensive suite of ninety-five piston cylinder experiments, which replicate the P,T conditions in the subduction zone, will form the basis of the study. The contents of each experimental capsule will undergo petrographic examination and geochemical analysis. The results will enable each of the project aims to be fulfilled.

1.3.2 THESIS OUTLINE

This thesis has been compiled using a traditional structure.

Chapter Two outlines the methodology employed in completing the experimental component of the study. The methods used in each set of experiments were similar and so they have been expounded in a single section. Firstly, the preparation of starting material is described. Secondly, step-by-step details of the experimental process have been explained: capsule and assembly production, the piston cylinder equipment and the running of the experiment, and the post—experiment procedure. Thirdly, a description of analytical procedures was provided including use of FE-SEM, XRD and Raman methods. This chapter concludes with a brief discussion on the P,T calibration of the piston cylinder equipment.

Ultramafic chlorite schist/mélange/hybrid formed the focus of Chapter Three. This is the first experimental study of chlorite stability in this rock type. Twenty-nine piston cylinder experiments determined the full extent of the chlorite stability field at sub-arc conditions with a focus on the terminal chlorite reaction - chlorite \rightarrow garnet + olivine + H₂O \pm spinel - identified in previous chlorite research. An unfamiliar hydrous mineral, 11.5Å-phase, appeared in run products accompanying chlorite breakdown at high pressure. This was also fully described in this chapter. As the bulk composition contained minor chromium and iron, the effect of the addition of these elements was able to be ascertained. Finally, experimental results were able to estimate the quantity and rate of water release that occurred with chlorite breakdown.

Chapter Four used data from forty-five piston cylinder experiments to examine chlorite stability in a model chlorite lherzolite and a chlorite harzburgite using two key chlorite reactions identified by previous research: the first - chlorite + clinopyroxene \rightarrow garnet + olivine + H₂O \pm spinel; and the second - chlorite + orthopyroxene \rightarrow garnet + olivine + H₂O \pm spinel. Experimental results enabled each reaction to be clearly differentiated in P,T space. The second reaction produced an unexpected phase at high pressure – Mg-sursassite (MgS) – which replaced garnet with increasing pressure. The presence of Ca in the starting material enabled its effect on chlorite stability to be determined.

Chapter Five comprised two parts. The first examined the stability of chlorite in a mafic chlorite schist. The results were used to check the validity of the mélange diapir model (Marschall and Schumacher, 2012). Experimental results enabled the determination of the maximum thermal stability of low Mg# chlorite at 3.0 GPa, and the density of product material at each experimental point. The second part of this chapter examined the same chlorite schist used in Chapters Three and Four to determine the onset of melting. This was to check the validity of a recent study (Till *et al.*, 2012) regarding the location of the wet peridotite solidus.

Chapter Six provided an overview of all research findings, their implications for subduction zone processes, and directions for further investigative work.

CHAPTER 2 : METHODOLOGY

The central design of this thesis was to explore the wider stability field of chlorite formed in a range of subduction settings. When metasomatic fluids released from the down-going slab contact peridotite in the mantle wedge, ultramafic chlorite peridotite is formed. Chlorite schist, by contrast, is formed within the narrow subduction channel between the slab and the mantle wedge when fluids released from the down-going slab are mixed metasomatically and tectonically, creating a mélangé rock of mafic to ultramafic composition. Chlorite formed from either process reflects complex, semi-open chemical systems which contrasts with the bulk of previous experimental studies of chlorite which involved synthesis experiments modelled in a closed chemical system. This thesis encompasses four series of experiments which use minerals extracted from only naturally-occurring rocks, reflecting more complex chemical systems associated with actual geological processes.

2.1 SAMPLE PREPARATION

Several natural minerals were used in the four series of experiments undertaken in this thesis. All minerals were extracted from natural rock samples collected by other researchers on various field expeditions.

2.1.1 SAMPLE SELECTION

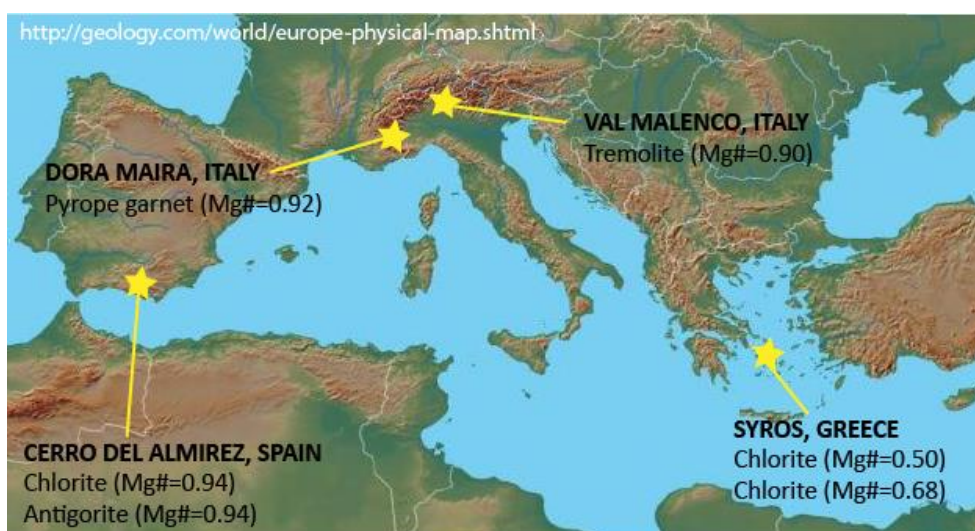


FIGURE 2.1: Location of the components of the starting mixes.

Series 1 experiments used two natural minerals. Chlorite was extracted from a chlorite schist sourced from the Cerro del Almirez in the Sierra Nevada mountains of south-east Spain. Subsequent analysis revealed trace amounts of natural antigorite. Natural pyrope garnet was sourced from the Dora Maira in the northern Italian Alps.

Experiments in Series 2 used four natural minerals. The chlorite schist and the pyrope garnet used in Series 1 experiments was also used in this series of experiments. Antigorite was extracted from a serpentinite also found from the Cerro del Almirez in the Spanish Sierra Nevada mountains. Tremolitic amphibole was sourced from Val Malenco in the Italian Alps.

In Series 3, chlorite with contrasting Mg# was required to complete the experiments. Thin-sections of fifteen different rock samples were examined prior to making a final selection of three. The chlorite schist used in Series 1 and 2 was selected due to its high Mg# (0.94). Two further rock samples from Syros in Greece were chosen – a chlorite-omphacite-ilmenite-epidote-titanite schist (Mg#=0.50) and a chlorite-apatite-ilmenite-garnet schist (Mg#=0.68).

Further details of each of the selected minerals are provided in the methods section of the relevant chapters.

2.1.2 SAMPLE PROCESSING

Each mineral was extracted by hand from the selected rock samples. Conveniently, the antigorite and garnet had already been extracted, ground and stored in sample bottles. Other minerals, however, had to be removed by hand from the sample. Using a microscope, tremolite was removed by hand from an amphibole schist then ground using an agate pestle and mortar under acetone for thirty minutes. Grain size consistency was checked under a microscope and the grinding process continued until a consistent grain size <40µm was attained. A rock saw was used to isolate the chlorite-rich vein from each sample of schist. Each was then hand-milled and ground using the same method as outlined above. Each resulting paste was placed in a drying oven at 110°C overnight to dry. The dried powder was placed in a sample bottle and retained until needed.

2.1.3 X-RAY DIFFRACTION (XRD) ANALYSIS OF NATURAL MINERALS

Since natural minerals were being utilised in this experimental series, it was crucial to confirm the constituents of each prior to preparing starting mixes. Powder X-Ray Diffraction was used to accomplish this.

A small quantity of the ground mineral was placed in an agate mortar and ground under acetone until a grain size of 10-20 μm was attained. Using a pipette, the material was gradually added to the surface of an amorphous silica plate, left to dry before being placed in a sample holder inside the apparatus. This was a Siemens D5005 Bragg-Brentano Diffractometer which emitted cobalt $K\alpha$ radiation. The device was equipped with a scintillation detector and a graphite monochromator. Each scan was conducted in the range 2° to 130° 2-theta, a step width of 0.02° , and a scan speed of two seconds per step.

This method successfully identified all constituent minerals. However, the platy minerals such as chlorite proved problematic due to crystal preferred orientation (CPO) which produced scans where peak positions were accurate but peak heights varied from those in the database. The resulting scans were corrected for background noise and interpreted using the software Eva Diffracplus version 10.0 with database PDF-2.

XRD scans were taken of a mystery phyllosilicate mineral to confirm its identity. This required an analytical method which would deal effectively with CPO of this mineral: the XRD device from the Research School of Chemistry at ANU was employed. It was fitted with a stage which revolved the sample through spherical space which overcame the difficulties posed by CPO. A sample from Run UHPPC332 was analysed with a PANalytical Empyrean powder X-ray diffractometer (Bragg Brentano geometry, fixed divergence slits) using CuK alpha radiation. The scan range was 4° to 140° 2-theta at a data point separation of 0.01313° 2-theta. The detector was a PIXcel 1D detector with an active detector length of 3.3473 degrees using 255 channels and collection time of 0.1438 secs per step. Background noise was eliminated from the scan and interpreted using Eva Diffracplus software.

2.1.4 MINERAL SEPARATION

XRD analysis revealed that the chlorite schist contained far more orthopyroxene and serpentinite than expected. An attempt was made to remove these by hand under a microscope but the relatively fine grade of the grains rendered this approach unproductive.

The sample was sent to the Mineral Separation laboratory at ANU. Density contrast technique was used to separate the chlorite from the other phases and the sample was returned as analytically $\sim 90\%$ chlorite. Visually it appeared to be more like 100% chlorite. To confirm the proportion of chlorite, an epoxy mount was made which contained a small amount of the treated chlorite and it was analysed using SEM to confirm phases present. SEM analysis revealed that it was $\sim 99\%$ chlorite with $\sim 1\%$ antigorite and no orthopyroxene present. Details of mount construction and SEM analysis is provided in 2.2.6 and 2.2.8 below.

2.1.5 PREPARATION OF STARTING MIXES

The ground minerals prepared above were used to prepare each of the starting mixes. Molar proportions of each were calculated, weighed and placed in an agate mortar with acetone. The minerals were ground for forty-five minutes to homogenise the mixture. The paste was transferred to a specimen bottle and placed in a drying oven at 110°C overnight to dry. The dried mix was retained until needed for experimentation.

2.1.6 STARTING MIX ANALYSES

The chemical composition of each of the starting mixes used in the current study are shown in red in Table 2.1. Further details (chemography, etc.) are provided as relevant in the ensuing chapters. For context, the starting mixes of four recent high-pressure experiments on chlorite stability have also been provided, shown in blue, green, purple and orange text respectively. All compositions shown have been normalised to anhydrous proportions for ease of comparison.

	LAKEY Series 1	LAKEY Series 2	LAKEY SY3	LAKEY SY4	F&P 2005	F&P 2005	F&P 2005	FUM 2014	FUM 2014	FUM 2014	PAWLEY 2003	TILL 2012
	Chl schist	Chl perid	Chl schist	Chl schist	PX	LZ	HZ	A	B	C		H&Z+H2O
Oxide	wt%	wt%	wt%	wt%	wt%	wt%	wt%	wt%	wt%	wt%	wt%	wt%
Na2O	0.00	0.11	1.96	0.18	0.82	0.19	0.30	0.00	0.00	0.00	0.00	0.33
K2O	0.00	0.00	0.02	0.00	0.00	0.00	0.00	0.00	0.00	0.00	0.00	0.03
MgO	39.48	37.38	8.81	20.56	27.38	40.59	42.42	41.28	40.62	39.64	41.08	37.82
SiO2	39.35	42.55	37.27	29.30	45.41	45.75	45.63	36.99	36.31	35.44	45.93	46.20
Al2O3	14.94	12.24	16.58	18.55	8.26	3.33	1.46	19.39	15.41	10.01	12.99	4.06
NiO	0.22	0.20	0.29	0.00	0.00	0.00	0.00	0.00	0.00	0.00	0.00	0.28
FeO	4.24	4.37	21.40	20.05	9.81	7.03	9.62	0.00	0.00	0.00	0.00	7.56
MnO	0.00	0.02	0.21	0.29	0.00	0.00	0.00	0.00	0.00	0.00	0.00	0.10
Cr2O3	1.77	1.56	0.00	0.00	0.00	0.00	0.00	2.34	7.66	14.91	0.00	0.40
CaO	0.00	1.58	8.31	4.52	8.32	3.11	0.57	0.00	0.00	0.00	0.00	3.22
TiO2	0.00	0.00	5.15	4.28	0.00	0.00	0.00	0.00	0.00	0.00	0.00	0.18
P2O5	0.00	0.00	0.29	2.27	0.00	0.00	0.00	0.00	0.00	0.00	0.00	0.00
Total	100.00	100.00	100.00	100.00	100.00	100.00	100.00	100.00	100.00	100.00	100.00	100.00

TABLE 2.1: A typical capsule assembly used in piston cylinder experimentation.

Table showing starting mixes used in the current study, and in recent high-pressure chlorite stability studies. Compositions have all been normalised to anhydrous proportions for clarity. Abbreviations: "F&P"=(Fumagalli and Poli, 2005); "FUM"=(Fumagalli et al., 2014).

2.2 EXPERIMENTAL PROCEDURE

All experiments were performed at the Research School of Earth Sciences at the Australian National University using end-loaded, Boyd-England–type piston cylinder apparatus across a range of pressures (1.0 GPa to 6.3 GPa) and temperatures (500°C to 1150°C).

Each experiment required the construction of several components: a capsule to house the powdered rock sample, sleeves comprising MgO and NaCl to provide the capsule with a physical buffer against a

high-pressure, high-temperature environment, and a graphite heater which created an electrical circuit for temperature readings. An overview of the entire experimental process is provided below.

2.2.1 CAPSULE PRODUCTION

Each capsule was constructed from a 9mm length of gold (Au) tubing with an external diameter of 2.3 mm. Gold was selected since it limits water loss at $T < 1000^{\circ}\text{C}$ (Truckenbrodt and Johannes, 1999) and Fe loss (Green *et al.*, 2014). One end was crimped, and using a Tungsten Inert Gas (TIG) bench welder and a microscope, the crimped end was welded to create a complete seal, then compressed to create a flat end surface. The completed capsule was weighed with the value recorded for future reference. A balance was used to measure 0.02 grams of starting mix which was pressed into the open end of the gold capsule. The open end of the capsule was then crimped, TIG-welded and compressed. The completed capsule was a cylinder approximately 5-6mm in length. The capsule was re-weighed and checked with previous measurements to ensure that the hydrous minerals in the starting mix did not dehydrate during the welding process.

2.2.2 CAPSULE ASSEMBLY

The sealed gold capsule was placed inside an elaborate assembly which is shown in Figure 2.2a. Four sections of MgO tubing were measured and cut to size using a lathe: the first (Figure 2.2c) was hollow to accommodate the thermocouple and was positioned above the capsule; the second (Figure 2.2g) was solid and was positioned below the capsule; the third (Figure 2.2f) was cut to match exactly the capsule's length and width and acted as a container for the capsule; the final piece (Figure 2.2d) was a 0.6mm spacer* placed between the end of the thermocouple and the capsule to prevent any reaction between the two. All four sections were inserted in order into a hollow, cylindrical graphite heater (Figure 2.2h) itself cut and shaped on the lathe to accommodate precisely the MgO tubing.

** The first twenty-eight capsules were prepared using a 1.5mm MgO spacer. This was changed to a 0.6mm spacer when it was realised that incorrect temperature readings may have been recorded using a too-thick spacer. A calibration experiment (D1651 at 3.5 GPa/770°C) was undertaken to compare results with the original one at these P/T conditions (D1644). The results were identical, confirmed by SEM and EMPA analyses and mass balance calculations, which verified the original experiments.*

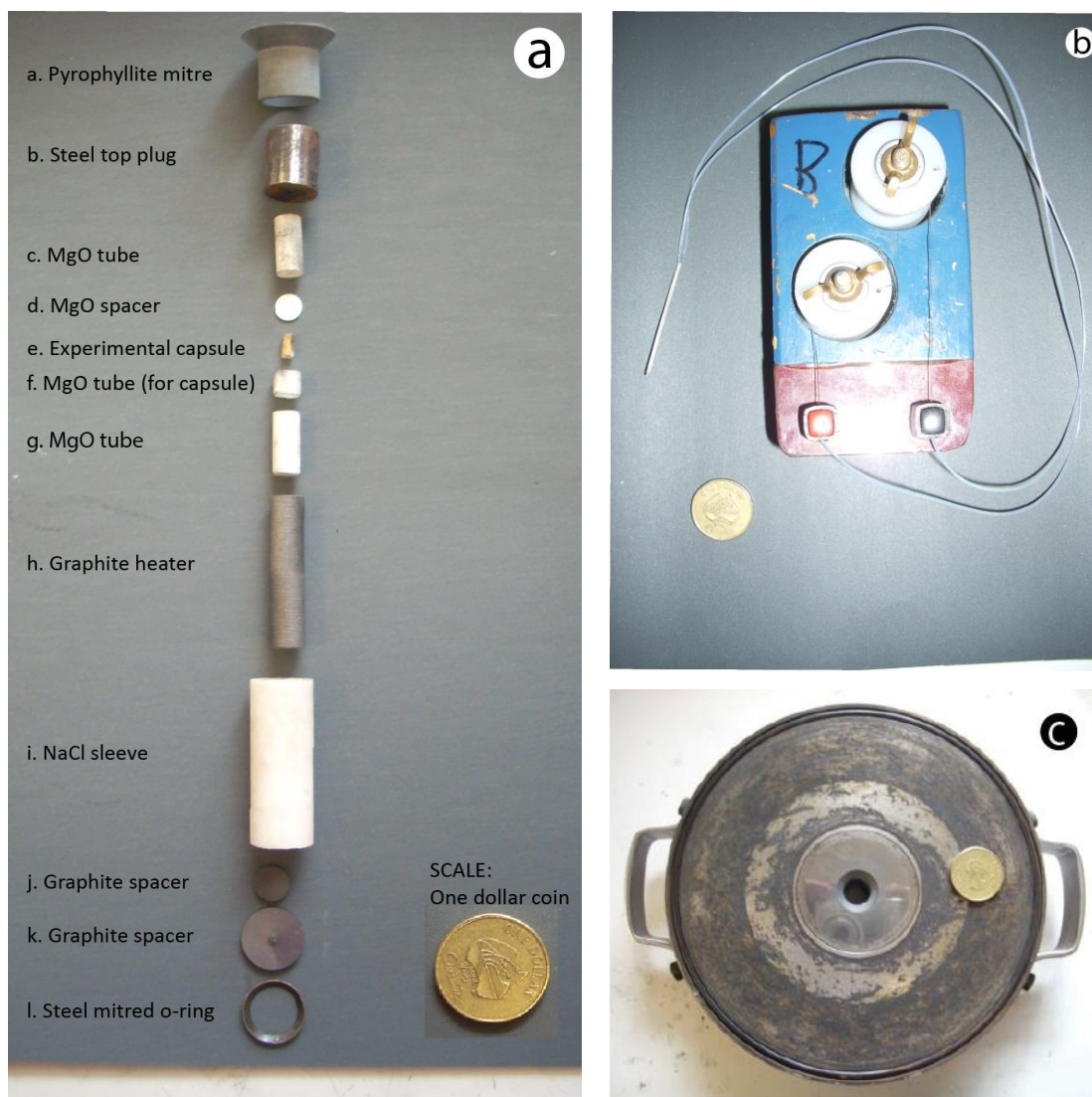


FIGURE 2.2: A typical capsule assembly used in piston cylinder experimentation.

a) a photograph of the actual components which comprise a single piston cylinder experimental assembly; b) completed thermocouple showing mullite tubing and spot-welded wires; c) 0.5-inch pressure vessel.

The graphite heater containing capsule and the MgO assembly was inserted into a NaCl sleeve (Figure 2.2i) which acted as a pressure medium. The salt sleeve was in turn wrapped in a teflon foil to minimise friction and both were inserted into the 0.5-inch diameter central chamber of a pressure vessel (Figure 2.2c). The graphite spacers (Figure 2.2j and k) were inserted into the base of the salt sleeve and were secured with a steel O-ring (Figure 2.2l). On the upper side of the pressure vessel, a steel-carbide top plug (Figure 2.2b) was placed inside a fitted 0.5-inch pyrophyllite mitre flange (Figure 2.2a) and both inserted to secure the capsule assembly inside the pressure vessel. Together, the top plug, graphite heater and two graphite spacers created an electrical circuit around the capsule, allowing the thermocouple to determine the temperature for the duration of the experiment.

2.2.3 THERMOCOUPLE PRODUCTION

The B-type thermocouple (Figure 2.2b) comprised two platinum-rhodium wires ($\text{Pt}_{94}\text{Rh}_6/\text{Pt}_{70}\text{Rh}_{30}$) inserted through an exact length of two-bore mullite tubing. The two wire ends were spot-welded which formed a small metal knob at the end of the mullite tubing. The completed thermocouple was inserted lengthways through the top plug and into the hollow MgO tubing assembly in readiness for the experiment.

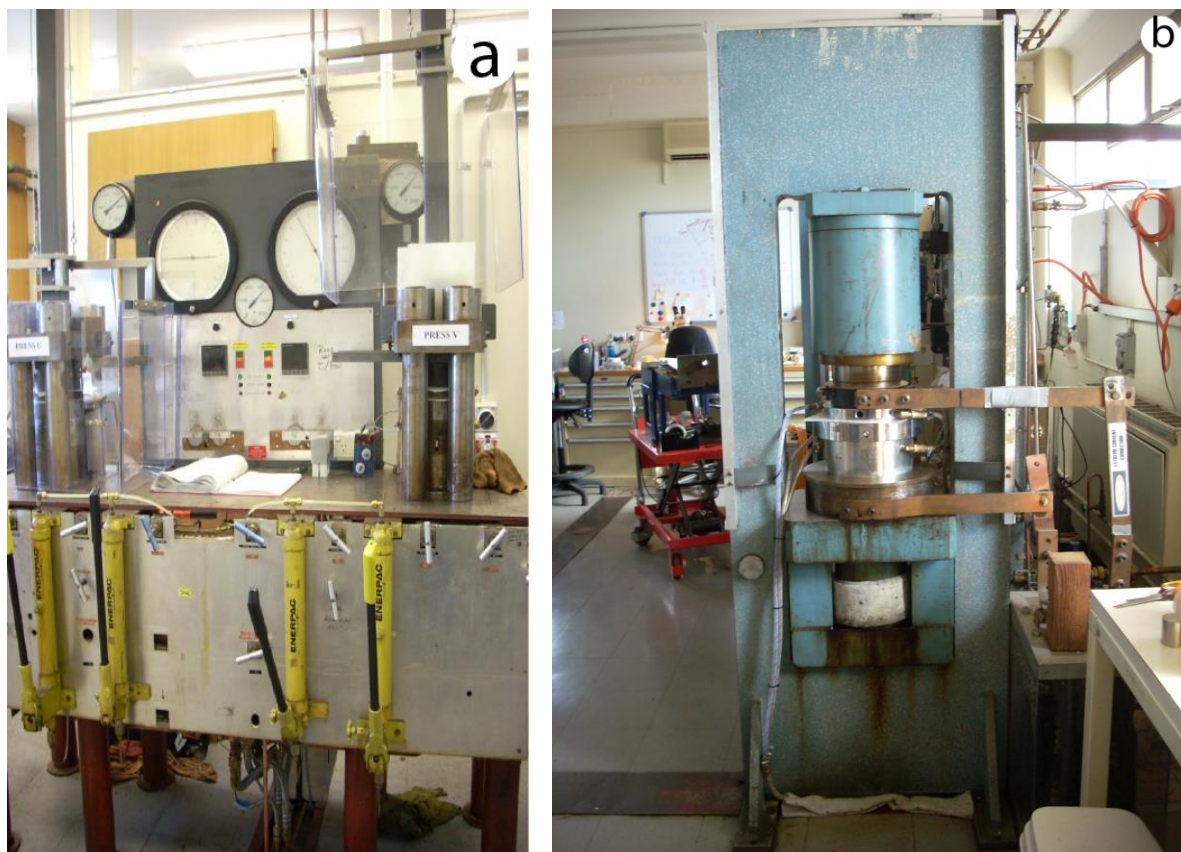


FIGURE 2.3: Piston cylinder devices in the ANU Experimental Petrology laboratories.

a) typical Boyd-England type, 200t high-pressure piston cylinder apparatus; b) an ultrahigh-pressure 500t piston cylinder apparatus.

2.2.4 EXPERIMENTAL RUN USING HP AND UHP PISTON CYLINDER APPARATUS

Experiments conducted <4.5 GPa were carried-out using a Boyd-England-type, 200t, end-loaded high-pressure (HP) piston cylinder apparatus (see Figure 2.3a). The HP apparatus consisted of three main sections: an upper section, comprising fixed and removable spacer plates; a central bridge area, which acted as the staging platform upon which the pressure vessel containing the capsule assembly was positioned; and a lower section, containing a pressure ram which moved up to provide both the confining and sample pressure during the experiment.

The loaded pressure vessel was placed onto the bridge and aligned with the protruding 32mm piston. The thermocouple was then inserted, attached wires secured and the pressure vessel covered with a mylar sheet. The top plate was positioned and confining pressure of approximately 8000 psi was added to the stack to secure all parts. After connecting electrical cables and high-pressure water hoses and setting the Eurotherm 904 temperature controller, water and power to the apparatus was switched on. Sample pressure was added manually to the system with ~69 MPa and ~276 MPa hand pumps, with care taken to ensure that the rate of increase for both temperature and pressure was even.

The experiment was monitored for the duration of each run. Notes were recorded in the official log book for future reference. Each experiment was quenched by switching off the power supply.

Experiments conducted at 4.5 GPa–6.0 GPa were carried-out using a 500t Harwood ultrahigh-pressure (UHP) piston cylinder apparatus (Figure 2.3b). The UHP apparatus had a similar design and operated under the same principles as the 200t press. The equipment also comprised three main sections. However, two separate rams were involved. The upper 500t ram lowered to provide the confining pressure whilst the lower 200t ram moved up to apply the sample pressure. The central bridge acted as staging platform for the assembling of the experimental components.

Once the pressure vessel was fitted with the capsule assembly, it was placed on the bridge over the shorter 27mm piston. Confining pressure of approximately 69 MPa (10,000psi) was added manually to the system. A micrometer was secured to the bridge and set to zero: its role was to monitor piston movement during the run. The experimental temperature was set and controlled using a Eurotherm 904 device, known to be accurate to $\pm 3^{\circ}\text{C}$ (Spandler *et al.*, 2010).

Once the apparatus was activated, its operation became fully automated. Users were able to create a program for individual experiments which determined pressure, duration of experiment and ramp rate. Once the program commenced, the entire operation was automated by LabView software, version 2.12 and so variations in confining and sample pressure were computer-controlled for the duration of the experiment. In the first few hours of each run, friction decay in the assembly led to relatively large piston movement and subsequent confining and sample pressure adjustments were made in response. This diminished within hours and typically ceased after twenty-four hours. When the program ended, the power was cut and quench duration was typically ~5 secs.

The capsule assembly and equipment were inspected for damage at the end of each experimental run on either press. If the capsule had ruptured or sheared, or the piston showed signs of cracking, the experiment was deemed a failure.

2.2.5 CALIBRATION OF PRESSURE AND TEMPERATURE ON PISTON CYLINDER APPARATUS

On the HP press, temperature was measured using a B-type thermocouple (Pt₉₄Rh₆/Pt₇₀Rh₃₀) known to be accurate to $\pm 5^\circ\text{C}$ (Padron-Navarta *et al.*, 2010a; Omega Engineering, 2011; Spandler *et al.*, 2014). Pressure calibrations determined in previous experimental studies have an accuracy to ± 0.1 GPa (Padron-Navarta *et al.*, 2010a; Spandler *et al.*, 2014; Hermann *et al.*, 2016).

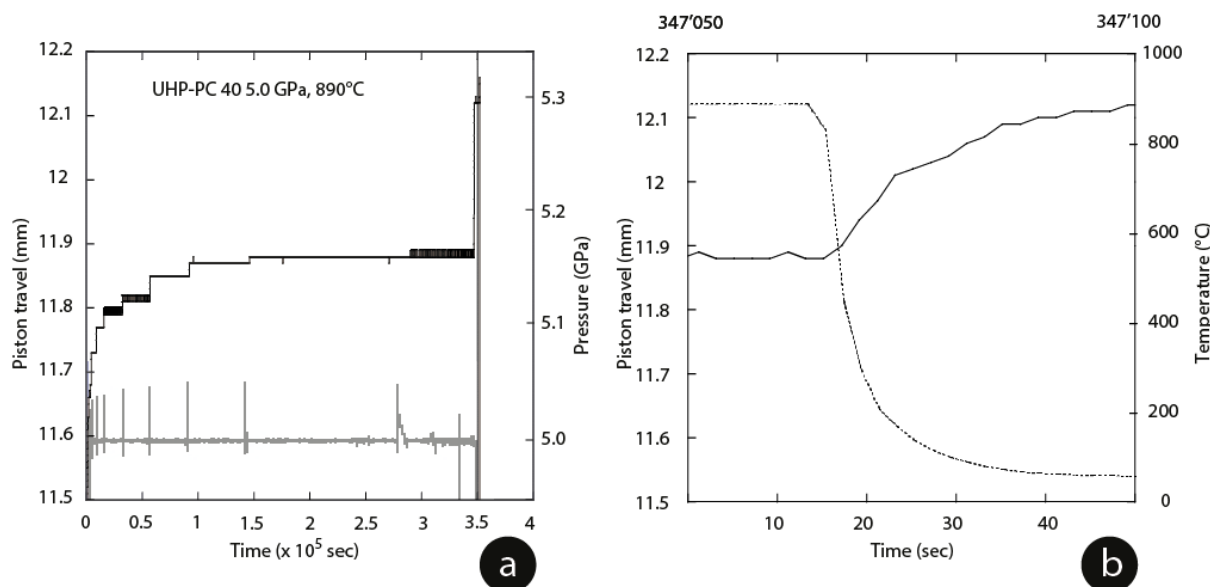


FIGURE 2.4: Experimental pressure log on the UHP 500t press at ANU laboratory.

a) The nominal pressure reading (grey line) and the piston travel (black line) during a 96-hour experiment. The piston has travelled $>0.2\text{mm}$ after the commencement of the experiment, indicating friction decay, with a steady state achieved after approximately 40 hours. Large vertical grey spikes indicate the automated system response in maintaining the 5.0 GPa nominal pressure. b) an expanded view of the quench period. Thanks to J. Hermann for permission to use this Figure, extracted from (Hermann *et al.*, 2016).

Experiments on the UHP press also used B-type thermocouples (Pt₉₄Rh₆/Pt₇₀Rh₃₀) as described above. Although this device has not been formally calibrated for its pressure readings, previous researchers have found high accuracy between readings of sample vs nominal pressure (Spandler *et al.*, 2014; Hermann *et al.*, 2016). In this series, piston travel was closely monitored for the entirety of each run (see Figure 2.4a). Since piston movement was minimal after the first 24 hours of the experiment, the charge was deemed to be at a constant state for a minimum of 48 hours in all experiments. Therefore, we can assume that the sample pressure was directly converted to nominal pressure and can be considered accurate to ± 0.1 GPa as for the HP press.

Several experimental studies attest to the accuracy of the nominal pressure of the UHP press. In Chapters 3 and 4, examination of phase relations revealed that two high-pressure hydrous phases - Mg-sursassite and 11.5Å-phase - first appeared in run products at temperature $<750^\circ\text{C}$ and pressures at 5.0 GPa or above. Previous studies of these phases showed that the low pressure boundary of their

respective stability fields concur with these P,T conditions (Bromiley and Pawley, 2002; Fumagalli *et al.*, 2014; Gemmi *et al.*, 2016). Hermann (Hermann *et al.*, 2016) conducted experimentation using the UHP press and reported pressure calibrations were accurate at low temperatures. Examined together, it can be assumed that the nominal pressure of the UHP press is accurate.

2.3 POST-EXPERIMENT PROCEDURE

After each run, the assembly was extracted from the pressure vessel and the gold capsule retrieved. It was re-weighed to ensure that it remained intact during the experiment. The capsule was pierced using a scalpel and a visual and aural check was made for 'free'-fluid, determined by a 'hiss' or 'fizz' at the point of incision. The capsule was re-weighed to ascertain any actual loss of weight at this point, then placed in the drying oven at 110°C overnight to fully dehydrate. The next day its weight was again checked against previously recorded values; any weight discrepancy resulted in the rejection of the capsule.

2.3.1 CONSTRUCTING THE MOUNT

The contents of the dry capsule were exposed using 1200 µm wet/dry emery paper. With the centre of the capsule exposed, a single drop of epoxy resin was placed over the contents and the capsule was placed inside a bench vacuum chamber for at least fifteen minutes to allow the epoxy to penetrate and secure the contents. A section of double-sided tape was attached to the cleaned surface of a 6cm glass square onto the centre of which was positioned the capsule, contents-side down. A plastic cylinder was placed over the capsule and secured by the double-sided tape to act as a mould. Epoxy resin was poured into the mould and the assembly returned to the bench vacuum for at least ten minutes to remove bubbles from the liquid resin. The assembly was left to harden overnight.

2.3.2 POLISHING THE MOUNT

The resulting disc containing the experimental capsule was cleaned with ethanol, and the capsule contents carefully re-exposed using 1200 µm dry emery paper. The disc was shaped to size using a lathe and then placed on a lapping machine and polished with discs of decreasing grit size (6 µm, 3 µm, 1 µm, ¼ µm) using a single drop of lubricating spirit on each disc. The polishing process took between fifteen to thirty minutes during which time the surface was checked under the microscope for absence of deep scratches. When suitably polished, the disc was cleaned with ethanol, dried and coated with a 12nm layer of carbon using a carbon-coating device, labelled and stored in a mount tray in preparation for chemical analysis.

2.3.3 PERFORMING CHEMICAL ANALYSES

To ascertain accurate chemical composition of the major and minor elements comprising run products, two different analytical techniques were used. A Scanning Electron Microscope (SEM) was used to identify the phases present in each charge and to take high quality microphotographs of phase textures. This was followed up with the use of an Electron Microprobe (EMPA) which was used to provide high quality, standardised chemical analysis of the product phases.

The SEM analysis was completed using a JEOL JSM-6610A apparatus fitted with a JEOL Energy Dispersive Spectrometer (EDS) enabling semi-quantitative analysis using Analysis Station software package version 2.24. Each analysis was undertaken with an accelerating voltage of 15 keV, a beam current of 1nA, a working distance of approximately 10mm, a count time of 100s and a count rate between 8000cps and 12000cps. Major oxides were calculated based on total cation number normalised to 100 wt% oxide using ZAF Gaussian methodology. Back-scattered electron (BSE) and Secondary Electron Image (SEI) modes were used to collect photographs of phase relations in each experiment, typically at 2000x resolution.

The first twenty-two charges were analysed using the EMPA which used a Cameca SX-100 electron microprobe utilising Wave-Dispersive Spectroscopy (WDS) with accelerating voltage set to 15keV and the beam current to 20nA. Peak and background count time varied between 10s and 30s depending on the element. A JEOL EDS detector was used to identify each phase prior to spot analysis. Secondary standards were used to quantify elemental concentrations. Natural standards included: garnet (Roberts Victor Mine South Africa USNM 87375), chromite (Tiebaghi mine, New Caledonia USNM 117075), olivine (San Carlos Olivine, Gila Co, Arizona USNM 111312/444), augite (Kakanui, New Zealand USNM 122142), hornblende (Kakanui, New Zealand USNM 143965) and a rutile standard.

Larger grains proved easy to analyse; unfortunately, most product phases were of small grain size and the poor quality of EDS images on the EMPA meant that many points of analysis were imprecise which led to a loss of confidence in overall accuracy of data. What to do? It was thought the SEM analyses would suffice since they showed strong agreement with analyses of the same charges from the EMPA. However, the absence of a Faraday Cup on the SEM meant that standardisation was a problem.

To ascertain the level of agreement in between SEM and EMPA analyses, the same experimental charges were analysed using EDS (SEM) and WDS (EMPA). The results are shown in Figure 2.5.

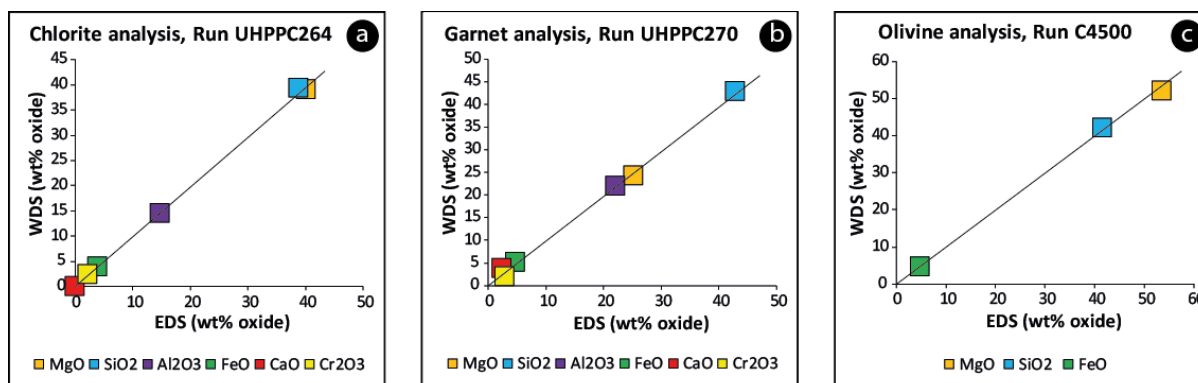


FIGURE 2.5: Comparison of EDS vs WDS analyses of major oxides in chlorite, garnet and olivine.

a) Plot comparing EDS and WDS analyses of in chlorite; b) Plot comparing EDS and WDS analyses in garnet; c) Plot comparing EDS and WDS analyses in olivine. Analyses of major oxides in each phase shows strong agreement between both analytical methods. This indicates that EDS analyses from the SEM could be used instead of WDS analyses from the EMPA.

The resulting 1:1 linear relationship between each EDS and WDS analysis show excellent agreement. However, the problem of data standardisation with the SEM, an obligatory requirement for any future publication, remained so another analytical device was sought.

Eventually, it was decided to use a Hitachi 4300 SE/N Schottky field-emission, scanning electron microscope (FE-SEM) housed at the Centre for Advanced Microscopy at the Australian National University (see Figure 2.6). A beam current of 0.600nA (standardised using a Faraday Cup), an accelerating voltage of 15kV, a working distance of 25mm, and a total scan time of 90 seconds were the operating conditions used for all analyses.

All twenty-two charges which had previously been analysed using the EMPA were re-analysed using the FE-SEM to ensure consistency of data. All later capsules were analysed only using the FE-SEM.

In each of the analytical devices used, chemical analyses were checked for stoichiometric accuracy, totals, cation number and relative proportion of each oxide. Errant results were rejected. See Appendix for tables of complete analytical results.



FIGURE 2.6: Hitachi 4300 SE/N Schottky field-emission, scanning electron microscope (FE-SEM)

2.3.4 MASS BALANCE

For each phase identified in each experimental run and in the starting composition, the average analysis and standard deviation was calculated for each element of interest. Using this data, phase abundances were calculated using the weighted least squares method (Herrmann and Berry, 2002). A summary is presented in Table 3.3; full results have been included in the Appendix.

FE-SEM analyses of garnet revealed a consistent 0.03 wt% deficiency on the Al site which was inferred to have been filled by Fe^{3+} . As no magnetite was identified in any run product, the Fe^{3+} was considered an analytical artefact. The H_2O content of hydrous phases could not be measured by FE-SEM and so were calculated stoichiometrically.

2.3.5 PERFORMING RAMAN ANALYSES

In order to better characterise a newly-identified hydrous mineral, it was decided to perform a series of Raman analyses. Once a Raman profile was identified, future researchers could use this technique to quickly identify this phase. Two samples of this mineral were analysed using a Renishaw inVia Raman spectrometer. The laser operated at 532 nm wavelength and 50 mW power. The spectrum was obtained using a diffraction grating (2400 lines/mm) and a Peltier-cooled CCD. Thirty-four scans were retrieved. Further details are provided in Chapter 3.

CHAPTER 3 : THE UPPER STABILITY LIMIT OF CHLORITE IN ULTRAMAFIC SCHISTS – IMPLICATIONS FOR WATER TRANSPORT INTO THE DEEP MANTLE

3.1 INTRODUCTION

Ultramafic chlorite schists, formed in the subduction channel between the down-going slab and the hanging wall of the mantle wedge, are an important reservoir for water. However, the stability of hydrous phases within these rocks, especially above 5.0 GPa, remains under-explored. The main constituent mineral, chlorite, has been well studied in peridotite compositions in the MgO-Al₂O₃-SiO₂-H₂O (MASH) system up to 5.0 GPa (Fawcett and Yoder, 1966; Staudigel and Schreyer, 1977; Jenkins and Chernosky, 1986; Pawley, 2003) and to varying degrees in related chemical systems (Fumagalli and Poli, 2005; Grove *et al.*, 2006; Dvir *et al.*, 2011; Till *et al.*, 2012; Fumagalli *et al.*, 2014; Spandler *et al.*, 2014). Only three studies have been undertaken on chlorite stability above 5.0 GPa (Fockenberg, 1995; Ulmer and Trommsdorff, 1999; Pawley, 2003; Fumagalli *et al.*, 2014) and whilst a maximum chlorite stability near 5.5 GPa/650°C is reported, the studies are based on few experiments. The paucity of data on chlorite stability above 5.0 GPa has resulted in a loosely-constrained chlorite stability field in the region between antigorite, chlorite and phase A, a region referred to as the ‘anhydrous nose’, and therefore calls into question the precise location of the hydrous-anhydrous boundary at high pressure.

Several synthesis experiments have identified hydrous minerals in this pressure-temperature (P/T) region including 10Å-phase (Pawley and Wood, 1995b; Pawley *et al.*, 2011), Mg-sursassite (Bromiley and Pawley, 2002), phase-HAPY (Gemmi *et al.*, 2011; Fumagalli *et al.*, 2014) and 11.5Å-phase (Fumagalli *et al.*, 2014; Gemmi *et al.*, 2016). Each is suspected to act as an intermediary hydrous phase between chlorite and Phase A. Experimental results show these phases possess narrow stability fields, and only seem to crystallise in specific bulk compositions atypical of many subduction zone settings. With a few exceptions (Smith, 1995; Khisina and Wirth, 2008), none of these minerals have been found in nature. By contrast, chlorite schists are common in subduction settings and possess varied compositions (Miller *et al.*, 2009) which makes them an ideal target for experimentation aimed at producing these minerals.

Significantly, no high-pressure studies on chlorite stability in ultramafic chlorite schists have been undertaken. This study is the first to provide comprehensive constraints on the upper

chlorite stability field between 1.0 GPa and 6.2 GPa and 640°C-880°C in a single study using only natural chlorite schist in the chemical system $\text{Cr}_2\text{O}_3\text{-NiO-FeO-MgO-Al}_2\text{O}_3\text{-SiO}_2\text{-H}_2\text{O}$ (CrNFMASH). Previous studies have identified two key reactions relevant to chlorite dehydration, applicable at low and high pressures respectively:

Reaction 1: chlorite (chl) = orthopyroxene (opx) + olivine (ol) + spinel (sp) + H_2O

Reaction 2: chlorite (chl) = garnet (grt) + olivine (ol) + spinel (sp) + H_2O

In this chapter, it will be shown that chlorite is stable to at least 6.2 GPa/680°C, considerably higher than found in previous studies. Below 5.7 GPa, it is shown that chlorite dehydration follows the model Reactions 1 and 2. However, at pressures above 5.7 GPa/735°C, chlorite does not break down to the anhydrous assemblage of olivine + garnet + spinel + H_2O . Instead two hydrous minerals form: Mg-sursassite and 11.5Å-phase, the latter furnishing an extensive stability field. Since these minerals have formed from natural-occurring source material and contain between 7-13 wt% water, they represent a plausible carrier of water into the deep mantle in a variety of cooler subduction settings. Their existence also signifies that the hydrous-anhydrous boundary is shifted to substantially higher temperatures than previously thought.

3.1.1 PREVIOUS STUDIES ON CHLORITE IN ULTRAMAFIC SCHISTS

Field geology studies have long reported the existence of layers of chlorite schist, often intermingled with actinolite, talc or antigorite and blocks of amphibolite, pyroxenite or eclogite (Sorensen and Barton, 1987). This rock type, not found in any other geological sequence, has variably been called *mélange* (Cloos and Shreve, 1988; Pirard and Hermann, 2015a), hybrid rocks (Miller *et al.*, 2009; Zanazzi *et al.*, 2009), or blackwall alteration (Zack & John 2007; Smith 1995; Spandler *et al.* 2008). Researchers now agree that chlorite *mélange* represents the exhumed remnant of a high-pressure metamorphic terrane which has survived subduction (Marschall and Schumacher, 2012) and therefore provides a valuable insight into subduction processes. How *mélange* is formed, however, remains contested including through tectonic mixing (Castro and Gerya, 2008; Mori *et al.*, 2014), metasomatic mixing (Sorensen & Grossman 1993) or a mixture of both (Bebout and Barton, 2002; Marschall, 2006).

Table 3.1 summarises key studies involving chlorite *mélange*. Most studies have involved trace element or isotope analyses of chlorite *mélange* to characterise the source/timing of metasomatic fluid interactions. In each instance, the chemical analyses followed on from a field work study. Whilst chemical analyses of chlorite have been published, no petrological study has been undertaken of chlorite schist.

Researchers	Study location	Type of study	MgO (wt%)	Al ₂ O ₃ (wt%)	SiO ₂ (wt%)
Angiboust et al 2014	Monviso	F, Pet, GCM (maj, tr, isot), TDM	9.3	13.1	44.1
Bebout & Barton 2002	Catalina, California	F, GCM (maj, tr)	23.9-28.9	14.5-22.0	27.9-31.9
Bulle et al 2010	Cyclades incl. Syros, Greece	F, GCH (U/Th dang), GCM (tr)	nr	nr	nr
Esteban et al 2007	Betic Cordillera, Spain	F, GCM (maj, tr)	19.2-24.0	19.7-23.2	25.9-28.7
King et al 2006	Catalina, California	Pet, GCM (maj, tr, isot)	8.38-26.17	9.02-16.87	41.92-45.19
King et al 2003	Franciscan, California	F, Pet, GCM (maj, tr, isot)	nr	nr	nr
Marschall 2006	Syros, Greece	F, Pet, GCM (maj)	13.0-22.9	19.2-20.0	25.3-27.7
Miller et al 2009	Syros, Greece	F, Pet, GCM	15.6-27.3	18.7-20.6	29.4-30.5
Marschall & Schumacher 2012	Syros, Greece Dominican Rep.	Conceptual involve Pet, GCM (maj, tr), GPH, GCR (Ba/Th)	nr	nr	nr
Smith 1994	Utah	F, GCM (maj, min)	31.0-35.3	13.7-19.9	29.1-33.8
Sorenson & Grossman 1993	Catalina	Pet, GCM (maj, tr)	5.0-25.7	10.3-19.9	28.9-53.1
Spandler et al 2008	New Caledonia	F, Pet, GCM (maj, tr, isot)	24.5	17.2	27.1

TABLE 3.1: Compilation of studies involving ultramafic chlorite schist.

Final three columns refers to the wt% of Mg, Al and Si oxides in chlorite analyses. Abbreviations used: Pet=petrology, GCM=Geochemical, GPH=Geophysical, GCR=Geochronological, TDM=Thermodynamic modelling, F=Field, maj=major elements, tr=trace elements, isot=isotope, EP=Experimental Petrology, Syn=Synthesis

To date there have been no experimental studies which constrain the maximum thermal stability of chlorite found in chlorite schist. Whilst the chlorite terminal reaction in chlorite schist is expected to be closely located in P/T space to the chlorite-out reactions in peridotite compositions (Fumagalli *et al.*, 2014), in the absence of specific research, the point remains moot. There have been numerous studies on chlorite stability in peridotite compositions at low pressure (see Chapter 4 for details) and a few conducted at higher pressures. Three experimental studies have been completed on chlorite stability >5.0 GPa (Pawley 2003; Fumagalli *et al.* 2014; Ulmer & Trommsdorff 1999 quoting Fockenberg 1995). In each instance, these studies comprised synthesis experiments conducted on multi-anvil apparatus, and although Fumagalli did use natural chlorite as seeds, none of the studies used natural rocks as starting materials. The resulting chlorite-out phase boundaries from each study exhibited a similar Clapeyron slope (see Figure 3.11) but since the data points were not tightly bracketed, the chlorite-out phase boundary even in peridotite compositions remains loosely constrained in P/T space.

sourced from the Cerro del Almirez ultramafic massif in Southern Spain. It comprised approximately 99 wt% chlorite with 1 wt% antigorite and trace talc. Previous research constrained the maximum stability of the Cerro del Almirez chlorite harzburgites at 1.8 GPa, 725°C (Padron-Navarta *et al.*, 2010a) signifying that this sample was prograde, high pressure chlorite and appropriate for this study. Pyrope garnet from the Dora Maira in northern Italy provided nucleation seeds in the starting material.

The starting material was analysed using two analytical techniques fully described in Chapter 2. X-Ray Diffraction (XRD) analysis confirmed the phases present and are displayed in the diffractogram in Figure 3.1.

a							b	
Oxide	CHL (n=11)		ATG (n=2)		GRT (n=9)		Phase	Proportion in starting material
wt%	Mean	sd	Mean	sd	Mean	sd		
Na ₂ O	0.00	0.00	0.00	0.00	0.08	0.06	Chlorite	98.50
MgO	34.02	0.44	37.77	1.40	26.75	0.20	Antigorite	1.00
SiO ₂	33.78	0.41	42.78	0.19	43.38	0.29	Garnet	0.50
Al ₂ O ₃	12.94	0.29	0.16	0.01	24.42	0.22	Total	100.00
NiO	0.19	0.15	0.16	0.16	0.00	0.00		
FeO	3.63	0.14	5.25	0.01	4.08	0.40		
MnO	0.00	0.00	0.08	0.08	0.00	0.00		
Cr ₂ O ₃	1.55	0.39	0.00	0.00	0.00	0.00		
CaO	0.00	0.00	0.00	0.00	0.43	0.02		
TiO ₂	0.00	0.00	0.00	0.00	0.00	0.00		
H ₂ O (calc)	12.53	0.13	12.57	0.19	0.00	0.00		
Total	98.64	0.94	98.77	1.54	99.15	0.69		
Na	0.00	0.00	0.00	0.00	0.00	0.00	Oxide	wt%
Mg	4.86	0.03	2.68	0.06	2.75	0.03	H ₂ O (calc.)	12.64
Si	3.24	0.01	2.04	0.02	3.00	0.01	MgO	34.49
Al	1.46	0.03	0.01	0.00	1.99	0.01	SiO ₂	34.38
Ni	0.01	0.01	0.01	0.01	0.00	0.00	Al ₂ O ₃	13.05
Fe	0.29	0.01	0.21	0.00	0.24	0.02	NiO	0.19
Mn	0.00	0.00	0.00	0.00	0.00	0.00	FeO	3.70
Cr	0.12	0.03	0.00	0.00	0.00	0.00	Cr ₂ O ₃	1.55
Ca	0.00	0.00	0.00	0.00	0.03	0.00	Total	100.00
Ti	0.00	0.00	0.00	0.00	0.00	0.00		
Total	9.98	0.01	4.95	0.02	8.01	0.00		
Mg#	0.94	0.00	0.93	0.00	0.92	0.01		
Cr#	0.07	0.02	0.00	0.00	0.00	0.00		

TABLE 3.2: Panel showing analyses of starting mix of Series 1.

a) *FE-SEM analyses of each mineral comprising the starting mix.* "sd" signifies one standard deviation. b) *Phase proportion of the starting material:* Since chlorite is the dominant phase, the bulk composition can effectively be considered chlorite; c) *Normalised FE-SEM analysis of the starting material:* The H₂O was calculated by stoichiometry. No talc was observed during FE-SEM analyses. Totals have been normalised to 100 wt%. Oxides with totals less than the detection limit were eliminated.

FE-SEM analysis provided the chemical composition of each phase as displayed in Table 3.2. Since chlorite comprised nearly the entirety of the bulk composition in Series 1, the bulk was effectively considered monomineralic chlorite. Analysis revealed that chlorite composition varied, however, from ideal clinocllore. The Mg# averaged 0.94 and the Cr# averaged 0.07. Aluminium and magnesium levels were both lower than ideal clinocllore (averaged 1.46 a.p.f.u. and 4.86 a.p.f.u. respectively) whilst silicon was higher (averaged 3.24 a.p.f.u.) which indicated

a cation exchange mechanism. Chlorite also contained minor chromium and trace nickel which broadened the chemical system used in Series 1. Cation ratios of the starting mix were $(\text{Mg}+\text{Fe}+\text{Ni}):(\text{Al}+\text{Cr}):\text{Si} = 5.13:1.56:3.22$ compared to the end-member clinocllore of 5:2:3.

Chemography (see Figure 3.2) shows the relationship between phases formed in the CrFNMASH sytem from the bulk composition used in experimental Series 1.

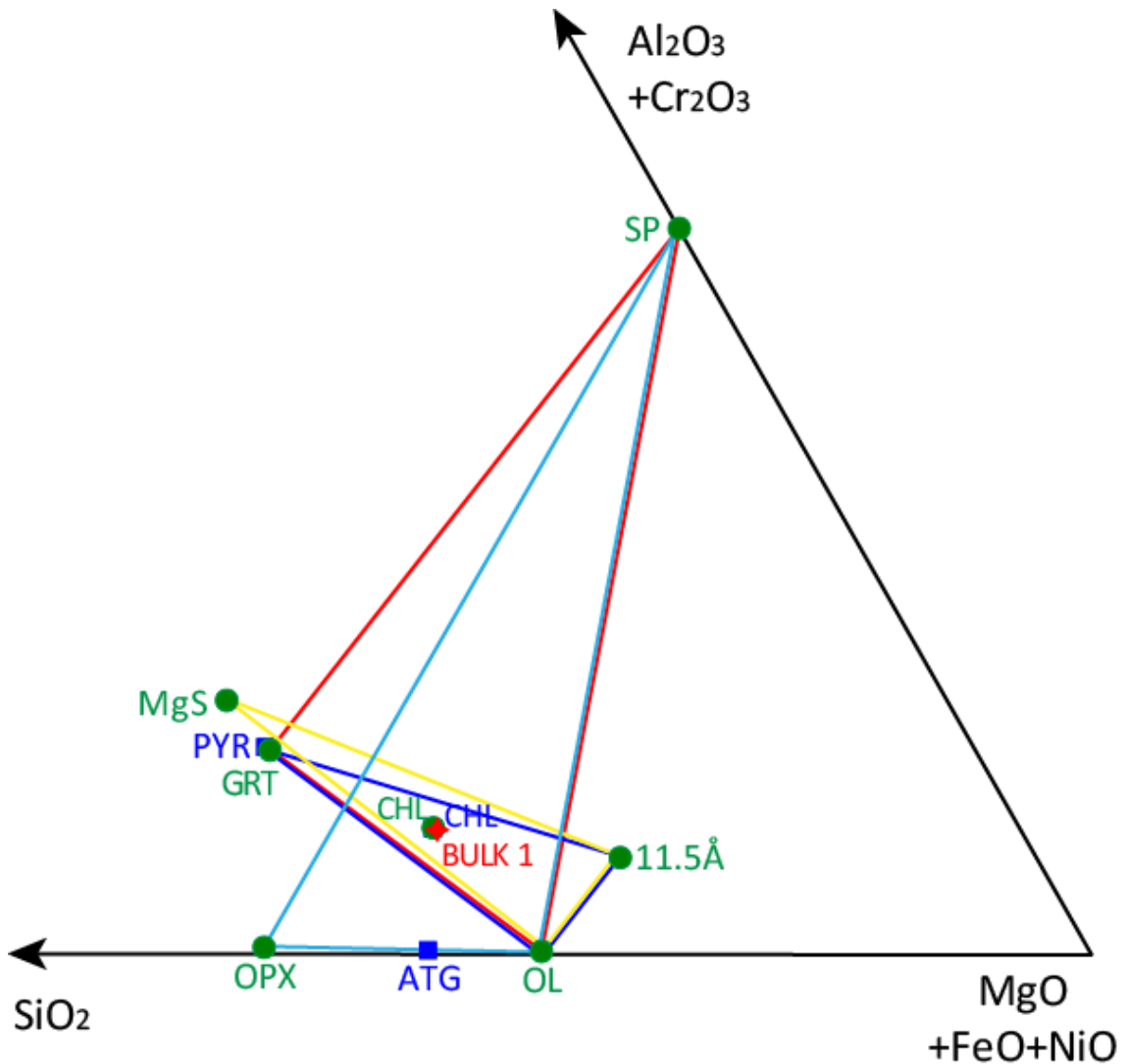


FIGURE 3.2: Chemography of the Series 1 starting materials

Triangular plot of the starting material in the system CrFNMASH. Compositions are in wt%. Blue squares mark minerals in the starting mix; green circles identify reaction products. Bulk 1 is marked with a red star. Note that chlorite is very close to the bulk composition. Coloured triangles refer to the chlorite terminal reactions identified in this experimental series: light blue triangle $\text{chl} = \text{opx} + \text{ol} + \text{sp} + \text{H}_2\text{O}$ (Reaction 1/A3); red triangle $\text{chl} = \text{grt} + \text{ol} + \text{sp} + \text{fluid}$ (Reaction 2/B2); dark blue triangle $\text{chl} = \text{grt} + \text{ol} + 11.5\text{\AA} + \text{fluid}$ (Reaction B6/E2); yellow triangle $\text{chl} = \text{MgS} + \text{ol} + 11.5\text{\AA} + \text{fluid}$ (Reaction E6/F2). This plot was made using the program C-Space (Torres-Roldan et al., 2000).

3.2 RESULTS

To inform this investigation, twenty-nine data points were determined at a range of pressures (1.0 GPa to 6.2 GPa) and temperatures (640°C to 880°C). A table of all experimental conditions

and run products in Series 1 is presented in Table 3.3. Due to the proximity of data points at high pressure, and the resulting complexity, phase relations are displayed in two separate diagrams: phase relations to 5.5 GPa are displayed in Figure 3.3, and those above 5.5 GPa are displayed in Figure 3.6. Phase boundaries were determined through a combination of chemical analysis and textural observation.

3.2.1 PHASE RELATIONS TO 5.5 GPa

Run products produced five minerals and one fluid phase within various stability fields as viewed in Figure 3.3. No melt was observed in any run product.

Experiment Number	Duration (hr)	P (GPa)	T (°C)	PHASES								
				CHL	GRT	OL	OPX	SP	11.5A	MgS	Fluid	TOTAL
D1861	72	1.0	800	88.7	0	4.7	3.7	1.6	0	0	1.3	100
D2156	72	1.0	820	0	0	34.2	37.5	15.6	0	0	12.6	100
D1859	72	2.0	840	8.9	0	30.5	34.8	14.4	0	0	11.4	100
C4887	72	2.0	860	0	13.2	36.6	25.2	12.4	0	0	12.6	100
D1850	72	2.0	880	0	0	34.3	37.8	15.4	0	0	12.6	100
D1812	120	3.0	800	98.7	0	0.6	0.6	0	0	0	0.1	100
D1819	120	3.0	820	95.9	1.7	1.7	0.2	0	0	0	0.4	100
D1824	98	3.0	840	64.6	12.8	15.6	0	2.7	0	0	4.3	100
C4884	71	3.0	860	0	38.4	41.7	0	7.2	0	0	12.6	100
D1867	72	4.0	780	92.2	3.6	2.9	0.4	0	0	0	0.9	100
D1855	72	4.0	800	52.6	17.4	20.8	0	3.4	0	0	5.8	100
D1871	72	4.0	820	0	39.1	41.6	0	6.7	0	0	12.6	100
UHPPC-323	72	5.0	720	99.1	0	0.3	0.6	0	0	0	0.1	100
UHPPC-327	68	5.0	760	71.5	10.9	12.2	0	2.0	0	0	3.5	100
UHPPC-334	120	5.0	780	0	39.3	41.4	0	6.5	0	0	12.7	100
UHPPC-337	120	5.5	740	0	39.3	41.5	0	6.7	0	0	12.6	100
UHPPC-336	71	5.7	720	82.4	4.9	3.3	0	0.6	7.7	0	1.1	100
UHPPC-339	120	5.7	760	0	39.2	41.3	0	6.8	0	0	12.6	100
UHPPC-345	120	5.8	720	66.6	13.3	9.0	0	0.5	7.4	0	3.2	100
UHPPC-325	0.5	6.0	680	97.1	0.4	1.4	0.6	0	0	0	0.3	100
UHPPC-335	168	6.0	700	0	44.6	19.2	0	0	26.8	0	9.4	100
UHPPC-332	120	6.0	720	0	44.2	20.7	0	0.5	24.9	0	9.6	100
UHPPC-356	118.5	6.0	740	0	44.4	20.9	0	0.5	24.6	0	9.7	100
UHPPC-364	120	6.0	760	0	41.8	28.4	0	2.6	16.5	0	10.7	100
UHPPC-361	120	6.0	800	0	38.7	42.1	0	6.5	0	0	12.6	100
UHPPC-341	113	6.2	640	64.9	3.8	7.7	0	0	11.6	9.8	2.2	100
UHPPC-341	113	6.2	680	61.8	9.8	8.0	0	0	12.6	4.9	2.8	100
UHPPC-385	120	6.2	720	0	43.1	19.1	0	0.8	27.6	0	9.4	100
UHPPC-386	120	6.2	800	0	39.8	41.0	0	6.5	0	0	12.7	100

TABLE 3.3: Table of experimental conditions, run products and mass balance in Series 1.

Run products identified in experimental Series 1. Phase quantities are determined by mass balance using least squares method (Herrmann and Berry, 2002). Zero values indicate phase not present.

3.2.2 PHASE TEXTURES TO 5.5 GPa

In general, olivine (ol) typically formed small anhedral grains (<2 μm) which increased in size ($\leq 20 \mu\text{m}$) with increased pressure. Orthopyroxene (opx) typically assumed acicular textures at low pressure and blocky to elongate crystals ($\leq 30 \mu\text{m}$) at $P > 2.0 \text{ GPa}$. Spinel (sp) generally formed

small, euhedral crystals (5-10 μm) which reduced in size and became poikiloblastic with increasing pressure. Chlorite (chl) textures were little affected by changes in pressure or temperature until immediately before decomposition when laths assumed a splintered appearance. Garnet (grt) showed no significant change with pressure but crystal size ($>50 \mu\text{m}$) increased with increasing temperature and crystals became poikiloblastic following chlorite decomposition.

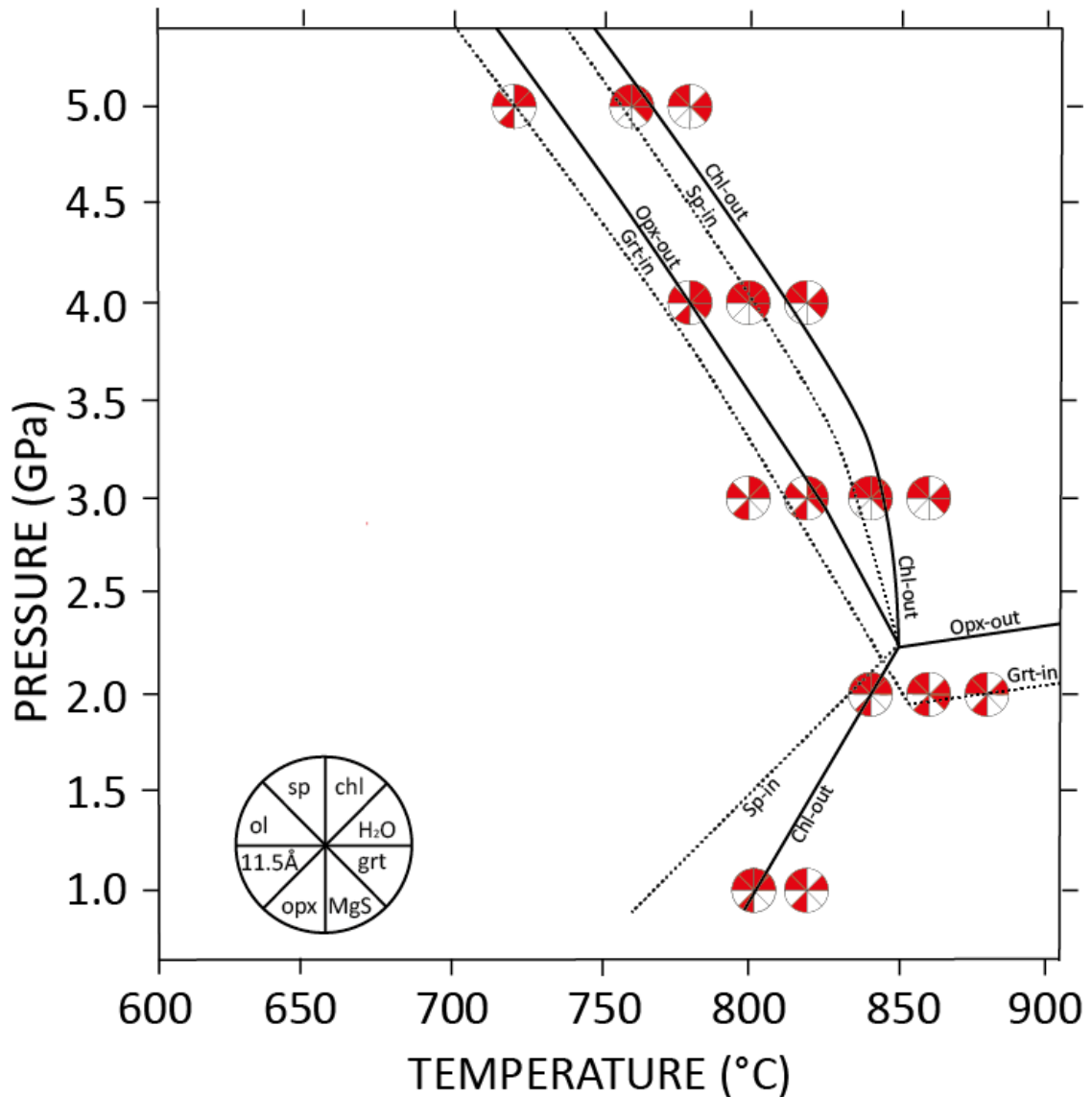


FIGURE 3.3: Phase relations of ultramafic low-Al chlorite <5.5 GPa.

Red segments indicate phase present. Phase abbreviations: chl=chlorite; H₂O=water/vapour; grt=garnet; opx=orthopyroxene; ol=olivine; sp=spinel; MgS=Mg-sursassite; 11.5Å=11.5Å-phase. Dotted lines indicate the low T and/or low P phase boundary in divariant field; solid lines mark the high T and/or high P phase boundary.

Changing textures have been illustrated through a series of back-scattered images (BSE) from a field-emission scanning electron microscope (FE-SEM) at three pressure intervals (see Figures 3.5 and 3.6). At each interval, changing phase assemblages and phase textures were tracked via isobaric temperature increase.

3.2.2.1 Textural relations at 2.0 GPa

Chlorite, olivine and orthopyroxene formed the dominant phases along with minor spinel and fluid. Assemblages changed over a narrow temperature interval.

At 840°C, chlorite coexisted with ol, opx, sp and H₂O and it had commenced decomposition. No garnet was observed at this temperature. Chlorite retained its characteristic lath shape up to 40 µm x 20 µm but predominantly it had disassembled into a splintery, almost acicular texture in some views (see Figure 3.4a). Opx appeared as both large, elongate crystals (>50 µm x 10 µm) and as tiny acicular crystals. Spinel usually occurred as large, subhedral crystals (30 µm x 20 µm) which were quite poikiloblastic (olivine inclusions), whilst olivine formed subhedral crystals (20 µm x 15 µm). Tiny anhedral blebs of both spinel and olivine were observed at this temperature.

At 860°C, chlorite had entirely decomposed. Opx had assumed elongate blades, some of which were poikiloblastic containing Al-rich cores. Acicular textures were entirely absent. Garnet appeared with subhedral, poikiloblastic textures (olivine) with a grain size up to 30 µm in diameter. Spinel formed variably as subhedral to euhedral crystals 5 - 10 µm across with numerous anhedral blebs also present.

At 880°C, garnet was absent, indicating the garnet-in boundary was very close in P-T space. The opx had retained its blocky shape with grain size consistently 10-20 µm in length. Olivine formed crystals up to 15 µm across, some exhibiting zoned rims (see Figure 3.4c). Spinel appeared as subhedral to euhedral grains <10 µm in length.

3.2.2.2 Textural relations at 3.0 GPa

There was a marked difference in phase relations at 3.0 GPa. Garnet was a dominant phase replacing both opx and spinel. Textures following chlorite disappearance were also quite different.

At 800°C, chlorite comprised >95 wt% of phases present. Decomposition had not commenced since no garnet was observed. The presence of minor olivine, trace opx and fluid indicated breakdown products of antigorite from starting material. Chlorite assumed a lath-like texture

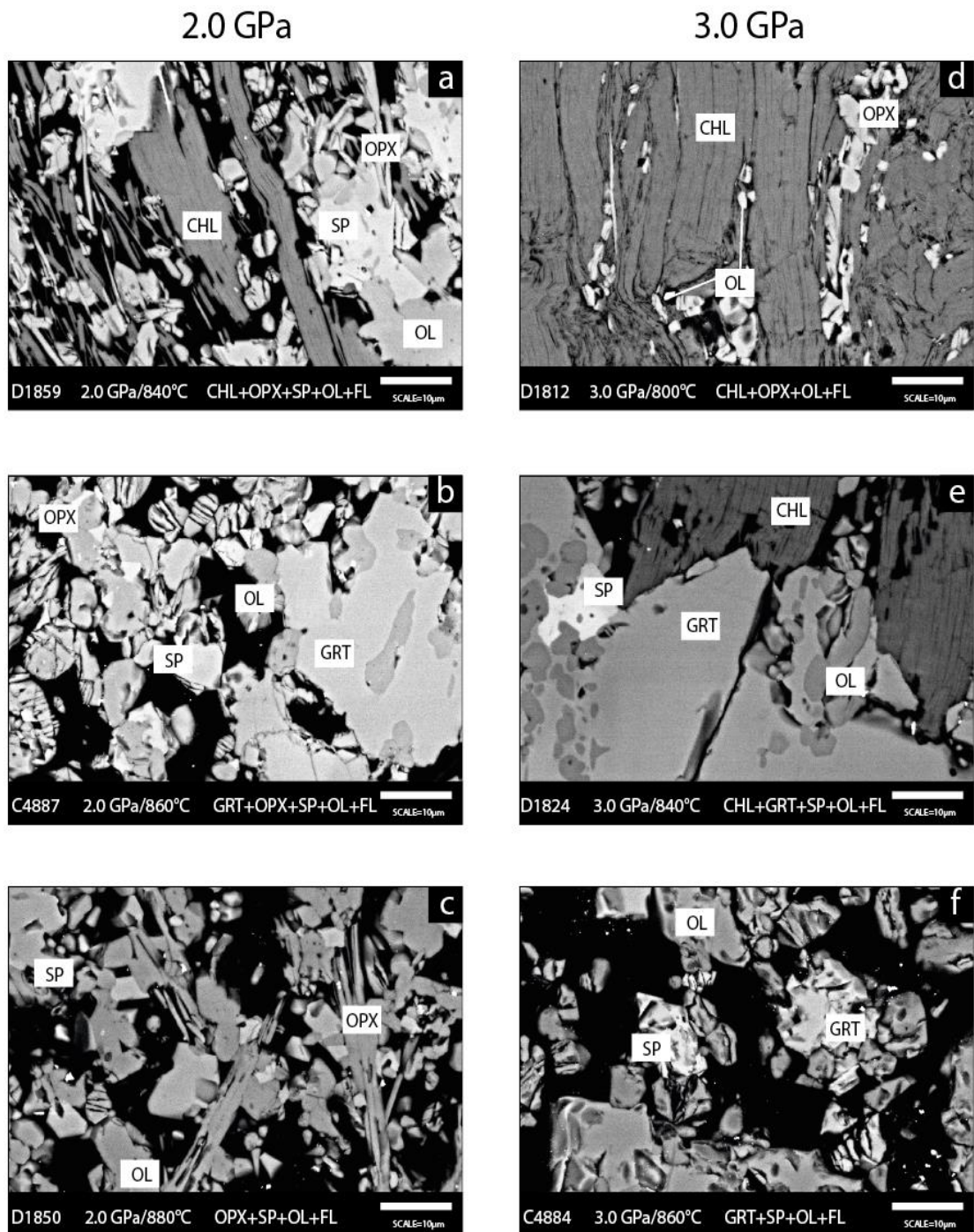


FIGURE 3.4: Representative FE-SEM BSE images of run products at 2.0 GPa and 3.0 GPa.

2.0 GPa series. a) Chlorite co-exists with all phases at this pressure except for garnet; b) Chlorite has entirely decomposed by 2.0/860°C and poikiloblastic garnet is now a reaction product; c) Opx returns as a stable phase at this temperature with no garnet present indicating the garnet-in boundary is very close in P-T space. **3.0 GPa series.** d) At this temperature, chlorite is entirely stable. The presence of minor opx, ol and fluid represent the product phases of the atg breakdown. No garnet is present; e) coexisting chl+grt+sp+ol+fluid at these P-T conditions. Garnet forms relatively large subhedral crystals compared with the olivine; f) Chlorite has entirely decomposed leaving a typical grt+ol+sp+fluid products. The fine-grained matrix is largely absent from this view – it probably disappeared during polishing.

with grain-size typically in the order of 40 x 10 μm. Olivine formed anhedral blebs, proximal to opx (see Figure 3.4d). Only a few small subhedral crystals of olivine were observed <4 μm. Opx occurred as blocky crystals (5-15 μm).

At 840°C, chlorite, garnet and olivine were the major phases along with minor spinel and fluid. Opx was not present. Garnet appeared as subhedral to euhedral crystals which exhibited a

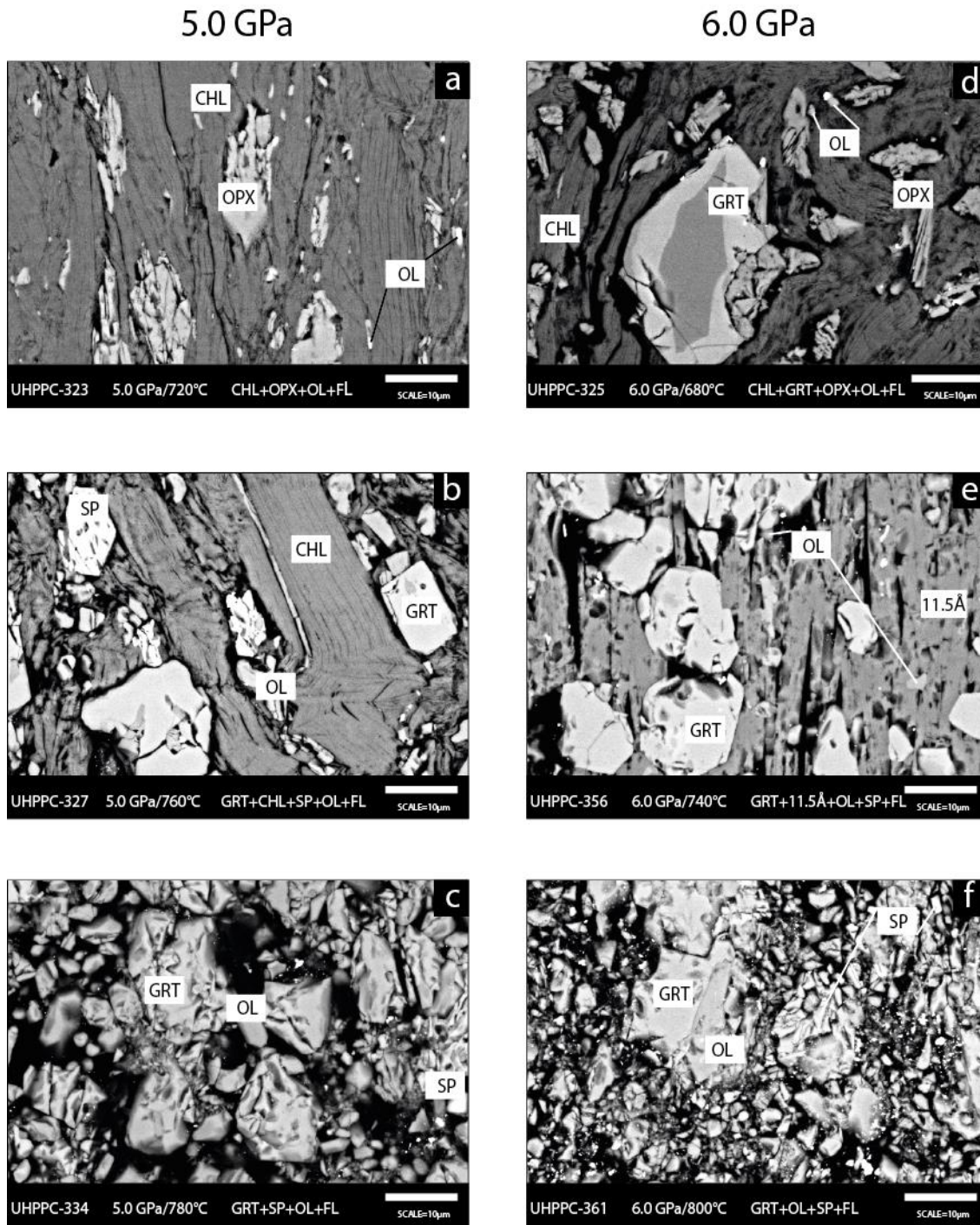


FIGURE 3.5: Representative FE-SEM BSE images of run products at 5.0 GPa and 6.0 GPa.

5.0 GPa series. a) Chlorite entirely stable at these P-T conditions. Ol and Opx are product phases from the breakdown of minor atg from the starting material; b) Chl+grt+ol+sp+fluid coexist at these P-T conditions and show equilibrated grain boundary textures; c) Breakdown products of chlorite form large crystals within a fine-grained crystalline matrix (mostly absent from this view). Textures show only local equilibration. **6.0 GPa series.** d) Chlorite commences breakdown as witnessed by the textural appearance of laths. 11.5Å-phase appears as a breakdown product for the first time at these P-T conditions although not visible in this view. Grt exhibits clear growth rims around the pyrope core; e) Chlorite has entirely decomposed by this temperature interval with 11.5Å-phase forming as a product. Grt+11.5Å are well equilibrated at a local level; f) By 800°C, all hydrous phases have disappeared leaving locally equilibrated grt+ol+sp+fluid phases within a very fine-grained crystalline matrix.

wide variation in size (20-100 μm in diameter). They were often strongly poikiloblastic containing olivine inclusions which exhibited a distinct lineation (see Figure 3.4e). This texture suggested that the growth rate of garnet was faster than that of olivine. Spinel and olivine each formed subhedral crystals (10-20 μm); however, the former exhibited poikiloblastic textures containing olivine inclusions.

At 860°C, the relatively simple system of garnet, olivine and fluid was observed, indicating the complete breakdown of chlorite at this temperature. Texturally, variation was prominent where larger crystals (>20 μm) assumed a poikiloblastic texture (see Figure 3.4f). Crystals which existed in isolation tended to have subhedral grain boundaries, compared with those in contact with other phases, which assumed euhedral boundaries. Numerous smaller (1-5 μm) crystals were subhedral and heterogeneous in appearance.

3.2.2.3 Textural relations at 5.0 GPa

Phase relations at 5.0 GPa were unchanged from those found at 3.0 GPa, however important changes were observed in textural relationships between phases. Garnet crystals remained subhedral to euhedral and poikiloblastic, but typically <20 μm compared with the larger grain size at 3.0 GPa (see Figure 3.5b). This could have been due to lower temperatures of runs at 5.0 GPa (some 80°C lower). Spinel and olivine retained similar textural and grain size as for 3.0 GPa. With the disappearance of chlorite by 780°C, though, the resulting phase textures were quite different at higher pressure. Some garnet and olivine crystals were subhedral with grain size >20 μm . However, there was an increased proportion of anhedral-subhedral fine-grained crystals, all <2 μm in size, contained within an extensive crystalline matrix (see Figure 3.5c).

3.2.3 PHASE RELATIONS ABOVE 5.5 GPa

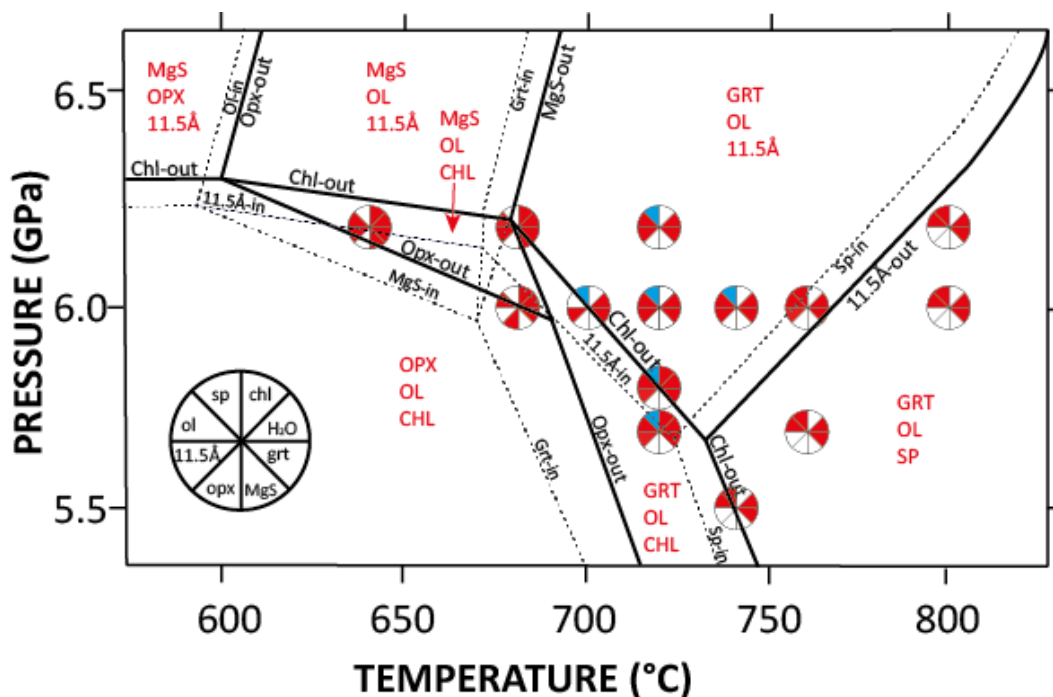


FIGURE 3.6: Phase relations of ultramafic low-Al chlorite >5.5 GPa.

Red segments indicate phase present. White segments indicate phase absent. Blue segments indicate phase is present in trace quantities, likely metastable at these P-T conditions. Solid lines indicate phase boundary. Dotted lines indicate the low-T phase boundary in divariant field. Phases present: chl=chlorite; H₂O=water/vapour; grt=garnet; opx=orthopyroxene; 11.5Å=11.5Å-phase; ol=olivine; sp=spinel, MgS=Mg-sursassite.

At P>5.5 GPa, run products yielded seven minerals and one fluid phase within a more complex set of stability fields (see Figure 3.6). No melt was observed in any run product.

An important change in phase relations was observed at high pressure. Chlorite decomposed to form an unexpected hydrous phase, identified as 11.5Å-phase, which coexisted with the anhydrous assemblage of garnet, olivine and spinel. Its presence warranted further detailed investigation to verify that it was indeed 11.5Å-phase.

3.2.3.1 XRD analysis of 11.5 Å phase

To confirm that this mineral was correctly identified as the 11.5Å-phase, an XRD scan was taken, the results of which were then compared to previously published XRD results (Cai *et al.*, 2015).

Run UHPPC 332 (6.0GPa/720°C) was analysed by XRD at the Research School of Chemistry at the Australian National University. Details of this process are provided in Chapter 2. A diffractogram of the scan is shown in Figure 3.7. Multiple peaks were in agreement with the results of Cai (Cai *et al.*, 2015) with the six largest occurring at 23.1, 35.0, 35.3, 36.1, 42.9, 44.6, 47.2 and 62.2 on the 2-theta scale. The largest peak at 23.1 confirmed the existence of 11.5Å-phase.

When XRD scans were compared, three differences were observed worthy of note. Peak intensities were not always of a similar magnitude with preferred orientation of the crystals and different scan durations the likely cause. Peak locations on the 2-theta scale were slightly offset when compared. This discrepancy may have been due to calibration differences against a known standard, or related to compositional differences since the Cai sample (Cai *et al.*, 2015) was Cr-free. Finally, the XRD scan in this study was completed up to 100 on the 2-theta where several additional large peaks were observed: at 92.6, 92.9, 94.7, 95.0, 98.8 and 99.9. These were unlikely to be coincident with the phases pyrope or forsterite and may well be new peaks diagnostic for the 11.5Å-phase.

3.2.3.2 *Raman analysis of 11.5Å-phase*

Raman analysis was undertaken to determine a new diagnostic test for the 11.5Å-phase. Samples UHPPC-347 (6.2 GPa/720°C) and UHPPC-356 (6.0 GPa/740°C) were analysed with Raman spectroscopy at the Research School of Physics at the Australian National University. Scan 03-00 was selected as representative of the 11.5Å-phase and one which contained small quantities of olivine and garnet. Numerical results of scan 03-00 are provided in the Appendix. The spectra appear in Figures 3.8a and b below.

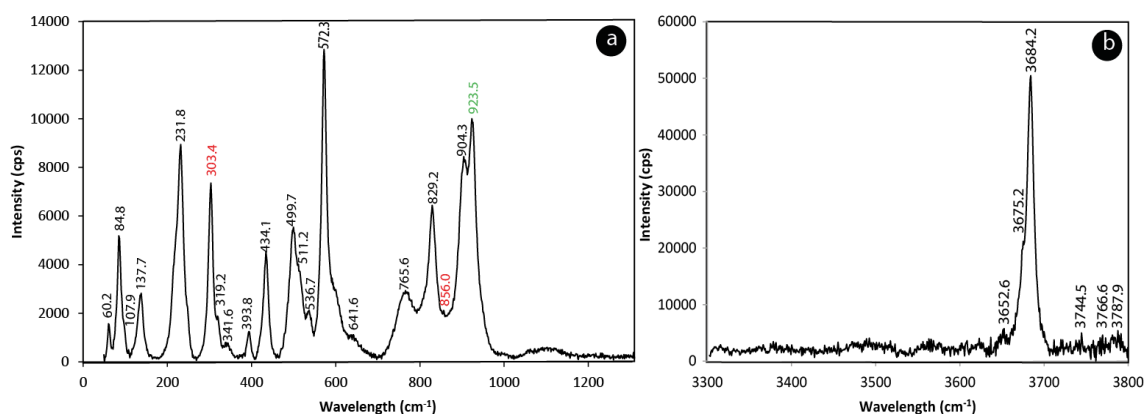
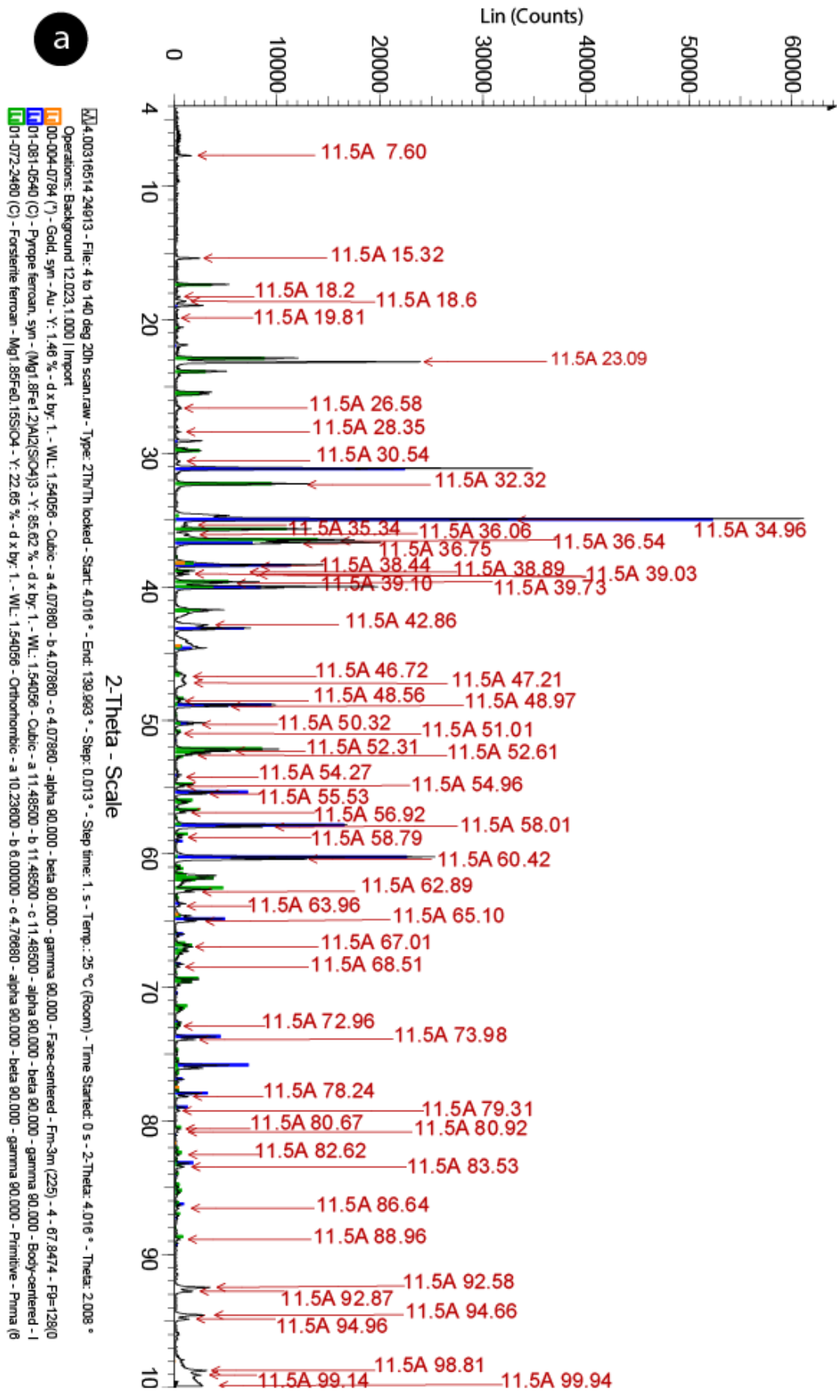


FIGURE 3.8: Raman spectrum of the 11.5Å phase

a) Raman spectrum in the 0-1300 cm^{-1} wavenumber range, the region displaying silicon and magnesium bonds. **b)** Raman spectrum in the 3300-3800 cm^{-1} wavenumber range, the region displaying OH-stretching bonds. Main peaks for 11.5Å-phase are labelled in black. Co-incident peaks (where 11.5Å-phase and one other phase occur at the same wavenumber) are labelled as follows: pyrope in green, forsterite in red.

The Raman spectra elicited numerous strong peaks. Those peaks located in the lower spectral region $<600 \text{ cm}^{-1}$ typically indicate movement of cations on octahedral and interlayer sites in the crystal lattice (Wang *et al.*, 2002). Figure 3.8a reveals peaks found at 60 cm^{-1} , 85 cm^{-1} , 138 cm^{-1} , 232 cm^{-1} , 303 cm^{-1} , 394 cm^{-1} , 434 cm^{-1} , 500 cm^{-1} , 537 cm^{-1} and 572 cm^{-1} .



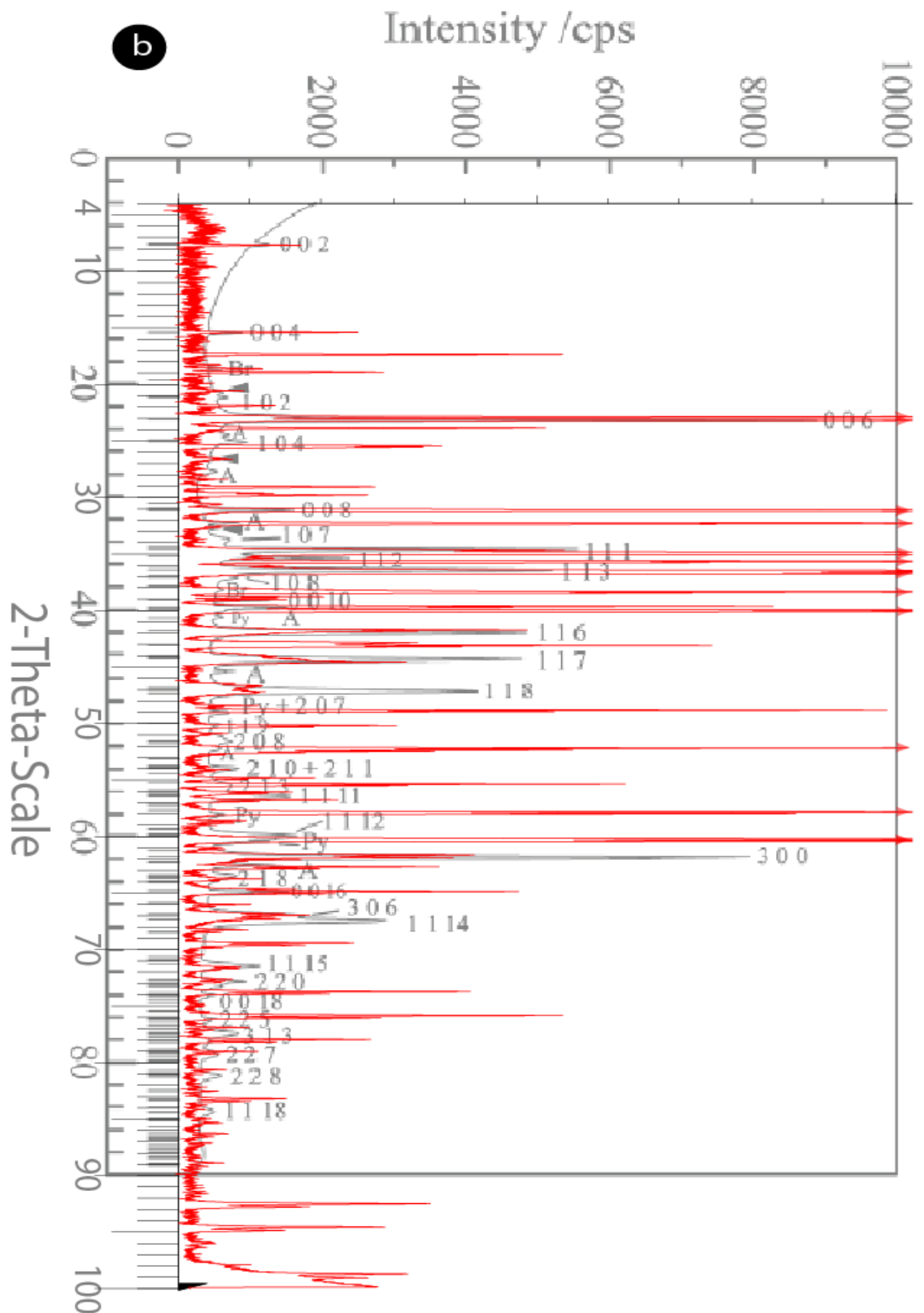


FIGURE 3.7: XRD spectra of the 11.5Å-phase.

a) XRD spectrum for Run UHPPC332 in the current series comprising garnet, olivine and 11.5Å-phase. Pyrope, forsterite and gold were identified using Eva Diffracplus software. All unidentified phases are assumed to be 11.5Å-phase and are marked with red arrows at the corresponding 2-theta value. There is a strong correlation between main peaks from both scans. **b).** XRD spectrum (grey) taken from Cai (Cai et al., 2015) overlain by XRD spectrum (red) from current study. There is strong agreement between peaks from both scans confirming the presence of 11.5Å-phase in the current study. Differences in peak intensity (Y-axis) likely due to different run times and preferred crystal orientation (PCO).

The spectral region between 600 cm^{-1} and 1150 cm^{-1} traces the vibration of Si-O bonds in SiO_4 tetrahedra (Wang *et al.*, 2002). Figure 3.8a shows four significant peaks which occur in this range: 766 cm^{-1} , 829 cm^{-1} , 904 cm^{-1} and 924 cm^{-1} .

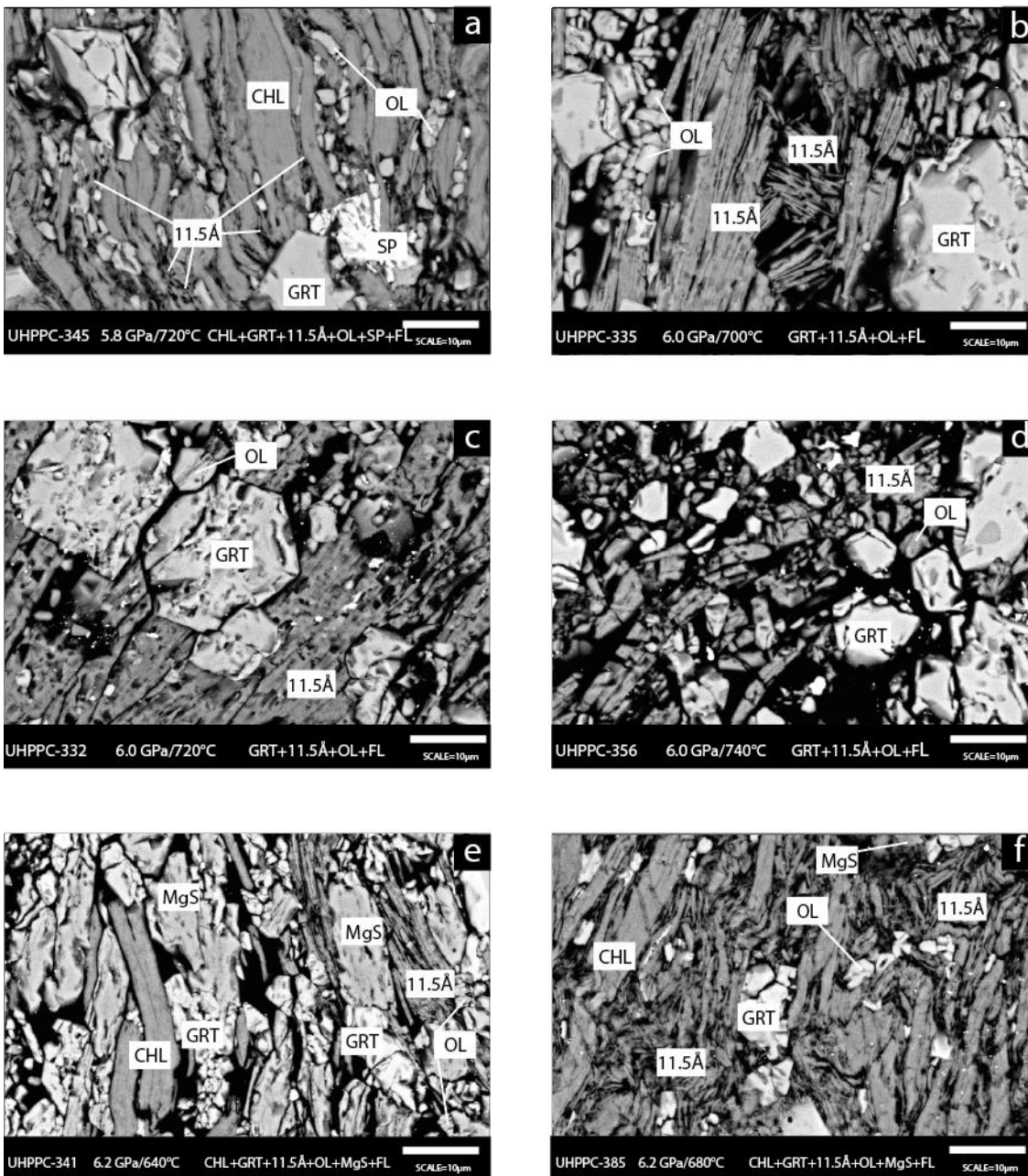


FIGURE 3.9: Representative FE-SEM BSE images of 11.5Å-phase.

a) 11.5Å-phase forms tiny, acicular grains intercalated with chlorite between chlorite laths; b) At 6.0,700°C, 11.5Å-phase has entirely replaced chlorite as the only hydrous phase. The fine needles form clumps. c and d) With increasing temperature, the 11.5Å-phase assumes a blocky appearance with little remnant of its acicular form. It also takes on a poikiloblastic texture. e) At 6.2 GPa, 640°C, we see the co-existence of three hydrous phases: 11.5Å-phase, MgS and chlorite. The subhedral grain boundaries and poikiloblastic appearance of the MgS phase suggest it is newly formed. f) With an increase of 40°C, MgS adopts anhedral grain boundaries indicating it is nearing its thermal maximum. Chlorite and 11.5Å-phase adopt an intercalated texture.

Figure 3.8b shows the spectral region concerned with H₂O or the stretching of -OH bonds (Wang *et al.*, 2002; Kleppe *et al.*, 2003). Three peaks are shown: 3653 cm⁻¹, 3675 cm⁻¹ and the largest at 3684 cm⁻¹, which confirm the presence of bound water.

The RRUFF database (Lafuente *et al.*, 2015) matched peaks with pyrope (924) and forsterite (303 and 856) but these were considered co-incident rather than evidence of a mixed scan. The strong peaks at 232, 829, 904 and 924 suggest a tri-octahedral crystal structure (Wang *et al.*, 2002) with the general pattern characteristic of a phyllosilicate mineral (Wang *et al.*, 2002) and together provide a diagnostic spectrum for the 11.5Å-phase.

3.2.3.3 Textural relations of 11.5Å-phase

The first appearance of 11.5Å-phase was at 5.7 GPa, 720°C where it formed sub-micron, acicular needles intercalated with chlorite between larger chlorite laths (see Figure 3.9a and f). Chlorite breakdown textures also adopted a splintery appearance and so initially it was difficult to distinguish the two phases. Closer inspection revealed that the 11.5Å-phase needles were consistently rigid in appearance compared with chlorite needles which tended to flex and bend (see Figure 3.9a, e and f).

At 6.0 GPa and above, 11.5Å-phase formed random clumps displaying a distinct lineation. Crystals formed long, narrow, individual blades 0.5-1 µm wide and up to 50 µm long (see Figure 3.9b). With increasing temperature, crystals assumed a more lath-like appearance up to 10 µm wide similar to other phyllosilicate minerals (see Figure 3.9b and c). Viewed laterally, crystals would possess a platy habit (Cai *et al.* 2015). 11.5Å phase often displayed a poikiloblastic texture comprising inclusions (usually olivine) and holes (Figure 3.9c and d). Experimental run time did not seem to affect the observed textures.

3.2.4 PHASE TEXTURES ABOVE 5.5 GPa

Textural observations for the phases olivine, garnet, spinel, orthopyroxene and chlorite were in accordance with observations at lower pressures (see section 3.5.1). However, at higher pressures, it was observed that the crystalline matrix became increasingly fine-grained.

Changing textures with temperature increase at 6.0 GPa have been illustrated through a series of BSE images from FE-SEM (see Figure 3.6).

3.2.4.1 Textural relations at 6.0 GPa

At 680°C, chlorite remained the dominant phase with minor olivine and trace amounts of opx, and garnet. Opx formed blocky to elongate subhedral crystals. Grain size was in the 5-15 µm range, and grain boundaries displayed obvious reaction rims. Olivine formed predominantly anhedral blebs at this temperature, but some small (<5 µm) subhedral crystals formed adjacent to garnet and chlorite, indicating a reaction product. Garnet formed homogeneous, subhedral rims up to 10 µm thick around pyrope cores.

At 740°C, neither chlorite nor opx were present, confirmed by mass balance calculations. Phase relations involved major 11.5Å-phase, olivine and garnet with trace spinel. Garnet formed subhedral to euhedral, poikiloblastic crystals 5-20 µm across. 11.5Å-phase formed elongate laths 5 µm wide and up to 50 µm in length which exhibited a consistent, poikiloblastic texture containing both olivine inclusions and numerous holes. Olivine formed small subhedral crystals up to 5 µm across but were typically found as inclusions in both 11.5Å-phase and garnet. Garnet and 11.5Å-phase displayed numerous euhedral grain boundaries indicative of equilibrium.

At 800°C, the anhydrous assemblage of garnet and olivine with minor spinel were the solid phases present. Much fine-grained material was observed creating a crystalline matrix interspersed with pore space. A few large subhedral crystals of garnet (10-20 µm) and olivine were observed randomly in the matrix.

3.2.4.2 Textural relations at 6.2 GPa, 640°C

Mg-sursassite formed only at this single data point in this experimental series (compared with multiple locations in Series 1 - see Chapter 4). Chlorite remained the dominant phase co-existing with major olivine, 11.5Å-phase, Mg-sursassite and minor garnet. Mg-sursassite formed subhedral, blocky crystals 5-10 µm wide and 15-30 µm long. It exhibited a poikiloblastic appearance and numerous jagged grain boundaries which suggested this phase was newly formed (see Figure 3.9e). Mg-sursassite formed euhedral grain boundaries with both chlorite and 11.5Å-phase. Olivine consisted of numerous anhedral blebs with a few random grains <2 µm long. Garnet formed numerous grains <1 µm in size but a few large homogeneous, subhedral grains <10 µm wide and <20 µm in length were observed. 11.5Å-phase formed clumps of acicular crystals up to 20 µm in length.

Run	Phase	n	P(GPa)	T (°C)	Wt%														Cations											
					H2O	Na2O	MgO	SiO2	Al2O3	Al2O3	NiO	FeO	MnO	Cr2O3	CaO	TiO2	Total	Na	Mg	Si	Al	Ni	Fe	Mn	Cr	Ca	Ti	Total	Mg#	Cr#
D1819	CHL	9	3	820	Mean	12.57	0.03	33.79	34.21	12.86	0.24	3.77	0.00	1.47	0.00	0.00	86.37	0.00	4.81	3.27	1.45	0.02	0.30	0.00	0.11	0.00	0.00	9.95	0.94	0.07
					SD	0.12	0.04	0.30	0.40	0.31	0.09	0.18	0.00	0.24	0.00	0.00	0.84	0.00	0.04	0.02	0.03	0.01	0.01	0.00	0.02	0.00	0.00	0.00	0.00	0.01
UHPPC323	CHL	8	5	720	Mean	12.61	0.02	34.20	34.12	13.13	0.27	3.60	0.00	1.27	0.00	0.00	86.62	0.00	4.85	3.25	1.47	0.02	0.29	0.00	0.10	0.00	0.00	9.97	0.94	0.06
					SD	0.08	0.04	0.17	0.27	0.26	0.16	0.18	0.00	0.27	0.00	0.00	0.57	0.00	0.02	0.01	0.03	0.01	0.01	0.00	0.02	0.00	0.00	0.00	0.01	0.00
D1812	OL	9	3	800	Mean	0.00	0.00	50.08	41.12	0.07	0.22	9.02	0.10	0.05	0.00	0.00	100.66	0.00	1.81	1.00	0.00	0.00	0.18	0.00	0.00	0.00	0.00	3.00	0.91	0.10
					SD	0.00	0.00	0.98	0.57	0.09	0.16	0.61	0.09	0.10	0.00	0.00	1.16	0.00	0.02	0.00	0.00	0.00	0.00	0.01	0.00	0.00	0.00	0.00	0.00	0.00
UHPPC339	OL	8	5.7	760	Mean	0.00	0.00	54.15	41.79	0.07	0.41	3.40	0.00	0.20	0.00	100.02	0.00	1.92	1.00	0.00	0.01	0.07	0.00	0.00	0.00	0.00	0.00	3.00	0.97	0.58
					SD	0.00	0.00	0.54	0.40	0.07	0.11	0.16	0.00	0.14	0.00	0.00	0.97	0.00	0.00	0.00	0.00	0.00	0.00	0.00	0.00	0.00	0.00	0.00	0.00	0.00
D1867	GRT	11	4	780	Mean	0.00	0.00	25.13	43.15	22.79	0.00	7.41	0.01	1.97	0.00	100.46	0.00	2.60	3.00	1.87	0.00	0.43	0.00	0.11	0.00	0.00	8.01	0.86	0.05	
					SD	0.00	0.00	0.33	0.47	0.31	0.00	0.52	0.04	0.24	0.00	0.00	1.07	0.00	0.03	0.01	0.01	0.00	0.03	0.00	0.01	0.00	0.00	0.00	0.01	0.01
UHPPC335	GRT	10	6	700	Mean	0.00	0.00	26.17	42.99	22.68	0.00	5.48	0.00	2.08	0.00	99.40	0.00	2.72	3.00	1.86	0.00	0.32	0.00	0.12	0.00	0.00	8.01	0.89	0.06	
					SD	0.00	0.00	0.83	1.07	0.68	0.00	0.30	0.00	0.19	0.00	0.00	2.44	0.00	0.03	0.00	0.02	0.00	0.02	0.00	0.01	0.00	0.00	0.00	0.01	0.01
D1861	OPX	2	1	800	Mean	0.00	0.00	35.09	57.20	0.20	0.00	5.94	0.00	0.10	0.00	98.54	0.00	1.82	1.99	0.01	0.00	0.17	0.00	0.00	0.00	0.00	4.00	0.91	0.12	
					SD	0.00	0.00	0.10	0.24	0.20	0.00	0.08	0.00	0.10	0.00	0.00	0.05	0.00	0.00	0.01	0.01	0.00	0.00	0.00	0.00	0.00	0.00	0.00	0.00	0.00
D1819	OPX	6	3	820	Mean	0.00	0.00	35.62	57.98	0.07	0.00	6.13	0.07	0.06	0.00	99.93	0.00	1.83	1.99	0.00	0.00	0.18	0.00	0.00	0.00	0.00	4.00	0.91	0.13	
					SD	0.00	0.00	0.58	0.66	0.10	0.00	0.22	0.11	0.09	0.00	0.00	1.38	0.00	0.01	0.00	0.00	0.00	0.01	0.00	0.00	0.00	0.00	0.00	0.00	0.00
D1859	SP	13	2	840	Mean	0.00	0.00	24.38	0.00	63.67	0.00	4.92	0.00	7.02	0.00	100.00	0.00	0.90	0.00	1.86	0.00	0.10	0.00	0.14	0.00	0.00	3.00	0.90	0.07	
					SD	0.00	0.00	0.37	0.00	0.57	0.00	0.28	0.00	0.51	0.00	0.00	0.00	0.00	0.01	0.00	0.01	0.00	0.01	0.00	0.01	0.00	0.00	0.01	0.01	0.01
UHPPC345	SPI	6	5.8	720	Mean	0.00	0.00	19.75	0.00	47.85	0.00	9.68	0.00	22.73	0.00	100.00	0.00	0.79	0.00	1.51	0.00	0.22	0.00	0.48	0.00	0.00	3.00	0.78	0.24	
					SD	0.00	0.00	0.55	0.00	0.89	0.00	0.53	0.00	0.88	0.00	0.00	0.00	0.00	0.02	0.00	0.02	0.00	0.01	0.00	0.02	0.00	0.00	0.00	0.01	0.01
UHPPC356	11.5Å	12	6	740	Mean	11.58	0.00	45.35	25.77	10.41	0.38	2.42	0.00	1.42	0.00	85.75	0.00	10.51	4.01	1.91	0.05	0.32	0.00	0.17	0.00	0.00	16.95	0.97	0.06	
					SD	0.36	0.00	1.56	0.85	0.40	0.14	0.20	0.00	0.15	0.00	0.00	2.68	0.00	0.10	0.05	0.04	0.02	0.03	0.00	0.02	0.00	0.00	0.04	0.00	0.04
UHPPC341	MgS	10	6.2	640	Mean	6.70	0.00	21.43	38.27	24.12	0.00	2.55	0.00	2.62	0.00	88.99	0.00	5.01	6.00	4.45	0.00	0.33	0.00	0.32	0.00	0.00	16.11	0.94	0.07	
					SD	0.08	0.00	0.30	0.68	0.26	0.00	0.12	0.00	0.28	0.00	0.00	1.02	0.00	0.05	0.05	0.04	0.00	0.02	0.00	0.03	0.00	0.00	0.03	0.00	0.03

TABLE 3.4: Representative analyses of run products in Series 1.

Two analyses were selected for each run product identified in this series. Where possible, two contrasting analyses were selected (eg: garnet both in and out of chlorite stability field). SD=one standard deviation from the mean. All FE-SEM analytical results can be found in the Appendix.

3.2.5 PHASE COMPOSITION

Each mineral phase identified in this series was analysed using FE-SEM to establish the average chemical composition. A representative set of analyses of run products is displayed in Table 3.4. A complete list of analyses is available in the Chapter 3 Appendix.

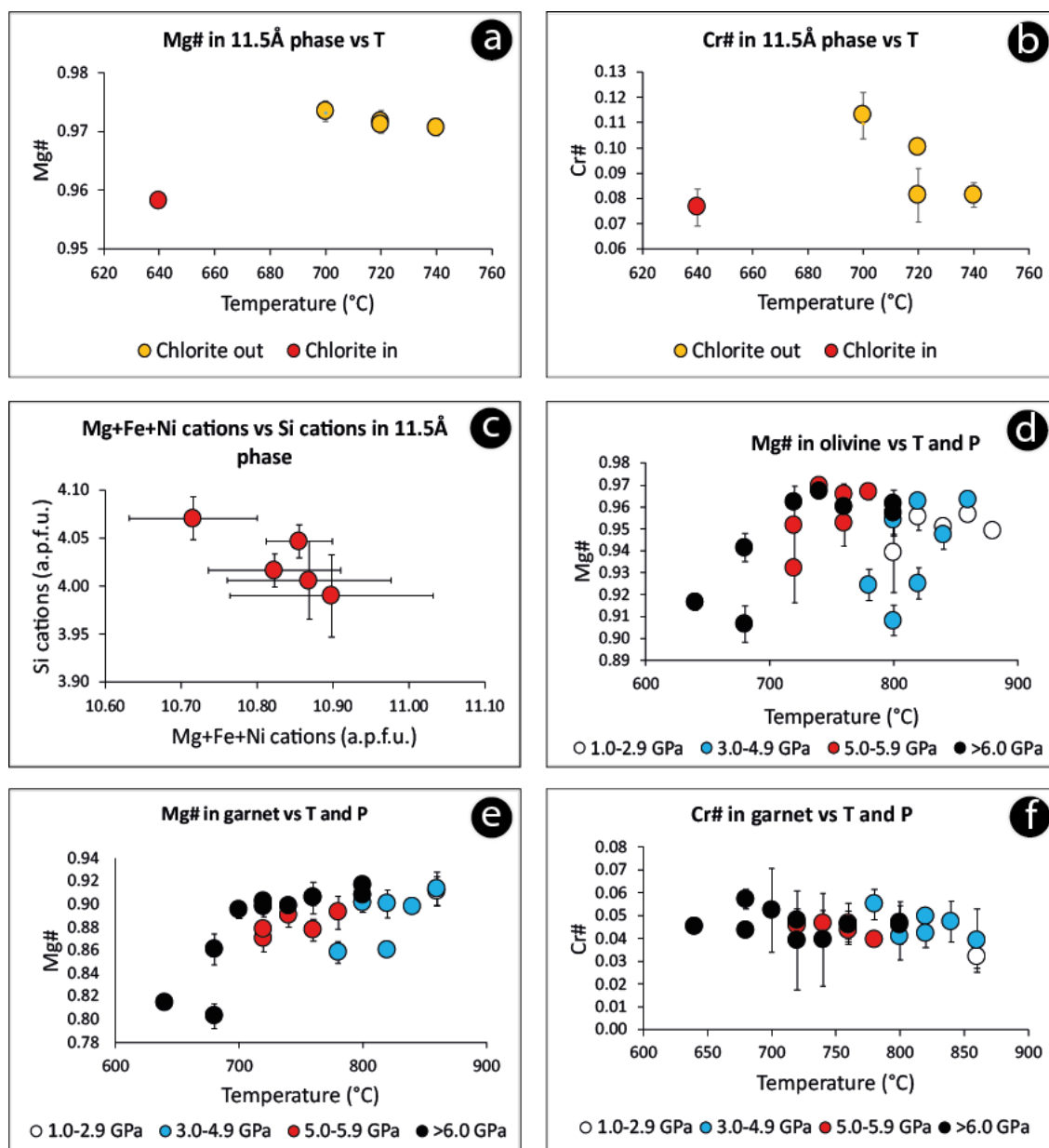


FIGURE 3.10: Compositional plots of 11.5Å-phase, olivine and garnet in Series 1

a and b) Plots of T vs Mg# and Cr# respectively in 11.5Å phase. A strong inverse relationship is apparent with both Mg# and Cr# reducing with increasing T. **c)** Atomic substitution in 11.5Å-phase. Experimental results indicate a coupled substitution with an inverse relationship between Si cations and Mg+Fe+Ni cations. Charge balance is attained through Al+Cr substitution on both the tetrahedral and octahedral sites. **d)** Plot of Mg# vs P and T in olivine show a strong correlation between increased Mg# and increased T, but no significant pattern between Mg# and P. **e and f)** Plots of P and T vs Mg# and Cr# respectively in garnet. A positive trend is discernible between Mg# and T with a moderate inverse relationship apparent between Cr# and T. The range of Mg# widens with increasing P; otherwise no relationship with P is detected. No significant relationship between Cr# and P is evident.

3.2.5.1 Chlorite

The stoichiometric composition of chlorite was calculated to be $(\text{Mg}_{4.81} \text{Fe}_{0.30} \text{Ni}_{0.02}) (\text{Al}_{1.45} \text{Cr}_{0.12}) \text{Si}_{3.26} \text{O}_{10} (\text{OH})_8$. Analyses of chlorite consistently revealed a mean Mg# of 0.94 and a Cr# of 0.07. Each showed slight variation but all within error. No significant correlation was observed between Mg# and Cr# with either pressure and temperature throughout the entire series which indicated that chlorite composition remained unchanged from the starting material.

3.2.5.2 11.5Å-phase

The 11.5Å-phase has not been detected previously in naturally-occurring rocks. This phase appeared in run products of seven experiments, five of which were successfully analysed by FE-SEM. The fine, intercalated texture of 11.5Å-phase hampered successful analysis of the two other samples. Mass balance calculations determined this phase was also present in an eighth experiment, Run UHPPC-364 (6.0 GPa/760°C). Whilst the 11.5Å-phase was not identified during analysis, textural observation elicited crystal outlines typical of the 11.5Å-phase which suggested that this phase was likely disgorged during mount polishing.

The 11.5Å-phase exhibited variable composition: Mg: 10.37-10.56 a.p.f.u.; Fe: 0.29-0.45 a.p.f.u., Si: 3.99-4.06 a.p.f.u., Al: 1.86-1.91 a.p.f.u., Cr: 0.16-0.24 a.p.f.u. and Ni: 0.04-0.06 a.p.f.u.. In the stability field of grt+ol+11.5A+sp+fluid, temperature increase was moderately correlated with a decrease in both Cr# and Mg# (see Figures 3.10a and b). No correlation with pressure was observed with either ratio (Cai *et al.*, 2015). An inverse relationship between Si and Mg cations was possibly due to a $\text{Si}^{4+}\text{Mg}^{2+}_{-1}\text{Mg}^{2+}_{-1}$ coupled substitution, as shown in Figure 3.10c, with charge balance achieved with Al and Cr cations substituting on both tetrahedral and octahedral sites. When coexisting with chlorite, the composition of 11.5Å-phase recorded lower Mg# and Cr# compared with its composition in the chlorite absent field (see Figures 3.10a and b).

3.2.5.3 Olivine

Olivine composition was close to forsterite with an average Mg# = 0.95 with moderate variation (0.91 - 0.97) across the series. No significant correlation was evident between Mg# and pressure. The Mg# showed a limited positive correlation with temperature throughout the series, most significant when the temperature increase occurred across the chlorite-out boundary (see Figure 3.6g).

A limited positive correlation was observed between Ni and Mg# following the disappearance of chlorite although the quantity of nickel within each olivine analysis was highly variable.

3.2.5.4 Garnet

FE-SEM analyses showed that garnet underwent consistent compositional change throughout the experimental series.

When new garnet nucleated around a pyrope-rich garnet seed ($Mg\#=0.92$), it formed pyrope-rich rims containing larger almandine component than the core ($Mg\#$ range 0.80 - 0.91). The almandine component decreased with increasing temperature (see Figure 3.7a). Garnet rims also contained a trace knorringite component ($Cr\#=0.03-0.05$) which showed moderate increase with increasing pressure (see Figure 3.7b). When garnet formed independent of garnet seeds, its composition was consistent with that of garnet rims previously described.

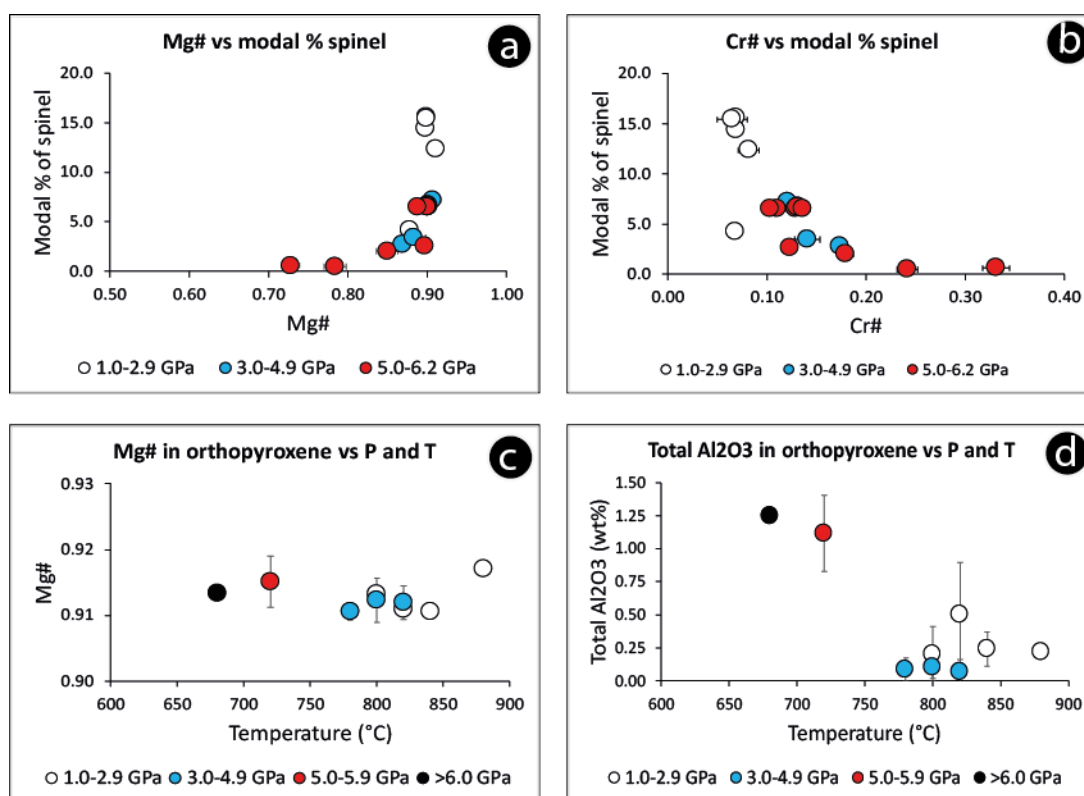


FIGURE 3.11: Compositional plots of spinel and orthopyroxene in Series 1

a) Plot of $Mg\#$ vs modal% of spinel at different pressure intervals. At low pressure, $Mg\#$ changes little regardless of the changing modal proportion. Above 3.0 GPa, a strong positive correlation is observed between modal % and $Mg\#$ with increased P . **b)** Plot of $Cr\#$ vs modal % of spinel at different pressure intervals. At low pressure, little variation occurs in $Cr\#$ of spinel regardless of the modal proportion formed. After 3.0 GPa, a strong inverse correlation is observed between the proportion of spinel phase and the $Cr\#$: as the former decreases, the latter increases. **c)** Plot of $Mg\#$ vs P and T in orthopyroxene. No apparent correlation is observed between $Mg\#$ and T but a slight negative trend between $Mg\#$ and P is observed although based on few analyses at high P . **d)** Plot of Total Al_2O_3 vs P and T in orthopyroxene. An inverse relationship is apparent: as T increases, total Al_2O_3 decreases but this observation is based on limited analyses at high P .

3.2.5.5 Spinel

Within the spinel stability field when garnet was not present ($P < 2.0$ GPa), little compositional variation was observed. Spinel was Mg-rich with limited variation in the hercynite component

(Mg#=0.88-0.91) and Al-rich with minor variation in the magnesiochromite component (Cr#=0.06-0.08).

By contrast, at higher pressure ($P > 3.0$ GPa) in the spinel + garnet stability field, large compositional variation was observed. The Mg# varied between 0.73-0.90 and exhibited a strong negative correlation with pressure and a strong positive correlation with temperature (see Figure 3.11a). The Cr# also displayed a wide range of values at high pressure varying between 0.10 and 0.52 with strong positive correlation with pressure and an inverse relationship with temperature. When plotted against phase abundance, the Cr# displayed a strong inverse correlation above 3.0 GPa (see Figure 3.11b).

Small grain size and its often poikiloblastic texture made FE-SEM analysis challenging.

3.2.5.6 *Orthopyroxene*

Orthopyroxene was close to enstatite (average Mg#=0.91) and displayed little variation (0.91-0.92) throughout the series. There was an absence of correlation between Mg# and P and Mg# and T (see Figure 3.11c). This was most likely due to the very low quantity of orthopyroxene contained in product runs and therefore the low number of analyses rather than any experimental or analytical error.

A weak inverse correlation was observed between total Al_2O_3 and temperature (see Figure 3.11d). The low stoichiometric number of Si cations and the presence of Al and Cr cations provides evidence of Tschermak exchange in orthopyroxene.

Large orthopyroxene crystals often formed which exhibited heterogeneous zoning with high aluminium concentrations (>10 wt%) in the core with rims recording low or zero aluminium readings. This was more common at low pressure. Compositional zoning and small crystal size combined to make orthopyroxene analyses troublesome throughout this series.

3.2.5.7 *Mg-sursassite*

Mg-sursassite exhibited considerable compositional variation although data was collected at only two P,T locations (6.2 GPa at 640°C and 680°C). The Mg# averaged a consistent 0.94 and the Cr# 0.07 at 640°C but these values reduced to Mg#=0.85 and Cr#=0.05 at 680°C. Ideal stoichiometry of $\text{Mg}_5\text{Al}_5\text{Si}_6\text{O}_{21}(\text{OH})_7$ was likely achieved by the presence of small amounts of Fe^{3+} .

Both Mg# and Cr# appeared to show a strong inverse correlation with temperature, however any relationship between pressure and composition remained unknown due to insufficient data.

3.2.6 ELEMENT PARTITIONING

An examination of the changing chemical composition of mineral phases in this experimental series enables the partitioning of major elements to be determined. Of importance is the exchange between Mg-Fe, sensitive to changes in temperature, and between Al-Cr, which is sensitive to changes in both temperature and pressure. The status of partitioning between these two elemental pairs provides an estimate of the extent of equilibrium of co-existing mineral phases, and thus provides verification of the analytical data in this study.

Mg-Fe partitioning between co-existing phases was illustrated by the Mg# ($Mg/(Mg+Fe)$) which displayed a consistent pattern at each pressure interval, listed here in descending order of magnitude: $11.5\text{\AA} > \text{MgS} > \text{chl} > \text{ol} > \text{opx} > \text{grt} > \text{sp}$. A few exceptions to this pattern were identified. Firstly, at 5.0GPa/780°C and at 5.5/740°C, spinel recorded a higher Mg# of 0.90 compared with garnet of 0.89, but this can be explained due to the limited number of spinel analyses ($n=1$ and 4 respectively) at these locations.

Select partitioning patterns are displayed in Figure 3.12. Figure 3.12a shows Mg-Fe partitioning between garnet and spinel vs temperature, with the partitioning coefficient calculated using $K_D = (X_{Mg}^{grt})(X_{Fe}^{sp}) / (X_{Fe}^{grt})(X_{Mg}^{sp})$. Mg always showed an affinity for garnet over spinel, however, Mg-Fe partitioning between spinel and garnet was insensitive to changes in temperature, as evidenced by the horizontal slope of the trend line. Mg-Fe partitioning between garnet and spinel was also insensitive to pressure.

Mg-Fe partitioning between the garnet-olivine mineral pairs is shown in Figure 3.12c, with the coefficient of partitioning determined using the equation $K_D = (X_{Mg}^{ol})(X_{Fe}^{grt}) / (X_{Fe}^{ol})(X_{Mg}^{grt})$. Fe always preferentially partitioned into garnet over olivine, but this trend diminished with increasing temperature as the $\ln K_D$ values approached zero.

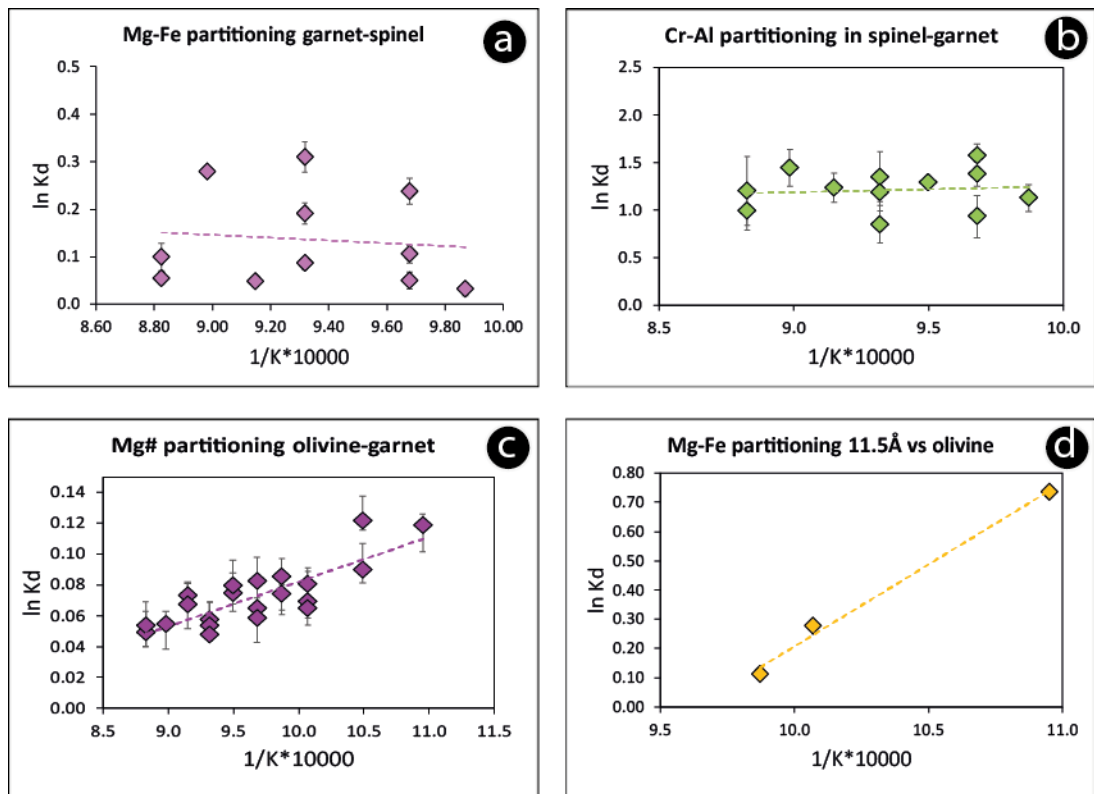


FIGURE 3.12: Element partitioning by selected phase in Series 1.

a) Plot of Mg-Fe partitioning between garnet and spinel vs T . Partitioning between these phases is unaffected by changes in temperature. **b)** Plot of Cr-Al partitioning between spinel and garnet vs T . Partitioning between these phases is unaffected by changes in temperature. **c)** Mg-Fe partitioning between garnet and olivine. With increasing temperature, the partitioning coefficient approaches zero. **d)** Plot showing partitioning between 11.5Å-phase and olivine. Although limited data is available, Mg partitioning favours 11.5Å-phase but this reduces with increasing temperature.

Partitioning patterns were also recognised when 11.5Å-phase was plotted against olivine (see Figure 3.12d) with the partitioning coefficient calculated using the equation $K_D = \frac{(X_{Mg}^{11.5A})(X_{Fe}^{ol})}{(X_{Fe}^{11.5A})(X_{Mg}^{ol})}$. Few data points were obtained, but a strong trend was observed: Mg always showed an affinity for 11.5Å-phase over olivine, but this reduced as temperature increased.

The Cr# ($Cr/(Cr+Al)$) was used to illustrate Cr-Al partitioning between co-existing phases. The resulting partitioning sequence, in descending order, was $sp > chl > 11.5\text{\AA} > MgS > grt$. Two co-existing phases were not considered since they contained only trace aluminium and/or chromium (ie: olivine) or contained too few data points for sensible comparison (ie: opx).

There were three exceptions to this partitioning sequence. Chlorite recorded a marginally higher Cr# than spinel at low pressure (D1861 and D1859), whilst at high pressure, grt and MgS swapped their sequencing order (UHPPC341 and UHPPC385), likely due to limited data collected for the MgS phase.

Figure 3.12b displays the Cr-Al partitioning between spinel and garnet vs temperature with the partitioning coefficient calculated using $K_D = (X^{sp}_{Cr})(X^{grt}_{Al}) / (X^{sp}_{Al})(X^{grt}_{Cr})$. At all times, Cr showed an affinity for spinel over garnet, but there was no significant change in partitioning patterns when plotted against temperature.

3.3 DISCUSSION

This experimental series aimed to constrain the upper stability boundary of natural chlorite using piston cylinder experimentation. The results indicated that chlorite and two other hydrous phases are stable to higher pressures and temperatures than previously thought which has implications for water transport through the mantle. Evidence has been detailed in five related sections. The first part will refer to the attainment of equilibrium. Secondly, the experimental results are examined within the context of the theoretical MAS system. Thirdly, the effect of Fe and Cr on chlorite phase stability is explored. Fourthly, the results of this study are compared to previous research on chlorite stability. Finally, the quantity and rate of water release from decomposing hydrous phases at high pressure is estimated.

3.3.1 ATTAINMENT OF EQUILIBRIUM

This experimental series was affected by two constraints which had the potential to disrupt the attainment of equilibrium. Firstly, experiments were conducted at relatively low temperatures, conditions which tend not to favour the kinetics of chemical reactions. Product phases, therefore, typically did not exhibit full equilibrium textures. Secondly, the starting material comprised natural minerals which resulted in several solid-solution reactions, the creation of multivariant fields, and compositional heterogeneity for some phases. This meant that care had to be taken in sampling only those regions of crystals which appeared to be in local equilibrium.

Notwithstanding these constraints, observation of phase textures revealed that local equilibrium was achieved, and this was verified by several methods. Grain boundaries between co-existing garnet-chlorite and garnet-11.5Å-phase were generally well-equilibrated (see Figures 3.3 e and 3.4b) whilst the anhydrous assemblage garnet-olivine-spinel (see Figures 3.4 c, f) were less well characterised. Nevertheless, euhedral grain boundaries between all co-existing phases could be found, indicating these locations were approaching equilibrium. It was from these sites that FE-SEM analyses were taken. Heterogeneous phase textures were common in olivine, garnet, opx and spinel phases. However, analyses were drawn from those regions of crystals which were homogeneous in appearance and therefore thought to be approaching equilibrium. Multiple analyses revealed consistent chemical composition at these

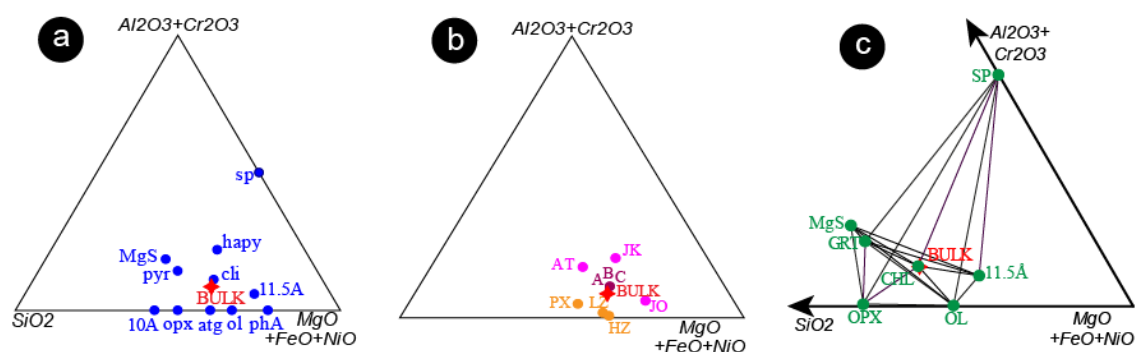
sites. Although pyrope seeds were not always resorbed, the boundary between the seed cores and the growth rims was sharp which indicated the rims approached chemical equilibrium. Analyses of garnet rims confirmed compositional homogeneity. Partitioning of Mg-Fe and Cr-Al between mineral pairs as detailed above indicate chemical equilibrium was achieved. Phase relations were consistent with the application of Schreinemakers' Rules – another indication that equilibrium was attained. Mass balance of phase composition of run products compared to the starting material showed excellent agreement which also indicated that analyses must have targeted crystals in chemical equilibrium. Mass balance calculations accounted for all Fe within error therefore there was no evidence of Fe loss to the gold capsule during experiments. Absence of Fe loss to the capsule also demonstrated that oxygen fugacity remained close to Ni-NiO buffer in each run.

3.3.2 THEORETICAL PHASE RELATIONS IN THE CRFNMASH SYSTEM

The theoretical phase relations based on the Series 1 bulk composition can be derived using chemography and Schreinemakers' method. This approach enables a petrogenetic grid to be created in the P-T space examined and assists with the verification of the experimental results.

In order to perform a Schreinemakers analysis of a complex natural system, some simplification of the elemental components was required. Due to their capacity to exchange with each other, Mg, Fe and Ni were treated as a single component, Al and Cr were combined to form a second component, and Si provided the third component. Figure 3.13 provides a detailed chemography of the starting material in the three-component (MgO+FeO+NiO)-(Al₂O₃+Cr₂O₃)-SiO₂ system, projected from H₂O. Colour-coded tie-lines show the location of all four chlorite terminal reactions observed in the Series 1 study.

Schreinemakers' method applied to this system confirmed that only five phases can be present at any invariant point. Since seven solid phases were identified in Series 1, two must always be absent at each invariant point, and are marked accordingly using square brackets.



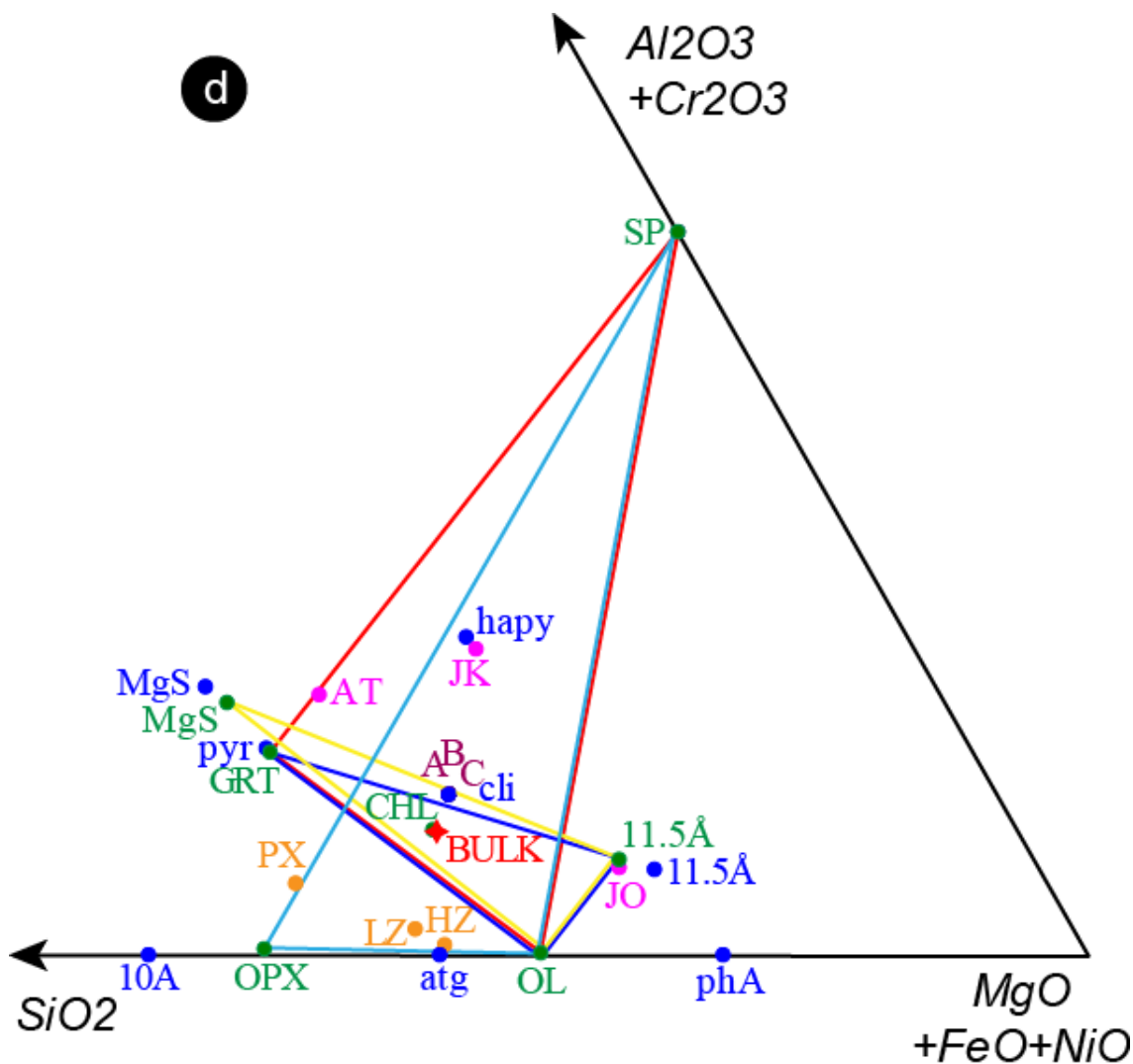


FIGURE 3.13: Chemography of low-Al chlorite in ternary compositional space.

a) Chemograph showing possible phases relevant to this bulk in ternary compositional space. Compositions are in wt%. **b)** Chemograph showing relevant high-pressure hydrous phases relevant to this bulk identified in recent studies: labelled in purple, A, B, C indicate different bulk compositions of Cr-chlorite (Fumagalli et al., 2014); labelled in orange, PX, LZ and HZ (Fumagalli and Poli, 2005) are analogues of naturally-occurring peridotite compositions; labelled in pink, AT, JK and JO (Fumagalli et al., 2014) represent differing bulk compositions aimed at crystallising specific high-pressure, hydrous phases, namely phase-HAPY, Mg-sursassite and 10A-phase. **c)** Chemographic relationship between phases identified in Series 1 experiments. Phases are marked in green lettering. The bulk composition is marked in red. Tie-lines connect each of the reactions. **d)** Compilation of a), b) and c) above highlighting the four chlorite terminal reactions in compositional space: Reaction 1/A3 $chl=opx+ol+sp+H_2O$ (light blue); Reaction 2/B2 $chl=opx+sp+ol+H_2O$ (red); Reaction B6/E2 $chl=grt+ol+11.5\text{\AA}+H_2O$ (dark blue); Reaction E6/F2 $chl=ol+11.5\text{\AA}+MgS+H_2O$ (yellow). Note that Reaction B6/E2 does not occur in clinocllore compositions. This plot was made using the program C-Space (Torres-Roldan et al., 2000).

The theoretical phase relations within the experimental P-T space are displayed in Figures 3.14 and 3.15.

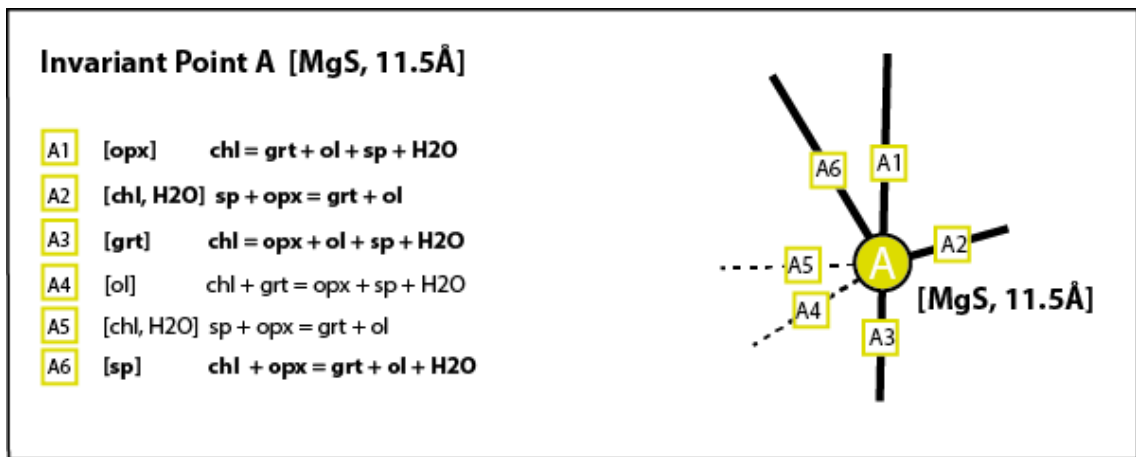
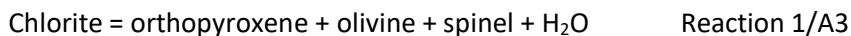


FIGURE 3.14: Schreinemaker plot showing theoretical phase relations in low-Al chlorite at low pressure.

Invariant Point A marks the convergence of the phases olivine, garnet, spinel, orthopyroxene and chlorite. Dotted reaction lines refer to reactions which do not occur in this bulk composition.

Figure 3.14 shows the stable paragenesis spinel, garnet, orthopyroxene, chlorite and olivine which converge to form Invariant Point A at the garnet-spinel boundary. In the spinel stability field (pressures below the invariant point), the chlorite-out reaction was informed by the two model Reactions 1 and 2:



At higher pressure, in the garnet stability field, Reaction 2 was relevant:



At higher pressure, four further invariant points were found, each proximal in P-T space. These are shown in Figure 3.15. Invariant Point B (chlorite, olivine, garnet, spinel and 11.5Å-phase) marked the low-pressure boundary of the hydrous 11.5Å-phase, the latter formed as a product of chlorite breakdown. At pressures above Invariant Point B, the chlorite terminal reaction was informed by:



and the low-pressure, high-temperature stability boundary of 11.5Å-phase was informed by:



Invariant Point D denoted the paragenesis Mg-sursassite, olivine, garnet, chlorite and orthopyroxene, with the upper stability boundary of orthopyroxene, delineated by Reaction 4/D3/D6.

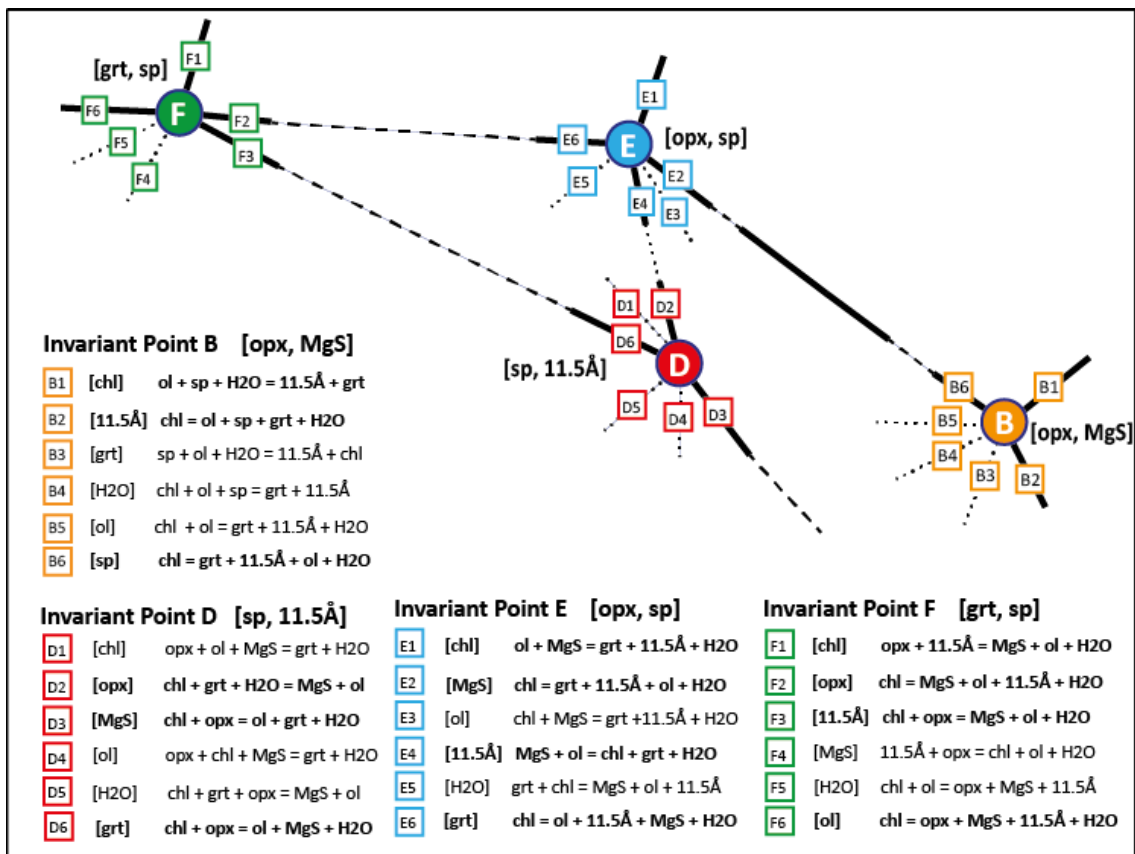
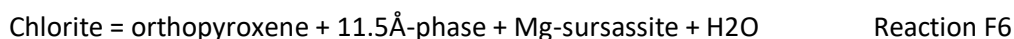
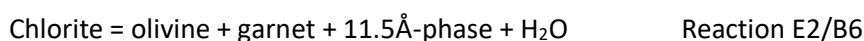


FIGURE 3.15: Schreinemaker plot showing theoretical phase relations of low-Al chlorite at high pressure

Each of the Invariant Points B to F involve a chlorite terminal reaction and/or two other high-pressure, hydrous phases: Mg-sursassite and 11.5Å-phase. Dotted reaction lines refer to reactions which do not occur in this bulk composition.

The co-existence of the three hydrous minerals occurred at both Invariant Points E and F. These points also delineated the high-pressure stability boundary of chlorite, shown respectively by the following three reactions:



The low-pressure boundary of the 11.5Å-phase is delineated by Invariant Points B-E-F whilst the high-temperature boundary of Mg-sursassite is demarked by Invariant Points D-E. The small stability field bound by Invariant Points D-E-F registered the co-existence of chlorite and MgS, evidence of a high-pressure hydrous phases forming contiguously with chlorite.

3.3.3 THEORETICAL PHASE RELATIONS – LOW-AL CHLORITE VERSUS CLINOCHLORE

Previous experimental studies of chlorite stability typically used end-member clinochlore as opposed to this study which utilised a naturally-occurring, low Al-chlorite. Figure 3.13 has marked both compositions as “cli” and “CHL” respectively. Although they are compositionally

close, they are sufficiently different to incur a significant change to phase relations. The most obvious concerns the chlorite terminal Reaction B6/E2 ($\text{chl}=\text{grt}+\text{ol}+11.5\text{\AA}+\text{H}_2\text{O}$), marked in dark blue on Figure 3.13. This reaction cannot occur in a clinochlore composition as clinochlore sits outside the grt-11.5A-ol triangle. Low-Al chlorite is contained within this triangular space and so does occur in Series 1 experiments.

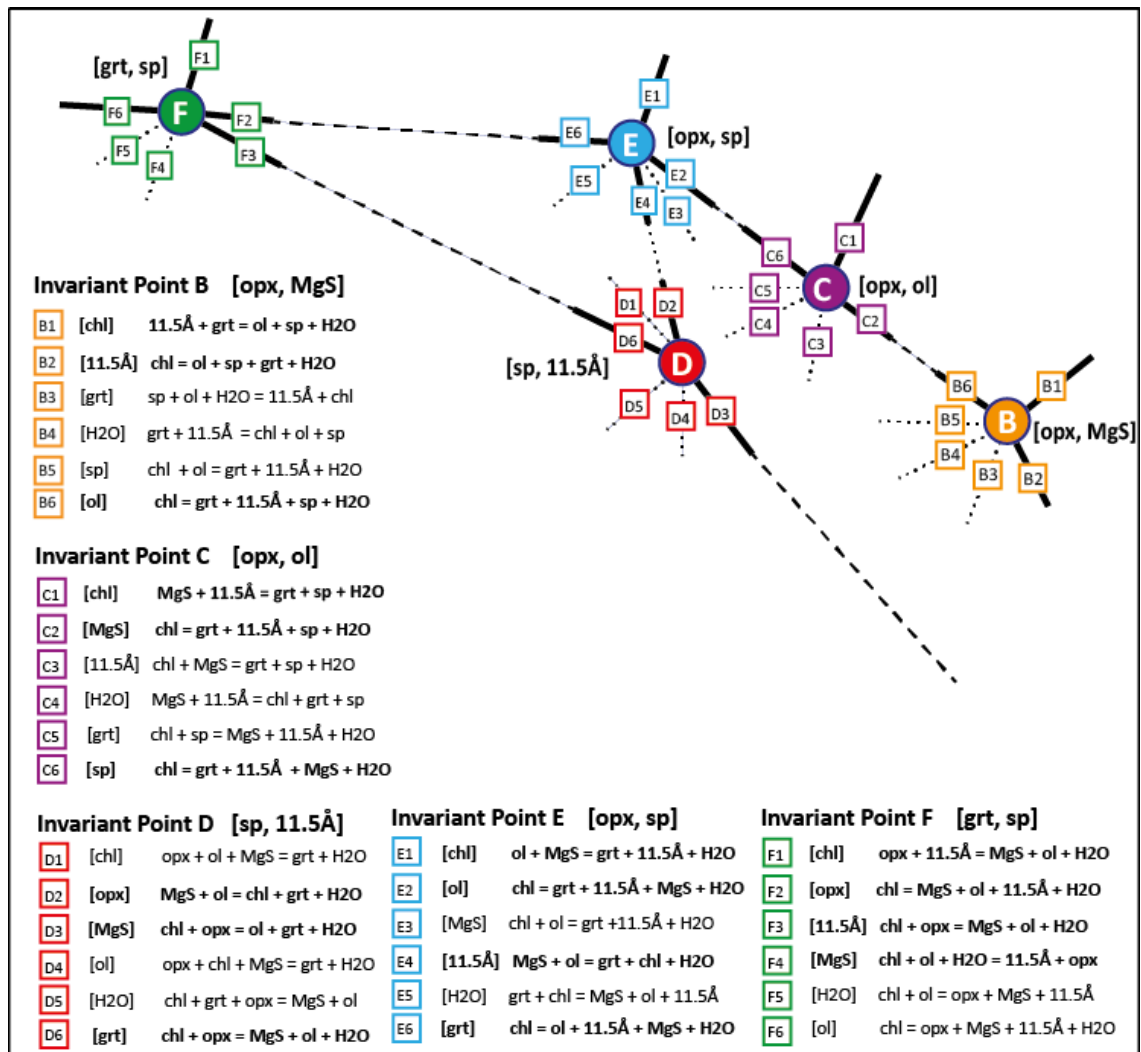


FIGURE 3.16: Schreinemaker analysis showing theoretical phase relations of clinochlore at high pressure

Each of the Invariant Points B to F involve a chlorite terminal reaction and/or two other high-pressure, hydrous phases: Mg-sursassite and 11.5Å-phase. Dotted reaction lines refer to reactions which do not occur in this bulk composition. Note that Invariant Point C occurs in clinochlore compositions and would disappear in chlorite of low-Al composition. Schreinemaker analysis of chlorite of clinochlore composition is shown in Figure 3.16. Three key differences are of note. Firstly, an additional invariant point - Invariant Point C – occurs in this system. The slight compositional change of clinochlore means that the spinel stability field extends to higher pressure (to Invariant Point C) and the MgS field extends to higher temperature (to Invariant Point C). This impacts the stability field of olivine, which disappears

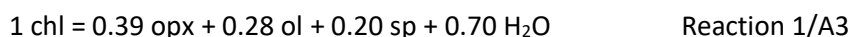
between Invariant Points E and B. Several phase reactions are affected, producing a significant contrast with the theoretical phase relations in naturally-occurring, low-Al chlorite.

3.3.4 KEY TERMINAL CHLORITE REACTIONS DETERMINED BY MASS BALANCE

Several important limiting reactions, identified by Schreinemakers analysis, were determined using the results from experimental Series 1. Mass balance calculations (see Table 3.4) provided modal % of each phase, which following conversion to mole %, were used by C-Space (Torres-Roldan *et al.*, 2000) to ascertain molar proportions of each reactant and product. This strategy confirmed two of the limiting reactions on chlorite stability (A1 and A3/B2), as well as the low-P, high-T boundary of 11.5Å-phase marked by Reaction B1.

Up to 5.7 GPa/735°C, the position of the chlorite-out curve was well-informed by two key reactions: A3, in the spinel stability field, and A1/B2 in the garnet stability field. When adjusted for the presence of Fe and Cr, these results confirmed those previously described in the literature (Staudigel and Schreyer, 1977; Jenkins and Chernosky, 1986).

Reaction 1/A3 was relevant at pressures below Invariant Point A located near 2.3GPa, 850°C. The chlorite breakdown reaction was located experimentally between 800°C and 820°C at 1.0 GPa and is represented by the equation:

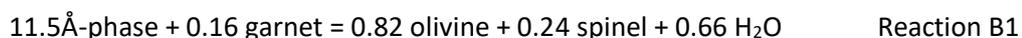


Reaction 2/A1/B2 linked Invariant Points A and B, the latter located near 5.7 GPa, 735°C. The breakdown of chlorite to an anhydrous assemblage was determined at 3.0GPa between 840°C and 860°C by the reaction:



Three additional reactions limiting chlorite stability were identified by Schreinemakers analysis which connected Invariant Points B-E-F. Insufficient data points were collected in this study to ascertain the molar proportions of these reactions.

However, the limiting reaction which marked the low P, high-T boundary of the 11.5Å-phase was determined experimentally at 6.2 GPa between 760°C and 800°C by the equation:



3.3.5 CHLORITE TERMINAL REACTION CURVES IN ULTRAMAFIC LOW-AL CHLORITE

A simplified phase diagram of Series 1 experimental results is shown in Figure 3.16. Reactions 1 and 2 have been highlighted. Other important reactions are shown in black. Key invariant points (letter symbols enclosed in a circle) show linkages between reactions.

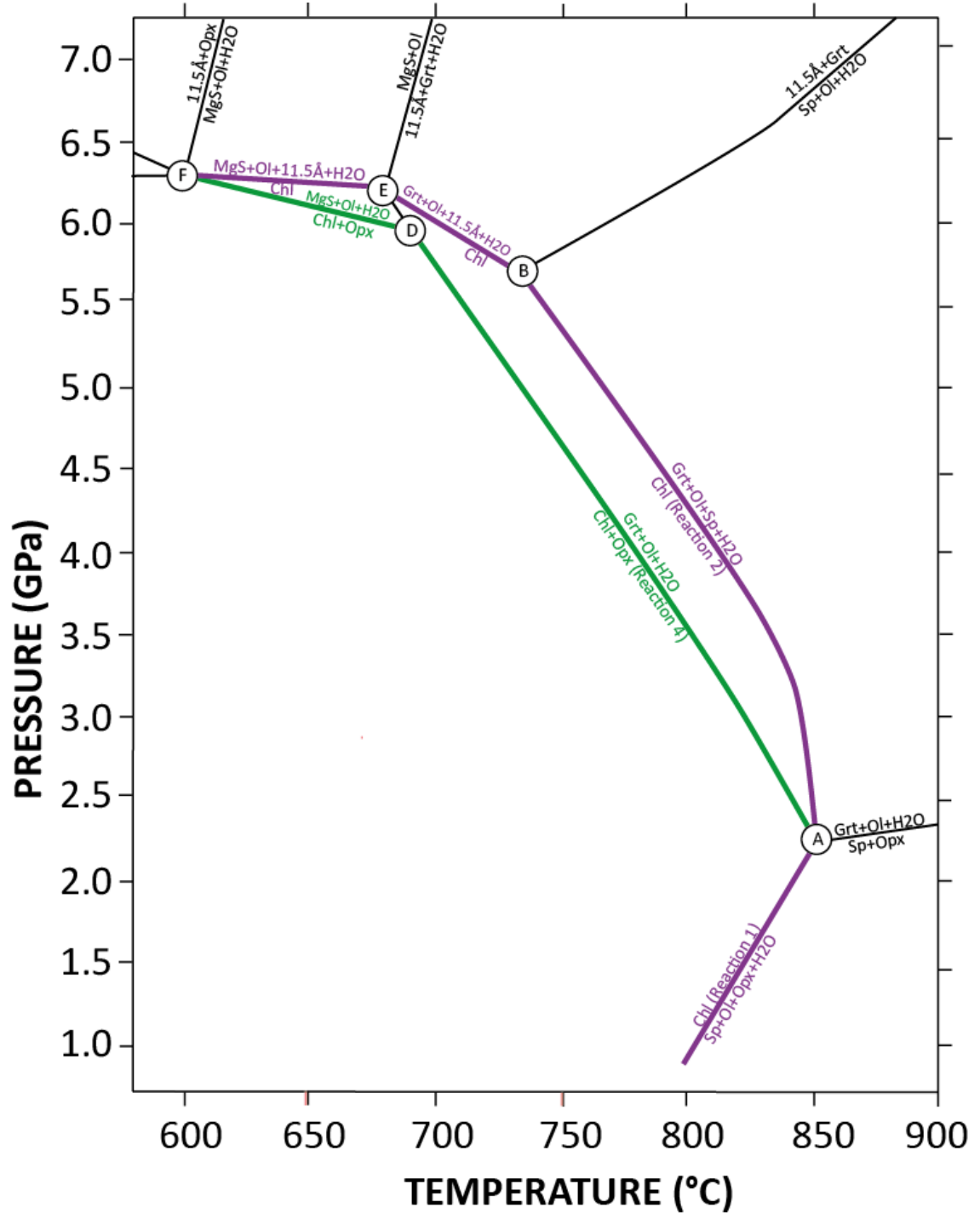


FIGURE 3.16: Phase relations in ultramafic, low-Al chlorite highlighting key Reactions 1, 2 and 4.

Chlorite dehydration curves (Reactions 1 and 2) are shown in purple; Reaction 4 is shown in green. Other key reactions in this system are indicated by black lines. Circled letters show location of key invariant points – see text for details. Phase abbreviations as previously denoted.

3.3.5.1 Slope of the chlorite terminal reaction curve (Reaction 1)

Reaction 1 was determined experimentally between 1.0 GPa, 800°C and its termination at Invariant Point A located near 2.3 GPa, 850°C. Its curve exhibited a steep, positive slope with no change in gradient and showed excellent agreement with Reaction 1 curves determined in previous studies (Staudigel and Schreyer, 1977; Jenkins, 1981).

3.3.5.2 Slope of the chlorite terminal reaction curve (Reaction 2)

From Invariant Point A, the chlorite-out curve progressed steeply to ~3.2 GPa, then underwent a slight backbend turning steeply negative through to Invariant Point B at 5.7 GPa/735°C. Invariant Points A and B marked the low-pressure and high-pressure termination of Reaction 2.

3.3.5.3 Slope of the chlorite terminal reaction curve to higher pressure

Experimental results from this study showed that chlorite remained stable to pressures above 5.7 GPa. In continuing its journey to higher-pressure, the chlorite dehydration curve encountered three additional invariant points which linked three new chlorite terminal reactions. These will be elucidated below.

The chlorite-out curve exhibited a moderate backbend at Invariant Point B and continued with the same gradient through Invariant Point C (6.0 GPa, 700°C) to Invariant Point E at 6.2 GPa, 680°C. A further moderate backbend saw the chlorite dehydration curve progress at a very low angle towards Invariant Point F inferred to be located near 6.3 GPa, 600°C.

Additional experimental work is required to fully constrain the Clapeyron slope of the curve between Invariant Points E and F.

3.3.6 LOCATION OF INVARIANT POINTS

This study revealed four invariant points which delineated the terminal chlorite reaction, two of which have not been identified in previous studies of chlorite stability. All showed excellent agreement with those points identified by Schreinemaker's method shown in Figures 3.14 and 3.15. Two showed strong agreement with invariant points determined in previous research when adjusted for the addition of Fe and Cr.

3.3.6.1 Invariant points relevant to the terminal chlorite reaction (Reaction 1)

Reaction 1/A3 was linked to a single invariant point.

Invariant Point A was located near 2.3 GPa, 850°C and marked the high-pressure termination of Reaction 1/A3. The equivalent point in chlorite peridotite experiments (see Chapter 4) was shifted to lower pressure and lower temperature and marked by Invariant Point A'.

Several key chlorite reactions converged at this invariant point: the high-pressure termination of Reaction 1/A3 and Reaction 3/A6, and the low-pressure termination of Reaction 2/A1. Reaction A2 also terminated at this point delineating the upper boundary of a ~0.2 GPa (2.1 GPa-2.3 GPa) divariant field which saw the appearance of garnet. This invariant point was first determined experimentally in the MASH system by Staudigel and Schreyer (Staudigel and Schreyer, 1977) at 2.03 GPa/894°C. Later research by Jenkins (Jenkins, 1981) necessitated a pressure correction down to 1.8 GPa, 894°C which placed it some ~0.5 GPa lower and ~45°C higher than determined in the current study. When corrected for the inclusion of iron and chromium in the starting mix, the current results show very good agreement with previous work.

3.3.6.2 Invariant points relevant to the terminal chlorite reaction (Reaction 2)

Reaction 2/A1/B2 linked two invariant points – A and B.

Invariant Point B was located at 5.7 GPa, 735°C. It saw the merging of three key reactions: the high-pressure termination of Reaction 2/A1/B2, and two reactions which involved the introduction of 11.5Å-phase – Reactions B1 and B6/C2 – which together delineated the low-P, low-T boundary of this phase. This invariant point has not been identified in previous high-pressure studies.

3.3.6.3 Invariant points relevant to additional high-pressure terminal chlorite reactions

Two new chlorite terminal reactions were identified at pressure >5.7 GPa which, in turn, linked to two new invariant points. These were labelled Invariant Points E and F.

Reaction B6/E2 connected Invariant Points B and E and delineated the thermal maximum of chlorite:



Invariant Point E occurred near 6.2 GPa, 680°C. The high-pressure termination of Reaction B6/E2 occurred here, along with the high-temperature termination of another new Reaction E6/F2:



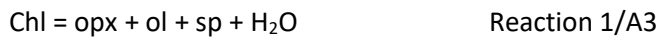
The chlorite terminal reaction E6/F2 witnessed the formation of olivine, 11.5Å-phase and MgS, the latter phase forming at the expense of garnet.

Invariant Point F was located near 6.3 GPa, 600°C. The low-temperature termination of Reaction F2 occurred at this point. Significantly, it also marked the high-pressure termination of Reaction D6/F3 which is the chl+opx reaction common in chlorite peridotite compositions. Chlorite is thought to disappear according to Reaction F6 but further experimentation is needed to support this.

The passage of the chlorite terminal reaction through Invariant Points B-E-F marked entirely new territory for chlorite stability in ultramafic lithologies since previous research had not identified chlorite at such high pressure. Since Reaction 2 was limited to pressures up to 5.7 GPa, two new chlorite limiting reactions were identified at high pressure, confirming those identified by Schreinemakers modelling, each of which warrant further experimental investigation.

3.3.7 PREVIOUS CHLORITE DEHYDRATION STUDIES IN THE MASH SYSTEM

The first studies of the terminal chlorite reactions were low pressure experiments based on end-member clinocllore compositions (Fawcett and Yoder, 1966) bracketing the reaction,



At pressures above the garnet-spinel transition, the chlorite terminal reaction changed,



and Reaction 2/A1/B2 was subsequently explored up to 3.5 GPa (Staudigel and Schreyer, 1977; Jenkins, 1981; Jenkins and Chernosky, 1986). However, experiments which aimed to establish the maximum stability of chlorite involving any of these reactions have been few. There has only been one experimental study to explore Reaction 2/A1/B2 to higher pressure (Ulmer and Trommsdorff, 1999 quoting Fockenberg 1995), and five which examined Reaction 4/A6 (Pawley, 2003; Fumagalli and Poli, 2005; Fischer *et al.*, 2010; Till *et al.*, 2012; Fumagalli *et al.*, 2014), relevant mainly to peridotite compositions:



Other high-pressure experimental studies have identified individual data points for chlorite as part of other investigations (Bromiley and Pawley, 2002, 2003; Padron-Navarta *et al.*, 2013; Spandler *et al.*, 2014). Significantly, there have been no previous experiments of stability of ultramafic chlorite at high pressure.

Seven relevant curves have been displayed in Figure 3.17: the current study, the bulk composition from this study modelled using PerpleX (Connolly, 1990), two curves tracing Reaction 1/A3 (Staudigel and Schreyer, 1977; Jenkins, 1981), the single curve for Reaction

2/A1/B2 (Fockenberg, 1995), and four high-pressure curves tracing Reaction 4/A6 (Pawley, 2003; Fumagalli and Poli, 2005; Till *et al.*, 2012; Fumagalli *et al.*, 2014).

3.3.7.1 Previous studies of Reaction 1/A3

The gradient of the Reaction 1/A3 curve in the current study shows excellent agreement with both previous experimental curves (see Figure 3.17, brown dotted line and red dotted line) of this reaction (Staudigel and Schreyer, 1977; Jenkins, 1981) when adjusted for compositional differences. The thermal reduction and the pressure elevation can readily be attributed to the presence of Fe and Cr respectively.

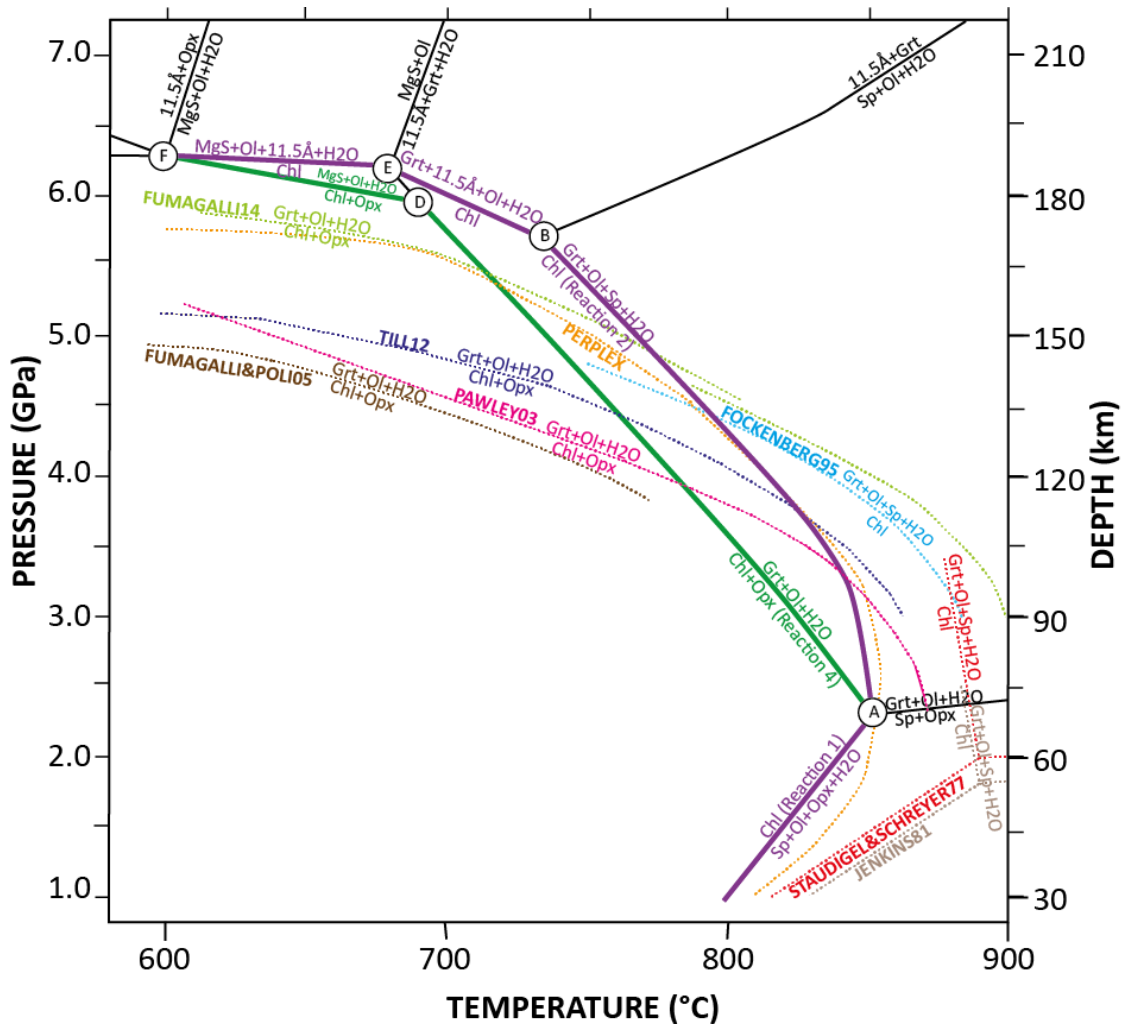


FIGURE 3.17: Key chlorite reactions – current study compared with previous studies.

Curves from this study: Reactions 1 and 2 are marked in heavy purple lines, Reaction 4 in heavy green lines; other reactions in black. Curves from previous chlorite studies are shown in coloured dotted lines and are marked accordingly. Phase abbreviations as previously denoted.

3.3.7.2 Previous studies of Reaction 2/A1/B2

Staudigel and Schreyer and Jenkins each traced the low-pressure portion of Reaction 2/A1/B2 which also showed excellent agreement with the current study when adjusted for bulk compositional differences.

Fockenbergl (Fockenbergl, 1995) examined the terminal chlorite reaction using a synthetic mix of clinocllore in the MASH system. The gradient of the curve (Figure 3.17, light-blue dotted line) was shallower than in the current study. At 3.0 GPa, it recorded a thermal maximum ~20°C higher than in this study. The curves crossed near 4.2 GPa and by 5.0 GPa, the maximum pressure stability, the curve recorded a thermal maximum some 40°C less than in the current study. The thermal displacement of the Fockenbergl curve could be explained by the presence of Cr and Fe in the current study; however, the 1.3 GPa pressure differential does not accord with the results of this study.

Perplex (Connolly, 1990) was used to compute the maximum stability of chlorite modelling the bulk composition of this study. The program utilised the Holland and Powell database (Holland and Powell, 2011) which did not account for the thermodynamic effect of chromium on chlorite stability. Notwithstanding, the slope of the resulting curve (Figure 3.17, orange dotted line) showed excellent agreement with the curve in this study. The lower thermal offset at low pressure and the elevated pressure offset at high pressure could be explained by the presence of Fe and Cr in the bulk composition.

3.3.7.3 Previous studies of Reaction 4/A6

The four curves (Pawley, 2003; Fumagalli and Poli, 2005; Till *et al.*, 2012; Fumagalli *et al.*, 2014) displayed in Figure 3.17 (pink, yellow, dark-blue and light-green dotted lines respectively) each modelled Reaction 4/A6. They shared several common features: the gradient of the reaction curve, the strong backbend which commenced after 3.0 GPa, and a generally shallow slope. However, when compared to the curve of Reaction 4/A6 from the current study (Figure 3.17, thick green solid line), there are noticeable differences, only some attributable to differing bulk compositions.

3.3.7.4 Previous 11.5Å-phase studies

Little has been published on the 11.5Å-phase; in fact, there are only four publications which have attempted its characterisation.

The first published account of a 'mystery' hydrous phase was reported in 2010 by Fischer (Fischer *et al.*, 2010) when an unknown mineral turned up in a single experiment at 5.4 GPa, 720°C.

In a detailed follow-up study, Fumagalli (Fumagalli *et al.*, 2014) reported on a new high-pressure hydrous magnesio-alumino-silicate, named 11.5Å-phase after the location of the first peak in the XRD scan. The series of multi-anvil experiments elicited three samples which contained 11.5Å-phase, from two different bulk compositions, stable at 6.0 GPa, 650°C and 6.5 GPa, 700°C.

Cai (Cai *et al.*, 2015) reported the discovery of an Al-bearing Phase A mineral, named 23Å-phase after the dimension of the c-axis parameter in the lattice configuration. This phase was found experimentally to be stable over a wide P-T region – from 8.0 GPa, 900°C to 12.0 GPa, 1000°C. TEM analysis partially characterised the lattice structure. Based on the chemistry, textures and crystal structures reported in the previous work of Fischer and Fumagalli, the 23Å-phase appeared to be the same mineral as the 11.5Å-phase.

Gemmi (Gemmi *et al.*, 2016) conducted multi-anvil experiments using the same technique as Fumagalli (Fumagalli *et al.*, 2014) to produce 11.5Å-phase. Due to small crystal size, a revised analytical method was used: a combination of EMPA, XRD and TEM using the fast electron diffraction tomography (EDT) mode. A fully quantitative description of the crystallographic properties of the 11.5Å-phase was thus determined. The mineral was categorised as a C-centred, monoclinic mineral belonging to the C2/c space group exhibiting a 2M₂ polytype (Gemmi *et al.*, 2016). TEM analysis showed the mineral comprised stacked T-O-T layers connected by a double dioctahedral layer of oxygen molecules which created disorder in the stacking arrangement. Whilst the octahedral sites were found to be fully occupied, the tetrahedral layers were disordered, a feature common in phyllosilicate minerals (Wang *et al.*, 2002).

The experimental results of this study showed that 11.5Å-phase co-existed with chlorite at several data points: at 5.7 GPa/720°C, 5.8 GPa/720°C, 6.0 GPa/680°C, 6.2 GPa/640°C and 6.2 GPa/680°C. This co-relationship confirmed the progression from chlorite to 11.5Å-phase with increasing pressure and therefore that the chlorite terminal reaction at high pressure did not produce the anhydrous assemblage of olivine, garnet, spinel and free water.

The existence of 11.5Å-phase forces a rethink not only of phase relations in this P/T region but most importantly as to the location of the hydrous/anhydrous boundary.

3.3.7.5 *Previous Mg-sursassite studies*

Mg-sursassite was first detected in high-pressure experiments and named Mg-Mg-Al pumpellyite as chemically it was viewed as the Mg analogue of Ca-pumpellyite (Schreyer *et al.*, 1986). Subsequent investigations established its stability field (Fockenberg, 1998) and crystal structure (Artioli *et al.*, 1999) which indicated this mineral was likely an Mg analogue of sursassite rather than pumpellyite. This finding was soon confirmed by TEM analysis (Gottschalk *et al.*, 2000) and the mineral was renamed Mg-sursassite.

Several experimental studies reported that Mg-sursassite had a highly variable composition. Mg:Al:Si ratios have been reported as 4.87:5.17:5.93 at 5.0 GPa, 650°C (Fockenberg, 1998); 5.28:5.02:5.81 at 7.0 GPa, 630°C (Bromiley and Pawley, 2002) and, with the addition of Cr to the system, 5.55:4.61:5.82 at 6.0 GPa, 650°C (Fumagalli *et al.*, 2014). The results from the current study calculated the (Mg+Fe):(Al+Cr):Si ratio to be 5.30:4.74:5.95 at 6.2 GPa, 640°C and 6.05:3.96:5.99 at 6.2 GPa, 680°C results in good agreement with those from previous studies.

The results of this study showed a temperature-dependent compositional change in MgS. The Mg# in MgS decreased from 0.94 at 6.2, 640°C to 0.85 at 6.2, 680°C. Since MgS and garnet coexisted at both P,T locations, these results showed a concurrent increase of Mg# in garnet, from 0.81 to 0.86. With increasing temperature, garnet becomes increasingly Mg-rich at the expense of MgS which becomes increasingly Fe-rich. Another study (Wunder and Gottschalk, 2002) showed a pressure-dependent compositional change in MgS, with Fe-rich compositions crystallising at lower pressures. This was not able to be confirmed in the current study due to insufficient data. Both aspects of compositional change warrant further investigation.

3.3.8 THE IMPACT OF FE AND CR ON CHLORITE STABILITY

The natural minerals used in this study incorporated minor iron and chromium and trace nickel which created a more complex chemical system CrFMASH. The different gradients and P/T location of other experimental chlorite stability curves can be explained by the combined effect of these elements.

The use of natural rocks in experimental petrology more accurately mimics actual petrological processes. Since 'pure' end-member minerals are not to be found in natural ultramafic systems due to solid-solution, understanding the impact of these 'impurities' on phase stability is crucial. The solid solution models Fe-Mg and Cr-Al are known to significantly impact the stability fields of co-existing mineral phases.

Several thermodynamic studies have been completed on the Fe-Mg exchange mechanism in chlorite (Goto and Tatsumi, 1990; Vidal *et al.*, 2001, 2005; Lanari *et al.*, 2014) but few experimental studies have been undertaken (Fumagalli and Poli, 2005). The current study showed an Fe-partitioning sequence at all pressures of: sp > grt > opx > ol > chl > 11.5Å, the effect of which was to shift the stability field of spinel to lower temperatures. In this experimental series, spinel is formed above Invariant Point A as a breakdown product of chlorite; therefore, if the spinel stability field is shifted to lower temperature, then the chlorite stability field must also be reduced.

The extent to which the chlorite stability field is reduced can be estimated through a comparison of experimental results. Fumagalli (Fumagalli *et al.*, 2014) recently completed a study which examined Reaction 4/A6 in the CrMASH system. The current study also examined this reaction in the chemical system CrMASH+Fe. Any differences between the two resulting curves, therefore, should be attributable to the impact of Fe. Table 3.5 provides a summary of these differences at selected pressure and temperature points.

Additional element effect	Exp Series	Selected Pressure			Selected Temperature				
		3.0 GPa	4.0 GPa	5.0 GPa	650°C	700°C	750°C	800°C	850°C
Fe	Fumagalli 14	900	855	760	5.7	5.5	5.2	4.6	4.0
	This study	825	785	735	6.1	5.7	4.7	3.6	2.3
	Effect	75°C ↓	70°C ↓	25°C ↓	0.4 GPa ↑	0.2 GPa ↑	0.5 GPa ↓	1.0 GPa ↓	1.7 GPa ↓
Cr	Pawley03	855	780	640	4.9	4.5	4.2	3.8	3.2
	Fumagalli14	900	855	760	5.7	5.5	5.2	4.6	4.0
	Effect	45°C ↑	75°C ↑	120°C ↑	0.8 GPa ↑	1.0 GPa ↑	1.0 GPa ↑	0.8 GPa ↑	0.8 GPa ↑
Combined effect of Fe+Cr		30°C ↓	5°C ↑	95°C ↑	1.2 GPa ↑	0.8 GPa ↑	0.5 GPa ↑	0.2 GPa ↓	0.9 GPa ↓

TABLE 3.5: Effect of Fe and Cr on chlorite stability in chlorite peridotite after Reaction 4/A6

The addition of Cr leads to a pressure enhancement of ~0.9 GPa. The addition of Fe reduces the thermal stability by ~70°C but this effect appears to diminish with increasing pressure. Abbreviations: "Fumagalli14" = (Fumagalli *et al.*, 2014); "Pawley03" = (Pawley, 2003); "This study" = current study, Series 1 experiments.

An interesting pattern was observed when the Fumagalli curve was compared to that of the current study. At 3.0 GPa, the addition of Fe lowered the stability field of chlorite by some 75°C. At 4.0 GPa, a 70°C difference was registered. However, at 5.0 GPa, the thermal difference between the two curves was reduced to 25°C. The curves intersected near 5.5 GPa. At higher pressure, Fe-bearing systems possessed an increased chlorite stability field to higher temperature compared with Fe-absent systems. When isothermal comparisons were made, we observed a reversal effect as temperature reduced. At 850°C, the chlorite stability field in Fe-bearing systems was reduced by 1.7 GPa. At 750°C, a 0.5 GPa difference was noted. At 650°C, a 0.4 GPa elevation to chlorite stability was detected in the current study. In summary, the chlorite stability field in Fe-bearing systems was shifted to lower temperature at low-pressure.

With increasing pressure, however, this effect diminished up to 5.5 GPa where the curves intersected. At higher pressure, the chlorite stability field was elevated to higher pressure.

The effect of Cr addition to a chlorite bulk composition can also be estimated by comparison of experimental data. Pawley (Pawley, 2003) examined Reaction 4/A6 in the MASH system whereas Fumagalli (Fumagalli *et al.*, 2014) examined the same reaction in the CrMASH system. Any differences between the two curves should be due to impact of chromium. These differences have been included in Table 3.5.

A consistent pattern emerged. With increasing pressure, Cr-bearing systems experienced an elevated chlorite stability field. At 3.0 GPa, the field was elevated by 45°C; at 5.0 GPa, by 120°C. At each pressure interval examined, Cr had the effect of increasing the stability field of chlorite to higher temperature. Under isothermic conditions, a consistent increase in the pressure regime was observed. At 850°C, chlorite stability was elevated by 0.8 GPa; by 1.0 GPa at 750°C, and 0.8 GPa at 650°C. In summary, the addition of Cr to the experimental system resulted in the enhancement of the chlorite stability field in both pressure and temperature. This effect was maximised at high-pressure, low-temperature locations.

Fumagalli recommended further research as to Cr partitioning prior to and during the chlorite terminal reaction. The current study provided such data. The partitioning sequence at $P > 2.0$ GPa was $sp > opx > 11.5\text{\AA} > chl > grt$, the same sequence (except for 11.5Å-phase) as previously reported (Fumagalli *et al.*, 2014). At 3.0 GPa, 820°C, prior to the commencement of the chlorite terminal reaction, the Cr partitioning sequence was $X_{Cr} opx=0.13$, $X_{Cr} chl = 0.07$, $X_{Cr} grt=0.05$. At 840°C, as chlorite had commenced breakdown, the Cr partitioning order was $X_{Cr} Sp=0.17$, $X_{Cr} chl=0.07$, $X_{Cr} grt = 0.05$. At 860°C, at the completion of chlorite breakdown, the values were $X_{Cr} sp=0.12$, $X_{Cr} grt=0.04$. These data demonstrated that Cr partitioning favoured opx during Reaction 4/A6 and spinel during Reaction 2/A1/B2.

When the Pawley and Fumagalli curves are compared, it is apparent they possess similar gradients with the latter curve simply displaced to higher pressure. Therefore, the effect of MASH vs CrMASH becomes apparent.

Does a similar trend exist with the partitioning of iron? The Fe-Mg partitioning sequence in this series was $11.5\text{\AA} > chl > MgS > ol > opx > grt > sp$, signifying that prior to the completion of Reaction 4/A6 and the appearance of spinel, Fe preferentially partitioned into the garnet phase. At 3.0 GPa, 820°C, prior to the completion of Reaction 4/A6, the partitioning sequence from experimental results was: $X_{Mg\#}grt= 0.86$, $X_{Mg\#}opx= 0.91$, $X_{Mg\#}ol= 0.93$, $X_{Mg\#}chl= 0.94$. At 3.0 GPa, 840°C, following the completion of Reaction 4/A6 and the first appearance of sp, the sequence was $X_{Mg\#}sp= 0.87$ $X_{Mg\#}grt= 0.90$, $X_{Mg\#}chl= 0.94$, $X_{Mg\#}ol= 0.95$. These results can be compared to

those at high pressure. At 6.0, 680°C the sequence was: $X_{Mg\#grt} = 0.80$, $X_{Mg\#opx} = 0.91$, $X_{Mg\#ol} = 0.94$, $X_{Mg\#chl} = 0.94$. At 6.0 GPa, 700°C, both Reaction 4/A6 and Reaction 2/A1/B2 had gone to completion and revealed the following values: $X_{Mg\#grt} = 0.89$, $X_{Mg\#11.5\text{\AA}} = 0.97$. Note the widening of the Mg# in garnet with pressure, 0.86 at 3.0 GPa reducing to 0.80 at 6.0 GPa. This suggests that Fe shows an increased affinity for garnet with increasing pressure in the opx stability field. These data show that Fe partitioning favoured garnet during Reaction 4/A6 and spinel, when present, in Reaction 2/A1/B2.

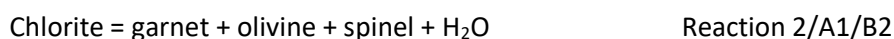
The combined effect of chlorite stability in the CrFMASH system vs CrMASH and MASH is a much-extended stability field to high pressure. The resulting curve possesses a steeply negative gradient than observed in any previous chlorite study and would warrant further experimental investigation.

3.3.9 Delineation of Reaction 4/A6 and Reaction 2/A1/B2

This is the first experimental study to show the clear delineation between the chlorite-out reaction, relevant to mantle peridotite compositions



and the chlorite terminal reaction, within the garnet stability field, relevant to chlorite schist compositions



This situation was made possible due to the small amount of antigorite present in the starting material which upon breakdown formed a small amount of opx according to the reaction:



The presence of the minor opx with abundant chlorite enabled Reaction 4/A6 to proceed to conclusion prior to the commencement of the terminal chlorite Reaction 2/A1/B2. Reaction 4/A6 was also examined in chlorite peridotite, the subject of Chapter 4, where it was found to have a lower thermal stability. Previous studies have shown both reactions were close in P/T space (Ulmer and Trommsdorff, 1999; Pawley, 2003; Fumagalli *et al.*, 2014), but this series has been able to distinguish the separate reactions as shown in Figure 3.18.

At 3.0 GPa, each reaction occurred over a temperature range of <20°C. Reaction 4/A6 commenced with the appearance of garnet near 810°C and ended with the disappearance of opx near 825°C. Reaction 2/A1/B2 commenced near 835°C and had finished near 845°C. A narrow region of chlorite stability of ~10°C provided a clear separation of these two reactions.

By 3.3 GPa, the temperature range of the combined reactions broadened to nearly 40°C. The width of each reaction remained <20°C but the field separating the reactions widened to >20°C. This thermal interval remained consistent to 5.7 GPa, the termination of Reaction 2/A1/B2.

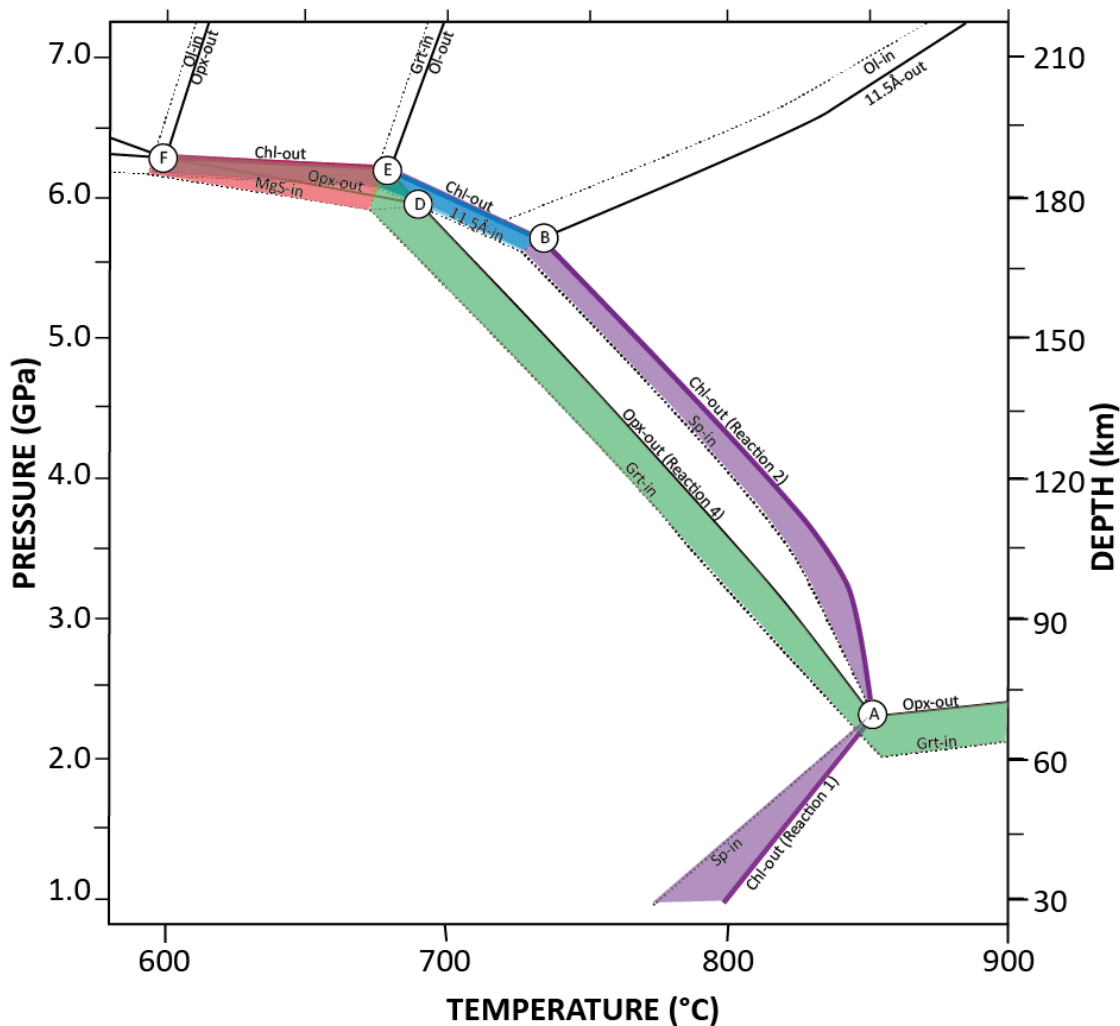


FIGURE 3.18: Delineation of Reaction 2/A1/B2 and Reaction 4/A6 in chlorite schist

The regions shaded green (grt) and red (MgS) denote the divariant field accompanying Reaction 4/A6. The region shaded purple (sp) and blue (11.5Å) indicate the divariant field accompanying Reaction 2/A1/B2. Although close in P/T space, the two reactions are thermally separated by some 20°C for most of the sub-arc. This is the first study to delineate both reactions in a single experimental study.

Both reactions underwent a sharp backbend at high pressure which indicated the termination of each reaction. Reaction 4/A6 turned sharply negative at Invariant Point D and saw MgS replace garnet as the stable Al-bearing phase at high pressure thus introduced a new reaction for the chl+opx reactants. Reaction 2/A1/B2 experienced a backbend after Invariant Point B which witnessed the introduction of 11.5Å-phase which replaced spinel as the Al-bearing mineral at high pressure. The divariant fields accompanying both new reactions overlapped and eventually converged at Invariant Point F at which point there was no separation between reactions.

This study showed that Reaction 4/A6 and Reaction 2/A1/B2 are separated in P,T space. This is significant in that the thermal stability of chlorite-rich schists and chlorite-rich veins within peridotites is elevated by >40° throughout the sub-arc.

3.3.10 THE FORMATION OF OTHER HIGH-PRESSURE HYDROUS MINERALS

Recent high-pressure experimental studies have reported the presence of never-before-seen hydrous minerals in reaction products following the breakdown of chlorite. These include phase-HAPY (Gemmi *et al.*, 2011; Fumagalli *et al.*, 2014), 10Å-phase (Pawley and Wood, 1995a; Fumagalli *et al.*, 2001; Dvir *et al.*, 2011; Pawley *et al.*, 2011), Mg-sursassite (Artioli *et al.*, 1999; Bromiley and Pawley, 2002) and 11.5Å-phase (Fumagalli *et al.*, 2014). The stoichiometric formulae of these minerals are listed in Table 3.6, followed by key reactions:

Hydrous Mineral	Stoichiometric formula	Notes
Clinocllore	$Mg_5Al_2Si_3O_{10}(OH)_8$	-
10Å phase	$Mg_3Si_4O_{10}(OH)_2 \cdot xH_2O$	-
11.5Å-phase (this study)	$Mg_{11}Al_2Si_4O_{16}(OH)_{12}$	Formula determined by experimentation
11.5Å-phase (Gemmi 2016)	$Mg_{12}Al_2Si_4O_{16}(OH)_{14}$	Formula determined by TEM analysis
Mg-sursassite	$Mg_5Al_5Si_6O_{21}(OH)_7$	-
Phase-HAPY	$Mg_{2.1}Al_{1.8}Si_{1.1}O_6(OH)_2$	Formula determined by TEM analysis

TABLE 3.6: Relevant high-pressure, hydrous minerals formed after chlorite breakdown

Abbreviations: L17=Lakey 2017, the current study; G16= Gemmi and others (Gemmi *et al.*, 2016).

Chlorite = garnet + olivine ± phase-HAPY + H₂O

Chlorite + orthopyroxene = olivine + Mg-sursassite + H₂O

Chlorite = olivine + 10Å-phase + spinel + H₂O

Chlorite = spinel + garnet + 11.5Å-phase + H₂O

Chlorite = Mg-sursassite + garnet + 11.5Å-phase + H₂O

Chlorite = Mg-sursassite + olivine + 11.5Å-phase + H₂O

Each has sparked considerable research interest because these phases crystallised in P/T conditions beyond chlorite stability which indicated the potential extension of the hydrous-anhydrous boundary in subducted rocks. To date, apart from two possible samples of the 10Å-phase (Smith, 1995; Khisina and Wirth, 2008) – none of these phases have been found in natural rocks. The current study was the first to explore this P/T space using only natural minerals and as a result confirmed the likelihood of both 11.5Å-phase and Mg-sursassite in natural rocks. The relevant chemography is shown in Figure 3.13.

In the bulk composition used in the current study, it appears unlikely that these high-pressure hydrous minerals could form, although a full thermodynamic analysis would be needed to confirm this: 10-Å phase seems too Si-rich and phase-HAPY is too Al-rich. However, in different bulk compositions, there appears to be no reason why they could not be found in nature.

3.3.11 IMPLICATIONS FOR BOUND WATER IN ULTRAMAFIC SCHISTS

This experimental study using natural minerals demonstrated that bound water was retained in chlorite, MgS and 11.5Å-phase to at least 6.2 GPa/780°C, beyond sub-arc depths, making possible its transportation to the deep mantle. This forces us to adjust our preconceptions of the extent of the planet's deep-water cycle.

3.3.11.1 Release of bound water in chlorite and 11.5Å-phase

The breakdown of chlorite at high-pressure released water over a small temperature range. In contrast, the breakdown of 11.5Å-phase led to a smeared release of water over a wider thermal interval.

Figure 3.19 displays the quantity of water retained in hydrous minerals with increasing temperature at two key pressure intervals: 3.0 GPa indicating sub-arc depths, and at 6.0 GPa indicating depths immediately beyond the sub-arc. The bulk composition contained 12.6 wt% water. The quantity of bound water remaining at each temperature interval is displayed in blue at the top of diagrams a and b.

At 3.0 GPa, chlorite decomposed entirely over a 30°C temperature interval. This occurred as two distinct reactions. Reaction 4/A6 led to the release of ~0.6 wt% fluid, its conclusion marked by the disappearance of the opx phase at just after 820°C. The second period of water release occurred with the terminal chlorite Reaction 2/A1/B2 which commenced after ~830°C and concluded by 860°C. The second reaction released 12.0 wt% water over a 30°C interval. After 860°C, no hydrous minerals were present.

At 6.0 GPa, water release occurred over a temperature range of >120°C. This time, three separate reactions were involved. At 680°C, chlorite had begun to break down as part of the Reaction D6/F3. With the disappearance of opx immediately after 680°C, and close in P-T space, the terminal chlorite Reaction B6/C2 commenced. The release of 9.4 wt% water occurred over a <20°C interval. Chlorite was absent by 700°C at this pressure. However, the new hydrous 11.5Å-phase was formed as a breakdown product of chlorite which sequestered nearly 3 wt% of the water contained in the parent mineral. Its thermal stability at this pressure persisted for over 100°C, its water released as a smear over this temperature interval: 0.2 wt% by 720°C,

another 0.1 wt% by 740°C, and a further 1.0 wt% by 760°C. The remaining 1.9 wt% water was released between 760°C and 800°C. By 800°C, no hydrous minerals remained.

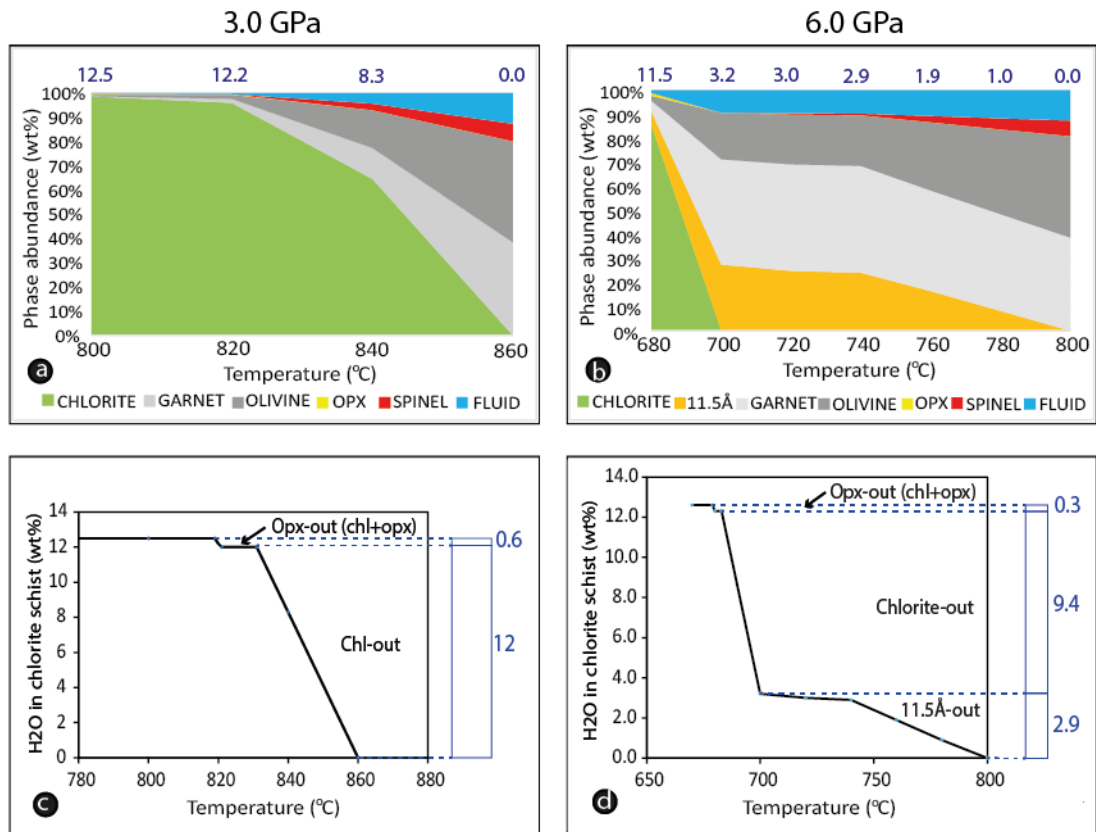


FIGURE 3.19: Release of bound water from hydrous phases in Series 1 at 3.0 GPa and 6.0 GPa.

a) Phase abundance at 3.0 GPa between 800°C and 860°C. **b)** Phase abundance at 6.0 GPa between 660°C and 800°C. Quantity of water (wt%) retained in hydrous minerals at each temperature is shown in blue at top of diagrams a and b. **c)** Quantity of water released at temperature intervals at 3.0 GPa. Note that at this pressure, chlorite dehydration occurs in a ~30°C interval. **d)** Quantity of water released in temperature intervals at 6.0 GPa. Chlorite breakdown releases water over ~30°C, but due to the formation of 11.5Å-phase, nearly one quarter of the water is retained in this new phase. In turn, the breakdown of 11.5Å-phase leads to a smeared release over a 100°C interval.

The presence of new hydrous phases stable to higher pressure and temperature than previously thought, along with the slow release of water upon their breakdown, signals a potential change to phase relations in this P-T region which would warrant further research.

3.3.11.2 Temperature at slab-surface and slab interior and impact on hydrous phase stability

Knowing the temperature of the descending slab is crucial in determining the fate of hydrous minerals during the subduction process. This study showed that water bound in chlorite, MgS and 11.5Å-phase can journey beyond sub-arc depths before being released into the deep mantle.

Figure 3.20 illustrates the P-T path taken by cooler slabs during subduction based on two recent geophysical models. The first, shaded purple, is from Arcay et al (Arcay *et al.*, 2007). The second, shaded in both orange and yellow tones (representing slab surface and internal slab

temperatures respectively) is from Syracuse et al (Syracuse *et al.*, 2010). The faint grey dashed line marks the P-T path of the Tonga slab – the slab with the fastest subduction rate and thus lowest slab surface temperature.

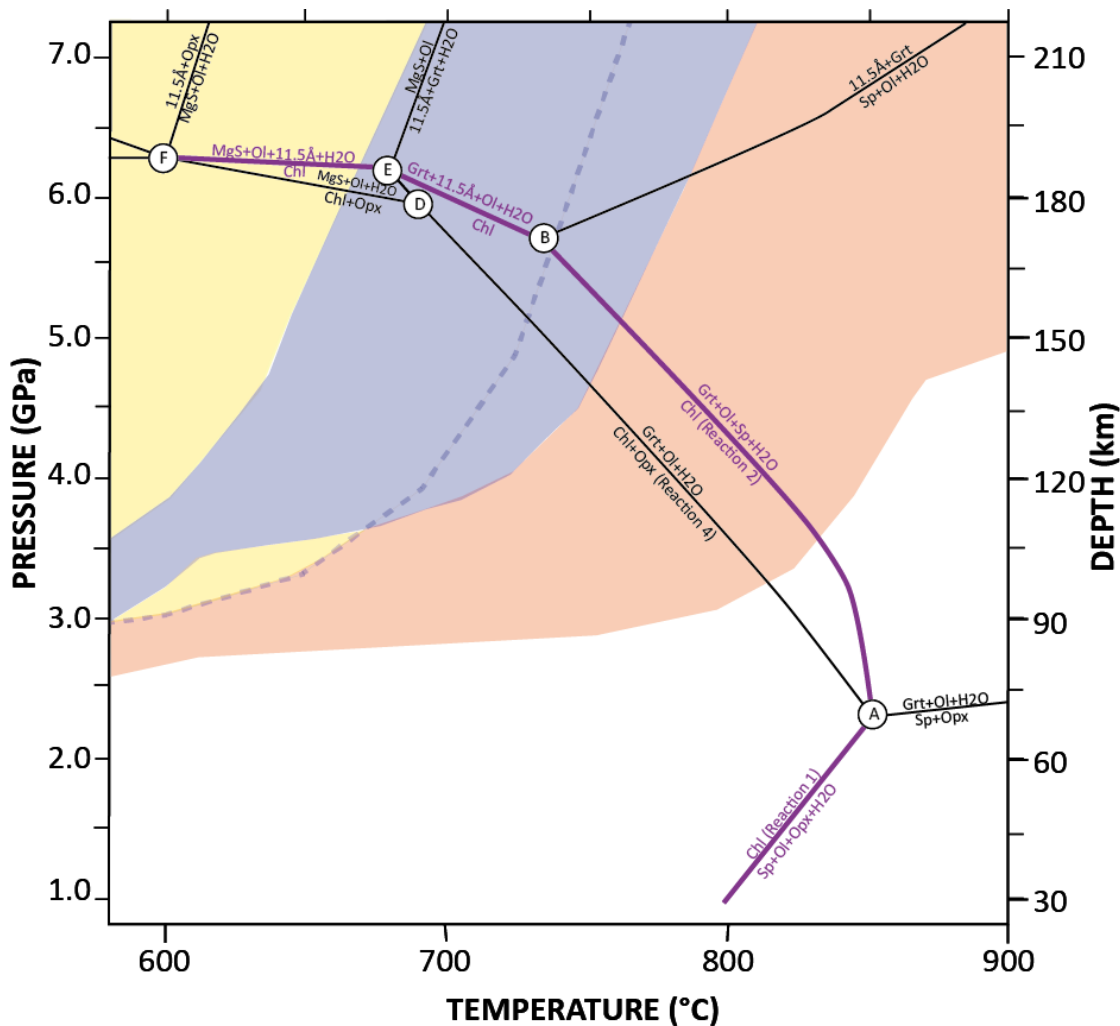


FIGURE 3.20: Slab surface temperature compared to chlorite, 11.5Å-phase and MgS stability fields.

Two recent geophysical models shown. Purple shading from Arcay et al (Arcay et al., 2007). This model estimates the strength reduction in slab rocks due to water; the high-temperature edge of the purple region thus indicates dry, stronger rocks. Orange and yellow shading is from Syracuse et al (Syracuse et al., 2010). The orange region indicates the slab surface temperature of all subducting slabs according to the D80 model. The yellow shading indicates the range of the internal temperatures within the slabs also calculated by the D80 model. The grey, dashed line is the P-T path of the Tonga slab, the coolest of all subducting slabs. Superimposed (purple lines) is the hydrous boundary from the current study.

In the Arcay model, a spectrum of dry to fully hydrated rocks at the slab surface is considered which encompasses a temperature range of ~150°C. The experimental results from the current study are representative of these temperatures indicating that the maximum stability field of hydrous minerals would survive the subduction process through the sub-arc to the deep mantle prior to the liberation of bound water.

Syracuse developed a more comprehensive 2-D model to simulate actual slab surface temperatures. According to the D80 component of this model, the P-T path of the Tonga slab,

the coolest of all subducting slabs modelled, is located at slightly higher temperatures than the tip of the anhydrous nose identified by the current study. All other slabs are situated at higher temperature profiles within the orange-shaded area. This means that any chlorite, MgS or 11.5Å-phase attached to the surface of the descending Tonga slab would dehydrate at sub-arc depths near 5.5 GPa, 740°C. However, there are several assumptions upon which the D80 model was based which leads one to question its veracity. The model used multiple parameters which were allocated numerical values to enable calculations to be completed. A change in any single value could result in large variation to the modelled results. For instance, the mantle potential temperature was given a value of 1421.5°C; a lower value would yield lower wedge temperatures. Equally, the transition depth was set at 80 kms. Whilst this value has accorded wide agreement with other researchers, a higher value would yield reduced slab surface temperatures. Whilst this concern should not be overstated, it is apparent that with only very minor adjustment to the existing model, the P-T location of the subducting Tonga slab could be shifted to slightly higher pressure and slightly lower temperature. This would mean that chlorite and 11.5Å-phase on the slab surface would successfully pass by the anhydrous nose and be transported to the deep mantle.

The Syracuse D80 model also calculated the interior temperature profile of subducting slabs. A wide range of values were published for slabs at 240 kms depth: from 265°C (Tonga) to 1043°C (Central Cascadia). Notwithstanding the concerns with the model raised above, any chlorite and 11.5Å-phase present within cooler slabs would remain stable to depths well beyond the sub-arc.

The results of this study were representative of the slab surface temperatures modelled by both Arcay and Syracuse. Therefore, chlorite, MgS and 11.5Å-phase present in the interior of cool subducting slabs would successfully be transported beyond sub-arc depths prior to their breakdown. However, it is unlikely that these same minerals present on the surface of even the coolest of subducting slabs could survive subduction to the deep mantle prior to their dehydration.

3.3.11.3 Estimation of free water contribution from ultramafic low-Al chlorite

The results of this study demonstrated that chlorite and 11.5Å-phase remain stable to higher pressures and temperatures than previously thought, and the bound water component of these phases can be transported to depths beyond the sub-arc. It follows, then, that this water component has not been considered in previous calculations of the deep-water cycle. In order to improve our understanding of this cycle, the water contribution from these hydrous minerals needs to be quantified.

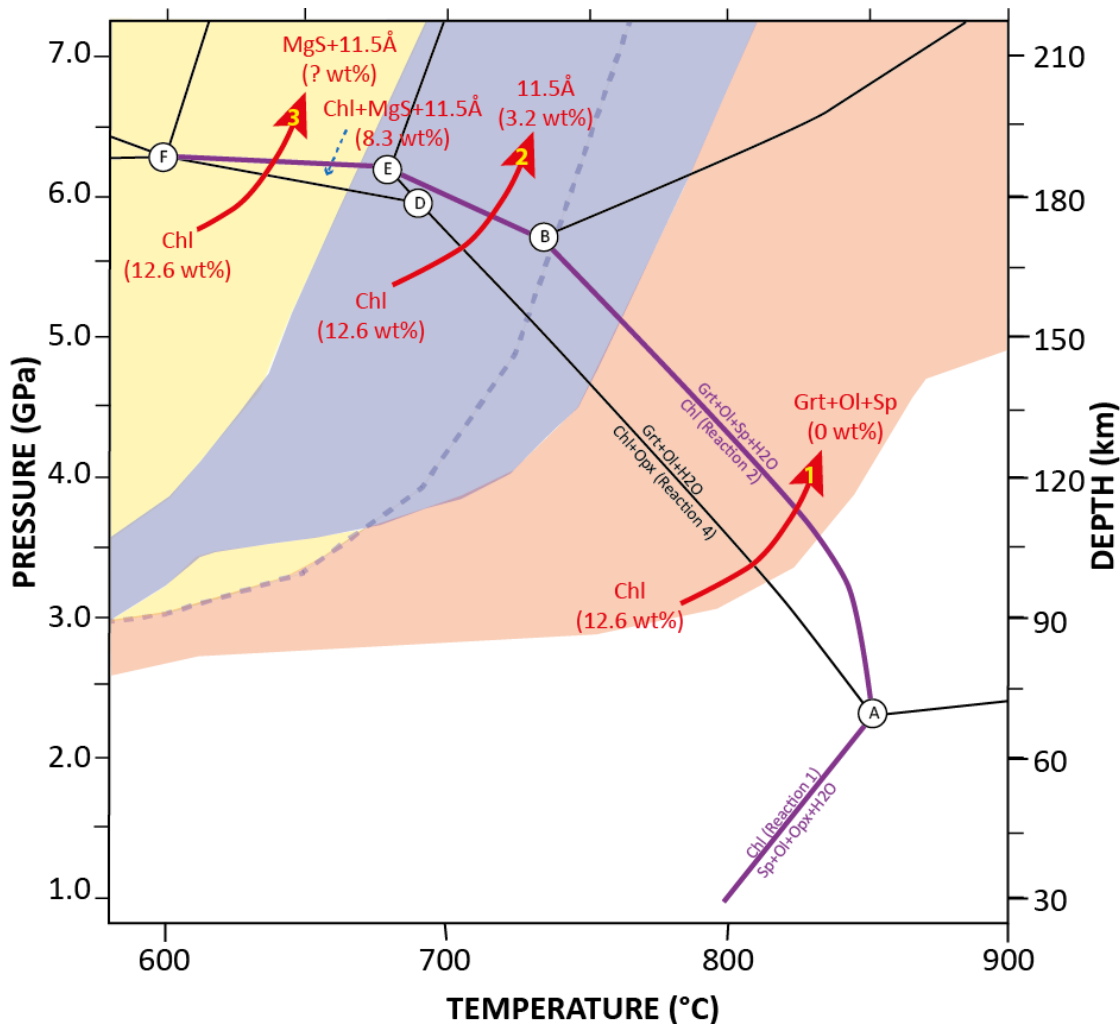


FIGURE 3.21: Water sequestration in hydrous phases along three select geotherms.

Assumptions on water budget and phase relations after Schmidt and Poli (Schmidt and Poli, 1998, 2014). The three selected P-T paths, marked by red arrows, represent the varied stability fields which arise following chlorite decomposition.

It is known that relatively pure, ultramafic chlorite schists can form zones more than 10m wide in the subduction channel (Spandler *et al.*, 2008)(Marschall and Schumacher, 2012). To estimate the water budget in an ultramafic chlorite schist, it was assumed that chlorite comprised 99 wt% of the rock. The quantity of water released at a specific P-T location, however, was dependent upon the phase relations at that point, especially the reaction products which formed at the point of chlorite decomposition. To illustrate this point, three different pathways have been selected. These are shown in Figure 3.21.

Pathway 1 shows the typical pathway experienced by a subducting slab in the sub-arc up to 5.7 GPa (~171 kms depth). Chlorite schist attached to the surface of the slab, or contained within the slab, would fully dehydrate to the anhydrous assemblage of grt+ol+sp+H₂O, releasing all of its 12.6 wt% water over a ~30°C interval. All of the released water would remain at sub-arc depths.

Pathway 2 is the P-T path taken by a rapidly-descending, and thus cooler, slab such as Tonga. Since its temperature profile is cooler at greater depth, it crosses the chlorite-out phase boundary at temperatures less than 735°C (the point of the anhydrous nose). As a result, chlorite does not dehydrate: rather it forms the 11.5Å-phase which binds nearly one quarter of the water contained in chlorite. Therefore, 9.4 wt% water is released when chlorite breaks down, and 3.2 wt% is retained, bound in the 11.5Å-phase. Potentially, 11.5Å-phase could be transported well into the deep mantle as it is known to be stable to at least 12 GPa, 1000°C (Cai *et al.*, 2015).

Pathway 3 marks a geotherm not relevant to the slab surface temperature (SST) of a descending slab – the rate of slab descent required to maintain such low temperatures makes this unfeasible. Therefore, Pathway 3 relates to hydrous minerals contained within the subducting slab rather than on its surface. A descending slab following Pathway 3 intersects three separate hydrous fields. It first crosses the boundary of Reaction D6/F3, to a field where chl co-exists with MgS and 11.5Å-phase. Mass balance calculations indicates that in this small field nearly 8.3 wt% H₂O is sequestered in the three hydrous phases chl, MgS and 11.5 A-phase. Following a small pressure increase, Pathway 3 crosses the boundary of Reaction E6/F2 which sees the complete dehydration of chlorite and the formation of additional quantities of MgS and 11.5 A-phase. Further experimental investigation is needed to ascertain the quantity of water sequestered in these phases beyond Reaction E6/F2.

The breakdown of the 11.5Å-phase along Pathways 2, 3 and 4 with the increased slab temperature with continued subduction would result in a smeared release of water.

The location of the anhydrous nose remains a limiting factor in the successful transfer of water via the slab to the deep mantle. Whilst this study has shown its shift to significantly higher temperatures, the sharpness of the boundary at 5.7 GPa/735°C acts as a hydrous barrier: chlorite and/or 11.5Å-phase must maintain a temperature less than 735°C during slab descent to access the higher P-T conditions in the 11.5Å-phase stability field.

3.3.11.4 Extension of the hydrous-anhydrous boundary.

The experimental results obtained in this study necessitated a significant up-temperature shift in the location of the hydrous-anhydrous boundary.

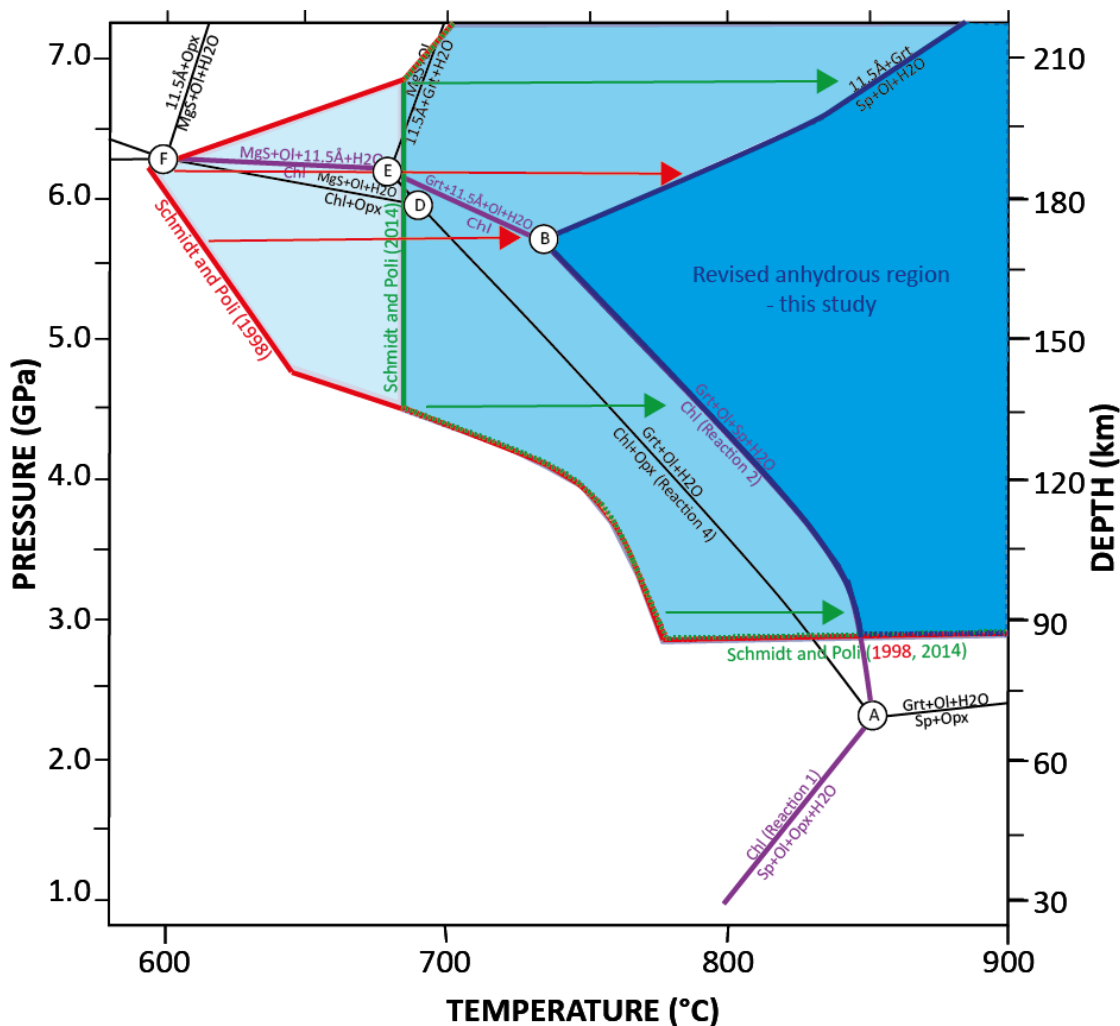


FIGURE 3.22: Extension of the hydrous-anhydrous boundary in ultramafic chlorite schists.

The red line shows the location of the existing hydrous-anhydrous boundary after Schmidt and Poli (Schmidt and Poli, 1998) with the revised boundary including 10Å phase (Schmidt and Poli, 2014). The dark blue lines indicate the new position of the hydrous-anhydrous boundary following this study. Red and green arrows indicate the extent and direction of the boundary shift.

Previous work located the maximum temperature stability of hydrous minerals at 6.2 GPa near 580°C. This was at an invariant point where the hydrous phases antigorite and Phase A (Luth, 2014)(Schmidt and Poli, 1998) and the anhydrous phases garnet and olivine met, forming an ‘anhydrous nose’. Due to the extended chlorite stability field identified in this study, a potential alignment not previously recognised was identified between chlorite and the above-mentioned phases near Invariant Point F (see Figure 3.22).

Figure 3.22 shows the previously reported location of the hydrous-anhydrous boundary in ultramafic rocks. The commonly reported boundary (Schmidt and Poli, 1998) is marked in red. A revised version (Schmidt and Poli, 2014), which included the hydrous 10Å-phase, is shown here in green. The location of the revised boundary, based on the experimental results of the current study, is marked in dark blue.

The shift in the hydrous-anhydrous boundary did not reflect a consistent thermal increase at all pressure intervals; the difference generally increased with increasing pressure. At 3.0 GPa, the boundary moved upward by 70°C and at 4.5 GPa by 110°C. Invariant Point B at 5.7 GPa marked the location of the revised 'anhydrous nose', which possessed a sharp corner due to the very low-angle slope of the 11.5Å-phase-in reaction. Using the 1998 boundary, this represented a thermal increase of ~115°C, or a more modest 55°C using the 2014 boundary. At pressures above the 'anhydrous nose', the shift in the location of the hydrous-anhydrous boundary was significant: at 6.2 GPa it experienced a thermal increase of 100°C (2014 boundary) or 200°C (1998 boundary); and an inferred increase at 6.7 GPa of 175°C.

With the significant extension of the hydrous-anhydrous boundary to higher temperatures, there exists a high probability that considerable quantities of bound water would be subducted to the deep mantle.

3.4 CONCLUSIONS AND IMPLICATIONS

The results of this study have contributed important new findings concerning the stability of hydrous minerals in the subduction zone and the transport of bound water into the deep mantle.

This was a study of firsts. It was the first experimental study to examine chlorite stability in chlorite schist at high pressure. It was the first to use only naturally-occurring minerals in the more complex chemical system CrFNMASH. It was the first study to show a clear delineation between Reaction 4/A6, relevant to mantle peridotite compositions, and the terminal chlorite Reaction 2/A1/B2, relevant to chlorite schist compositions, within the garnet stability field.

These experimental results showed strong agreement with the ideal phase assemblages determined by Schreinemaker's analysis. Reaction 2/A1/B2 was constrained to higher pressures and temperatures than found in previous chlorite studies. The curve of the resulting chlorite-out boundary exhibited a steep Clapeyron slope to 5.7 GPa/735°C, quite different in appearance to any previous chlorite-out curves, explained by the presence of Fe and Cr in the system. The elevated chlorite stability field created new phase relations: the 11.5Å-phase formed following the breakdown of chlorite at pressures above 5.7 GPa; Mg-sursassite formed following the Reaction 4/A6 above 5.9 GPa. The appearance of these uncommon, high-pressure, hydrous minerals in this experimental series established that they could be found in naturally-occurring rocks.

The elevated stability field of chlorite, MgS and 11.5Å-phase necessitated a shift in the hydrous-anhydrous boundary to higher temperature - by as much as 175°C at 6.2 GPa. Modelling of slab-surface temperatures and the chlorite, MgS and 11.5Å-phase stability fields showed that these

phases would remain stable beyond sub-arc depths within cooler descending slabs but they would be unlikely to survive on the slab surface of even the fastest subducting slabs. Chlorite dehydration releases free water over a narrow temperature interval whereas the breakdown of the 11.5Å-phase liberates water in a smear over a wider temperature range.

Ultramafic chlorite schists are a common feature of many subduction zones settings. With the chlorite stability field being far more extensive than previously imagined, and chlorite schist containing nearly 13 wt% water, there are important implications for future studies of mantle geology. Since even minute quantities of water added to the mantle are known to have a profound impact upon both the rheology and phase relations of mantle rocks, there is a pressing need to more fully understand the process of water liberation in the deep mantle.

CHAPTER 4 : THE THERMAL STABILITY OF CHLORITE PERIDOTITE AT HIGH PRESSURE – IMPLICATIONS FOR WATER TRANSPORT IN THE MANTLE WEDGE AND THE DEEP MANTLE

4.1 INTRODUCTION

Peridotite is a common lithology within convergent margins where it is exposed within the slab as well as along the entire hanging wall of the mantle wedge in the subduction channel. As the slab journeys downward, there is a progressive release of water from metamorphic reactions, firstly from sediments and then from within the slab itself. This leads to the hydration of peridotite for tens of kilometres along the mantle wedge profile producing at depth, the hydrous lithology chlorite peridotite. The composition of the peridotite determines the type of chlorite peridotite formed. Fertile peridotite forms chlorite lherzolite which can comprise up to 16% chlorite. Depleted peridotite, however, produces chlorite harzburgite which can contain up to 8% chlorite (Schmidt and Poli, 1998). Current thinking indicates that chlorite peridotite has a maximum stability somewhere between 120 and 150 kms after which chlorite breaks down, releasing all its water to the sub-arc, and peridotite returns to its anhydrous composition at greater depth.

However, apart from a few studies beyond 4.0 GPa, the stability of chlorite has not been well constrained. What if chlorite peridotite is stable to higher pressure? This would mean that water bound in this rock type could feasibly transport water beyond the sub-arc to the deep mantle prior to its breakdown. This has huge implications for the water budget, mantle rheology, not to mention our understanding of general geological processes within convergent margins. So, under what P,T conditions does chlorite peridotite actually breakdown? This chapter will shed light upon this important question.

Most studies to date have been in the MASH system and have used only synthetic starting materials. The purpose of this study was to constrain the chlorite stability field at high pressure in a chlorite peridotite. This required the investigation of the key reactions involving chlorite, clinopyroxene and orthopyroxene, relevant to both fertile lherzolite and depleted harzburgite, namely:

Reaction 3: chlorite (chl) + clinopyroxene (cpx) → garnet (grt) + olivine (ol) + H₂O

Reaction 4: chlorite (chl) + orthopyroxene (opx) → garnet (grt) + olivine (ol) + H₂O

This study is the first to examine the relationship between these two reactions in a single study. The experimental program was conducted at a range of pressures (1.0 GPa-6.2 GPa) and temperatures (620°C-880°C) using four natural minerals which comprised a bulk composition modelling a chlorite lherzolite in the CrCFMASH system. A typical chlorite lherzolite would see chlorite entirely react-out following Reaction 3. To facilitate a study of both reactions, a peridotite with abundant chlorite was required so the bulk composition used here does not reflect a true peridotite composition.

Below 4.9 GPa, these phases acted according to the model Reactions 3 and 4. Above 4.9 GPa, 710°C, however, Mg-sursassite (MgS) - a hydrous phase - began to replace garnet as the stable Al-bearing mineral. After 6.3 GPa, 635°C MgS replaced chlorite and remained a stable hydrous mineral in this system to higher pressure and temperature. This result shows that in convergent boundaries experiencing rapid slab subduction, MgS would conceivably act as a water transport vehicle beyond the sub-arc to the deep mantle.

4.1.1 PREVIOUS EXPERIMENTS ON THE STABILITY OF CHLORITE PERIDOTITE

Early studies of chlorite (Yoder, 1952; Segnit, 1963; Fawcett and Yoder, 1966) were completed in the MASH system using synthetic minerals in piston cylinder experiments up to 1.0 GPa. Segnit's study was the first to synthesize clinocllore from antigorite and identify its dehydration curve above 1.0 GPa. Fawcett and Yoder provided the first systematic study of chlorite breakdown reactions to 1.0 GPa. These experiments established important constraints for future researchers.

Over the last half century, eleven experimental studies (Staudigel and Schreyer, 1977; Jenkins, 1981; Jenkins and Chernosky, 1986; Bromiley and Pawley, 2002, 2003; Pawley, 2003; Fumagalli and Poli, 2005; Dvir *et al.*, 2011; Till *et al.*, 2012; Fumagalli *et al.*, 2014; Spandler *et al.*, 2014) have investigated the upper limits of chlorite stability at pressures >1.0 GPa involving one or more of the two key chlorite-out reactions examined in the current study. Key attributes of these studies are compared in Table 4.1.

Staudigel and Schreyer (Staudigel and Schreyer, 1977) completed the first comprehensive study of clinocllore up to 3.5 GPa. Their experimentation established the first P/T brackets between 1.0 GPa (825°C, 840°C) and 3.5 GPa (870°C, 880°C). The resulting chlorite-out curve assumed an almost vertical slope between 2.0 GPa and 3.5 GPa, similar to dehydration curves for many hydrous minerals. They published a chlorite dehydration curve up to 4.0 GPa but the addition was based solely on extrapolated data. Jenkins (Jenkins, 1981) repeated the

Researcher/s	System	P/T range	Relevant reactions studied	Starting materials	Mg#	Capsule	Thermo	Duration (hours)	Apparatus	Analysis
Jenkins 1981	CMASH	0.8 – 1.4 GPa and 700 – 900°C	Chl+cpx=opx+ol+V±sp	Synthetic oxides	1.0	Pt	<1000°C cromel/alumel >1000°C W/3%Re/W/25%Re	6-144	Boyd-type piston cylinder	Optical microscope; XRD (too fine-grained for EMP)
Bromiley & Pawley 2002	MASH	5.5-9.0GPa and 630-800°C	Chl+opx=grt+ol+V	Synthetic ol, opx, grt, Mg-sur	1.0	Pt	S-type Pt/Pt10Rh	47-63.5	Walker-type multi-anvil	XRD; SEM
Bromiley & Pawley 2003	MSH MASH	1.5-5.0GPa and 520-680°C	Chl+opx=grt+ol+V	Synthetic ol, opx & chl 2 natural samples of ant	1.0 0.99 0.86	Pt & Au	Pt/Pt10Rh	48-65	Boyd-type piston cylinder >4GPa Walker-type multi-anvil	XRD; SEM; EMP; TEM
Pawley 2003	MASH	2.2-5.4GPa and 650-880°C	Chl+opx=ol+grt+V	Synthetic chl, ol, opx, grt	1.0	Pt	Pt/Pt10Rh	8-93	Boyd-type piston cylinder >3.8GPa Walker-type multi-anvil	Synchrotron; SEM
Fumagalli & Poli 2005	NCFMASH	2.0-6.5GPa and 680-800°C	Chl+cpx=ol+grt+opx Chl+opx=ol+grt+V	Synth Px, Lz & Hz from gels, seeded with natural chl+grt & synth ol+cpx	0.83 0.91 0.89	Au	K-type S-type	111- 1400	Boyd-type piston cylinder >3.0GPa Walker-type multi-anvil	XRD; EMP; SEM (BSE)
Till et al 2012	CMASH	3.2-6.0GPa and 740-1200°C	Chl+opx+cpx=ol+grt+V	Synth oxides (X _{gm})	0.94	Au	W97Re3/W75Re25	6-338	Piston cylinder Multi-anvil	EMP
Fumagalli et al 2014	CrMASH	1.5-6.5GPa and 650-900°C	Chl+opx=ol+grt+V	Synthetic gels + natural chl seeds	1.0 0.87	Au	K-type and S-type	67-289	Boyd-type piston cylinder >3.4GPa Walker-type multi-anvil	XRD synchrotron; EMP
Spandler et al 2014	(CA)MASH	3.5-4.0GPa and 700-900°C	Chl+cpx=ol+grt+V	Serpentine, grt, SC ol doped with rb	0.92	Ag (<800°C) Au (>800°C)	B-type (Pt94Rh6/Pt70Rh30)	264-672	Boyd-type piston cylinder	EMP; SEM; optical microscope; Raman; LA-ICP-MS

TABLE 4.1. Compilation of previous experiments on Reactions 3 and 4

Note, the following research has not been included in this table: experiments conducted < 1.0 GPa; experiments unrelated to Reactions 3 and 4; non-experimental studies.

experiments of early researchers and found their pressure calibrations had been too high. His study, conducted in the CMASH system, concluded that chlorite stability was indifferent to the presence of calcium, a point taken up by later researchers.

Ulmer and Trommsdorff (Ulmer and Trommsdorff, 1999) completed an extensive review of the experimental literature on chlorite stability confirming that little was known of its chemical behaviour at or beyond sub-arc depths.

Pawley (Pawley, 2003) conducted the first experimental study on chlorite above 3.5 GPa completing twelve piston cylinder and ten multi-anvil (>3.8 GPa) experiments. Numerous new data points were contributed in this study. Her findings showed that after 2.0 GPa, the chlorite dehydration curve assumed a negative slope, which continued to flatten with pressure. Pawley suggested from XRD analyses that the run products had equilibrated even though the reported run times were rather short.

Fumagalli and Poli (Fumagalli and Poli, 2005) conducted the first chlorite study incorporating natural rocks up to 6.5 GPa in the NCFMASH system. Three new P/T brackets were obtained at 3.0, 4.0 and 5.5 GPa but too few experiments were completed to accurately constrain chlorite dehydration. Their experiments confirmed Pawley's findings that the chlorite dehydration curve bent and flattened rapidly with pressure after approximately 3.5 GPa. Their study also concluded that the presence of Fe, Ca and Na greatly altered the chlorite stability field. Using the same Iherzolite composition, Dvir (Dvir *et al.*, 2011) examined the phase transition of chlorite into 10Å-phase between 4.0-6.0 GPa, concluding that the upper stability limit of chlorite at sub-arc depths had been constrained.

Till (Till *et al.*, 2012) completed multiple piston cylinder experiments between 3.2 GPa-6.0 GPa and from 740°C-1200°C in an attempt to better constrain the wet peridotite solidus. Results provided numerous new data points regarding chlorite stability across this P/T space but few as brackets on the chlorite-out curve. Controversially, she claimed to have identified melt in her samples at 820°C between 3.0 and 4.0 GPa concluding that the wet peridotite solidus was found some 300°C lower than previously identified.

Fumagalli (Fumagalli *et al.*, 2014) recently published data on chlorite in the Cr-MASH system after experiments which used natural and synthetic rocks. Results demonstrated an increased chlorite stability field to higher temperatures and pressures but with bulk compositions comprising ≤2wt% chromium, the saturation level of Cr in chlorite.

Spandler (Spandler *et al.*, 2014) also reported on chlorite formation after the breakdown of antigorite at 3.5-4.0 GPa in a complex natural system. Neither study found evidence of melt textures at the P/T conditions previously reported by Till.

4.2 STARTING MATERIAL

To enable Reactions 3 and 4 to progress in a single experimental run, the system had three requirements: excess water so that components remained fully saturated for the duration of the experiment, a Ca-bearing mineral (tremolite) to enable the formation of cpx, and for the starting material to contain more chl than cpx so that chlorite was not fully consumed along Reaction 3.

		a								b		
	Oxide	TRE (n=8)		ATG (n=11)		GRT (n=9)		CHL (n=9)		Oxide	wt%	
		Mean	sd	Mean	sd	Mean	sd	Mean	sd			
Wt%	H ₂ O (calc)	2.13	0.02	12.63	0.07	0.00	0.00	12.47	0.10	Na ₂ O	0.10	
	Na ₂ O	0.80	0.29	0.00	0.00	0.08	0.06	0.00	0.00	MgO	33.12	
	MgO	21.27	0.35	36.67	0.29	26.75	0.20	33.82	0.30	SiO ₂	37.70	
	SiO ₂	56.55	0.61	41.85	0.33	43.38	0.29	33.66	0.35	Al ₂ O ₃	10.84	
	Al ₂ O ₃	0.72	0.28	3.04	0.20	24.42	0.22	12.78	0.31	NiO	0.17	
	NiO	0.00	0.00	0.02	0.07	0.00	0.00	0.21	0.16	FeO	3.87	
	FeO	4.39	0.31	3.83	0.10	4.08	0.40	3.72	0.39	MnO	0.02	
	MnO	0.15	0.09	0.02	0.05	0.00	0.00	0.00	0.00	Cr ₂ O ₃	1.38	
	Cr ₂ O ₃	0.09	0.12	0.31	0.06	0.00	0.00	1.65	0.38	CaO	1.40	
	CaO	11.69	0.51	0.00	0.00	0.43	0.02	0.00	0.00	TiO ₂	0.00	
	TiO ₂	0.00	0.00	0.00	0.00	0.00	0.00	0.00	0.00	H ₂ O (calc)	11.41	
	Total	97.79	0.87	98.37	0.48	99.15	0.69	98.31	0.72	Total	100.00	
	Cations (a.p.f.u.)	Na	0.05	0.02	0.00	0.00	0.00	0.00	0.00	0.00	c	
		Mg	4.47	0.06	2.60	0.01	2.75	0.03	4.85	0.02	Mineral	wt%
Si		7.97	0.03	1.99	0.01	3.00	0.01	3.24	0.02	Chlorite	79.87	
Al		0.12	0.05	0.17	0.01	1.99	0.01	1.45	0.03	Tremolite	11.67	
Ni		0.00	0.00	0.00	0.00	0.00	0.00	0.02	0.01	Antigorite	7.96	
Fe		0.52	0.04	0.15	0.00	0.24	0.02	0.30	0.03	Pyrope (seeds)	0.50	
Mn		0.02	0.01	0.00	0.00	0.00	0.00	0.00	0.00	Total	100.00	
Cr		0.01	0.01	0.01	0.00	0.00	0.00	0.13	0.03			
Ca		1.76	0.08	0.00	0.00	0.03	0.00	0.00	0.00			
Ti		0.00	0.00	0.00	0.00	0.00	0.00	0.00	0.00			
Total		14.91	0.02	4.92	0.00	8.01	0.00	9.98	0.01			
Mg#	0.90	0.01	0.94	0.00	0.92	0.01	0.94	0.01				
Cr#	0.06	0.07	0.07	0.01	0.00	0.00	0.08	0.02				

TABLE 4.2: FE-SEM analysis of the starting mix

a) The H₂O quantities are calculated stoichiometrically. The totals listed include the H₂O component; b) Bulk composition showing normalised major and minor oxides; c) Proportion of natural minerals used in starting mix.

To ensure high levels of water, the starting mix comprised three natural hydrous minerals. Mg-chlorite (clinocllore, Mg# 0.95) was sampled from the Cerro del Almiraz ultramafic massif in south-east Spain. Previous research constrained its maximum stability to 1.6-1.9 GPa and 680-710°C (Padron-Navarta, *et al.*, 2010a). Mg-antigorite (Mg# 0.92), sourced from the same location, was added to the experimental mix to ensure excess water and also to ensure the presence of opx for Reaction 4. Finally, Ca-amphibole (tremolite, Mg# 0.84) was sampled from

the Malenco ophiolite in the Italian Alps. Pyrope garnet seeds (Mg# 0.93), extracted from the white schists from the Dora Maira in northern Italy, were added to facilitate garnet nucleation.

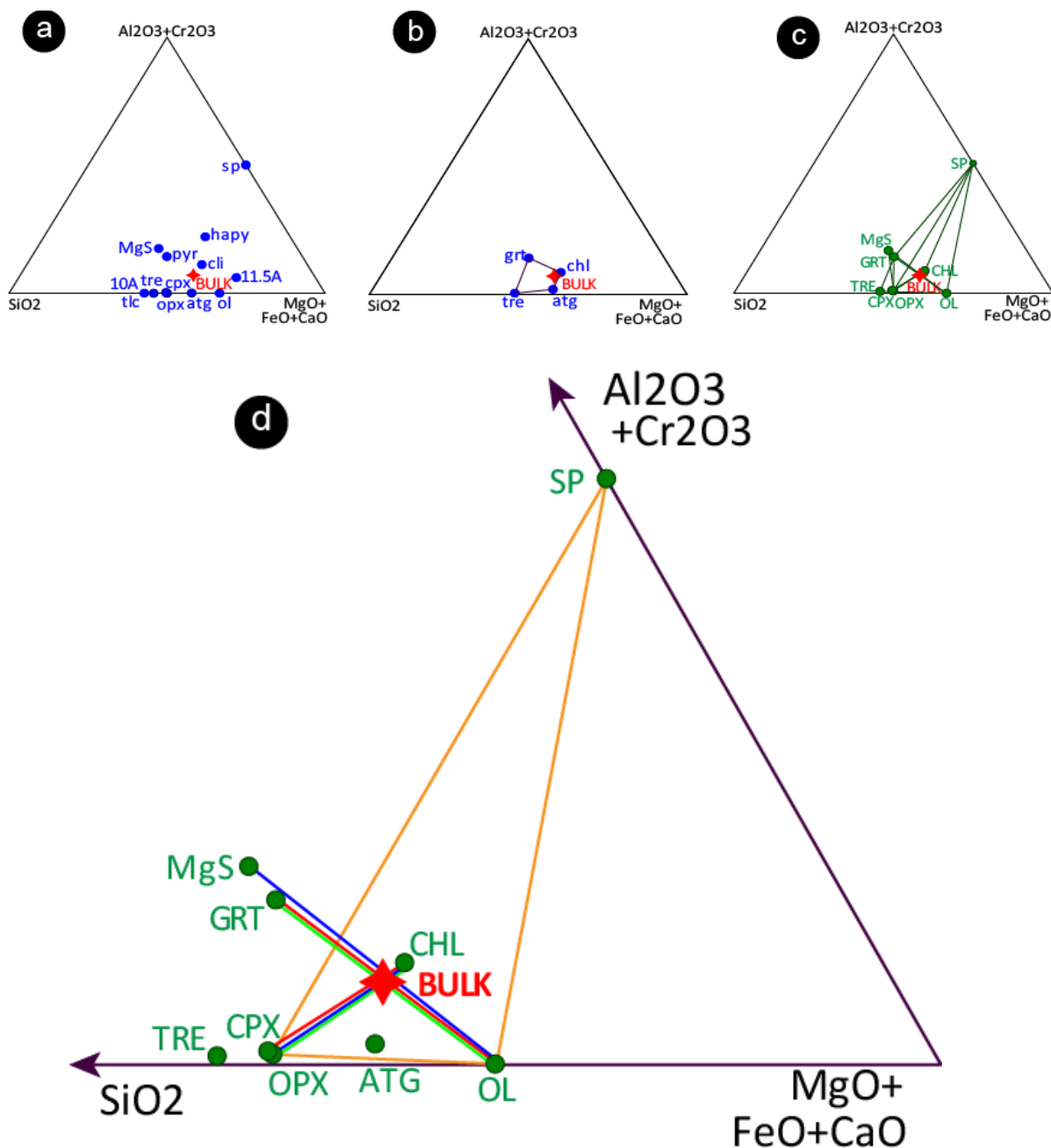


FIGURE 4.1: Chemography of the starting mix in Series 2

Ternary plot of the bulk composition in the system CrCFMASH. Compositions are in wt%. a) Ternary plot showing phases relevant to this bulk composition; b) Ternary plot showing the composition of the four minerals used in the starting mix; c) Chemograph showing reaction net connecting phases produced in this bulk composition; d) Section of a ternary plot highlighting the four key chlorite reactions identified in this bulk composition. At low pressure: the chlorite terminal Reaction 1 $chl=ol+opx+sp+H_2O$ (orange triangle), Reaction 3 $chl+cpx=grt+ol+H_2O$ (red tie-lines), and Reaction 4 $chl+opx=grt+ol+H_2O$ (green tie-lines) occur. At high pressure: Reaction D'6/F3 $chl+opx=MgS+ol+H_2O$ (blue tie-lines) occurs. Note the location of bulk composition lies slightly on the SiO_2 side of the garnet-olivine tie-line which has implications for the phase assemblages following chlorite disappearance. Plot completed using C-Space software (Torres-Roldan et al., 2000).

The bulk composition has been characterised in Table 4.2. Average analyses of each mineral in the starting material are shown in Table 4.2a. Normalised FESEM analysis of the bulk

composition is shown in Table 4.2b. Stoichiometric proportions of each mineral in the starting mix are shown in Table 4.2c. Full analytical results are provided in the Chapter 3 Appendix. Details of the methodology used in this experimental series have been outlined in Chapter 2.

Figure 4.1 shows the chemography of the seven mineral phases that formed in this experimental series from this bulk composition as well as the potential phases that could have formed. The location of the starting mix fell slightly to the opx side of the garnet-olivine tie-line which indicated a slight excess of silica in the system. This situation likely favoured opx formation over spinel and potentially the location of the chlorite-out reaction.

Following sample preparation, the starting mix was placed in a drying oven overnight. X-Ray Diffraction (XRD) analysis was then undertaken to confirm the minerals within the starting mix. The resulting diffractogram is shown in Figure 4.2.

The diffraction peaks of the XRD standards showed good alignment with the sample on the 2-theta scale indicating correct phase identification. However, there was poor alignment between the XRD standards and the sample with counts per second almost certainly due to preferred grain orientation, typical of platy minerals (Jenkins, 1981).

4.3 RESULTS

Series 2 experiments established forty-five data points encompassing a range of pressures (1.0 GPa-6.2 GPa) and temperatures (620°C-880°C). Table 4.3 presents a complete list of experimental conditions and run products.

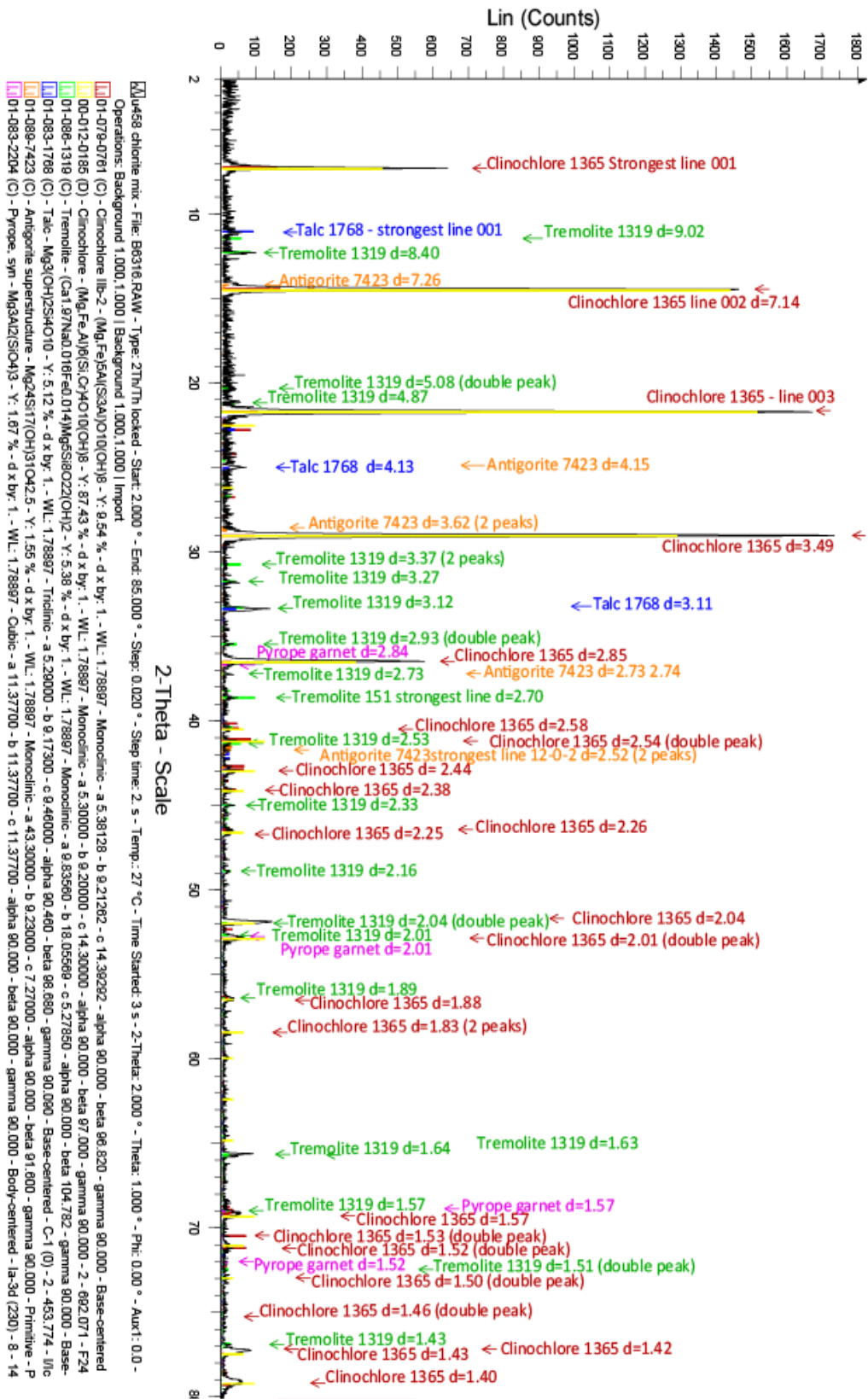


FIGURE 4.2: X-Ray Diffraction analyses of Series 2 starting mix.

The strong alignment between diffractogram peaks and mineral standards on the 2-theta scale confirm the identity of the target minerals. The weaker alignment on the Y-scale is certainly due to the preferred orientation of platy minerals which are notoriously difficult to scan. Nevertheless, hydrous minerals dominate.

Expt Number	Time (hrs)	P (GPa)	T (°C)	PHASES										
				OL	GRT	CHL	OPX	CPX	SP	TRE	MgS	ATG	Fluid	TOTAL
D1802	168	1.0	730	3.6	0.0	79.9	4.2	0.0	0.0	11.3	0.0	0.0	1.0	100.0
D1617	168	1.0	760	10.8	0.0	57.7	12.5	0.0	4.2	11.0	0.0	0.0	3.7	100.0
D1625	168	1.0	780	30.1	0.0	0.0	37.4	0.0	12.2	9.2	0.0	0.0	11.1	100.0
D1632	168	1.0	800	29.3	0.0	0.0	37.9	0.0	12.4	9.3	0.0	0.0	11.1	100.0
D1806	168	1.5	730	4.4	0.0	79.9	2.8	0.0	0.1	11.7	0.0	0.0	1.0	100.0
D1645	168	1.5	780	4.2	0.0	78.3	5.1	0.0	0.7	10.6	0.0	0.0	1.1	100.0
D1652	168	1.5	800	8.3	1.2	67.8	8.3	0.0	2.3	9.7	0.0	0.0	2.5	100.0
D1647	168	1.5	820	30.4	7.3	0.0	35.5	0.0	11.2	4.5	0.0	0.0	11.2	100.0
C4792	168	2.0	760	2.6	0.0	79.9	8.7	4.4	0.1	3.0	0.0	0.0	1.2	100.0
D1178	168	2.0	800	7.6	1.2	61.0	18.4	4.1	3.1	1.1	0.0	0.0	3.5	100.0
C4489	168	2.0	820	33.4	20.9	0.0	27.0	0.0	7.3	0.0	0.0	0.0	11.4	100.0
D1575	168	2.0	860	33.9	21.8	0.0	26.8	0.0	6.1	0.0	0.0	0.0	11.4	100.0
D1587	168	2.0	880	34.7	23.5	0.0	24.7	0.0	5.6	0.0	0.0	0.0	11.4	100.0
C4530	168	2.5	750	2.7	0.0	79.9	9.7	6.3	0.0	0.0	0.0	0.0	1.3	100.0
D1700	168	2.5	765	3.7	0.0	79.5	9.5	5.9	0.0	0.0	0.0	0.0	1.4	100.0
D1642	168	2.5	780	10.4	8.8	63.6	11.1	2.5	0.4	0.0	0.0	0.0	3.2	100.0
D1646	168	2.5	800	14.2	11.5	54.4	12.1	2.1	1.2	0.0	0.0	0.0	4.4	100.0
C4497	168	2.5	820	36.4	35.8	0.0	13.1	0.0	3.3	0.0	0.0	0.0	11.4	100.0
D1784	168	3.0	700	1.9	0.0	80.0	10.4	6.4	0.0	0.0	0.0	0.0	1.3	100.0
C4482	168	3.0	730	4.9	1.3	78.1	9.1	5.2	0.0	0.0	0.0	0.0	1.4	100.0
D1567	168	3.0	750	5.7	4.1	74.1	9.5	4.6	0.0	0.0	0.0	0.0	2.0	100.0
D1551	168	3.0	780	15.1	14.9	57.4	8.4	0.0	0.2	0.0	0.0	0.0	4.0	100.0
D1581	168	3.0	800	37.8	48.6	0.0	1.7	0.0	0.4	0.0	0.0	0.0	11.4	100.0
D1571	168	3.0	820	38.5	48.2	0.0	1.7	0.0	0.2	0.0	0.0	0.0	11.4	100.0
D1629	168	3.5	750	7.7	6.1	72.3	8.2	3.5	0.0	0.0	0.0	0.0	2.1	100.0
D1651	168	3.5	770	38.8	48.9	0.0	0.7	0.0	0.2	0.0	0.0	0.0	11.4	100.0
C4765	168	4.0	620	2.1	0.2	79.9	8.2	7.0	0.0	0.0	0.0	1.4	1.1	100.0
D1606	168	4.0	660	3.5	1.4	79.1	8.9	5.8	0.0	0.0	0.0	0.0	1.3	100.0
D1600	168	4.0	700	4.2	3.1	77.2	8.5	5.5	0.0	0.0	0.0	0.0	1.5	100.0
D1872	72	4.0	740	6.7	5.3	70.8	10.6	4.3	0.0	0.0	0.0	0.0	2.4	100.0
C4500	168	4.0	750	38.7	47.4	0.0	2.0	0.0	0.6	0.0	0.0	0.0	11.4	100.0
UHPPC-270	120	4.5	720	2.7	2.8	76.9	11.1	4.9	0.0	0.0	0.0	0.0	1.6	100.0
C4633	168	4.5	740	38.3	49.4	0.0	0.9	0.0	0.0	0.0	0.0	0.0	11.4	100.0
UHPPC-262	168	5.0	620	3.2	0.0	79.9	7.9	6.6	0.0	0.0	0.0	1.2	1.1	100.0
UHPPC-264	168	5.0	660	4.2	2.9	77.1	9.0	5.2	0.0	0.0	0.0	0.0	1.6	100.0
UHPPC-360	168	5.0	680	19.1	14.1	44.6	8.7	0.0	0.0	0.0	8.3	0.0	5.2	100.0
UHPPC-268	142	5.0	700	28.9	29.0	23.0	5.2	0.0	0.0	0.0	5.8	0.0	8.1	100.0
UHPPC-274	120	5.0	720	37.6	50.3	0.0	0.6	0.0	0.0	0.0	0.0	0.0	11.4	100.0
UHPPC-300	120	5.5	620	3.8	1.8	78.9	7.8	6.3	0.0	0.0	0.0	0.0	1.3	100.0
UHPPC-285	120	5.5	650	8.0	4.2	68.3	7.5	5.4	0.0	0.0	4.2	0.0	2.4	100.0
UHPPC-288	120	5.5	680	37.6	42.2	0.0	0.4	0.0	0.0	0.0	9.0	0.0	10.8	100.0
UHPPC-283	120	6.0	620	4.4	1.8	75.8	7.6	6.9	0.0	0.0	1.9	0.0	1.5	100.0
UHPPC-299	120	6.0	640	11.4	3.4	62.2	7.2	4.2	0.0	0.0	8.8	0.0	2.7	100.0
UHPPC-286	120	6.0	660	39.2	36.3	0.0	0.6	0.0	0.0	0.0	13.4	0.0	10.5	100.0
UHPPC-362	116	6.2	620	10.5	2.8	67.0	4.4	7.1	0.0	0.0	5.8	0.0	2.5	100.0

TABLE 4.3. Table of results for experimental Series 2.

Table displays, for each run, the experimental conditions, run products and their modal proportions determined by mass balance. Numbers in blue indicate either phase observed but analysis not obtained or phase not observed but was present according to mass balance calculations.

4.3.1 PHASE RELATIONS

Phase relations of the nine solid and one fluid phase identified in this series are displayed in the phase diagram in Figure 4.3.

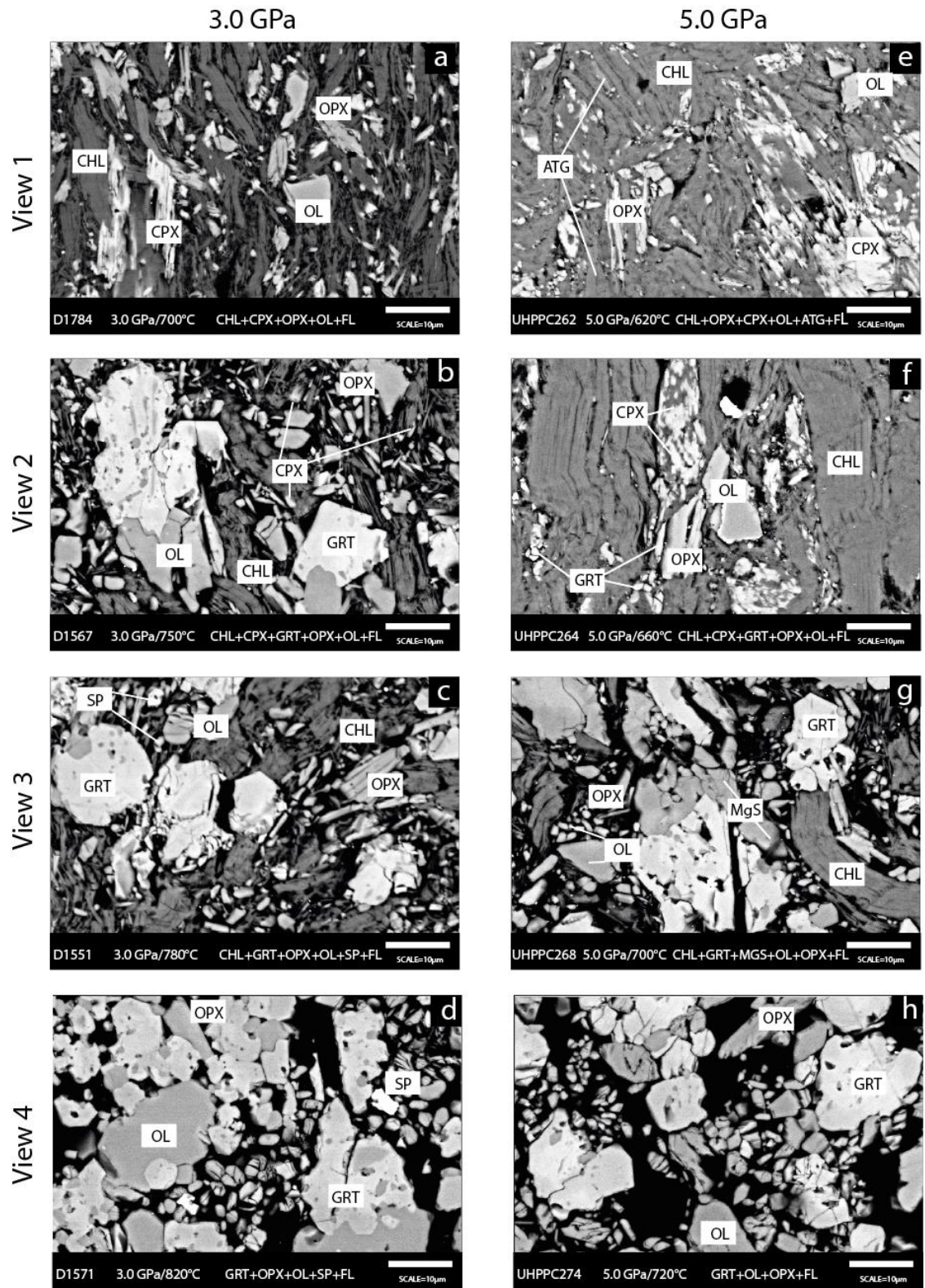


FIGURE 4.4. Changing phase relations of Reaction 3 (chl+cpX) and Reaction 4 (chl+opX).

Figures 4.4a and e) View 1: Chl+cpX field. No garnet is present indicating both phases co-exist in equilibrium. **Figures 4.4b and f) View 2:** Chl+cpX+grt. The presence of garnet indicates that Reaction 3 has commenced. **Figures 4.4c and g) View 3:** Chl+grt field. The absence of cpX at this temperature indicates that Reaction 3 has concluded having used all available cpX. Reaction 4 has also commenced. This is indicated by the presence of spinel at low pressure and by MgS at high pressure. **Figures 4.4d and h) View 4:** Grt field. This anhydrous assemblage indicates that Reaction 4 has concluded having used all available chlorite.

4.3.2 PROGRESS OF REACTIONS 3 AND 4

Figure 4.4 highlights the progression of Reactions 3 and 4 by use of microphotographs. Each picture has been selected to illustrate the changing textures and phase relations which occurred with increased temperature at isobaric conditions. At each pressure interval, the width of both reactions was ~100°C.

View 1 (Figures 4.4a and e) indicates that Reaction 3 has not commenced. Chlorite is the dominant phase with minor cpx, opx and olivine, the latter phases being replacement phases for atg and tre in the starting mix. No garnet is present in either view indicating that chlorite and cpx co-exist in equilibrium at these P/T conditions.

View 2 (Figures 4.4b and f) shows that Reaction 3 is in progress as evidenced by the presence of garnet, a product phase of this reaction, and numerous reaction rims which exist between chl and cpx grains.

View 3 (Figures 4.4c and g) captures the narrow region between both reactions: Reaction 3 has progressed to completion as no cpx is present in either view, but Reaction 4 has not commenced since no reaction rims can be seen where chlorite and opx are in contact.

View 4 (Figures 4.4d and h) shows that Reaction 4 is complete since no chlorite remains in either view.

4.3.3 TEXTURAL ANALYSIS

Figures 4.5 and 4.6 illustrate the changing phase textures, at low pressure and high pressure respectively, observed throughout this experimental series. The textures of each phase found in this experimental series are described in detail.

4.3.3.1 *Chlorite*

Within the chlorite stability field, chlorite was the dominant mineral phase. This mineral occurred in elongate laths <30 µm wide and <50 µm long within a crystalline matrix (see Figures 4.5b and 4.6c) in co-existence with each of the phases at various P-T conditions. When the maximum thermal stability of chlorite was approached, large chlorite laths began to dissociate into a splintery collection of acicular grains <5 µm long and <1 µm wide (see Figures 4.5b and 4.6d).

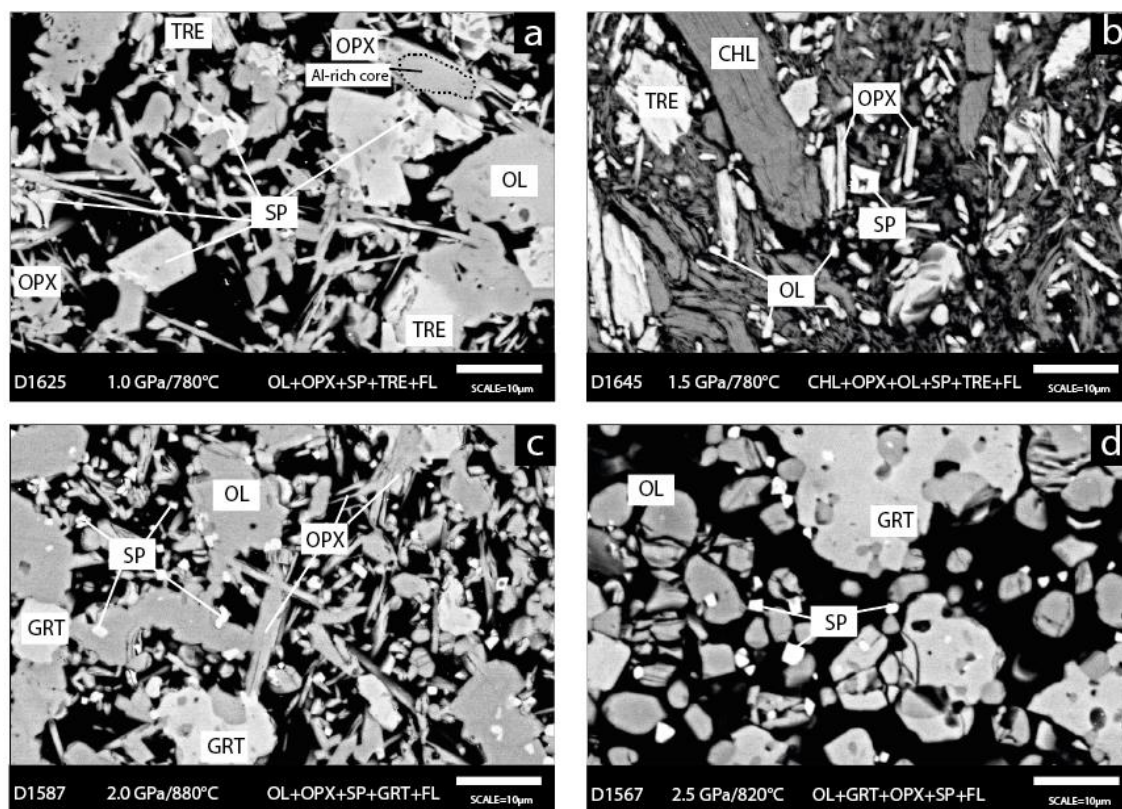


FIGURE 4.5: Representative low-pressure phase textures from Series 2

Typical low-pressure phase relations observed in this series. *Chl* typically assumed a lath-like appearance but developed a splintery texture when breakdown commenced. *Opx* commonly formed acicular textures following *chl* breakdown and when co-existing with it. *Sp* and *ol* formed large, euhedral crystals but also anhedral blebs in a crystalline matrix. When present, *grt* assumed a poikiloblastic appearance. *Tre* grains occurred in various sizes and shapes often with subhedral edges as it commenced breakdown.

4.3.3.2 Olivine

Olivine was identified in all experimental capsules in this series. Its appearance varied depending on co-existing phases and temperature. At lower pressures, olivine was typically found as tiny anhedral grains $<1\ \mu\text{m}$ as part of the crystalline matrix (see Figure 4.5b). co-existing with *opx*, *spinel* and *chlorite*.

With increasing temperature, olivine formed larger, subhedral crystals (5-15 μm). They were frequently spatially associated with *garnet* of similar size and proximal to *chlorite* laths undergoing chemical reaction (see Figures 4.4b and 4.4g). Following the disappearance of *chlorite*, olivine often appeared as small, anhedral inclusions ($<3\ \mu\text{m}$) in *garnet* crystals (see Figure 4.5d). In larger olivine crystals, euhedral grain boundaries with co-existing *garnet* evidenced well-equilibrated textures (see Figures 4.4d and 4.4h). Occasionally, growth rims were observed in olivine (see Figure 4.4f), most apparent following the disappearance of *chlorite*.

Although olivine was present in excess in this experimental series, it was frequently difficult to analyse due to small grain size as described above.

4.3.3.3 *Garnet*

Garnet first appeared at 1.5 GPa when it began to replace spinel as the stable Al-phase, a process which was complete by 4.0 GPa. Commencing near ~5.5 GPa, 660°C, garnet itself began to be replaced by Mg-sursassite as the stable Al-phase.

In this study, garnet assumed two distinct textures, closely associated with temperature. At first appearance, garnet comprised numerous small (<1 µm) anhedral grains spatially associated with both olivine of similar textures and size (see Figure 4.6d) and with chlorite (see Figure 4.4f). These garnet blebs formed only a minor part of the crystalline matrix. Their size made them very difficult to analyse.

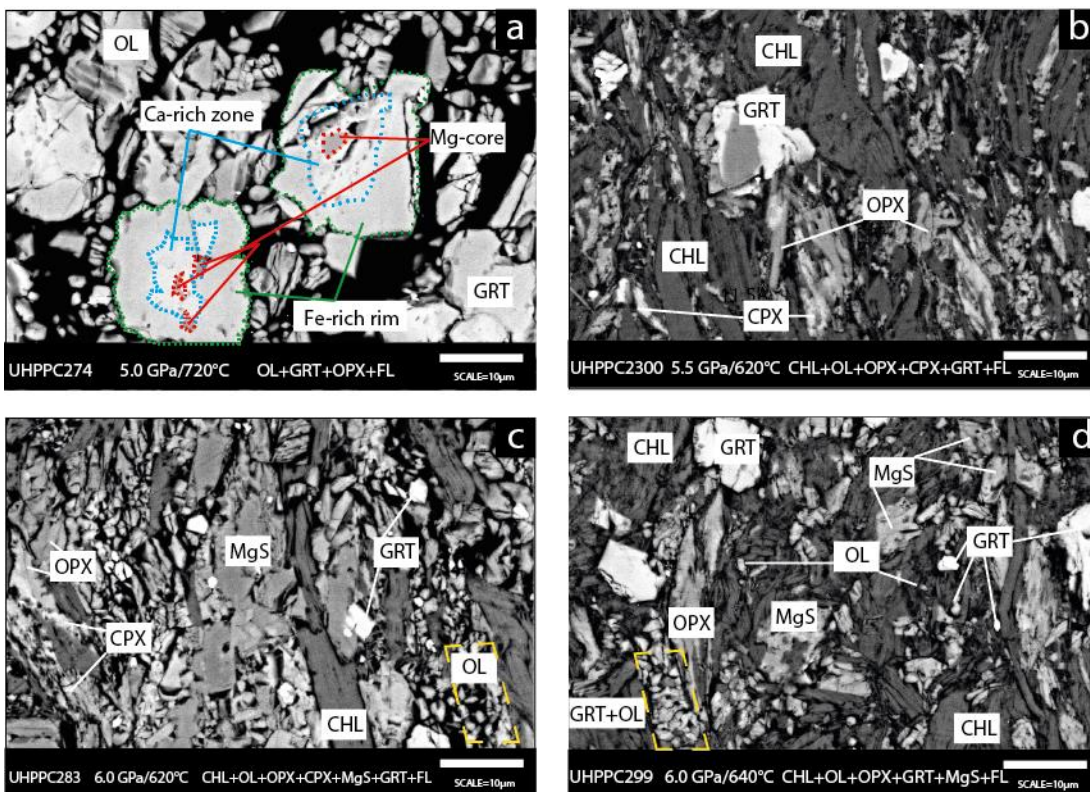


FIGURE 4.6: Representative high-pressure phase textures from Series 2

Typical high-pressure phase relations observed in this series. *Chl* retained its lath-like appearance within its high-pressure stability field and its splintery texture when breakdown commenced. *Grt* formed large, subhedral to euhedral crystals, often poikiloblastic, when in equilibrium with *ol*. *Ol* was always smaller than *grt* and frequently found as tiny blebs in the matrix. *Opx* and *cpx* typically formed pseudomorphically in former *tr* grains leading to an intercalated texture. Following *chl* disappearance, *opx* was observed with a blocky and spear-like appearance. *MgS* formed crystals of a similar size to *ol* but with a very poikiloblastic appearance.

At higher temperature, garnet formed subhedral to euhedral crystals ranging in size from 5 µm (see Figure 4.6c) to 40 µm (see Figure 4.5d). Following the disappearance of chlorite, garnet

often formed large subhedral crystals (>10 μm) with distinct poikiloblastic textures (see Figure 4.5d), or less commonly, heterogeneous growth rims with characteristic Mg-rich core, a Ca-rich inner zone surrounded by a Fe-rich outer margin (see Figure 4.6a).

4.3.3.4 *Spinel*

At low pressure, spinel formed subhedral to euhedral crystals up to 10 μm in diameter which indicated equilibrium textures (Figure 4.5a) with co-existing phases. At pressures above 2.0 GPa when co-existing with garnet, spinel was smaller in size, typically <2 μm in diameter, but still exhibited subhedral to euhedral grain boundaries (see Figure 4.6d). Spinel was also observed with poikiloblastic textures containing olivine crystals (see Figure 4.5a) and occasionally itself enclosed within olivine crystals (see Figure 4.5c). With increasing pressure, small (<2 μm) anhedral grains of spinel formed part of the crystalline matrix (see Figure 4.5c).

4.3.3.5 *Orthopyroxene*

Orthopyroxene exhibited three distinct textures throughout this series.

At low pressures, opx typically formed randomly-oriented fine, acicular needles <2-30 μm in length (see Figure 4.5c) co-existing variously with chlorite, spinel, amphibole and olivine, often as part of the crystalline matrix.

Opx and cpx also formed an intercalated, fine-grained mass within relict amphibole crystals (see Figures 4.5a and 4.6b) creating spear-shaped grains 5-30 μm in length. These pseudomorphs exhibited a braided appearance (see Figure 4.4f) and retained their amphibole grain shape to high pressures (see Figure 4.6d).

Within the garnet stability field, opx commonly formed larger prismatic crystals (see Figures 4.4b and 4.5c) ranging in length from 2 μm to 15 μm within a matrix of chlorite. At pressures below the garnet stability field, and concurrent with the disappearance of chlorite, prismatic crystals of opx grew around Al-rich cores (see Figure 4.6a).

The minute size and form of many opx crystals hampered accurate analysis.

4.3.3.6 *Clinopyroxene*

Clinopyroxene formed subhedral prismatic grains up to 2 μm x 1 μm (see Figure 4.6c) which usually aggregated into clumps (see Figure 4.4e). Larger independent crystals were uncommon. Cpx formed from tremolite breakdown and with opx typically grew pseudomorphically in relict amphibole crystals (see Figure 4.6b) which created a woven appearance (see Figure 4.4f).

Crystal size, shape and habit seemed little affected by changing pressure or temperature. The size and location of cpx grains made accurate analysis extremely difficult.

4.3.3.7 *Amphibole*

Typically, amphibole was observed as medium (~5x10 µm) to large (5-10 µm x 20-40 µm) bladed to spear-shaped subhedral to euhedral crystals which exhibited characteristic amphibole cleavage (see Figure 4.5b). Smaller subhedral crystals formed part of a fine crystalline matrix as this phase commenced decomposition (see Figure 4.5a). Amphibole stability was limited to a single data point at 2.0 GPa and had entirely reacted-out by 2.5 GPa.

4.3.3.8 *Mg-sursassite*

This phase formed as a high-pressure, low-temperature phase replacing garnet, although Mg-sursassite and garnet co-existed in a large divariant field (see Figure 4.3). MgS formed blocky, subhedral grains 10 µm long and 5 µm wide (see Figure 4.6c) with the occasional poikiloblastic appearance (see Figure 4.6d). MgS co-existed variously with chlorite, garnet, olivine, opx and cpx. Its first appearance, like olivine and garnet, was spatially associated with chlorite.

4.3.3.9 *Antigorite*

This phase remained in the run products of only two experiments: C4765 and UHPPC262. Its existence helped to ascertain the maximum thermal stability of antigorite in this series. This phase exhibited elongate laths with a similar grain size and texture to chlorite and was only distinguished during FE-SEM analyses by its contrasting chemistry.

4.3.4 COMPOSITIONAL ANALYSIS

FE-SEM analysis ascertained the chemical composition of all nine solid phases identified in this experimental series. Table 4.4 provides representative analyses of each phase. A complete set of FE-SEM phase analyses is provided in the Chapter 3 Appendix.

Three of the phases which appeared as run products in this experimental series were components added to the starting mix. FE-SEM analyses revealed no significant compositional variability which indicated that they were not reaction products but had retained their original starting composition. These phases were chlorite, antigorite and tremolite.

Run	C4792	C4633	D1567	UHPPC286	D1632	D1571	D1652	D1600	D1178	C4482	D1647	UHPPC283	C4530	
Phase	OL	OL	GRT	GRT	SP	SP	EN	EN	CPX	CPX	TRE	MGS	CHL	
n	6	8	9	9	15	11	2	4	4	4	5	8	10	
P(GPa)	2	4.5	3	6	1	3	1.5	4	2	3	1.5	6	2.5	
T(°C)	760	740	750	660	800	820	800	700	800	730	820	620	750	
	Mean	SD	Mean	SD	Mean	SD	Mean	SD	Mean	SD	Mean	SD	Mean	SD
H2O	0.00	0.00	0.00	0.00	0.00	0.00	0.00	0.00	0.00	0.00	2.17	0.03	12.25	0.14
Na2O	0.00	0.00	0.04	0.05	0.00	0.00	0.00	0.00	0.19	0.04	0.50	0.14	0.00	0.06
MgO	49.74	0.73	19.73	0.80	23.78	0.64	35.31	0.09	17.45	0.20	21.85	0.59	32.77	0.47
SiO2	40.84	0.69	43.02	0.57	0.00	0.00	58.16	0.41	52.87	0.47	57.76	0.94	33.40	0.39
Al2O3	0.03	0.06	22.14	0.39	60.11	1.05	1.44	1.14	3.44	0.39	0.72	0.28	12.52	0.25
NiO	0.26	0.19	0.00	0.00	0.00	0.00	0.00	0.00	0.00	0.00	0.00	0.00	0.16	0.13
FeO	8.48	0.26	6.54	0.50	7.00	0.63	6.45	0.46	1.72	0.09	4.50	0.39	3.63	0.11
MnO	0.00	0.00	0.08	0.09	0.00	0.00	0.07	0.10	0.00	0.00	0.05	0.11	0.00	0.00
Cr2O3	0.03	0.06	2.14	0.40	9.12	0.94	0.40	0.24	0.74	0.23	0.24	0.17	2.75	0.43
CaO	0.01	0.03	7.87	0.84	0.00	0.00	0.17	0.05	23.29	0.50	11.77	0.47	0.99	0.25
TiO2	0.00	0.00	0.15	0.12	0.00	0.00	0.00	0.00	0.10	0.10	0.00	0.00	0.00	0.00
Total	99.38	1.47	101.80	0.83	100.00	0.00	102.00	0.41	99.82	0.93	97.40	1.15	84.15	0.93
Na	0.00	0.00	0.00	0.00	0.00	0.00	0.00	0.00	0.01	0.00	0.13	0.04	0.00	0.00
Mg	1.82	0.01	2.06	0.08	0.90	0.02	1.78	0.01	0.94	0.00	4.50	0.07	5.06	0.08
Si	1.00	0.00	3.01	0.01	0.00	0.00	1.97	0.02	1.92	0.01	7.98	0.03	6.08	0.05
Al	0.00	0.00	1.83	0.03	1.79	0.02	0.06	0.05	0.15	0.02	0.12	0.05	4.22	0.08
Ni	0.01	0.00	0.00	0.00	0.00	0.00	0.00	0.00	0.00	0.00	0.00	0.00	0.01	0.01
Fe	0.17	0.00	0.38	0.03	0.15	0.01	0.18	0.01	0.05	0.00	0.52	0.05	0.29	0.03
Mn	0.00	0.00	0.00	0.01	0.00	0.00	0.00	0.00	0.00	0.00	0.01	0.01	0.00	0.00
Cr	0.00	0.00	0.12	0.02	0.18	0.02	0.01	0.01	0.02	0.01	0.03	0.02	0.33	0.05
Ca	0.00	0.00	0.59	0.06	0.00	0.00	0.01	0.00	0.90	0.02	1.74	0.05	0.16	0.04
Ti	0.00	0.00	0.01	0.01	0.00	0.00	0.00	0.00	0.00	0.00	0.00	0.00	0.00	0.00
Total	3.00	0.00	8.01	0.01	3.01	0.01	4.00	0.00	4.00	0.01	15.02	0.02	16.14	0.04
Mg#	0.91	0.00	0.84	0.01	0.86	0.01	0.91	0.01	0.95	0.00	0.90	0.01	0.95	0.01
Cr#	0.17	0.37	0.06	0.01	0.09	0.01	0.20	0.06	0.12	0.03	0.15	0.07	0.07	0.01

TABLE 4.4. Table of representative phase analyses in Series 2

4.3.4.1 Chlorite

Chlorite composition remained homogeneous throughout this experimental series as evidenced by the consistency of the Mg# at 0.94 and a Cr# of 0.09. Its stoichiometry therefore could be described as $(\text{Mg}_{4.81} \text{Fe}_{0.30} \text{Ni}_{0.02}) (\text{Al}_{1.45} \text{Cr}_{0.14}) \text{Si}_{3.28} \text{O}_{12} (\text{OH})_8$, placing it at the Mg-rich end of the clinochlore-chamosite solid-solution.

Neither Mg# nor Cr# showed any significant correlation with pressure or temperature across the series. Minor compositional variation within experimental runs were within one standard deviation of the mean.

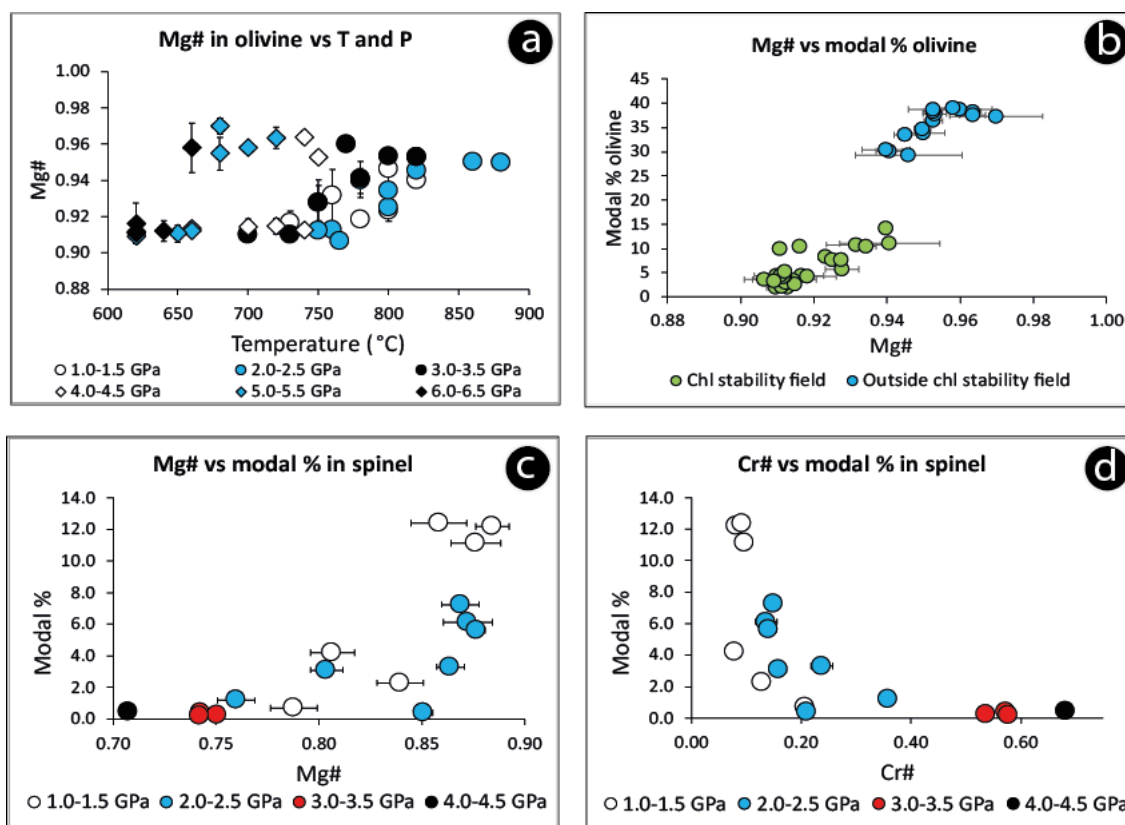


FIGURE 4.7. Compositional plots for olivine and spinel in Series 2

a) Plot of Mg# vs T and P in olivine which shows no significant correlation with pressure and a moderate positive correlation with temperature. b) Plot of Mg# vs modal% olivine. A rapid rise in Mg# in olivine occurs with the breakdown of chlorite as Mg preferentially partitions into this phase in the anhydrous field. c) Mg# vs modal% spinel. A clear positive logarithmic correlation emerges: Mg# increases with increasing modal % spinel although there is greater variability at lower pressure. d) Plot of Cr# vs modal% spinel which signifies a strong inverse logarithmic relationship between these variables: as the proportion of spinel decreases, its Cr# increases.

4.3.4.2 Antigorite

Antigorite was identified in only two experimental runs (C4765 and UHPPC262) which provided three data analyses. Notwithstanding the limited data, the experimentally-determined stoichiometry was $\text{Mg}_{2.62} \text{Fe}_{0.15} \text{Al}_{0.16} \text{Cr}_{0.01} \text{Si}_{2.06} \text{O}_5 (\text{OH})_4$, identical to the start mix composition within error.

4.3.4.3 *Ca-amphibole*

The Ca-amphibole used in the starting mix was positioned near the Mg-rich end member of the tremolite-actinolite series, characterised by the stoichiometry:

$(\text{Na, Ca})_{1.79} (\text{Al, Cr})_{0.20} (\text{Mg, Fe, Ni, Mn})_{5.03} \text{Si}_{7.97} \text{O}_{22} (\text{OH})_2$. The Mg# showed limited variation across the series (0.88-0.90) whilst the Cr# exhibited greater variability (0.13-0.23). However, this compositional variability was evident in the starting mix and therefore was not attributable to chemical reaction during experimentation.

4.3.4.4 *Olivine*

The Mg# of olivine ranged between 0.91 and 0.97 with the higher readings recorded following the disappearance of co-existing hydrous phases. This is illustrated in Figure 4.7b which shows two contrasting groups of olivine composition: one in the chlorite stability field and the other in the anhydrous field after chlorite breakdown. No correlation was observed between Mg# and pressure but a weak association between Mg# and temperature was evident (Figure 4.7a) which highlighted the transition across the hydrous-anhydrous phase boundary.

Nickel concentration in olivine averaged 0.34 wt% (0.17 wt% in the starting mix) which suggested a partitioning preference of nickel to olivine. However, no significant correlation could be identified between NiO and Mg#, pressure or temperature.

4.3.4.5 *Spinel*

Spinel exhibited much compositional variation throughout this series. A moderate positive correlation was evident between Mg# and temperature and an inverse relationship between Mg# and pressure (see Figure 4.7c). The strength of this pattern was limited by the data scatter at low pressure; nevertheless, the highest Mg# values were observed at high temperature points at low pressure (Mg#=0.88 at 1.0 GPa, 780°C) and the lowest Mg# values were recorded at low temperature points at high pressure (Mg#=0.71 at 4.0 GPa, 750°C). Figure 4.8c displays a positive logarithmic correlation between Mg# and modal % spinel. Spinel is most plentiful at low pressure where its Mg# is also highest. As the quantity of spinel declines with increasing pressure, it becomes increasingly iron-rich.

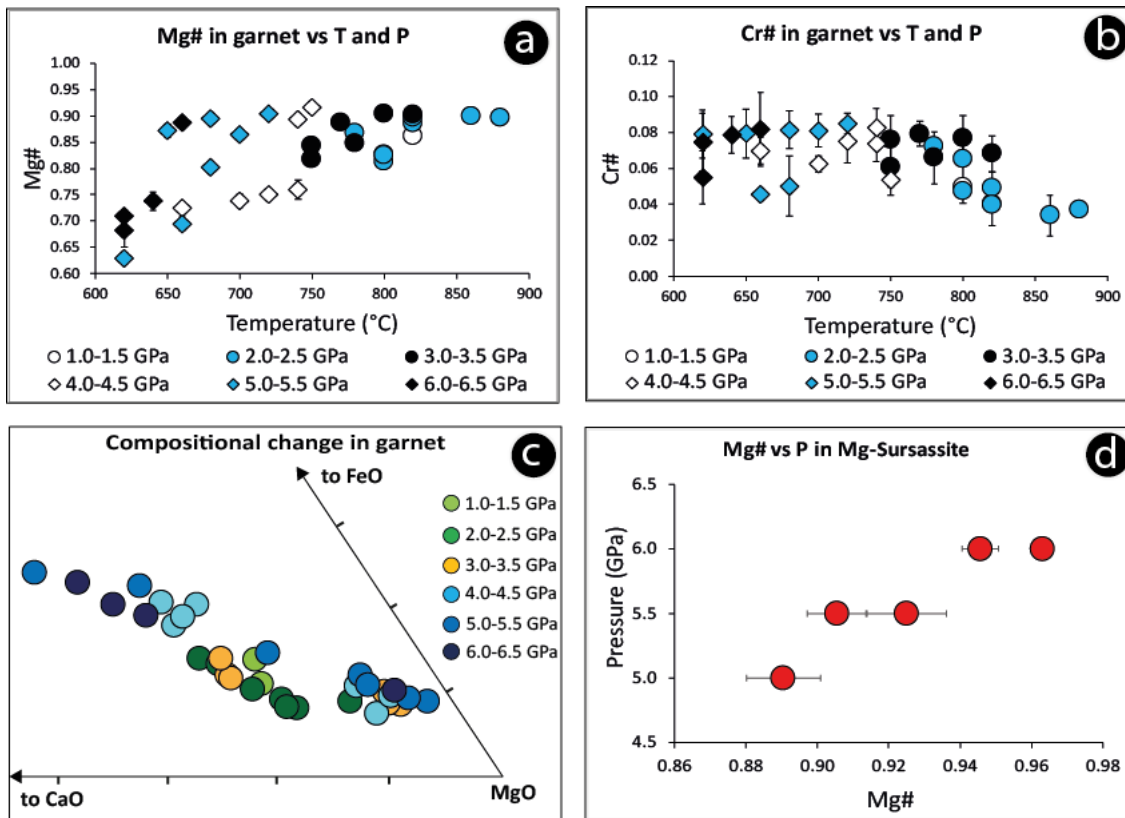


FIGURE 4.8. Compositional plots for garnet and Mg-Sursassite in Series 2

a) Plot of Mg# in garnet vs P and T. A moderate positive correlation is evident between Mg# and T. The range of Mg# reduces with decreasing pressure. b) Plot of Cr# in garnet vs P and T. A weak inverse correlation is evident between Cr# and T up to 4.0 GPa after which this trend levels out. The Cr# also shows a weak inverse relationship with pressure. c) Plot of almandine, grossular and pyrope composition in garnet by P. The almandine and grossular components increase with increasing pressure. d) Mg# vs P in Mg-sursassite show a strong positive correlation.

The Cr# displayed greater variability with an overall range of 0.08 – 0.68. Cr# displayed a strong positive correlation with pressure and a considerably weaker inverse relationship with temperature. Figure 4.8d shows the changing nature of the Cr# plotted against modal% of spinel formed. The resulting logarithmic pattern shows that in regions where spinel is most plentiful (ie: at low pressure) it possesses a low Cr#; with increasing pressure where it co-exists with the garnet phase, less spinel is formed but it registers a higher Cr#.

FE-SEM analyses of the spinel phase were made difficult by grains which were either small, or large but poikiloblastic.

4.3.4.6 Garnet

Garnet experienced considerable compositional variation throughout this experimental series. Pyrope added to the bulk composition provided seeds to encourage nucleation of new garnet. Textural observation confirmed the growth firstly, of grossular-rich rims followed by almandine-rich rims as key reactions progressed. The compositional plot (Figure 4.8c) illustrates the changing composition of garnet between the almandine, grossular and pyrope end-member

compositions. With increasing pressure, the garnet composition broadens from the pyrope-rich corner towards a mid-point between the almandine-rich and grossular-rich corners.

The Mg# in this series ranged from 0.63 (5.5 GPa, 620°C) to 0.92 (4.0 GPa, 750°C). A strong positive correlation between Mg# and temperature was evident (see Figure 4.8a). Although the Mg# range increased with increasing pressure, no other significant relationship was observed between Mg# and pressure.

The Cr# ranged from 0.03 to 0.09. The Cr# displayed a weak inverse correlation with temperature, most apparent when garnet and spinel co-existed up to 4.0 GPa. Data at higher pressures showed no relationship between Cr# and T likely due to the disappearance of the spinel phase. Cr# also displayed a weak inverse trend with pressure across the garnet series (see Figure 4.8b).

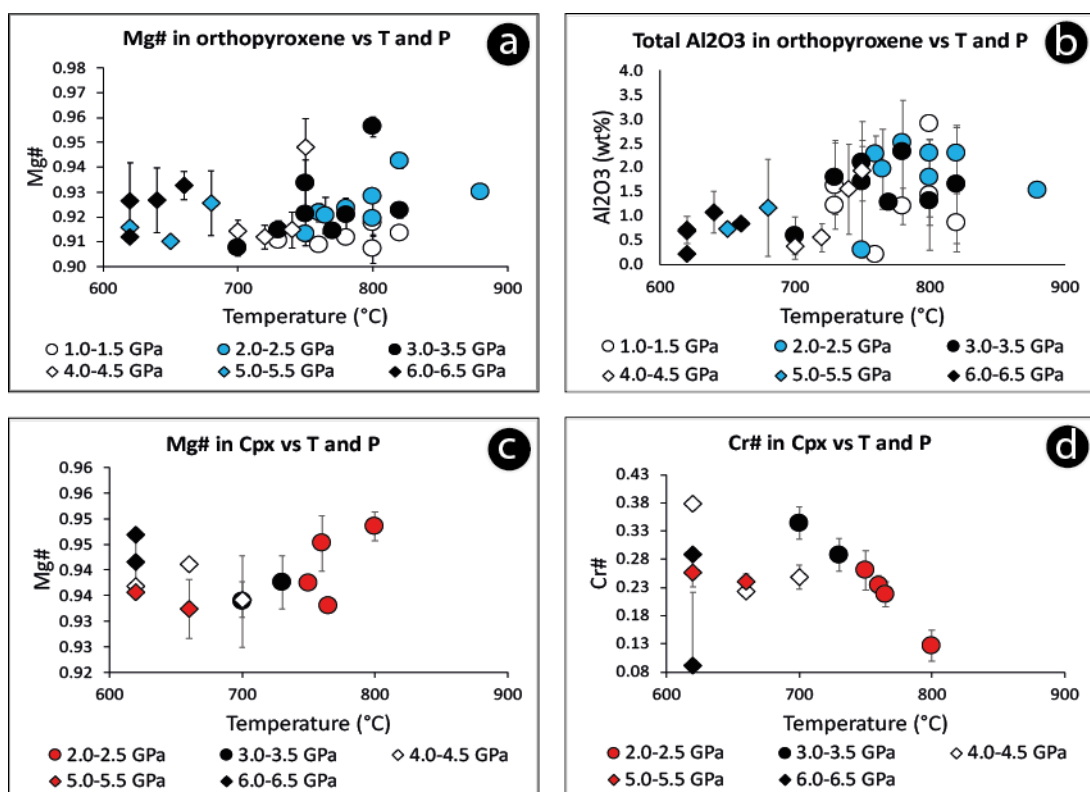


FIGURE 4.9. Compositional plots for orthopyroxene and clinopyroxene in Series 2

a) Plot of Mg# vs T and P in opx. Whilst a weak positive correlation was evident between Mg# and temperature, no relationship was observed between Mg# and P. b) Plot showing total Al₂O₃ vs T and P in opx. Total Al₂O₃ shows a positive correlation with temperature and an inverse correlation with pressure. The large error bars, however, weakened the veracity of both trends. c) Plot of Mg# in cpx vs T and P. Mg# showed no significant correlation with pressure but a weak positive trend with temperature. d) Plot of Cr# vs T and P in cpx. A weak inverse trend was evident between Cr# and pressure, but a stronger inverse correlation was observed between Cr# and temperature although this lessened with increasing pressure.

4.3.4.7 *Mg-sursassite*

Mg-sursassite underwent extensive compositional change in this series. The Mg# ranged from 0.89-0.96 and was strongly correlated with pressure (see Figure 4.8d). A moderate inverse trend with temperature was also detected. The Cr# varied between 0.06-0.08. No relationship with temperature was evident but a weak positive correlation with pressure was observed.

It was noted that Cr cations increased consistently with increasing pressure whilst Ca cations decreased. Whilst Ca and Cr cations conceivably occupy different crystallographic sites in the Mg-sursassite molecule, this trend is interesting and would warrant further investigation.

4.3.4.8 *Orthopyroxene*

Orthopyroxene displayed minimal compositional variation throughout the series.

The Mg# ranged between 0.91-0.96 but only three values were recorded above 0.94. No significant correlation was observed between Mg# and pressure although a weak relationship existed between Mg# and increasing temperature (see Figure 4.9a).

The Cr# recorded large variation, even in analyses within the same charge, however, most results were contained within the 0.11-0.26 range (see Appendix for full table of results on opx analyses). No significant correlation was observed between Cr# and either pressure or temperature. However, a pattern was observed in relation to the incorporation of aluminium oxide into the opx phase (see Figure 4.9b). Total Al₂O₃ was moderately correlated with temperature and inversely with pressure. This was confirmed by textural observation. At low pressure, opx grains sometimes exhibited strong compositional zoning with Al-rich cores (>8.0 wt% Al₂O₃) reducing to Al-poor (even Al-absent) rims. These textures diminished with increasing pressure and were not observed in charges above 3.0 GPa.

Small crystal size, compositional zoning and grains intercalated with other phases meant that the attainment of quality chemical data on opx was problematic throughout this series.

4.3.4.9 *Clinopyroxene*

Cpx exhibited minor compositional variation throughout this experimental series. The Mg# varied only between 0.93 and 0.95 but showed a weak correlation with temperature. No relationship was observed between Mg# and pressure (see Figure 4.9c).

The Cr# varied between 0.13 and 0.38. A strong inverse correlation was observed between Cr# and temperature although this pattern seemed to lessen with increased pressure. A weak

inverse correlation between Cr# and pressure was also observed (see Figure 4.9d). The table of cpx analyses can be viewed in the Chapter 3 Appendix.

FE-SEM analyses of cpx grains was difficult due to very small grain size and especially when it frequently formed intercalated with opx grains.

4.3.5 ELEMENT PARTITIONING

Mg-Fe partitioning between co-existing phases was determined by the Mg# ($Mg/(Mg+Fe)$). The partitioning sequence, in descending order of magnitude, was: MgS > *atg* > *chl* > cpx > ol > opx > *tre* > grt > sp.

A few deviations from this rank were detected. Mg# of opx occasionally exceeded those of olivine (eg: D1700, UHPPC299) and Mg# of olivine exceeding those of MgS (runs UHPPC360 and UHPPC288), likely due to the small numbers of opx and MgS analyses respectively in those runs. The Mg# of minerals comprising the starting mix (eg: chlorite and tremolite, shown here in italics) showed limited reaction across the series. Their order in the partitioning sequence, therefore, was likely based on their relict Mg# and not one determined by chemical reaction in this series.

Four partitioning plots are shown in Figure 4.10. Figure 4.10a displays Mg-Fe partitioning between garnet and spinel vs pressure using $K_D = (X_{Mg}^{grt})(X_{Fe}^{sp}) / (X_{Fe}^{grt})(X_{Mg}^{sp})$. At all times, Mg preferentially partitioned into garnet over spinel. Mg increasingly partitioned into the garnet phase as pressure increased, although several data points did not fit this pattern. No correlation was observed between $\ln K_D$ of these phases and temperature.

Mg-Fe partitioning between garnet and olivine is shown in Figure 4.10c with the partitioning coefficient calculated using $K_D = (X_{Mg}^{ol})(X_{Fe}^{grt}) / (X_{Fe}^{ol})(X_{Mg}^{grt})$. The strong pattern was revealed in which Mg always partitioned into olivine over garnet, but as temperature increased, Mg showed increasing preference for garnet. A similar pattern was observed between Mg-Fe partitioning between olivine and garnet with pressure.

The coefficient for the partitioning of Mg-Fe between Mg-sursassite and olivine was calculated using the equation $K_D = (X_{Mg}^{MgS})(X_{Fe}^{ol}) / (X_{Fe}^{MgS})(X_{Mg}^{ol})$. The resulting plot is displayed in Figure 4.10d. A clear trend, albeit based on few data, showed that Mg preferred the hydrous phase over olivine, but with increasing temperature, Mg preferentially partitioned into olivine over MgS which led the $\ln K_D$ to approach unity.

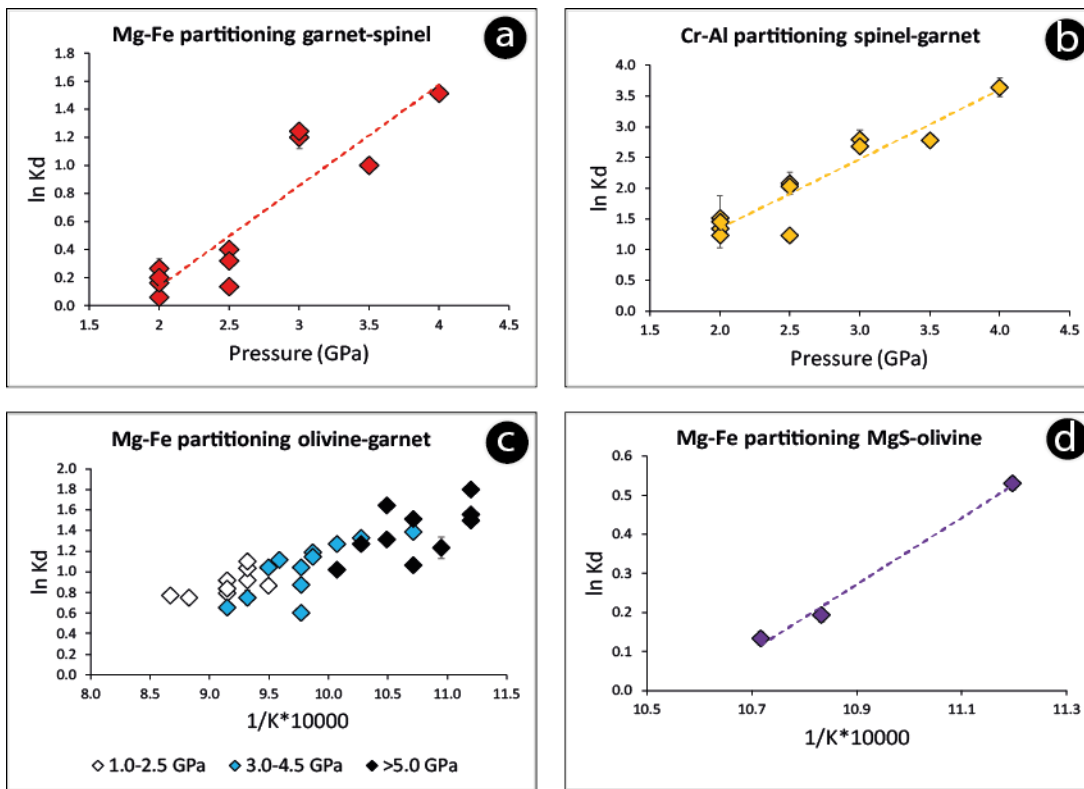


FIGURE 4.10. Partitioning plots for select pairs in Series 2

a) Partitioning of Mg-Fe between garnet and spinel versus pressure. Mg favours garnet with increasing pressure. b) Partitioning of Cr-Al between spinel and garnet versus pressure which shows Cr favouring spinel with increasing pressure. c) Partitioning of Mg-Fe between olivine and garnet. With increasing temperature, Mg favours garnet although each phase becomes increasingly Mg-rich. d) Partitioning of Mg-Fe between Mg-sursassite and olivine. Mg preferentially partitions into MgS over olivine but with increasing temperature, each phase becomes increasingly Mg-rich.

The Cr# ($\text{Cr}/(\text{Cr}+\text{Al})$) was used to ascertain Cr-Al partitioning between co-existing phases, which revealed the sequence, in descending order, of: sp > chl > grt > MgS. Spinel consistently recorded a higher Cr# than garnet, whilst MgS recorded a lower Cr#.

A single exception was observed to these partitioning patterns: MgS recorded a higher Cr# than garnet (run UHPPC288), likely due to few data points for MgS at this P,T location.

Figure 4.10b showed the Cr# partitioning between spinel and garnet vs pressure, with the partitioning coefficient calculated using $K_D = \frac{(X_{\text{Cr}}^{\text{sp}})(X_{\text{Al}}^{\text{grt}})}{(X_{\text{Al}}^{\text{sp}})(X_{\text{Cr}}^{\text{grt}})}$. A consistent pattern emerged: with increasing pressure, Cr increasingly preferentially partitioned into the spinel phase, creating a steeply sloping curve. Whilst Cr and Al were identified in orthopyroxene, clinopyroxene and tremolite, the amounts were insufficient for partitioning purposes.

4.4 DISCUSSION

This experimental series aimed to examine the two key chlorite reactions in chlorite peridotite: Reaction 3, which traced the stability of chlorite lherzolite, and Reaction 4, which examined the stability of chlorite harzburgite. The results successfully constrained each reaction to a thermal maximum near 6.2 GPa, 635°C, an invariant point where both reactions converged. Regardless of Reaction 3 being situated some 40°C lower than Reaction 4, these results showed that the stability field of chlorite is considerably larger than previously identified, moving to both higher temperature and higher pressure than revealed by any previously published data. Chlorite breakdown according to Reaction 4 yields MgS at high-pressure, a hydrous mineral which forms contiguously with chlorite, and therefore sequesters water and has important implications for water transport in the mantle.

The discussion will comprise three parts. The first examines the approach to equilibrium. The second part provides justification for these new findings through a comparison of these results with previous experimental investigations on chlorite and with theoretical considerations within this chemical system. The third part explores patterns of water release upon chlorite breakdown, its implications for water availability in the sub-arc, and the wider significance for water transport to the deep mantle.

4.4.1 ATTAINMENT OF EQUILIBRIUM

This experimental series was affected by similar sets of constraints as encountered in Chapter 3, each of which had the potential to disrupt the attainment of equilibrium. Experiments were conducted at relatively low temperatures and therefore did not always exhibit fully equilibrated textures. The use of natural minerals created divariant fields and thus more complex phase compositions in run products. This necessitated great care when analysing phases to ensure that only those regions of minerals in local equilibrium were sampled.

Several methods were employed to select only equilibrated phase textures. Euhedral grain boundaries typically indicate the attainment of equilibrium. These were common with spinel (see Figure 4.5a) and observed between garnet and olivine, particularly in high-temperature runs (see Figure 4.4b,d,g,f). Euhedral boundaries were less-common in run products following the breakdown of chlorite (see Figure 4.5d) but could always be located.

Heterogenous textures were observed in most phases. Poikiloblastic textures were common in garnet and spinel (see Figure 4.4d and 4.5a), as were growth rims in garnet, olivine and opx (see Figure 4.4f, 4.5a and 4.6a). Intercalated textures were common in both opx and cpx when these

phases co-existed (see Figure 4.4a and 4.6b). Pyrope seeds added to the starting mix were not always fully resorbed, however the boundary between seed and growth rims was well-defined, indicative of local equilibrium within the outer rim. Whilst at times challenging, analyses were taken only from newly-formed rims, and from those parts of the grain distal to inclusions.

The success of this technique has been vindicated by an examination of chemical analyses. Chemical analyses of phases exhibited minimal variation. Partitioning data between mineral pairs revealed expected patterns, and phase relations showed excellent agreement with Schreinemakers modelling. Mass balance calculations of run products were in excellent agreement with the starting mix compositions which suggested that analyses must have successfully targeted equilibrated regions of minerals. There was no evidence of Fe loss to the gold capsule during experiments and therefore oxygen fugacity remained close to Ni-NiO buffer. Taken together, these factors indicate that phases in experimental runs in this series had attained equilibrium.

4.4.2 THEORETICAL PHASE RELATIONS IN THE CMASH SYSTEM

The phases identified in the run products from this experimental series were used to create a phase diagram (see Figure 4.3). How closely did the experimentally-determined phase relations align with those determined by theoretical topology of this system? The Schreinemakers method was used to determine the theoretical phase relations of the bulk composition used in this study and these were employed as a reference point for the topological arrangement of the experimentally-determined phase boundaries.

Theoretical phase relations are illustrated in Figures 4.11 and 4.12 which represent the high-pressure and low-pressure regions of the P,T grid respectively. For thesis continuity, invariant points and relevant reactions introduced in this chapter will continue the number/letter sequence from previous chapters (therefore the first new labels in this chapter will relate to Invariant Point G). To enable Schreinemakers analysis of this natural system, some simplification was required. Guided by mineral analyses, Mg and Fe were combined into a single component, as were Al and Cr. In this way, phase relations were variously modelled using the four-component MASH system, the four-component CMSH system, or the five-component CMASH system.

Seven relevant Invariant Points were identified, three of which – Invariant Points A, D and F – have been described previously (see Chapter 3 for details). Together, they provided a clear framework of the two key reactions investigated in this study. The boundary for Reaction 3 was

traced by Invariant Points J-H-K. The limit of Reaction 4 was delineated by Invariant Points A-D-K-F. Invariant Point K intersected both sets of reactions.

4.4.2.1 *Invariant points and reactions related to Reaction 4*

Reaction 4 traced the upper stability boundary of the chlorite + orthopyroxene reaction in the simpler Ca-free MASH system. The reaction boundary linked the Invariant Points A'-D'-K-F. A summary of the key reactions is provided.

Invariant Point A' (see caption in Figure 4.12 for explanation) denoted the low-pressure termination of the reaction involving phases chlorite and orthopyroxene:

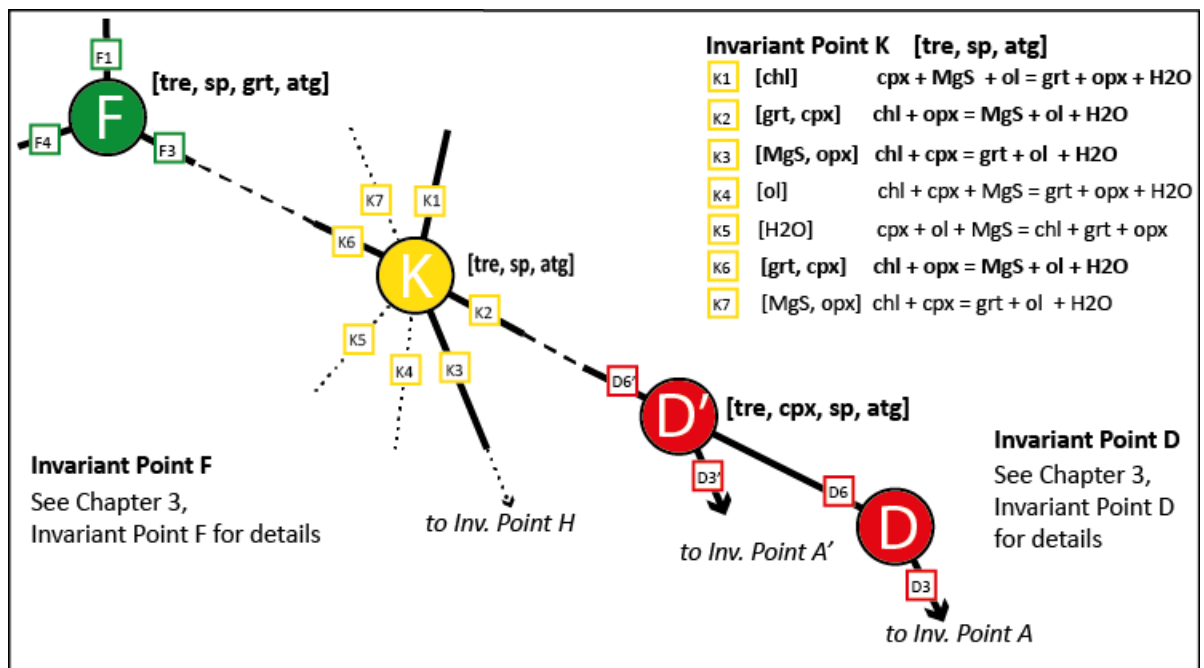
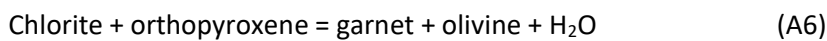
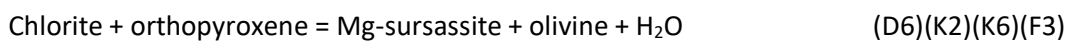


FIGURE 4.11. Schreinemakers network in Series 2 at high pressure.

Each of the Invariant Points D, K and F mark the upper pressure stability of chlorite. The disappearance of chlorite along Reaction 4 creates the hydrous phase MgS. Note Invariant Point D', which is a variation of Invariant Point D found in the MASH system. Calcium lowers the stability field of chlorite which necessitates its inclusion in the CMASH system. Dotted lines indicate reactions which do not occur in this bulk composition.

The high-pressure Invariant Point D' (see caption in Figure 4.11 for explanation) formed an important reference: at pressures above this point, garnet was replaced by Mg-sursassite as the main Al-bearing phase described by the reaction:



Invariant Point K witnessed the high-pressure convergence of the phases clinopyroxene, chlorite and orthopyroxene and therefore the termination of both Reactions 3 and 4 in this bulk composition. Reactions K2 and K6, which marked the upper pressure limit of chlorite, operated

on both the high-temperature and low-temperature sides of this invariant point and linked Invariant Points D' and F.

Invariant Point F marked the convergence of the hydrous phases chlorite, MgS and 11.5Å-phase. It formed an important reference point as it marked the upper pressure boundary of chlorite stability, the low-pressure boundary of the 11.5Å-phase, and the low-temperature boundary of the MgS phase.



4.4.2.2 Invariant points and reactions related to Reaction 3

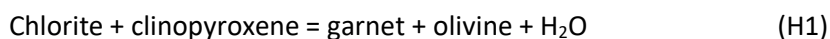
Reaction 3 traced the upper thermal stability boundary of the chlorite + clinopyroxene reaction in the more complex CMASH system. This reaction linked the Invariant Points H-K. The Reaction G2/H6 marked the low-pressure boundary of cpx and so has been included in this section. A summary of the key reactions is provided below.

Invariant Point G, modelled in the simpler CSMH system, saw the creation of cpx following the breakdown of tremolite. It was possible to project from chlorite since it was the only Al-bearing phase in the low-temperature, low-pressure region of the pseudosection. Schreinemakers analysis confirmed that in the CSMH system, only six phases could be present at any invariant point. Invariant Point G formed the conjunction of the phases antigorite, tremolite, clinopyroxene, orthopyroxene, olivine and water. It is significant to this investigation as it provides a previously studied reference point (Padron-Navarta, *et al.*, 2010b) where the antigorite-out and tremolite-out reactions intersected, informed by the reactions:



Invariant Points H, J and K were modelled in the full CMASH system since they each involved a Ca-bearing phase in co-existence with chlorite and therefore seven phases converged at each invariant point.

Invariant Point H marked the low-pressure termination of Reaction 3 and the convergence of the stable paragenesis of chlorite, tremolite, garnet, clinopyroxene, orthopyroxene, olivine and water. Two chlorite-out reactions were involved:



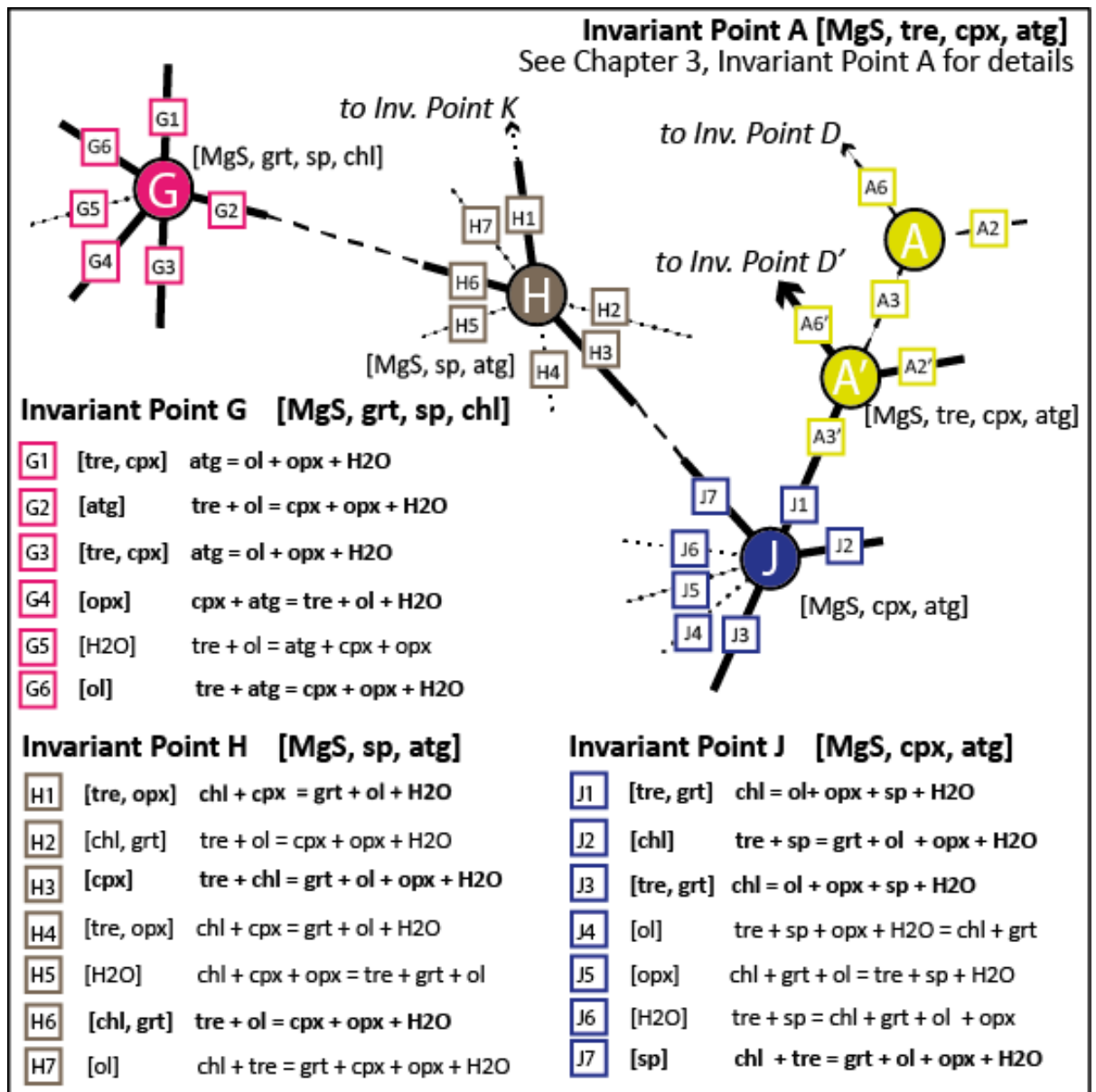


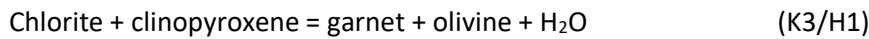
FIGURE 4.12. Schreinemaker network in Series 2 at low pressure

Four relevant Invariant Points identified in the low-pressure region of Series 2 experiments. Invariant Point G (CMASH system), Points H and J (CMASH system) and Point A (MASH system) involve chlorite in either Reaction 3 or Reaction 4. Invariant Point A', which is the CMASH equivalent of Invariant Point A found in the MASH system. The presence of Ca reduces chlorite stability down-P and down-T which requires this variation in this system. Dotted lines indicate reactions which do not occur in this bulk composition.

Invariant Point J marks a key chlorite-out boundary at low pressure and thereby links with Invariant Point H, the low-pressure termination of Reaction 3, and with Invariant Point A, the low-pressure termination of Reaction 4. Invariant Point J sees the convergence of chlorite, tremolite, garnet, spinel, orthopyroxene, olivine and water. On the high-pressure and low-pressure side of this invariant point was located the chlorite-out reaction:



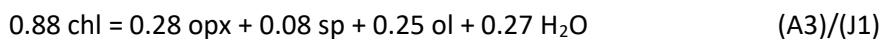
At higher pressure, Invariant Point K saw the convergence of Reaction 3 and 4 which saw the phases chlorite, garnet, olivine, orthopyroxene, clinopyroxene, Mg-sursassite and H₂O exist in equilibrium. The main chlorite-out reaction involved a Ca-bearing phase:



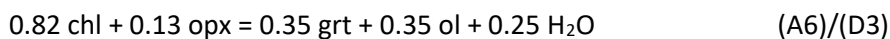
4.4.3 KEY CHLORITE REACTIONS DETERMINED BY MASS BALANCE

This experimental series identified several reactions involving chlorite in the CMASH, MASH and CSMH chemical systems. Where experimental data points were located on either side of a reaction, phase data was extracted from the experimental results, converted to molar proportions and used to mass balance the reaction equations using C-Space (Torres-Roldan *et al.*, 2000). This process revealed that chlorite disappearance was controlled by six different chemical reactions.

Reaction A3/J1 formed the thermal boundary of chlorite stability between Invariant Points A and J. Chlorite disappeared according to the low-pressure dehydration reaction. The mass balance reaction, determined at two locations (1.0 GPa, 760-780°C and 1.5 GPa, 800-820°C), showed excellent agreement:



Up to 6.1 GPa, the most important reaction involving chlorite disappearance was controlled by Reaction A6/D3, which linked Invariant Points A and D. It was calculated at four separate locations where each showed excellent agreement.



At pressures above Invariant Point D, Mg-sursassite began to replace garnet as the main Al-bearing phase. Reaction D6/K2 linked Invariant Points D and K; between 5.0 GPa, 680°C and 5.5 GPa, 680°C this reaction was controlled by:

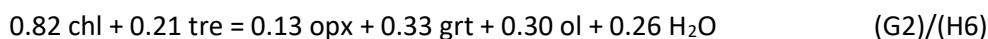


Two important reactions involving chlorite and a Ca-bearing phase were also confirmed by experimental results.

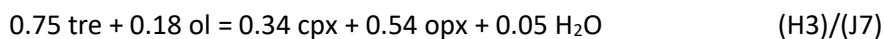
Reaction H1/K3 connected Invariant Points H and K. Chlorite breakdown with clinopyroxene occurred between 4.0 GPa, 700°C and 4.5 GPa, 720°C controlled by:



The linkage between Invariant Points H and G was made by Reaction H6/G2. Between 800°C and 820°C at 2.0 GPa, chlorite disappearance was controlled by:



The transformation of tremolite to clinopyroxene was determined by Reaction J7/H3. Between 1.5 GPa, 730°C and 2.5 GPa, 750°C this was informed by:



Antigorite dehydration, whilst not strictly relevant to this series, was able to be determined at 5.0 GPa between 620°C and 660°C informed by:



4.4.4 CHLORITE REACTION CURVES IN CHLORITE PERIDOTITE

Figure 4.13 is a simplified phase diagram of the experimental results showing the key chlorite reactions in chlorite peridotite and their relationship to key invariant points (letter symbols enclosed in a circle). The blue curve denotes Reaction 3 whilst the green curve indicates the location of Reaction 4. Other reactions are marked in black.

4.4.4.1 Slope of the chlorite + orthopyroxene curve (Reaction 4)

Reaction 4 commenced at Invariant Point A', located near 1.9 GPa, 835°C, where this reaction first diverged from the chlorite terminal reaction. The designation Invariant Point A' was required because the Series 2 composition contained calcium which reduced the stability field of chlorite to slightly lower P,T conditions; the A' designation contrasted with Invariant Point A which applies to the Ca-free system. From 1.9 GPa, the curve underwent a negative backbend unchanged to Invariant Point D', near 6.1 GPa, 655°C. A significant backbend occurred at this point after which the curve assumed a very shallow slope through Invariant Point K (6.2 GPa, 635°C) to Invariant Point F, located near 6.3 GPa, 600°C. The reaction line D-K-F represented changed reaction products with Mg-sursassite replacing garnet as the stable Al-bearing phase. Further experimentation is needed to fully constrain the upper boundary of the Reaction 4 at pressures above 6.3 GPa.

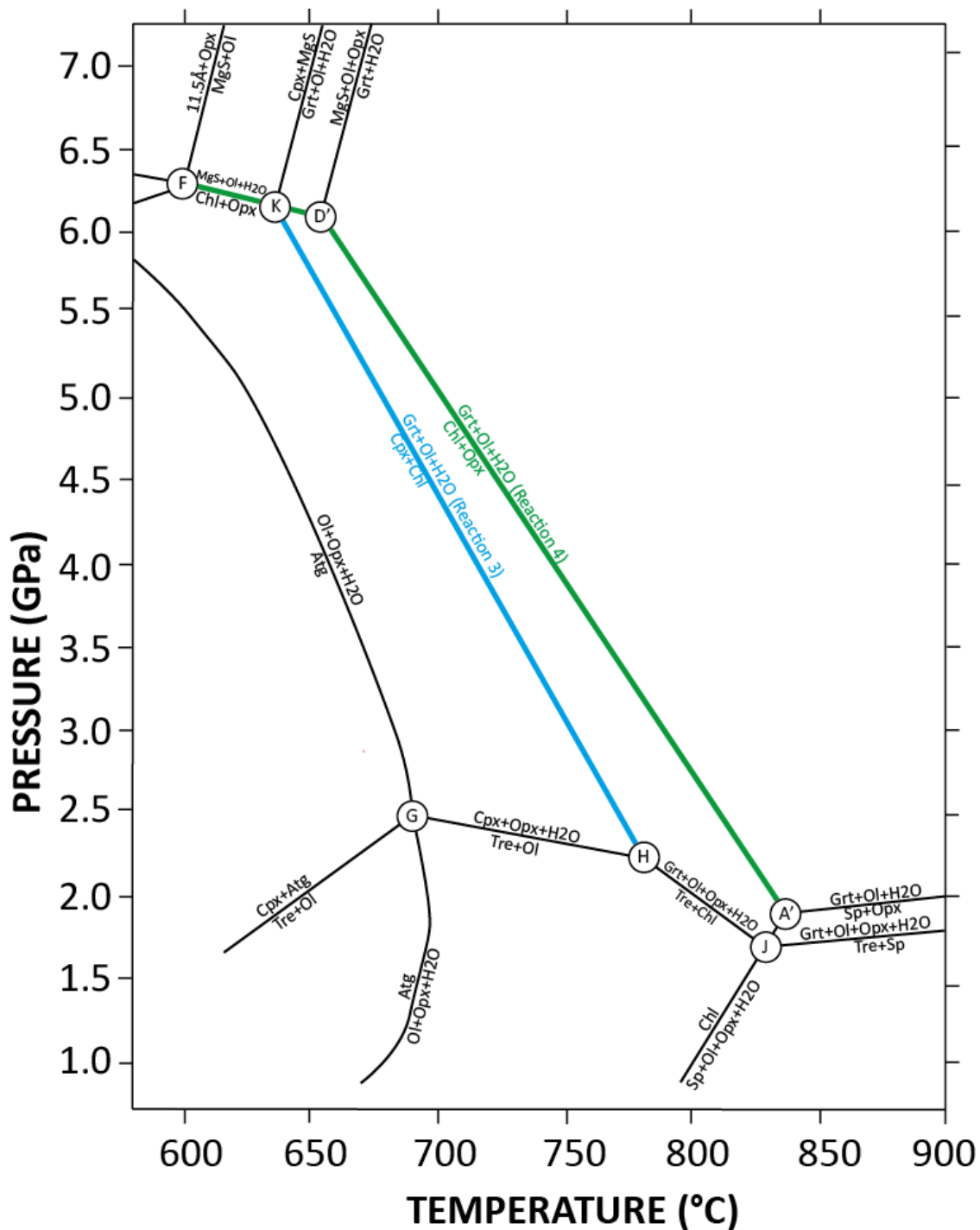


FIGURE 4.13: Phase relations in chlorite peridotite highlighting key Reactions 3 and 4.

Reaction 3 indicated by blue curve, Reaction 4 by green curve. Other key reactions in this system indicated by black lines. Circled letters show location of key invariant points – see text for details. Phase abbreviations as previously denoted.

4.4.4.2 Slope of the chlorite + clinopyroxene curve (Reaction 3)

The Reaction 3 curve maintained a consistent slope from its inception at Invariant Point H, located near 2.3 GPa, 780°C. With increasing pressure, the curve assumed a negative Clapeyron slope which rose slightly more steeply than Reaction 4. The slope was unchanged until attaining

its termination at Invariant Point K, near 6.2 GPa, 635°C. Importantly, this point marked the convergence of Reactions 3 and 4 in this system.

4.4.5 LOCATION OF INVARIANT POINTS

The experimental results obtained in this study located seven invariant points which showed strong agreement with those determined by Schreinemakers analysis and those from previous studies when adjusted for compositional differences.

4.4.5.1 Invariant points relevant to Reaction 4

Reaction 4 linked the four invariant points A'-D'-K-F.

Invariant Point A' marked the convergence of several important reactions: the chlorite terminal reaction, the garnet-spinel transition and the low-pressure termination of the chl+opx reaction. It was located near 1.9 GPa, 835°C. The designation A' was necessitated as the equivalent point in the chlorite schist experiments (Chapter 3) was located at higher P,T conditions due to compositional differences, namely the absence of Ca. Nevertheless, Invariant Point A' showed excellent agreement with those of previous studies (Staudigel and Schreyer, 1977; Jenkins, 1981).

Invariant Point D' was located near 6.1 GPa, 655°C. It involved the termination of both chl+opx reactions: the D3 reaction which produced grt+ol+H₂O and the high-pressure D6 reaction which produced MgS+ol+H₂O. Invariant Point D was located at higher temperature in chlorite schist experiments (Chapter 3) also due to the absence of Ca in the system, and this required a D' designation to be allocated for this series. The location of this invariant point shows strong agreement with that of Bromiley and Pawley (Bromiley and Pawley, 2002) who located this invariant point near 5.6 GPa, 670°C in a Cr-free system. It contrasts with that of Fumagalli (Fumagalli *et al.*, 2014) who placed this point at 5.0 GPa, 670°C. However, the complex solid solution of the MgS phase (Fumagalli *et al.*, 2014, p.979) may have seen its appearance at much lower pressure.

Invariant Point K was located near 6.2 GPa, 635°C and witnessed the convergence of both key chlorite reactions in chlorite peridotite: the K2/K6 reaction, the high-pressure form of Reaction 4, and the termination of the K3 reaction (Reaction 3). This point has not previously been identified in the experimental literature.

Invariant Point F was inferred to be located near 6.3 GPa, 600°C where four important chlorite reactions converge. It represents the highest-pressure stability of the chlorite phase at 6.3 GPa,

and the appearance of the 11.5Å-phase in this chemical system. Further experimental investigation is needed to constrain the upper pressure boundary of the chl+opx reaction and other reactions around this invariant point.

4.4.5.2 Invariant points relevant to Reaction 3

Reaction 3 linked the two invariant points H-K.

Invariant Point H was located at 2.3 GPa, 780°C and formed the low-pressure termination of Reaction 3 (reaction H1). It also saw the convergence of reactions H3 and H6 which together formed the upper pressure boundary of tremolite. The H3 reaction was a chl+tre reaction which produced garnet to higher pressure; the H6 reaction between ol+tre saw the appearance of cpx at higher pressure.

Invariant Point K was located near 6.2 GPa, 635°C and saw the termination of the K3 reaction (Reaction 3). This point has been described above.

Two additional invariant points – J and G – were also identified in this study which support the topological arrangement of the key reactions.

Invariant Point J was located at ~1.7 GPa, 825°C and marked the convergence of several key chlorite reactions: the terminal chlorite reaction (J1 and J3) and the garnet-producing reaction J7. This invariant point provides an indirect low-pressure connection between Reaction 3 and Reaction 4.

Invariant Point G was notionally placed at 2.5 GPa, 680°C since few experimental constraints were established in the current experimental series. This point marked the convergence of the terminal antigorite reaction (G1 and G3) and the G2 reaction which saw the production of cpx at the expense of tre. It showed good agreement with Padron-Navarta (Padron-Navarta, *et al.*, 2010b) who located this invariant point experimentally at 1.9 GPa, 680°C in a Cr-poorer system.

4.4.6 PREVIOUS STUDIES OF CHLORITE STABILITY IN CHLORITE PERIDIOTITE

Chlorite stability in peridotite has been the subject of numerous experimental studies over the past fifty years. Early studies were typically synthesis experiments conducted at low pressure; more recent studies have attempted to constrain the upper stability limits of chlorite + pyroxene reactions. Studies in related chemical systems have contributed specific data points on chlorite stability as a by-product of investigations into other mineral phases. Even so, at this point, a definitive understanding of chlorite stability in peridotite compositions remains elusive.

There are two main chemical reactions governing chlorite stability in peridotite compositions at high pressure. The first,



relevant for depleted harzburgite compositions, has been the focus of the bulk of investigative work (Bromiley and Pawley, 2002, 2003; Pawley, 2003; Fumagalli and Poli, 2005; Fumagalli *et al.*, 2014). The second reaction,



relevant for fertile lherzolite compositions, has been little researched (Jenkins, 1981; Fumagalli and Poli, 2005; Spandler *et al.*, 2014). Whilst both reactions are thought to occur close in P,T space (Fumagalli and Poli, 2005), no study has yet investigated this relationship. This is the first study to examine both reactions within a single study.

4.4.6.1 Previous studies of Reaction 3

There has been little previous work on Reaction 3. Jenkins (Jenkins, 1981) explored the phase relations of hydrous minerals in the CMASH system but this was restricted to low pressure and therefore focused on the chlorite reaction with amphiboles. The first experimental study above 2.0 GPa was conducted by Fumagalli and Poli just over a decade ago (Fumagalli and Poli, 2005).

Fumagalli and Poli studied Reaction 3 in the more complex NCFMASH system. The resulting phase boundary is shown in Figure 4.14 as a red dotted line (the vertical sector). Their results provided the first data points on this reaction up to 4.0 GPa. The slope of the curve between 2.0 GPa and 4.0 GPa rises more steeply compared to the Reaction 3 curve from the current study and therefore is not in agreement with the findings of this study. However, it is noted that their experimental data points were separated by 50°C so the published curve could easily be adjusted thereby showing good alignment with the current study.

Spandler (Spandler *et al.*, 2014), investigating serpentinite but also working in the NCFMASH system, located Reaction 4 between 700°C and 750°C at 3.5 GPa, which is in good agreement with the results of this study.

4.4.6.2 Previous studies of Reaction 4

Pawley (Pawley, 2003) completed the most extensive research into Reaction 4 with a contribution of 22 data points to constrain the reaction boundary in an Fe-free, Cr-free system.

Six of these were above 4.0 GPa. The resulting purple dotted curve is displayed in Figure 4.14. Between ~2.0 GPa to 3.2 GPa and 4.6 GPa to 5.2 GPa, the slope of the curve showed good agreement with the current results. However, the Pawley curve underwent a sharp backbend near 3.2 GPa and maintained a low-angle slope to its termination ~5.2 GPa, 620°C. In the current study, this backbend occurred at considerably higher pressure near 6.1 GPa but the slope of each curve aligned well following the backbend. Compositional differences provide some explanation for these differences.

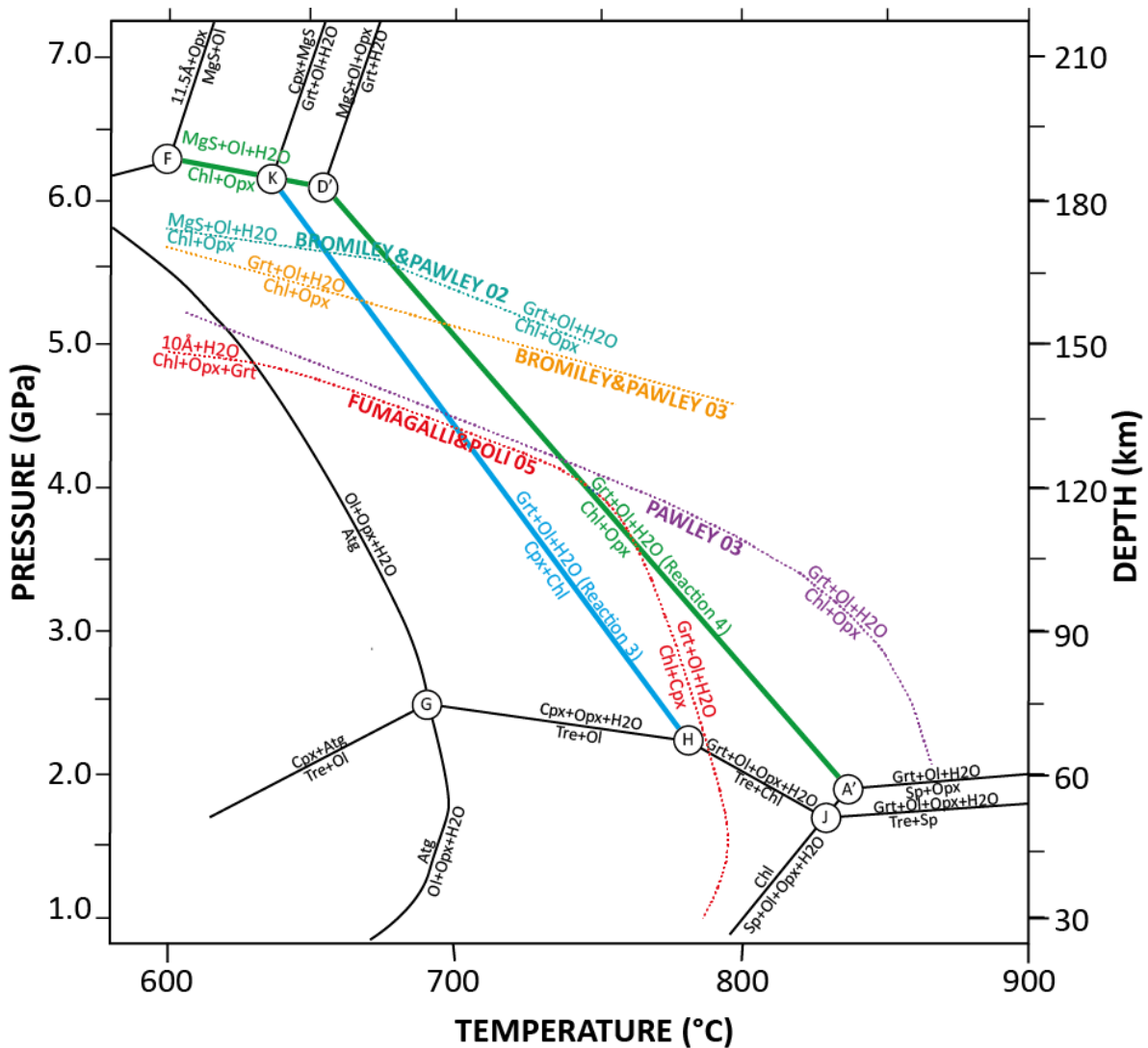


FIGURE 4.14: Key chlorite reactions from current study compared with previous studies.

Solid black lines indicate the phase diagram from current experimental work. Reaction 3 is highlighted in blue; Reaction 4 is coloured in green. Dotted coloured lines indicate reaction curves from previous studies. Note the contrasting gradients, especially at high pressure, of curves from this study compared with previous studies. Note also the similarity of slope between current study and the antigorite dehydration curve. Phase abbreviations as previously denoted.

Fumagalli and Poli (Fumagalli and Poli, 2005) examined the stability of chlorite peridotite using a proxy 'natural' bulk composition in the NCFMASH system. Their exploration of Reaction 4 produced 10Å-phase instead of the expected grt+ol+H₂O combination. The reaction curve

appears in Figure 4.14 as a red, dotted line (the low-angle section). Its slope and its location closely mirrored that of Pawley which is surprising given the compositional differences. The absence of additional data in the high P, low T region of their study suggests that other phases, including chlorite, may be stable there. Except for Cr and Na, the bulk composition used in the Fumagalli study is close to that used in the current study. The slope of each curve after the backbend is very similar, therefore it is hard to account for the displacement of the Fumagalli curve to significantly lower pressure compared with the current results.

Bromiley and Pawley identified new data points on chlorite stability at high pressure from synthesis experiments conducted on Mg-sursassite and antigorite (Bromiley and Pawley, 2002, 2003). Both curves are shown in Figure 4.14 as yellow and orange curves respectively. The slope of the curve in the B&P02 study shows strong alignment with that of Reaction 4 in the current study once adjusted for various compositional differences. The location of the invariant point shown on all three studies also show good agreement. The slope of the B&P03 curve shows little agreement with the results of the current study at high pressure. However, the slope is well aligned with the P03 curve although elevated by more than 0.5 GPa. This is interesting since it is of the same reaction in the same chemical system.

4.4.7 ABSENCE OF 10Å-PHASE IN THE CURRENT STUDY

10Å-phase has been investigated in several high-pressure experimental studies (Bauer and Sclar, 1981; Wunder and Schreyer, 1992; Pawley and Wood, 1995; Fumagalli *et al.*, 2001; Fumagalli and Poli, 2005; Pawley *et al.*, 2011; Rashchenko *et al.*, 2016) to accurately determine its composition, crystallographic structure and the dimension of its stability field. Some debate remains surrounding composition including water content, swelling behaviour and potential reaction with acetone at the preparation stage, experimental run time, and the capacity of the 10Å-phase to form mixed-layer structures. Regardless, the lower 10Å-phase stability field corresponds to a large segment of the P,T region of the current study. So why wasn't the 10Å-phase identified? There are several possible explanations.

The bulk composition used in the current study did not favour the formation of 10Å-phase. As shown in the bulk chemography (see Figure 4.1), this was a chlorite-rich starting mix, and so there was insufficient SiO₂ to crystallise 10Å-phase. The current study comprised <37 wt% SiO₂ whereas in the Fumagalli study, for example, (Fumagalli and Poli, 2005) SiO₂ formed >45 wt% in each of the PX, HZ and LZ samples.

This study contained chromium which elevated the chlorite stability field to higher pressure and temperature. The follow-on effect of this may have been to elevate the low-pressure boundary

of any potential 10Å phase to pressures beyond the constraints here. Alternatively, the elevated chlorite field may have favoured the formation of MgS, for example, over 10Å-phase at the higher P,T conditions.

Starting mixes may impact stability of the 10 Å-phase. Gels have commonly been used in the preparation of the starting material (Bauer and Sclar, 1981; Wunder and Schreyer, 1992; Fumagalli and Poli, 2005; Pawley *et al.*, 2011) as opposed to crystalline starting material in the current study. This was done to facilitate phase synthesis (Fumagalli and Poli, 2005). Perversely, this may have resulted in the 10Å-phase remaining as a metastable phase (Wunder and Schreyer, 1992) at high pressure.

The quantity of Al in the 10Å-phase remains unresolved at present. Two natural samples of 10Å-phase have been reported (Smith, 1995; Khisina and Wirth, 2008) which contained trace aluminium (≤ 0.05 a.p.f.u. Al). However, all experimental studies of 10Å phase have been entirely Al-free with the exception of two studies (Fumagalli and Poli, 2005; Dvir *et al.*, 2011) where 10Å-phase contained considerable aluminium at >0.7 a.f.p.u. Al. A probable explanation for Al-rich 10Å phase would be a mixed-layer structure, with chlorite accommodating talc or another phyllosilicate in the interlayers of the crystal (Fumagalli and Poli, 2005; Dvir *et al.*, 2011), or by other exchange mechanisms, such as a di-tri-octahedral exchange (Fumagalli and Poli, 2005) or hydrogarnet substitution (Welch *et al.*, 2006) which suggests that 10Å phase is an Al-free mineral. In the current study, the chemography of the starting mix locates the 10Å-phase, using the Al-free stoichiometry, some distance from the bulk composition indicating that it is unlikely to form in this bulk composition. However, if this phase could accommodate up to 10 wt% Al, then it would be repositioned within the tie-lines connecting grt-ol-opx, increasing the likelihood of its formation. Further investigation of the thermodynamic relationship of these phase relations would be useful.

4.4.8 THE IMPACT OF CA ON CHLORITE STABILITY

The effect on chlorite stability in the MASH system was explored through the addition of Fe and Cr to the bulk composition (see Chapter 3). It was shown that Cr enhanced chlorite stability to both higher pressure and temperature. The presence of Fe, however, reduced the stability field of chlorite to lower temperatures but this effect reduced as pressure increased. At pressures above ~ 4.4 GPa, Fe enhanced chlorite stability to higher pressure.

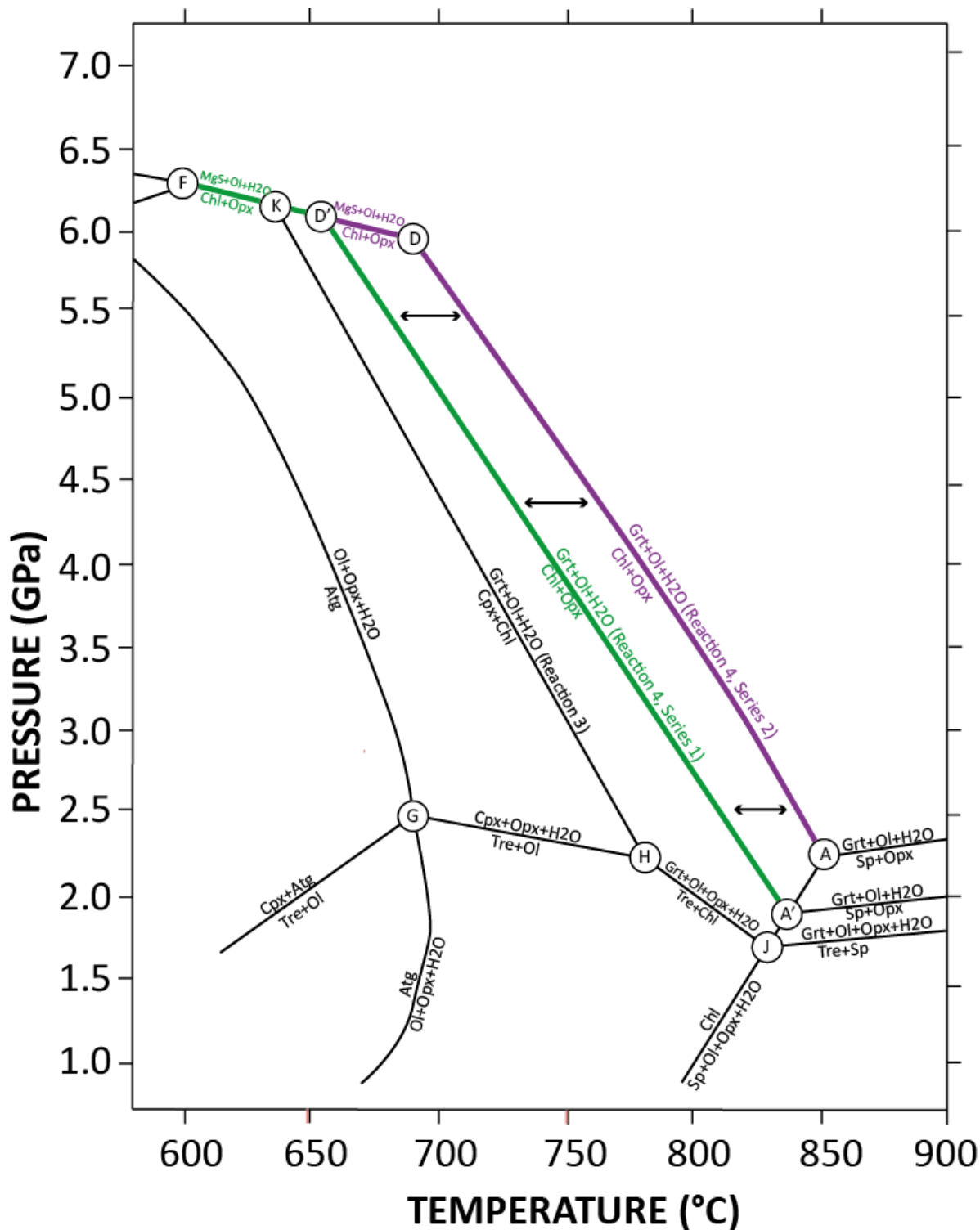


FIGURE 4.15: Reaction 4 curves from Series 1 and Series 2.

Reaction 4 occurred in both chlorite peridotite (green curve, CMASH system) and in chlorite schist (purple curve, MASH system). The difference in P,T location of this reaction in both systems is inferred to be due to the impact of Ca. Phase abbreviations as previously denoted.

Series 2 experiments included a third element in the bulk composition - calcium. What effect, if any, did this additional component have on chlorite stability in the CMASH system? This was readily determined through a direct comparison of experimental results of Reaction 4 from

Series 1 and Series 2. Curves are displayed in Figure 4.15. Results of the comparison are displayed in Table 4.5.

At each selected pressure interval, the thermal stability of chlorite in Series 2 was reduced by 30-40°C compared with Series 1. This was due to the incorporation of Ca into garnet thereby expanding the garnet stability field to lower temperature. In low pressure experiments (2.5 GPa), chlorite breakdown occurred at 840°C in Series 1 compared to 810°C in Series 2. In high pressure experiments (6.0 GPa), chlorite disappeared at 660°C in the Ca-bearing composition against 690°C in the Ca-free system. At intermediate pressures, the space between the reactions widened slightly to >35°C creating a slight bulge.

Experimental series	Ca present	Selected Pressure (GPa)				
		2.5	3.0	4.0	5.0	6.0
Series 1 (Schist)	NO	840	825	780	740	690
Series 2 (Peridotite)	YES	810	790	745	705	660
Effect of Ca addition		30+	35+	35+	35+	30+

TABLE 4.5: Effect of Ca on chlorite stability

There is a consistent temperature reduction at all pressure intervals due to the addition of calcium to the chemical system. Abbreviations: L17=Lakey 2017, the current study.

Few studies have been undertaken examining the chemical relationship between chlorite and Ca-bearing phases. Jenkins (Jenkins, 1981) was the first to examine reactions between chlorite and Ca-amphibole up to 1.5 GPa, concluding that chlorite stability was indifferent to the presence of calcium. In contrast, Fumagalli and Poli (Fumagalli and Poli, 2005) found that the stability field of chlorite was increased to lower temperature when reacted with clinopyroxene, results which concur with the current study. Presumably, the conflicting results are due to differences in phase relations or to the difficulties with pressure calibration.

4.4.9 DELINEATION OF REACTION 3 AND REACTION 4

This is the first experimental study to examine Reactions 3 and 4 in the same study. Each curve has been examined separately but how close are they in P,T space? What is their importance to the stability of chlorite peridotite?

Previous studies have suggested that both reactions were close in P/T space (Ulmer and Trommsdorff, 1999; Pawley, 2003; Fumagalli *et al.*, 2014) and this was confirmed by this study as displayed in Figure 4.16.

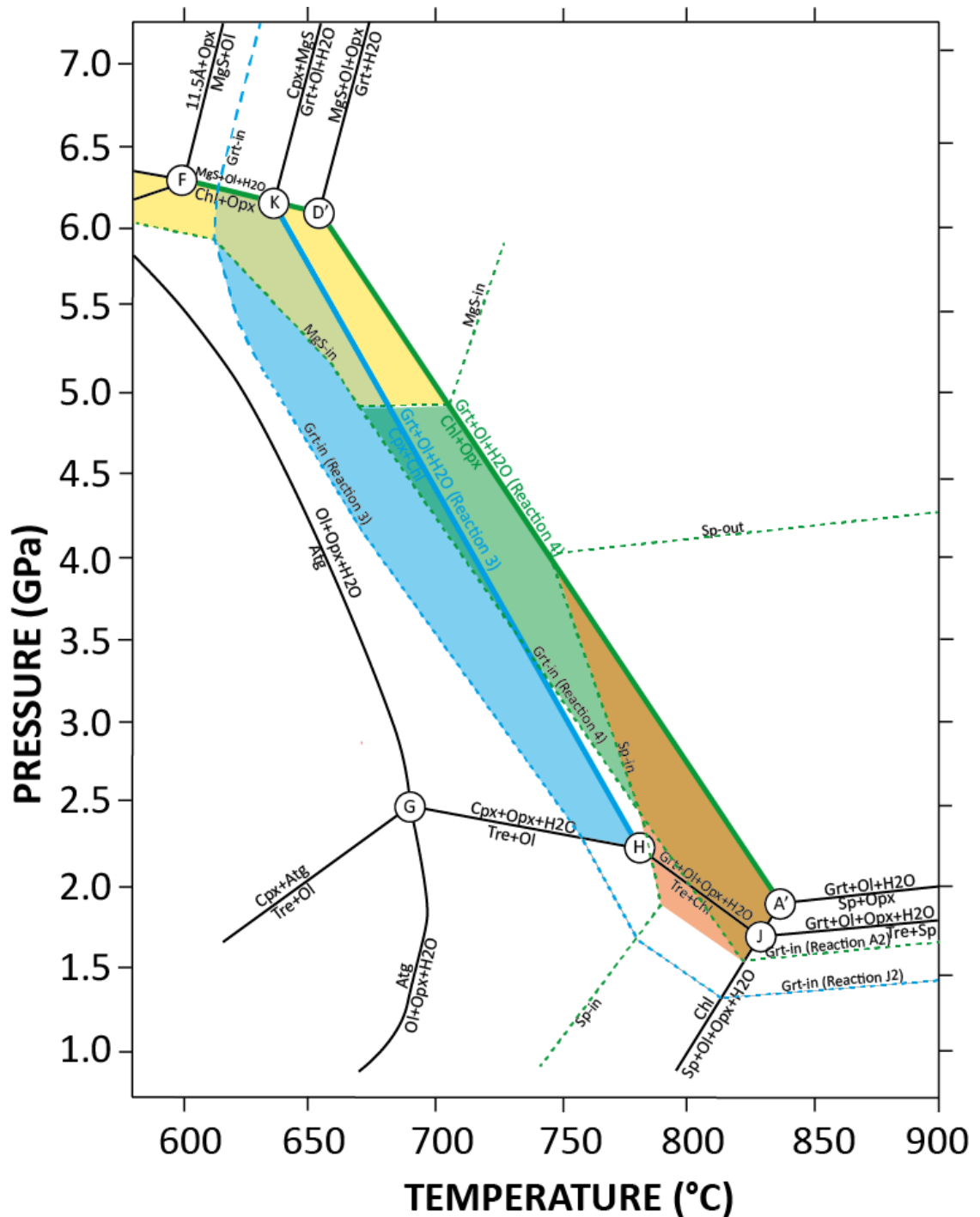


FIGURE 4.16: Arrangement of divariant fields in Reactions 3 and 4

Solid solution led to the creation of a complex arrangement of divariant fields. The garnet divariant field formed by Reaction 3 is shown in blue. Reaction 4 involved three divariant fields: a garnet field (green), an MgS field (yellow) and an associated spinel field (orange). As can be seen, several of these fields overlap.

The maximum thermal stability of chlorite peridotite at low pressure was found at different P,T locations: fertile lherzolite, determined by Reaction 3, terminated at Invariant Point H near 2.3 GPa, 780°C. Depleted harzburgite, denoted by Reaction 4, terminated at Invariant Point A' near 1.9 GPa, 835°C. With increasing pressure, the chlorite-out boundary for each reaction underwent gradual convergence. At 2.5 GPa, they were separated by ~45°C. At 4.0 GPa, the

temperature range had reduced to $\sim 30^{\circ}\text{C}$. At 4.9 GPa, where MgS first appeared, the curves were separated by only 20°C . By Invariant Point D at 6.1 GPa, 655°C , the curves were separated by $<20^{\circ}\text{C}$. They converged at Invariant Point K at 6.2 GPa, 635°C .

Due to Mg-Fe and Al-Cr solid solution, each reaction created several divariant fields, the width of which varied with pressure and phases involved. The result was a complex arrangement of divariant fields, many of which overlapped. A single narrow region was identified where true separation existed between Reactions 3 and 4 which revealed a small temperature interval between 2.3 GPa and 3.4 GPa. At higher pressure, divariant boundaries intersected. With garnet being a product phase in each key reaction, combined with their proximity, clear delineation of divariant fields accompanying each reaction was unable to be constrained experimentally in this series. The location of boundaries marked here have been informed by the change in garnet composition of garnet rims.

The appearance of garnet marked the commencement of Reaction 3 (Figure 4.16, blue region). The width of the divariant field increased with pressure. At the low-pressure termination of this reaction, the width of the grt+cpx field was $\sim 30^{\circ}\text{C}$. At 4.0 GPa, this had increased to $\sim 40^{\circ}\text{C}$, and to 50°C by 5.0 GPa. Between 5.0 GPa and Invariant Point K, the width of this field began to reduce such that it was only 20°C wide at its high-pressure termination.

Reaction 4 also commenced with the appearance of garnet (Figure 4.16, green region). At the low-pressure termination of this reaction, the garnet field extended to around 35°C wide. The width of this field remained consistent to 4.9 GPa, when MgS made an abrupt appearance and began to replace garnet as the stable Al-phase at high pressure. At pressures above 4.9 GPa, the MgS divariant field (Figure 4.16, yellow region) encompassed a 40°C temperature interval which widened with increasing pressure to $>60^{\circ}\text{C}$ at 6.2 GPa. The MgS phase had an extended stability field in Series 2 compared with that reported in Chapter 3, almost certainly due to the presence of calcium. Like garnet, Mg-sursassite can accommodate calcium, which enables the stability field to be increased to lower pressure and temperature.

The presence of spinel (Figure 4.16, orange region) indicated that the garnet-spinel transition had moved to higher pressure due to the addition of Cr. Whilst not a product phase of Reaction 4, this phase was only present in run products of this reaction hence its inclusion here. At Invariant Point A', this created a field $\sim 50^{\circ}\text{C}$ wide. With increasing pressure, this field narrowed consistently to zero at 4.0 GPa which marked the maximum stability of spinel.

These results show that Reaction 4 played a significantly more important role in chlorite peridotite than Reaction 3. The formation of MgS, a hydrous mineral formed contiguously with chlorite disappearance at high pressure, enabled water, which would otherwise have been

released as free water with chlorite breakdown, to be sequestered to much higher pressures. This issue will be covered later in the discussion.

Reactions 3 and 4 were found to be proximal in P,T space, separated by some 45°C at low pressure and converging by 6.2 GPa. However, the complex arrangement of divariant fields associated with both reactions show that in natural systems, at sub-arc depths, Reactions 3 and 4 cannot be neatly separated in high-pressure P,T space.

4.4.10 CONTRASTING PATTERNS OF CR-AL PARTITIONING

A comparison of experimental results from Series 1 and Series 2 revealed contrasting patterns in the partitioning of chromium and aluminium.

Series 1 experiments in a chlorite schist composition showed that Cr-Al partitioning displayed no correlation when plotted against temperature and pressure (see 3.2.6). This contrasted significantly with the experimental results from the current Series 2 in a chlorite peridotite composition. Here, Cr-Al partitioning between spinel and garnet revealed a significant positive association with increasing pressure and a moderate positive association with increasing temperature (see 4.3.5). The explanation for this marked difference was related to the different chemical reactions involved in each series. In the current series, the spinel stability field was extended to ~4.0 GPa whereas in Series 1, it was extended further to ~5.7 GPa. However, the field extension was not a determining factor in the change to Cr-Al partitioning. Instead, it concerned the key reactions involved.

In the current Series 2, chlorite disappeared according to Reaction 4, namely $\text{chl} + \text{opx} = \text{ol} + \text{grt} + \text{H}_2\text{O}$ which occurred between 1.9 GPa and 6.2 GPa. Spinel was not a product phase of this reaction. The presence of spinel up to 4.0 GPa was as a result of Reaction A2, namely $\text{sp} + \text{opx} = \text{grt} + \text{ol} + \text{H}_2\text{O}$ which commenced ~2.0 GPa and, due to spinel-garnet solid-solution, continued up-pressure to 4.0 GPa where the upper boundary of spinel stability was attained. Cr-Al partitioning between spinel and garnet accorded with previous studies (O'Neill, 1981; Brey *et al.*, 1990; Zibera *et al.*, 2013; Fumagalli *et al.*, 2014) with spinel partitioning greater quantities of Cr with increasing pressure, as shown in Figure 4.10b.

In Series 1, however, chlorite disappeared according to the terminal chlorite Reaction 2/A1, namely: $\text{chl} = \text{grt} + \text{ol} + \text{sp} + \text{H}_2\text{O}$ between 2.3 GPa and 5.7 GPa. In this case, spinel was a reaction product, but it marked a predominantly thermal stability boundary and Cr-Al partitioning between newly-formed spinel and garnet was unaffected by change in temperature, as shown in Figure 3.12b.

X_{Cr} spinel and garnet vs pressure

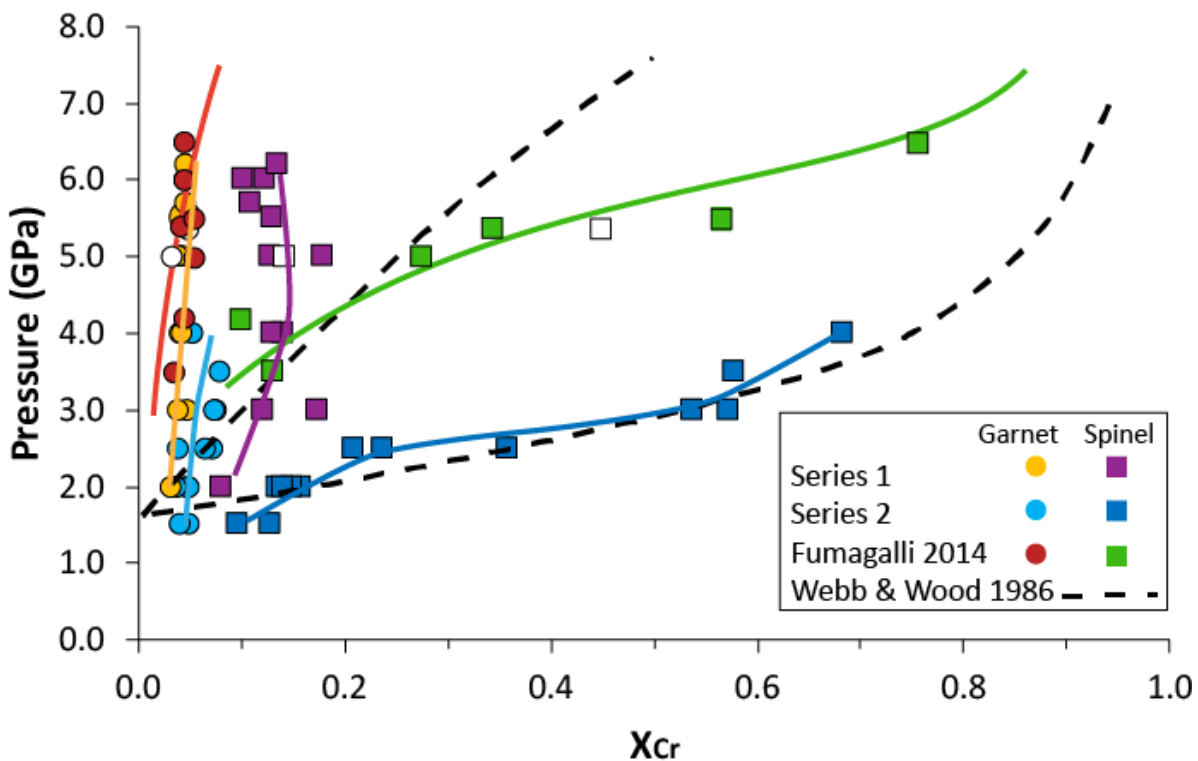


FIGURE 4.17: X_{Cr} in garnet and spinel vs pressure

Plot showing X_{Cr} in garnet and spinel vs pressure from three experimental studies: the current study (Series 1 and Series 2) and Fumagalli (Fumagalli *et al.*, 2014). The black dotted line marks the solid-solution boundaries between garnet and spinel at high temperature after Webb and Wood (Webb and Wood, 1986). The experimental results from Series 2 (chlorite peridotite) show a widening gap between garnet and spinel as pressure increases. This trend shows excellent agreement with results of both Fumagalli and Webb and Wood (Webb and Wood, 1986; Fumagalli *et al.*, 2014). However, the results from Series 1 (chlorite schist) show a narrow gap between garnet and spinel with increasing pressure with the X_{Cr} values in both phases remaining relatively constant.

A similar contrasting pattern was observed when the concentration of chromium in co-existing spinel and garnet from three studies was plotted against pressure, as shown in Figure 4.17.

Results from Series 2 showed the gap in X_{Cr} values between garnet and spinel widened persistently as pressure increased, predominantly due to change in spinel composition. Garnet values remained consistent: ~0.05 at 1.5 GPa and at 4.0 GPa whilst those of spinel rose from ~0.13 at 1.5 GPa to ~0.68 at 4.0 GPa.

Series 2 results showed excellent agreement with the general trend reported by Fumagalli (Fumagalli *et al.*, 2014) where X_{Cr} values of garnet rose only slightly with increased pressure whilst those of spinel rose considerably across the same pressure interval. However, whilst Fumagalli's experiments were conducted at a similar pressure range to Series 2, they were conducted at higher temperatures (>100°C) and with composition greatly enriched in Cr compared to Series 2 which displaced the spinel boundary to higher pressure. Using

experiments conducted at 3.5 GPa as a comparison point, Fumagalli reported $X_{Cr}^{grt} \sim 0.05$ and $X_{Cr}^{sp} \sim 0.15$ (3.5 GPa, 900°C) whilst in Series 2 (3.5 GPa, 770°C) $X_{Cr}^{grt} = 0.08$ and $X_{Cr}^{sp} = 0.58$.

Series 1 results displayed little similarity with results of either Series 2 in the current study or with those of Fumagalli and stood in stark contrast. In Series 1, X_{Cr} values showed a narrow gap as pressure increased. Garnet varied little with increasing pressure across the series, increasing from ~ 0.03 at 2.0 GPa to 0.05 at 6.2 GPa whereas spinel values ranged from ~ 0.08 at 2.0 GPa to ~ 0.14 at 6.2 GPa with a high value of 0.18 at 5.0 GPa.

4.4.11 IMPLICATIONS FOR BOUND WATER IN CHLORITE PERIDOTITE

Previous studies report that fertile lherzolites could comprise between 16 wt% (Schmidt and Poli, 1998) and 23 wt% (Tatsumi, 1989) chlorite whilst depleted harzburgites could contain up to 8 wt% chlorite (Schmidt and Poli, 1998; Till *et al.*, 2012). However, the quantity of chlorite that can exist in any part of a subduction zone is dependent upon P,T conditions and the phase relations that occur at those conditions. This study has demonstrated that chlorite is stable to pressures >6.3 GPa with ~ 1.0 wt% water sequestered in the hydrous MgS phase. This is a considerable increase in the previously reported chlorite stability field. Consequently, chloritized peridotite should comprise a larger proportion of mantle rocks to depth and this will have implications for water release and availability in the sub-arc. This section examines three related issues concerning chlorite peridotite: P,T conditions governing water release, estimate volume of water released upon breakdown, and the temperature profile of the subducting slab in contact with mantle rocks.

4.4.11.1 Release of bound water in chlorite peridotite

The breakdown of chlorite in chlorite peridotite was controlled by two key reactions. At all pressure intervals, the Reaction 3 yielded the anhydrous products grt+ol and the release of all water over a narrow temperature interval. At low pressure, Reaction 4 also produced an anhydrous assemblage and a water release; at high pressure, however, an additional hydrous phase MgS formed at high pressure which sequestered nearly 1 % of the water originally contained in chlorite.

Figures 4.18a and 4.18b show the pattern of water release at 3.0 GPa and 6.0 GPa respectively. At 3.0 GPa, a total of 10.14 wt% water was released over an 80°C interval between 720°C and 800°C. Due to the proximity of Reactions 3 and 4, this likely occurred as a continuous release over this temperature interval. The chl+cpx reaction occurred over $\sim 30^\circ\text{C}$ (720°C-750°C) and yielded between 0.7 wt% and 2.7 wt% water. The chl+opx reaction occurred over a narrower

20°C interval between 770°C and 790°C and delivered between 7.4 wt% and 9.4 wt% water. Precise estimations of water release from each reaction was not able to be determined experimentally due to the proximity of both reactions. After 800°C, no hydrous minerals were present.

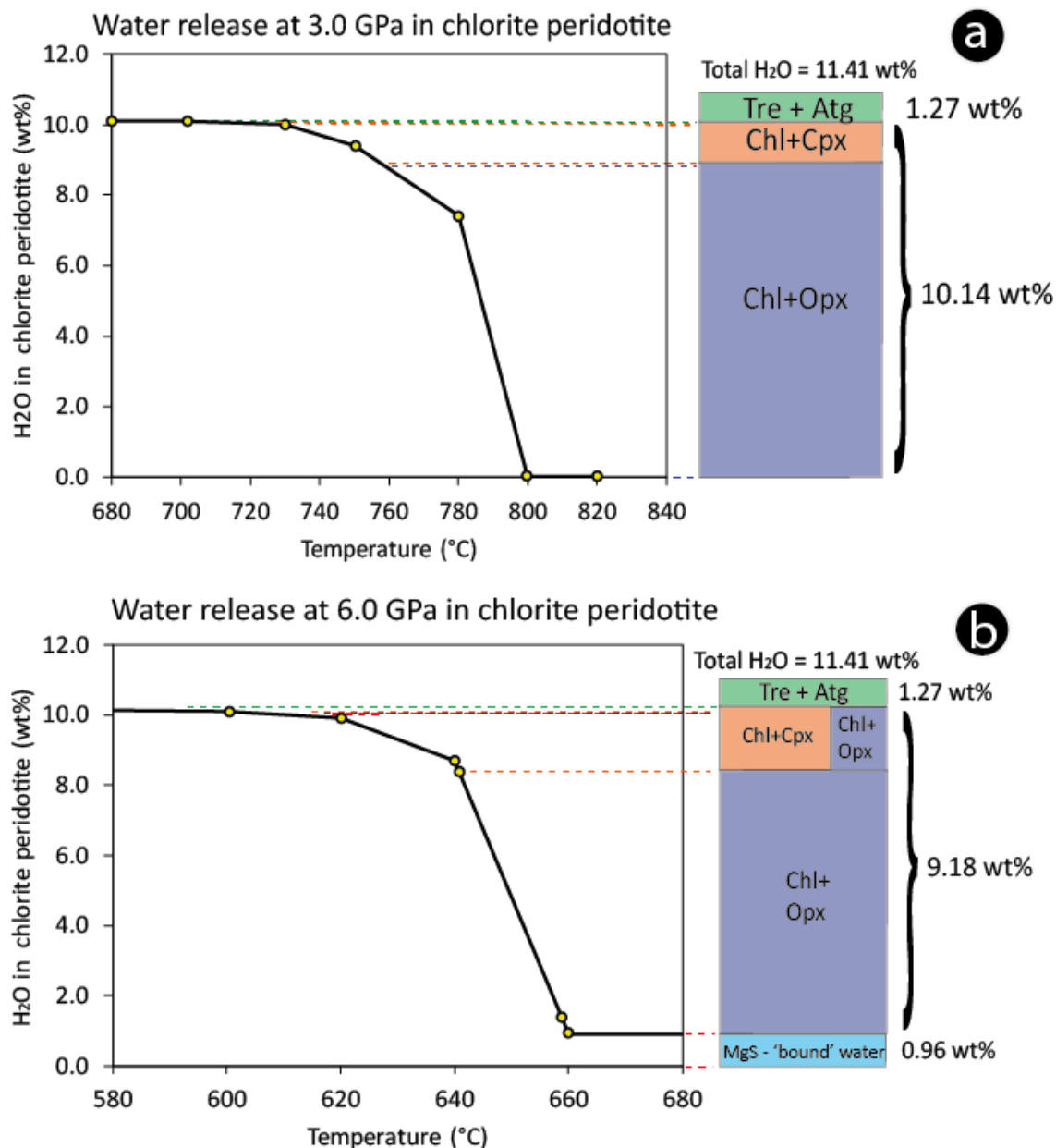


FIGURE 4.18: Release of water from hydrous phases in chlorite peridotite.

a) Quantity of water released at temperature intervals at 3.0 GPa. Note that Reaction 3 releases less water than the does Reaction 4. Chlorite breakdown according to Reaction 4 occurs over a ~40°C interval. **b)** Quantity of water released in temperature intervals at 6.0 GPa. Chlorite breakdown releases water over a narrow ~40°C interval. However, nearly 10 wt% of its water remains sequestered in the MgS phase, which itself remains stable to temperatures beyond this study.

At 6.0 GPa, water release of 9.18 wt% occurred over a slightly narrower temperature interval between 590°C and 650°C. Both reactions occurred in the same P,T space. The chl+cpx reaction contributed <2.7 wt% water between 610°C and 640°C. Reaction 4 occurred over the full

temperature interval at this pressure and released <9.8 wt% water. Whilst the maximum thermal stability of chlorite was near 650°C at 6.0 GPa, the hydrous MgS phase appeared as a breakdown product from Reaction 4 which, importantly, retained ~0.96 wt% water. Previous research indicates MgS would be stable to near 750°C at this pressure (Bromiley and Pawley, 2002) raising the prospect that MgS could be subducted to pressures beyond the sub-arc.

Patterns of water release in Figure 4.18 show a semi, stepwise progression (Padron-Navarta *et al.*, 2013) as each reaction is encountered with increasing temperature, hydrous phases release water over a narrow temperature interval which has implications for subduction metasomatism.

4.4.11.2 Slab surface and mantle wedge temperature and its impact on chlorite stability

The temperature at the surface of a descending slab ultimately determines the stability of any hydrous minerals in contact with its surface; that is, those minerals which have formed on the slab itself, in the subduction channel, or are present on the hanging wall of the overlying mantle. Several geophysical models have estimated the thermal profile of the descending slab using data determined from across the earth sciences. One data component concerns the P,T stability of mineral phases: the more accurate their determination, the better the model. This study has shown that chlorite is stable to much higher pressures and temperatures than previously thought, and importantly, its thermal breakdown leads to the formation of Mg-sursassite. This hydrous mineral retains 1.0 wt% water from chlorite, is stable to much higher pressure than chlorite and so can act as a vehicle for the transportation of water to beyond sub-arc depths. This new experimentally-determined chlorite data can be used to improve the accuracy of subduction zone geophysical models.

Figure 4.19 illustrates the P-T path taken by cooler slabs during subduction based on two recent geophysical models. The first, shaded purple, is from Arcay (Arcay *et al.*, 2007). The second, shaded in both orange and yellow tones (representing slab surface and internal slab temperatures respectively) is from Syracuse (Syracuse *et al.*, 2010). The grey dashed line, which largely passes through the Arcay model, marks the P-T path of the coolest of modelled subducting slabs, the Tonga slab. The choice of these models was justified in Chapter 3. The upper thermal stability of chlorite lherzolite (Reaction 3) is marked in light blue, and chlorite harzburgite (Reaction 4) in green. The green dotted line shows the extent of the MgS stability field which was only produced from Reaction 4 and therefore becomes the focus of this section.

The Arcay model indicates that slab surface temperatures (SST) encompass a maximum thermal range of ~150°C. At 4.9 GPa, the range expected is between ~630°C and ~760°C. The current study indicated that the breakdown of chlorite and formation of MgS via Reaction 4 commenced

at 4.9 GPa near 710°C. Therefore, these experimental results are considered representative of SST's modelled by Arcay, and so supports the feasibility of MgS maintaining stability to mantle depths.

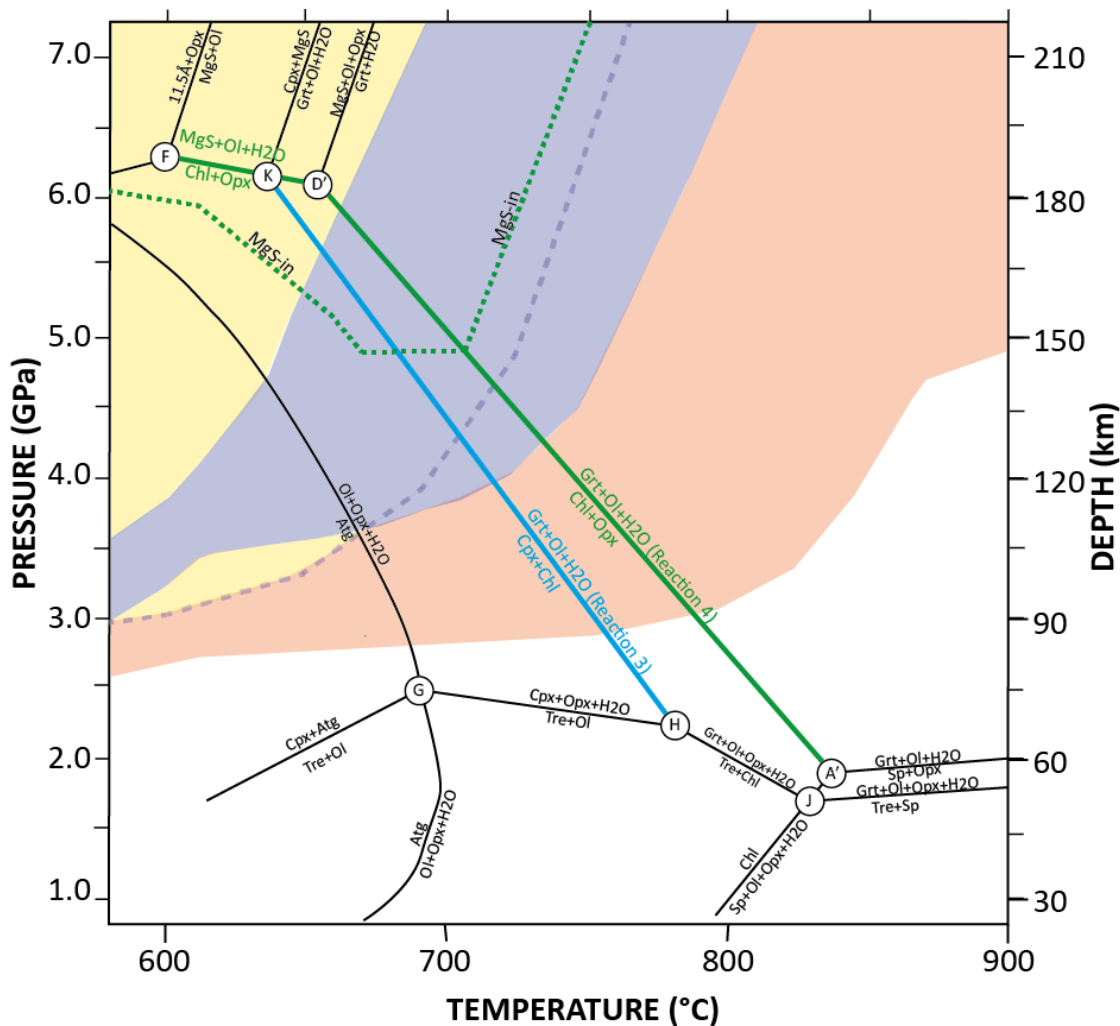


FIGURE 4.19: Model slab surface temperatures (SST) compared to Reactions 3 and 4.

Stability fields of Reactions 3 and 4 are compared with two recent geophysical models: Arcay (Arcay et al., 2007), shown in purple, and Syracuse (Syracuse et al., 2010) shown in orange and yellow. The grey, dashed line marks the P-T path of the Tonga slab, the coolest of all subducting slabs, also from Syracuse. Stability field of MgS is shown as green dotted line. Stability fields of other key chlorite reactions (black) from current study. These results show that at the slab surface, chlorite breakdown would be complete with all water released to the sub-arc. In contrast, within the slab, chlorite and MgS would remain stable thereby transporting bound water to the deep mantle.

When curves for Reactions 3 and 4 were compared to the Syracuse model (Figure 4.19, orange region), it was apparent that beyond 4.6 GPa, the point where the Tonga slab surface temperature (SST) intersected the chlorite breakdown reaction, the SST would be too hot for chlorite to survive. According to their D80 model, the fast subduction rate of the Tonga slab meant that its P-T path did not intersect the MgS stability field, exceeding it by some 0.4 GPa and 20°C. This means chlorite would breakdown entirely, releasing its water prior to the formation of MgS. However, this model is based on many numerical assumptions, small changes in which can markedly alter the modelled results. The D80 model produced a wide temperature

variation in predicted slab surface temperatures - from 24°C to 397°C at 30km depth and 850°C to 1141°C at 240 kms depth. Other thermal models report similar temperature variations (Cooper *et al.*, 2012; Penniston-Dorland *et al.*, 2015). Therefore, small variations in pressure and temperature between these experimental results and estimates from the D80 model does not diminish the feasibility of a cooler subducting slab, such as Tonga, being able to intersect the MgS stability field enabling the carriage of water to the deep mantle.

The D80 model incorporated an extensive temperature range: the model estimated the SST at 240 kms as well as the minimum SST at the same depth (Syracuse *et al.*, 2010, p.78). In the case of the Tonga plate, this created a temperature range of 871°C to 265°C respectively. Since the interior of the slab is considerably cooler than its surface, the minimum SST in the D80 model could easily be considered a proxy for the temperature of the slab interior, which is what has occurred here. This is shown in Figure 4.19 in yellow.

The experimental results of Reactions 3 and 4 showed they are representative of interior slab temperatures. At pressures between 4.6 GPa and 4.9 GPa, chlorite would remain stable, and at any pressure above 4.9 GPa, MgS would remain within its stability field. This indicates that water would remain sequestered in chlorite and/or MgS beyond the sub-arc to mantle depths.

4.4.11.3 Estimation of free water contribution from chlorite peridotite

Figure 4.20 shows the pathway taken by subducting slabs of various temperatures according to their rate of descent. This affects the depth at which hydrous minerals break down. The yellow, orange and purple regions refer to slab temperatures by geophysical models. Reaction 3 is shown in light blue; the green shades refer to Reaction 4.

Pathway 1 tracks a typical route taken by a slab which exhibits a comparatively moderate to hot surface temperature profile. Most subduction zones fit this profile. This pathway would apply equally to either Reaction 3 or 4 since the descending slab would cross the maximum thermal stability of either reaction curves at any point below 4.9 GPa. At the crossing point, all 10.1 wt% water would be released over a small temperature interval and it would remain entirely within the sub-arc.

Pathway 2 would apply to a slab with a much cooler surface thermal profile indicative of rapid descent during subduction. Existing geophysical models suggest that few slabs possess such a low temperature surface profile - a handful in the Pacific including Tonga are closest – but numerous slabs have internal slab temperature profiles in agreement with geophysical models. At any crossing point above 4.9 GPa, 710°C, the slab would enter a small divariant stability field where chlorite and Mg-sursassite co-exist in accordance with reaction K2/D6 discussed

previously. This reaction would lead to the release of ~1.4 wt% water over a small temperature interval with the remaining 8.7 wt% bound in the hydrous phases chlorite and MgS. With a temperature increase of ~50°C, Reaction 4 reaches maximum thermal stability whereby chlorite would disappear and lead to the release of 7.8 wt% of the water bound in chlorite and 0.9 wt% water retained MgS. This equates to a slightly broader temperature band over which water is released.

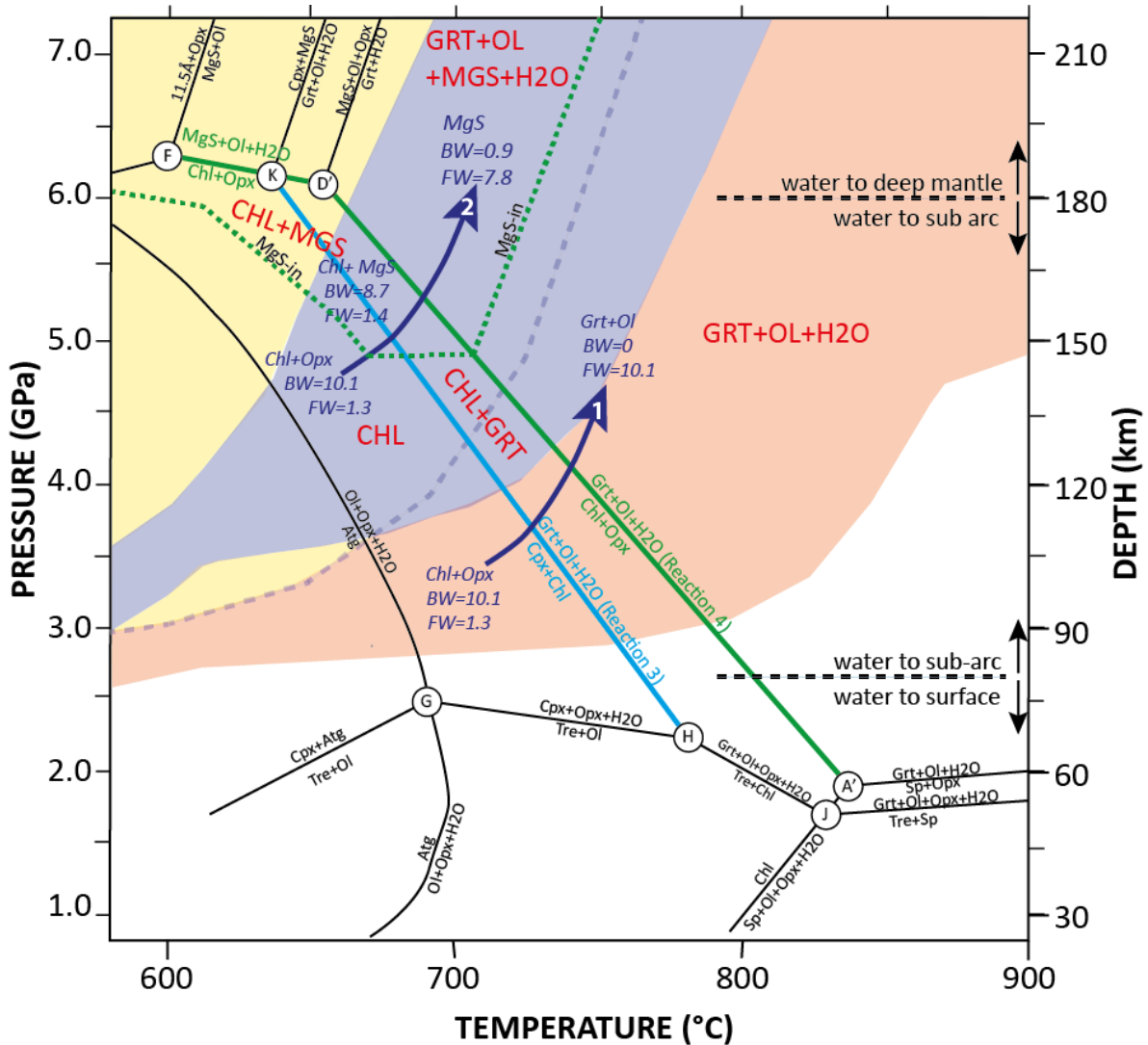


FIGURE 4.20: Estimated water liberation from chlorite peridotite along three P,T paths

Two P-T paths represent the different phase products following chlorite Breakdown. Below 4.9 GPa, Reactions 3 and 4 (blue and green lines and text respectively) release all water when maximum thermal stability is reached. This is shown by Pathway 1. Above 4.9 GPa, however, chlorite breakdown along Reaction 4 produces the hydrous MgS. This creates a small region where chl and MgS co-exist, and then an MgS only region following chl disappearance. This is shown by Pathway 2 and results in a slower release of water. Stability fields marked in red text. Assumptions on water budget and phase relations after Schmidt and Poli (Schmidt and Poli, 1998, 2014).

This study has identified an increased stability field of chlorite which has important implications regarding water in the subduction zone.

In the subduction zone, chlorite formation is made possible due to the provision of water from the dehydration of antigorite. As antigorite exceeds its maximum thermal stability, it dehydrates, releasing all its water over a small temperature interval. As this water contacts peridotite, some will be incorporated into newly-formed chlorite. The remainder rises as free water through the sub-arc and no longer plays a role in deeper subduction zone dynamics.

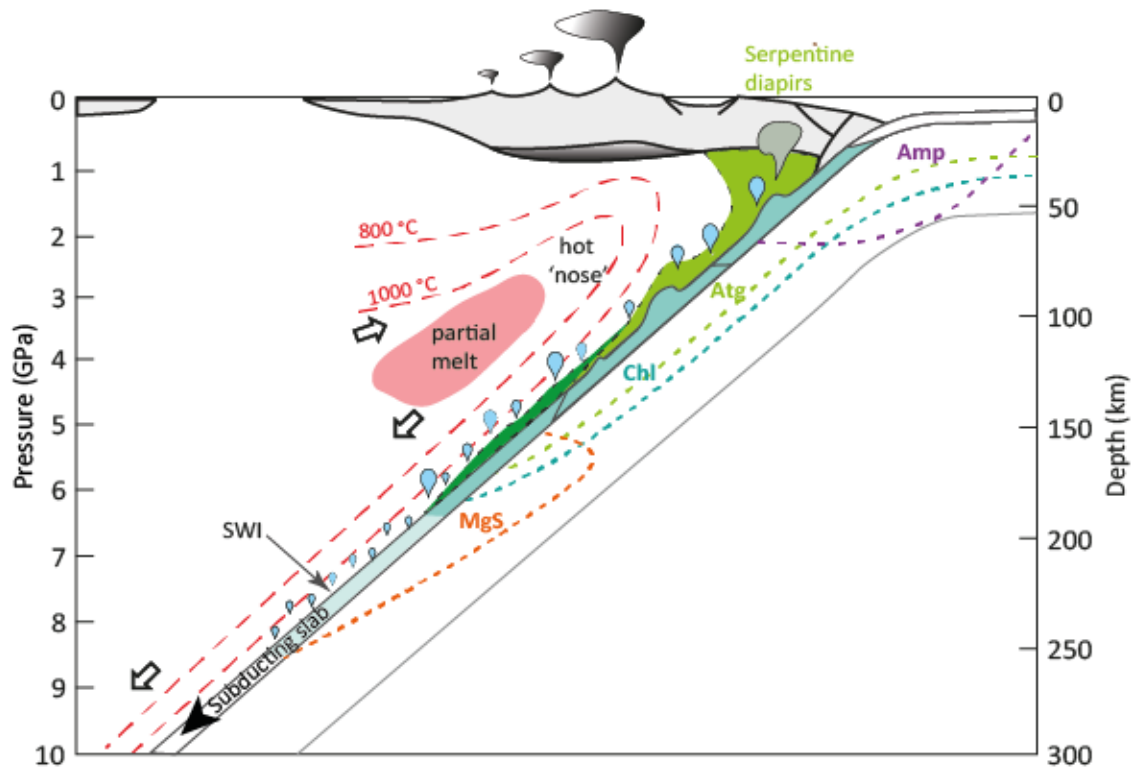


FIGURE 4.21: Subduction zone profile showing stability of ultramafic hydrous minerals.

Cartoon adapted from Schmidt and Poli (Schmidt and Poli, 2014) which shows a vertical profile of a subduction zone. The area of the slab shaded turquoise indicates the stability field of hydrous minerals found in chlorite peridotite. Coloured dotted lines marked below the slab represent the stability field of each hydrous mineral. The narrow region above the slab shaded mid-green and light-green indicate the area of mantle wedge peridotite which has been chloritised and serpentinitised respectively following fluid release from the descending slab. Large black arrows indicate the direction of advected mantle flow following slab-mantle coupling. The results of this study show that, in cooler subduction zones, chlorite and MgS are stable hydrous minerals to nearly 200 kms depth which greatly affects the release rate and distribution of free water in the subduction zone. "SWI"=Slab-wedge interface.

This study showed that chlorite possesses a larger stability field than previously recognised: its maximum pressure stability increased from ~5.0 GPa to ~6.3 GPa. In this region, chlorite would form and remain stable for a further 40 kms deeper in the subduction zone than previously thought. This is shown graphically in Figure 4.21. A fertile lherzolite is estimated to produce 16.4 wt% chlorite (containing 2.1 wt% water) and a depleted harzburgite up to 8.2 wt% chlorite (comprising 1.06 wt% water) (Schmidt and Poli, 1998). It follows then, that in this pressure interval, as antigorite undergoes dehydration, some 43 % of the water released would be sequestered into newly-formed chlorite lherzolite, and around 22 % water would be incorporated into chlorite harzburgite. Therefore, between one quarter and one half of the

water released during the antigorite terminal reaction, previously thought to be 'free', is bound in chlorite-rich rocks at 150 kms and 190 kms depth in the subduction channel. This is a significant reduction in the quantity of free water thought to be present in the sub-arc.

At depths below 190 kms, chlorite breakdown leads to the storage of around 9.5 wt% of its original water content in the MgS phase. This equates to 1.5 wt% water retained in chlorite lherzolite and 0.8 wt% water in a chlorite harzburgite. MgS is stable to at least 10 GPa, 800°C (Fockenberg, 1998; Bromiley and Pawley, 2002; Wunder and Gottschalk, 2002) which provides a significant volume of water available for transportation to the deep mantle.

These results bring into question two prevailing views about the importance of chlorite in the subduction zone (Schmidt and Poli, 2014).

The first concerns antigorite as the main hydrous mineral in the subduction zone. It is contended that the high-pressure stability curve for chlorite crosses that of antigorite near 4.8 GPa, rendering chlorite of less importance as a purveyor of water beyond 140 kms in the sub-arc. This study has shown that chlorite is stable to considerably higher pressure and in fact never crosses the antigorite-out curve at any point. The thermal stability of chlorite is also greater by >80°C. This provides compelling evidence that chlorite, in fact, should be considered the most important mineral in the subduction zone.

The second point concerns the place of the 10Å-phase. It has been proposed that the 10Å-phase replaces chlorite as the stable Al-bearing phase in peridotites at pressure above 4.8 GPa. This study and others (Fumagalli *et al.*, 2014; Spandler *et al.*, 2014) failed to identify this phase in experiments using peridotite compositions. Instead, chlorite has been shown to fill most of the P,T space thought to be occupied by the 10Å-phase.

An interesting observation concerns the comparison of the MgS stability field with the 10Å-phase as shown in Figure 4.21. Both fields show a high level of congruence which may signal a possible relationship. This warrants further investigation. This study has highlighted the importance of MgS as a hydrous mineral in peridotite compositions as it forms congruently following chlorite breakdown and is thus able to sequester large quantities of water to mantle depths.

4.4.11.4 Extension to the hydrous-anhydrous boundary

The results of the current study provide justification for the realignment of the hydrous-anhydrous boundary up-temperature to the new experimentally-determined thermal boundary of hydrous minerals relevant to chlorite peridotite. This is represented graphically in Figure 4.22.

temperature 'anhydrous nose' and the commencement of the MgS stability field. With increasing pressure, the thermal displacement of the hydrous-anhydrous boundary continues to increase. At 6.2 GPa, the revised boundary is situated near 730°C compared with 580°C (1998) and 670°C (2014). At 7.0 GPa, the results of this study infer a 70°C increase in the hydrous-anhydrous boundary compared to previous measures.

Whilst the thermal increase is not enormous, the up-temperature boundary shift increases the number of slabs with low SSTs able to transport chlorite and MgS to depths beyond the sub-arc before liberating water, which raises the importance of both hydrous minerals in subduction zones.

4.5 CONCLUSIONS AND IMPLICATIONS

This experimental series established new data on chlorite stability at high pressure. At low pressure, chlorite stability was determined by the model reactions:

Reaction 3: chlorite + clinopyroxene → garnet + olivine + H₂O

Reaction 4: chlorite + orthopyroxene → garnet + olivine + H₂O

For Reaction 3, increased pressure did not affect reaction products. However, above 4.9 GPa, in Reaction 4, MgS began to replace garnet as the stable Al-bearing phase at high pressure which enabled ~1 wt% water to be sequestered in this hydrous phase which is stable to at least 10 GPa, 800°C. Therefore, Reaction 4 is more important in relation to the stability of chlorite peridotite.

The maximum thermal stability curve for Reaction 3 and Reaction 4 each exhibited a steep, negative Clapeyron slope which contrasted with all previous experimental studies. At 2.5 GPa, the curves were separated in P,T space by ~45°C, with Reaction 3 at the lower temperature, but with increasing pressure they gradually converged until finally meeting at 6.2 GPa, 635°C. After this invariant point, the upper phase boundary underwent a sharp backbend to lower temperature, and although the upper boundary remains to be fully constrained, the chlorite stability field is shown to be greatly expanded to higher pressure. The addition of calcium to the bulk composition was shown to lower the chlorite stability field by a consistent 35°C. Even so, the net impact was that the curves for Reaction 3 and Reaction 4 moved to slightly higher temperatures compared to previous research which necessitated an adjustment to the anhydrous boundary by up to 70°C.

These experimental findings have important implications for water transport in the subduction zone. The increased chlorite stability field signifies that chlorite is stable to 190 kms depth, some 40 km deeper than determined by previous investigations. Geophysical modelling suggests that

chlorite peridotite could remain stable in cooler subduction environments. This means that the release of water from chlorite into the sub-arc would be delayed and would occur at greater depth which would impact models which depend upon water being released at shallower levels. Chlorite breakdown reactions at all pressures releases water over a narrow temperature interval but the results of this study indicate that the width of this interval increases slightly with increased pressure - from 30°C to 40°C. The water contribution from Reaction 3 is less than for Reaction 4. Significantly, around 10 wt% of the water contained in chlorite following Reaction 4 is retained in the hydrous MgS phase. With its stability to pressures beyond the sub-arc, it is entirely feasible that MgS could act as a transport vehicle for bound water to the deep mantle.

CHAPTER 5: THE STABILITY OF MAFIC CHLORITE SCHISTS AT SUB-ARC PRESSURES – IMPLICATIONS FOR SLAB DIAPIRS AND MANTLE MELTING

5.1. INTRODUCTION

Subduction zone mélanges contain chlorites of varied composition, but our knowledge of their stability fields extends little beyond that of the end-member clinocllore. To enhance our understanding of the numerous fluid processes and mechanisms in subduction settings, an investigation of mafic chlorites, in addition to the Mg-rich chlorites already studied, is essential. In this chapter, the stability of chlorite at sub-arc pressures will be explored over a more extensive range of temperatures than in previous chapters. To ascertain the maximum thermal stability field of mafic chlorite, experiments will be conducted at lower temperatures using a variety of chlorite compositions exhibiting differing Mg#. Conversely, to determine the temperature at which chlorite begins to melt, the same high Mg# chlorite can be used as in the previous chapter. These results will shed new light upon two issues: whether the mélange diapir model is feasible as a unifying, conceptual model to explain the source of arc magmas, and the intractable debate over the location of the wet peridotite solidus.

This experimental series aimed to determine chlorite stability at sub-arc conditions using three contrasting bulk compositions. To facilitate a stability study of Fe-rich chlorites, two samples were selected: SY3 (Mg#=0.50) and SY4 (Mg#=0.68). To establish the melting temperature of high-Mg chlorite, the bulk composition used in Series 2 (Chapter 4) was used (Mg#=0.94). In each instance, only natural rocks were used.

Twenty-two isobaric (3.0 GPa) data points were established, encompassing a temperature range of 500°C to 1150°C. For convenience, starting materials for each experimental set have been described separately in the section 5.2 below.

5.1.1. MÉLANGE DIAPIRS

Geophysical studies have identified regions of low-density instability within a low viscosity channel (Hebert *et al.*, 2009) or subduction channel (Blanco-Quintero *et al.*, 2010) between the subducting plate and the mantle wedge, thought to represent diapiric upwellings (Cloos and Shreve, 1988; Hall and Kincaid, 2001). Diapirs are a well-recognised geological phenomenon

known to transport sediments (Behn *et al.*, 2011; Miller and Behn, 2012; Tsuno and Dasgupta, 2012) and serpentinite (Hyndman and Peacock, 2003; van Keken, 2003; Schuiling, 2011; Deschamps *et al.*, 2013; Bebout and Penniston-Dorland, 2016) as well as salt and mud to the surface. Recent thinking suggests that diapirs could also transport chlorite mélange, formed within the subduction channel, through the mantle wedge to arc volcanoes (Gerya and Yuen, 2003; Gerya *et al.*, 2006; Hebert *et al.*, 2009; Castro *et al.*, 2010; Dilek *et al.*, 2012). If so, this could help to solve the long-standing enigma: how fluids present in arc magmas preserve three different source ‘signatures’ – slab, sediments and mantle.

Marschall and Schumacher (Marschall and Schumacher, 2012) have developed a conceptual model which they claim resolves this problem (see Figure 1.2). Their model proposes that chlorite mélange forms in the subduction channel at pressure below 2.5 GPa where rocks and fluids from all three sources are mixed. A density contrast causes the newly-formed chlorite mélange to rise rapidly upward through the peridotite in the hanging wall of the mantle wedge, creating a tube-like diapiric structure as it ascends. Corner flow drags the chlorite-containing diapir obliquely into the hottest part of the mantle wedge. This incurs partial melting of the outer rocks with the melt acting as a protective sheath around the ascending diapir, shielding the inner rocks from further melting and importantly preventing the escape of fluids from dehydrating chlorite. As the diapir continues its rapid ascent, all rocks eventually melt entirely and become part of an arc magma chamber.

This model has been framed around the behaviour of chlorite in chlorite mélange from Syros, Greece. They claim that chlorite remains stable inside the diapir until it melts. There is no intermediate state where chlorite dehydrates. In this way, the fluid phase is never freed and therefore the ‘slab and sediment signatures’ are preserved. But does chlorite behave in the way described in this model?

5.1.2. THE LOCATION OF THE WET PERIDOTITE SOLIDUS

The source of arc magmas, especially the origin, composition and transport of melt to magma chambers, has an extensive research history. A crucial ingredient in this story is the precise location of the wet peridotite solidus in P,T space for that determines where melt first occurs. Unfortunately, its location has long been a matter of dispute. Whilst there is universal agreement that the introduction of water lowers the melting point of peridotite, there is continued debate as to the temperature at which this occurs.

Experimental work since the 1960s has positioned the wet solidus in peridotite near 1100°C at 3.0 GPa, sub-arc depths (Green, 1973, 1976, 2015; Millhollen *et al.*, 1974; Niida and Green, 1999;

Kessel *et al.*, 2005; Poli *et al.*, 2009). The solidus curve assumes a positive slope to higher temperature with increasing pressure and does show slight variation according to bulk composition. These results represent the dominant view regarding the onset of melt in peridotite.

By contrast, other researchers (Mysen and Boettcher, 1975; Gaetani and Grove, 1998; Grove *et al.*, 2006; Till *et al.*, 2012a) identify the wet peridotite solidus at considerably lower temperature, near 810°C at 3.0 GPa, some 300°C lower. How is this possible?

The debate centres around what constitutes melt, what constitutes quench and the confusion surrounding the very grey areas in-between. Much has been written about quench textures in experiments which involve the partial melt of saturated peridotite. When experiments are quenched, the rapid decrease in both pressure and temperature creates an array of quench textures. But do they represent water vapour or melt? Differentiating the two phases is tricky as vapour quench contains silica, and melt quench contains vapour, with the amount of the other in each increasing with increasing pressure and temperature (Stalder, 2012). At P,T conditions below the second critical end point (SCEP), two fluid phases co-exist – water vapour and melt. At P,T conditions above the SCEP, vapour and melt become indistinguishable (Mibe *et al.*, 2011; Green, 2015). This study aims to add some clarity to this debate.

5.2. STARTING MATERIAL

Detailed methodology used in this experimental series have been outlined in Chapter 2.

Complete FE-SEM analyses of starting mix phases are provided in the Appendix.

5.2.1. DESCRIPTION OF SY3 STARTING MATERIAL

The SY3 experimental set performed nine experiments at 3.0 GPa between 500°C and 740°C. They used chlorite with an Mg# =0.50, part of a sample of omphacite-epidote-chlorite schist sourced from Syros island, part of the Cyclades archipelago in Greece (Miller *et al.*, 2009).

a

Oxide wt%	ALB (n=2)		APA (n=12)		CHL (n=10)		EPI (n=10)		ILM (n=9)		OMP(n=13)		TTN (n=7)		PYR (n=9)	
	Mean	SD														
H ₂ O	0.00	0.00	1.72	0.00	11.02	0.11	1.86	0.02	0.00	0.00	0.00	0.00	0.00	0.00	0.00	0.00
Na ₂ O	11.08	0.09	0.00	0.00	0.05	0.06	0.00	0.00	0.00	0.00	7.97	0.45	0.00	0.00	0.08	0.06
MgO	0.00	0.00	0.00	0.00	14.60	0.94	0.00	0.00	0.09	0.11	5.68	0.43	0.00	0.00	26.75	0.20
Al ₂ O ₃	19.16	0.11	0.10	0.00	18.55	0.18	23.62	0.77	0.00	0.00	7.40	0.63	0.72	0.08	24.42	0.22
SiO ₂	67.99	0.39	0.00	0.00	25.69	0.32	37.36	0.41	0.14	0.11	54.51	0.75	30.23	0.32	43.38	0.29
P ₂ O ₅	0.00	0.00	41.22	0.00	0.00	0.00	0.00	0.00	0.00	0.00	0.00	0.00	0.00	0.00	0.00	0.00
K ₂ O	0.00	0.00	0.00	0.00	0.01	0.02	0.00	0.00	0.00	0.00	0.00	0.00	0.00	0.00	0.00	0.00
CaO	0.04	0.04	52.36	0.00	0.06	0.07	21.87	0.17	0.24	0.14	10.28	0.73	27.57	0.18	0.43	0.02
TiO ₂	0.00	0.00	0.00	0.00	0.06	0.09	0.15	0.08	49.11	0.97	0.09	0.10	38.55	0.14	0.00	0.00
Cr ₂ O ₃	0.00	0.00	0.00	0.00	0.00	0.00	0.00	0.00	0.00	0.00	0.00	0.00	0.00	0.00	0.00	0.00
MnO	0.00	0.00	0.00	0.00	0.14	0.10	0.23	0.04	1.49	0.37	0.09	0.10	0.00	0.00	0.00	0.00
FeO	0.52	0.05	0.70	0.00	26.65	1.37	0.00	0.00	42.02	0.93	5.71	0.27	1.00	0.22	4.08	0.40
NiO	0.00	0.00	0.00	0.00	0.00	0.00	0.00	0.00	0.00	0.00	0.00	0.00	0.00	0.00	0.00	0.00
Fe ₂ O ₃	0.00	0.00	0.00	0.00	0.00	0.00	13.01	0.75	5.23	0.12	7.59	0.36	0.00	0.00	0.00	0.00
Total	98.79	0.58	94.39	0.00	85.80	0.84	98.11	0.93	98.31	0.75	99.32	1.27	98.07	0.53	99.15	0.69
Na	0.95	0.00	0.00	0.00	0.01	0.01	0.00	0.00	0.00	0.00	0.57	0.03	0.00	0.00	0.00	0.00
Mg	0.00	0.00	0.00	0.00	2.37	0.14	0.00	0.00	0.00	0.00	0.31	0.02	0.00	0.00	2.75	0.03
Al	1.00	0.00	0.01	0.00	2.38	0.03	4.49	0.11	0.00	0.00	0.32	0.02	0.03	0.00	1.99	0.01
Si	3.00	0.00	0.00	0.00	2.80	0.01	6.03	0.02	0.00	0.00	2.01	0.01	1.01	0.01	3.00	0.01
P	0.00	0.00	3.05	0.00	0.00	0.00	0.00	0.00	0.00	0.00	0.00	0.00	0.00	0.00	0.00	0.00
K	0.00	0.00	0.00	0.00	0.00	0.00	0.00	0.00	0.00	0.00	0.00	0.00	0.00	0.00	0.00	0.00
Ca	0.00	0.00	4.90	0.00	0.01	0.01	3.78	0.03	0.01	0.00	0.41	0.03	0.98	0.01	0.03	0.00
Ti	0.00	0.00	0.00	0.00	0.00	0.01	0.02	0.01	0.95	0.01	0.00	0.00	0.97	0.01	0.00	0.00
Cr	0.00	0.00	0.00	0.00	0.00	0.00	0.00	0.00	0.00	0.00	0.00	0.00	0.00	0.00	0.00	0.00
Mn	0.00	0.00	0.00	0.00	0.01	0.01	0.03	0.01	0.03	0.01	0.00	0.00	0.00	0.00	0.00	0.00
Fe	0.02	0.00	0.05	0.00	2.43	0.13	0.00	0.00	0.90	0.03	0.18	0.01	0.03	0.01	0.24	0.02
Ni	0.00	0.00	0.00	0.00	0.00	0.00	0.00	0.00	0.00	0.00	0.00	0.00	0.00	0.00	0.00	0.00
Fe ₃	0.00	0.00	0.00	0.00	0.00	0.00	1.58	0.10	0.10	0.00	0.21	0.01	0.00	0.00	0.00	0.00
Total	4.97	0.00	8.02	0.00	10.01	0.01	15.92	0.01	2.00	0.01	4.01	0.01	3.01	0.00	8.01	0.00
Mg#	0.00	0.00	0.00	0.00	0.49	0.03	0.00	0.00	0.00	0.00	0.64	0.02	0.00	0.00	0.92	0.01
Al#	1.00	0.00	1.00	0.00	1.00	0.00	0.74	0.02	0.00	0.00	0.60	0.03	1.00	0.00	0.00	0.00

b

Oxide	wt%
H ₂ O	5.75
Na ₂ O	1.85
MgO	8.30
Al ₂ O ₃	15.63
SiO ₂	35.13
P ₂ O ₅	0.27
K ₂ O	0.02
CaO	7.83
TiO ₂	4.85
MnO	0.20
Fe total	20.17
Total	100.00

c

Phase	wt%
APA	0.6
CHL	47.9
EPI	13.8
ILM	3.8
OMP	22.6
TTN	6.7
GRT	2.4
ALB	2.5
TOTAL	100.0

TABLE 5.1: FE-SEM analysis of the SY3 starting mix

a) FE-SEM analyses of each mineral identified in the starting mix. The H₂O quantities are calculated stoichiometrically. The totals listed include the H₂O component; b) Bulk composition shows normalised major and minor oxides; c) Modal proportion of natural minerals used in starting mix are calculated using least-squares method.

Table 5.1 provides compositional information on the starting mix: FE-SEM analysis of each component mineral, the bulk composition normalised to 100wt% oxide, and the modal proportion in wt% of each mineral in the starting mix.

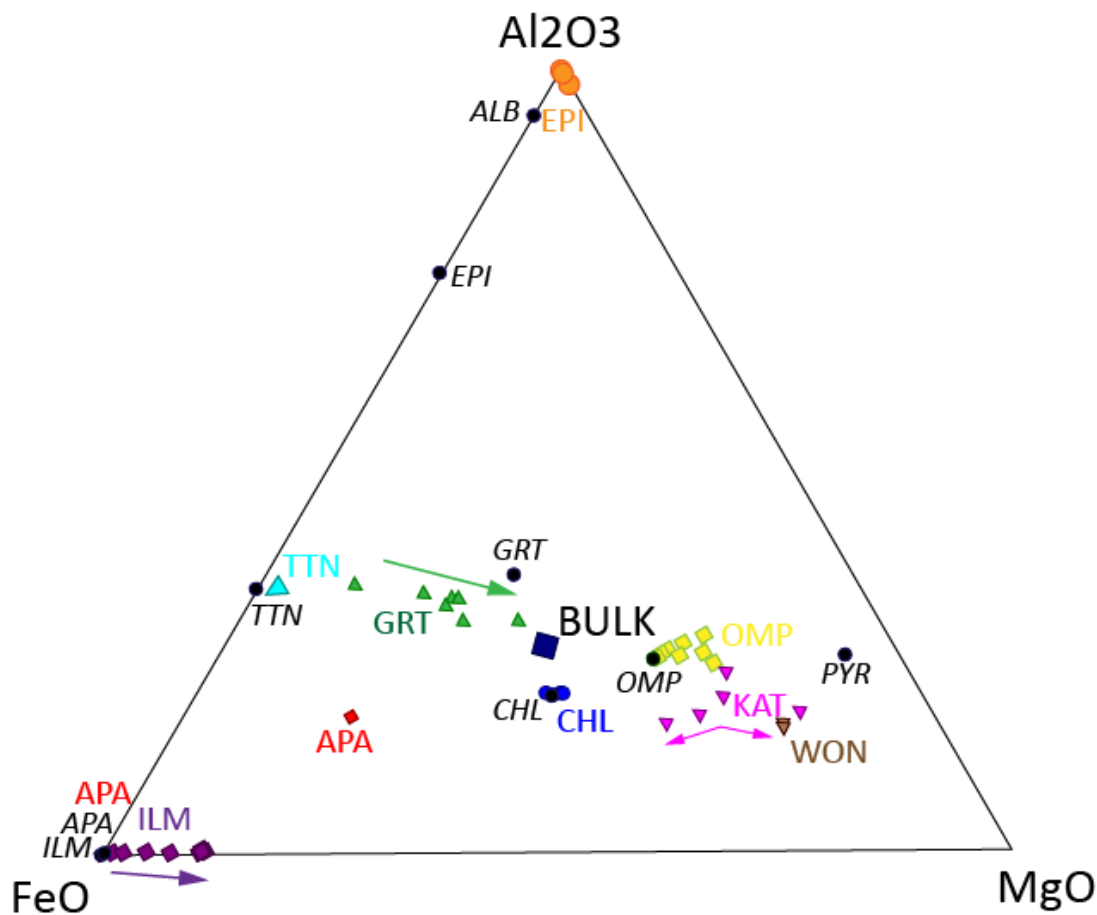


FIGURE 5.1: Chemography of the SY3 starting mix and run products.

Triangular plot of the bulk composition in the system CFMnMASH. Bulk composition in dark blue capitals; minerals included in starting mix in black italics; phases found in experimental runs in colour-coded capitals. Plot completed using C-Space software (Torres-Roldan et al., 2000).

Figure 5.1 shows the chemography of minerals comprising the SY3 starting mix in addition to those which formed in experimental runs. As can be seen, little compositional variation was observed.

Figure 5.2 shows the XRD diffractogram of the starting mix. The five main phases – clinocllore, omphacite, epidote, titanite and ilmenite – have been correctly identified, matching peak standards on the 2-theta scale. Clinocllore, as the major component in the start mix, showed poor alignment with the standard on the Y-axis almost certainly due to crystal preferred orientation. Subsequent FE-SEM analysis elicited trace apatite and minor albite which were not identified in this scan. In the case of apatite, this was likely due to its presence in trace amounts. In the case of albite, it may have been due to its platy habit and so was under-represented in the counts on the Y-axis.

Starting Mix Series 3 (Sample SY3, Scan A27945)

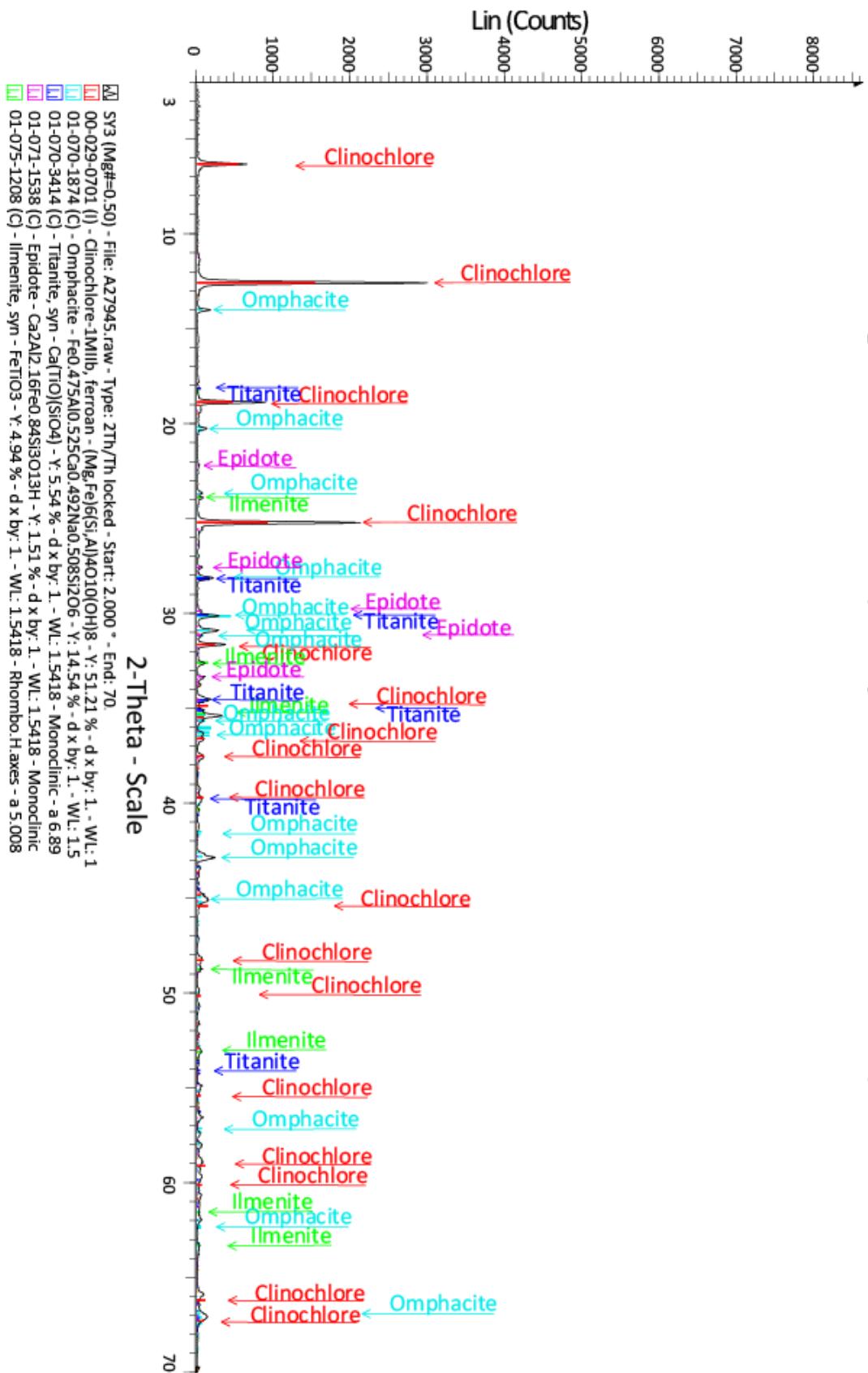


FIGURE 5.2: X-Ray Diffraction analysis of SY3 starting mix.

The strong alignment between diffractogram peaks and mineral standards on the 2-theta scale confirms the identity of five minerals. Subsequent FE-SEM analyses of the starting mix identified apatite and albite, neither of which were identified in this scan. Garnet was added manually to the starting mix after this scan. The poor chlorite alignment on the Y-scale is likely due to PCO.

5.2.2. DESCRIPTION OF SY4 STARTING MATERIAL

The SY4 experimental set also contained nine experiments at 3.0 GPa between 540°C and 800°C. They used chlorite with an Mg# =0.68, part of a sample of chlorite schist containing minor apatite, ilmenite and titanite, also sourced from Syros island, part of the Cyclades archipelago in Greece (Miller *et al.*, 2009).

Oxide wt%	APA (n=12)		CHL (n=11)		EPI (n=2)		ILM (n=11)		OMP (n=2)		MGT (n=7)		TTN (n=9)		GRT (n=9)	
	Mean	SD	Mean	SD	Mean	SD	Mean	SD	Mean	SD	Mean	SD	Mean	SD	Mean	SD
H ₂ O	1.71	0.01	11.66	0.19	1.87	0.02	0.00	0.00	0.00	0.00	0.00	0.00	0.00	0.00	0.00	0.00
Na ₂ O	0.02	0.04	0.00	0.00	0.00	0.00	0.00	0.00	8.60	0.71	0.00	0.00	0.02	0.04	0.08	0.06
MgO	0.00	0.00	21.57	1.38	0.00	0.00	0.24	0.10	5.49	0.62	0.00	0.00	0.00	0.00	26.75	0.20
Al ₂ O ₃	0.00	0.00	18.92	0.59	25.47	0.15	0.00	0.00	7.75	0.52	0.02	0.04	0.53	0.33	24.42	0.22
SiO ₂	0.05	0.06	27.72	0.79	39.56	0.56	0.11	0.07	55.34	0.11	0.02	0.05	30.59	0.23	43.38	0.29
P ₂ O ₅	42.58	0.22	0.00	0.00	0.00	0.00	0.00	0.00	0.00	0.00	0.00	0.00	0.00	0.00	0.00	0.00
K ₂ O	0.00	0.00	0.00	0.00	0.00	0.00	0.00	0.00	0.00	0.00	0.00	0.00	0.00	0.00	0.00	0.00
CaO	53.90	0.83	0.03	0.05	22.11	0.11	0.21	0.15	9.48	0.75	0.20	0.16	27.51	0.18	0.43	0.02
TiO ₂	0.01	0.05	0.00	0.00	0.08	0.08	49.68	0.86	0.00	0.00	0.42	0.13	38.54	0.64	0.00	0.00
Cr ₂ O ₃	0.00	0.00	0.00	0.00	0.07	0.07	0.00	0.00	0.00	0.00	0.00	0.00	0.00	0.00	0.00	0.00
MnO	0.00	0.00	0.18	0.10	0.17	0.02	2.11	0.42	0.00	0.00	0.00	0.00	0.00	0.00	0.00	0.00
FeO	0.32	0.25	17.68	1.49	0.00	0.00	41.99	1.01	12.90	2.11	0.00	0.00	0.97	0.22	4.08	0.40
NiO	0.00	0.00	0.00	0.00	0.00	0.00	0.00	0.00	0.00	0.00	0.00	0.00	0.00	0.00	0.00	0.00
Fe ₂ O ₃	0.00	0.00	0.00	0.00	12.67	0.27	4.09	0.10	0.00	0.00	101.73	0.62	0.00	0.00	0.00	0.00
Total	98.59	0.73	86.10	1.17	102.00	0.87	98.42	1.23	99.57	1.04	102.39	0.66	98.17	0.60	98.17	0.60
Na	0.00	0.01	0.00	0.00	0.00	0.00	0.00	0.00	0.62	0.05	0.00	0.00	0.00	0.00	0.00	0.00
Mg	0.00	0.00	3.31	0.18	0.00	0.00	0.01	0.00	0.30	0.03	0.00	0.00	0.00	0.00	2.75	0.03
Al	0.00	0.00	2.30	0.08	2.40	0.01	0.00	0.00	0.34	0.02	0.00	0.00	0.02	0.01	1.99	0.01
Si	0.00	0.01	2.85	0.05	3.17	0.01	0.00	0.00	2.05	0.00	0.00	0.00	1.02	0.00	3.00	0.01
P	3.16	0.02	0.00	0.00	0.00	0.00	0.00	0.00	0.00	0.00	0.00	0.00	0.00	0.00	0.00	0.00
K	0.00	0.00	0.00	0.00	0.00	0.00	0.00	0.00	0.00	0.00	0.00	0.00	0.00	0.00	0.00	0.00
Ca	5.06	0.06	0.00	0.01	1.90	0.03	0.01	0.00	0.38	0.03	0.01	0.00	0.98	0.00	0.03	0.00
Ti	0.00	0.00	0.00	0.00	0.00	0.00	0.96	0.01	0.00	0.00	0.01	0.00	0.96	0.01	0.00	0.00
Cr	0.00	0.00	0.00	0.00	0.00	0.00	0.00	0.00	0.00	0.00	0.00	0.00	0.00	0.00	0.00	0.00
Mn	0.00	0.00	0.02	0.01	0.01	0.00	0.05	0.01	0.00	0.00	0.00	0.00	0.00	0.00	0.00	0.00
Fe	0.02	0.02	1.52	0.14	0.00	0.00	0.90	0.02	0.40	0.07	0.00	0.00	0.03	0.01	0.24	0.02
Ni	0.00	0.00	0.00	0.00	0.00	0.00	0.00	0.00	0.00	0.00	0.00	0.00	0.00	0.00	0.00	0.00
Fe ₃	0.00	0.00	0.00	0.00	0.76	0.01	0.08	0.00	0.00	0.00	1.98	0.01	0.00	0.00	0.00	0.00
Total	8.26	0.03	10.00	0.01	8.25	0.02	2.00	0.01	4.09	0.03	2.00	0.00	3.01	0.00	8.01	0.00
Mg#	0.00	0.00	0.68	0.03	0.00	0.00	0.01	0.00	0.43	0.07	0.00	0.00	0.00	0.00	0.92	0.01
Al#	0.00	0.00	1.00	0.00	0.76	0.00	0.00	0.00	1.00	0.00	0.00	0.00	1.00	0.00	1.00	0.00

Oxide	wt%
H ₂ O	10.02
Na ₂ O	0.16
MgO	18.50
Al ₂ O ₃	16.69
SiO ₂	26.37
P ₂ O ₅	2.04
CaO	4.07
TiO ₂	3.86
MnO	0.26
Fe total	18.04
Total	100.00

Phase	wt%
APA	4.7
CHL	82.9
EPI	1.6
ILM	4.8
OMP	1.9
MGT	0.2
TTN	3.5
GRT	0.5
TOTAL	100.0

TABLE 5.2: FE-SEM analysis of the SY4 starting mix

a) FE-SEM analyses of each mineral identified in the starting mix. The H₂O quantities are calculated stoichiometrically. The totals listed include the H₂O component; b) Bulk composition shows normalised major and minor oxides; c) Modal proportion of natural minerals used in starting mix calculated using least-squares method.

The bulk composition has been characterised in Table 5.2. Average FE-SEM analyses of each mineral in the starting material are shown in Table 5.2a. FESEM analysis of the bulk composition, normalised to 100wt%, is shown in Table 5.2b. The modal proportion of each mineral in the starting mix are shown in Table 5.2c.

Figure 5.3 shows the chemography of the eight mineral phases which comprised the starting mix in the SY4 experimental set. Also displayed in purple are the minerals which formed in run

products. Garnet and titanite were the only phases which showed significant compositional variation.

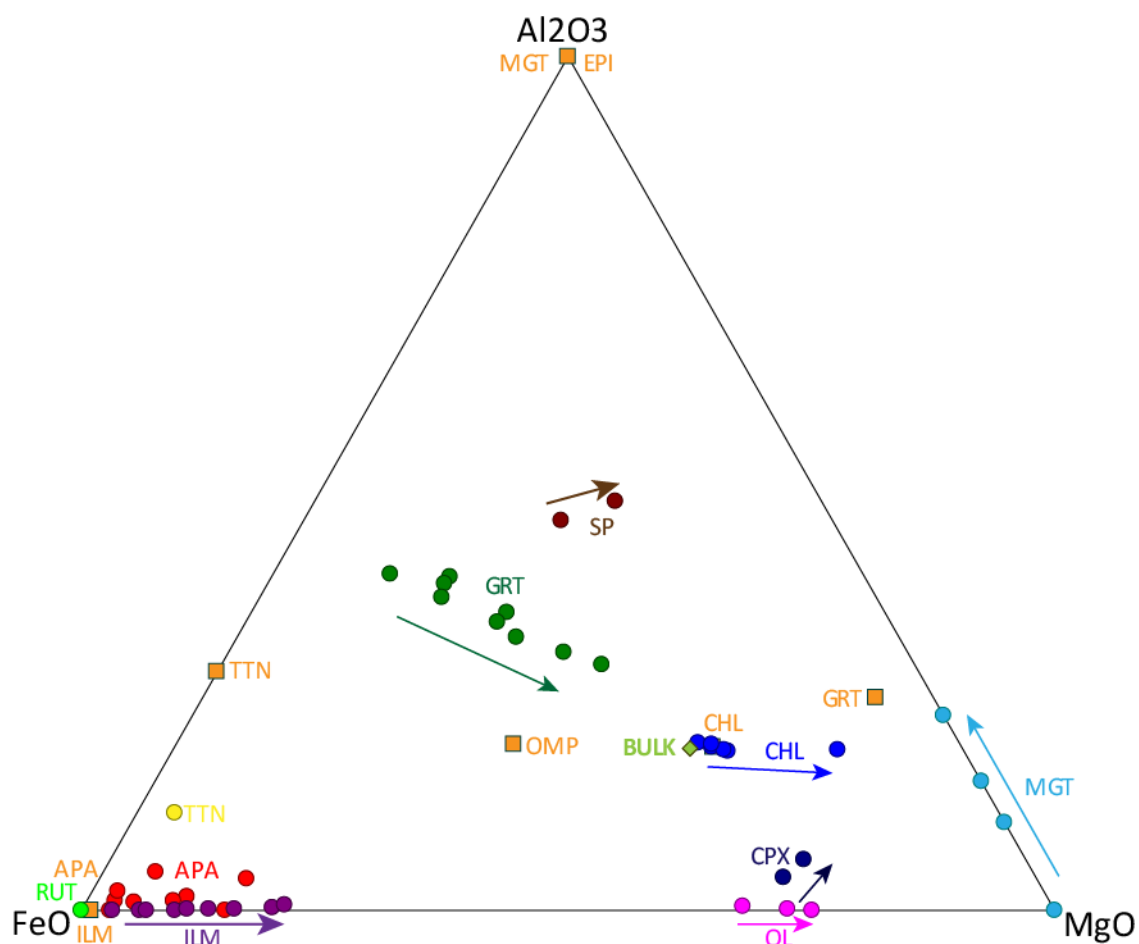


FIGURE 5.3: Chemography of the SY4 starting mix and run products.

Triangular plot of the bulk composition illustrating compositional change through the experimental set.. Bulk composition in light green font; minerals comprising the starting mix in orange font; run products are identified by colour-coded capitals. Plot completed using C-Space software (Torres-Roldan et al., 2000).

An XRD diffractogram of the SY4 starting mix is provided in Figure 5.4. Each of the main component phases have been correctly identified – clinocllore, apatite, ilmenite and titanite. However, minor omphacite and epidote and trace magnetite were not; FE-SEM analysis revealed the presence of these minerals.

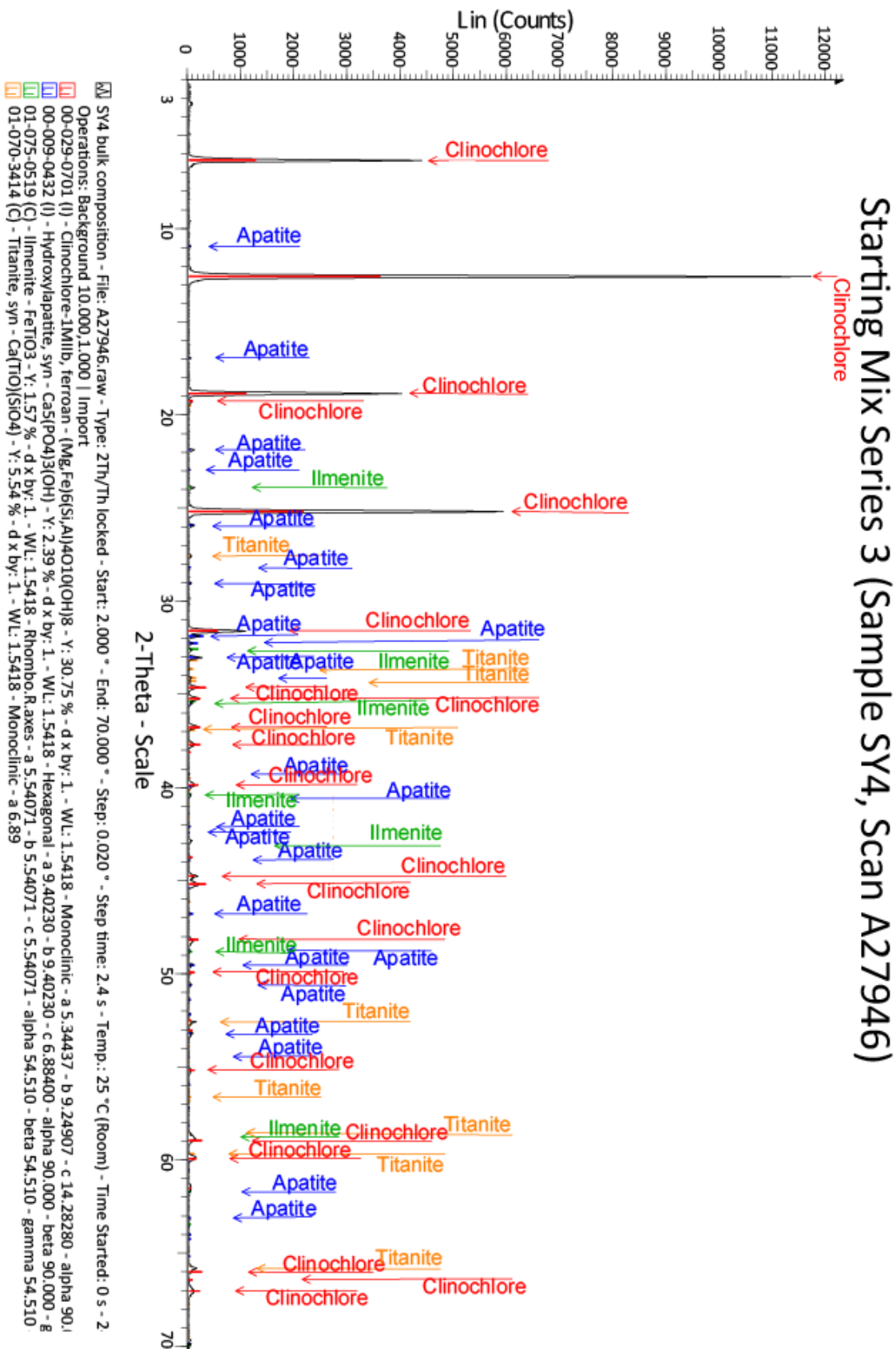


FIGURE 5.4: X-Ray Diffraction analysis of SY4 starting mix.

The strong alignment between diffractogram peaks and mineral standards on the 2-theta scale confirms the identity of four of the target minerals. The starting mix comprises mainly clinocllore. PCO of the platy mineral clinocllore accounts for its poor alignment on the Y-scale. Subsequent FE-SEM analyses of the starting mix identified trace amounts of epidote, omphacite and magnetite which were not identified in this scan.

5.2.3. DESCRIPTION OF HIGH TEMPERATURE STARTING MATERIAL

The sample used for the third experimental set used chlorite with an Mg#=0.94. It was sourced from a vein of ultramafic chlorite schist from the Cerro del Almiraz in southern Spain, the same sample used in experimental work outlined in chapter four above.

For a description of the chemical analysis of this starting mix, the XRD scan of starting materials and its chemography, refer to Chapter 4 above.

5.3. RESULTS

The results have been divided into three sections, corresponding to the three different bulk compositions studied.

5.3.1. SAMPLE SY3 (MG#=0.50)

The SY3 experiments determined nine data points at 3.0 GPa encompassing a temperature range of 500°C to 740°C. Table 5.3 lists the experimental conditions and run products identified in each experiment.

Expt	Time	P	T	Run products
Run	(hrs)	(GPa)	(°C)	
C5159	192	3	500	chl, epi, omp, ttn, ilm, rut, apa
C5138	192	3	540	chl, epi, omp, ilm, rut, grt, apa, fluid
C5127	192	3	580	chl, epi, omp, grt, ilm, rut, apa, fluid
D2036	120	3	640	chl, omp, grt, ilm, won, kat, rut, fluid, apa
C5143	168	3	660	grt, ilm, won, kat, omp, rut, fluid, apa
C5114	120	3	680	grt, ilm, won, kat, omp, rut, fluid, apa
C5137	120	3	700	grt, ilm, won, kat, fluid, rut, omp, apa
D2021	120	3	720	grt, kat, fluid, won, ilm, rut, omp, apa
D2013	120	3	740	grt, kat, ilm, fluid, omp, rut, won, apa

TABLE 5.3. Experimental conditions and run products in SY3 experimental set.

Run products – major (>5 wt%) in bold text; minor (1-5 wt%) in regular text; trace (<1 wt%) in italicized text.

5.3.2. SAMPLE SY3 (MG#=0.50)

5.3.2.1. Changes in phase relations with increasing temperature in SY3 set

Figure 5.5 provides six microphotographs which illustrate the changing phase relations which occurred with increasing temperature in the SY3 set of experiments. At 500°C, phases present

show marked similarity to those in the starting mix which indicated the thermal stability of all minerals to this temperature. The single exception was observed with titanite, which was approaching its thermal maximum as evidenced by the appearance of rutile along its grain boundaries (see Figure 5.5a). By 580°C, titanite had entirely disappeared replaced by the phases garnet, ilmenite and rutile. Epidote had also commenced breakdown as evidenced by the appearance of Ca-rich garnet. Epidote had also commenced breakdown as evidenced by the appearance of Ca-rich garnet.

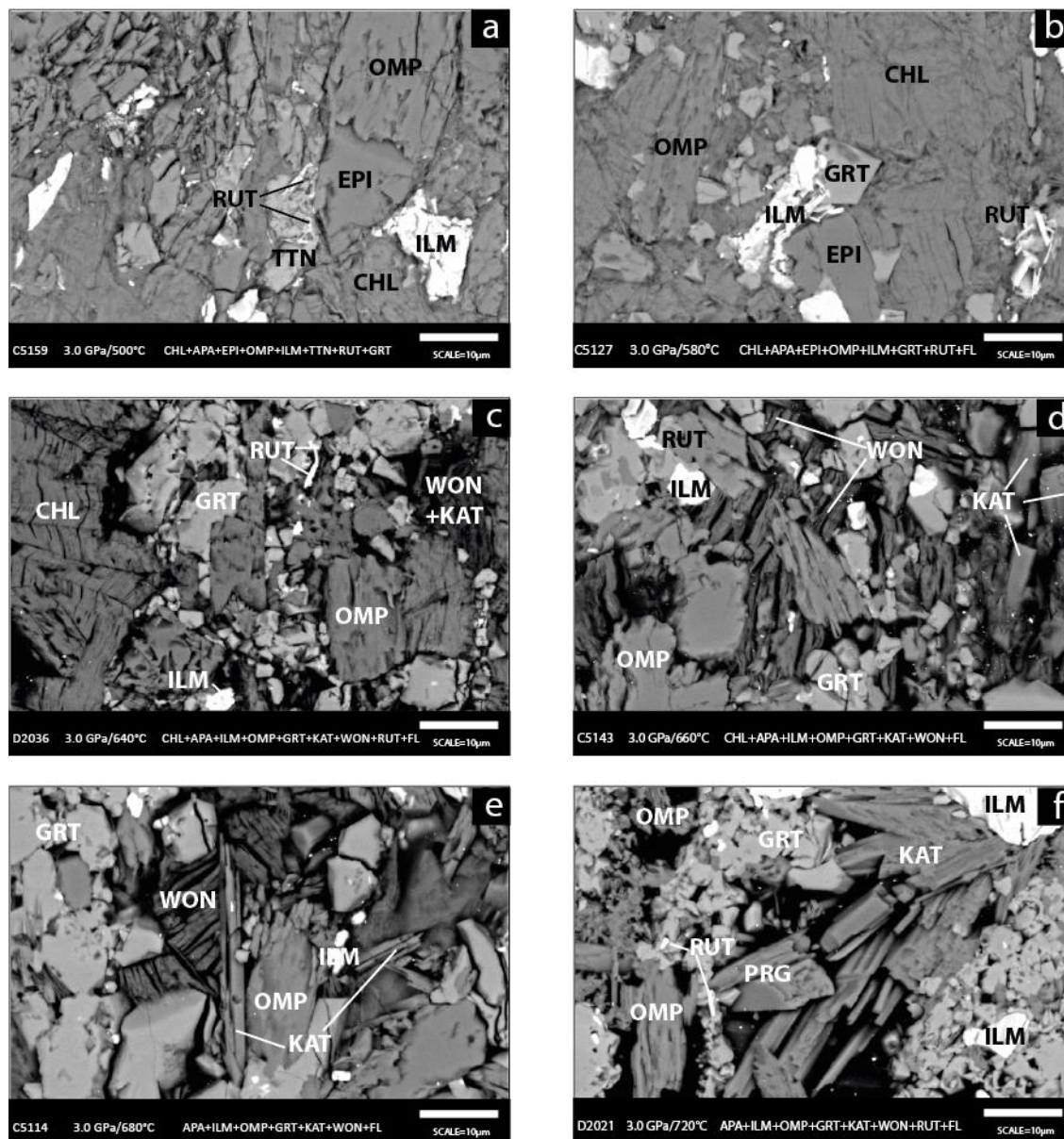


FIGURE 5.5. Changing phase relations by temperature in SY3 experiments.

a) 500°C Titanite is approaching its thermal maximum as evidenced by the presence of rutile. b) 580°C Titanite has completely disappeared and epidote has commenced its breakdown. c) 640°C Several significant changes are evident: epidote has entirely reacted out; chlorite and omphacite are in reaction, confirmed by the appearance of two new hydrous minerals –wonesite and magnesiokatophorite - as reaction products, both forming an intercalated texture with chlorite. d) 660°C. Chlorite has entirely reacted out. Magnesiokatophorite and wonesite are now visibly distinguished. Garnet has a poikiloblastic appearance. e) 680°C Garnet, wonesite and magnesiokatophorite are the dominant minerals at this temperature. f) 720°C. Magnesiokatophorite has reached its thermal maximum comprising ~24wt% of phases. Wonesite has (almost) completely disappeared.

At 640°C, epidote had entirely reacted out. Following the reaction between chlorite and omphacite, two hydrous minerals - the sodic amphibole magnesiokatophorite and the sodic mica wonesite (Veblen, 1983) - appeared as run products. These minerals formed an intercalated texture with chlorite making analysis challenging. By 660°C, however, all chlorite had decomposed leaving wonesite and magnesiokatophorite as the only stable hydrous phases. Magnesiokatophorite, with its lighter, elongate bladed crystals were easily distinguished from the darker, stubby wonesite grains. Garnet crystals had increased in size and assumed a poikiloblastic in appearance. After 680°C, wonesite neared its thermal maximum and quickly decreased in modal proportion. By contrast, magnesiokatophorite continued to increase its stability field until 720°C where it comprised ~24 wt% of all phases. At higher temperature, this phase too began to decrease in favour of newly-formed omphacite. By 740°C, garnet and magnesiokatophorite were the main phases present.

5.3.2.2. Textural analysis of SY3 experimental set

This experimental set produced eleven run products - ten solid and one fluid. The number varied in accordance with temperature and stability fields. No melt was observed.

Chlorite was the dominant phase in the bulk composition, with omphacite and epidote forming the bulk of the remaining phases.

Chlorite existed as subhedral, elongate laths <30 µm long and <15 µm wide and formed an interlocking fabric in run products (see Figure 5.5a and b). Near its thermal maximum, chlorite began to dissociate into a splintery, needle-like collection of crystals.

Omphacite was observed as homogeneous, subhedral, blocky grains. At lower temperature, these were typically 20-30 µm long and 10-15 µm wide. At higher temperature, grains were smaller - 10-15 µm long and 5-10 µm wide. Those grains remaining following the reaction with chlorite assumed a more anhedral appearance (see Figure 5.5d and e). Above 720°C, there was clear evidence of omphacite reforming following the disappearance of the sodic wonesite (see Figure 5.5f).

Epidote was observed in the run products of three experiments, forming subhedral-euhedral equant grains (<8 µm across) and elongate grains (15x5 µm). Near its maximum stability, reaction rims were observed (see Figure 5.5b).

Titanite appeared in a single experimental run at 500°C where it exhibited typical spear-shaped grains ~10 µm in length and ~5 µm wide. At this temperature, titanite was near its thermal

maximum and so was frequently observed intercalated with ilmenite and rutile, two of its breakdown products (see Figure 5.5a).

The Fe-Ti oxides ilmenite and rutile were observed in most experimental runs. Ilmenite formed subhedral to anhedral grains up to 25 μm across and possessed a strong poikiloblastic appearance. Rutile was typically found as thin, almost acicular blades $<2 \mu\text{m}$ in length always proximal to ilmenite.

Garnet occurred in all run products above 540°C. At temperatures $<640^\circ\text{C}$, it formed subhedral-euhedral grains up to 5 μm in diameter with a distinct, poikiloblastic appearance. By 740°C, grain size increased to 10-20 μm although newly-nucleated garnets invariably formed aggregations containing multiple small grains 1-3 μm in size (see Figure 5.5f).

Apatite occurred as isolated grains in trace quantities in each experimental run. Since no reaction textures were observed, it was concluded that all apatite grains were remnant from the starting material.

Wonesite first appeared at 640°C where it formed small, intercalated clumps with the amphibole, magnesiokatophorite (see Figure 5.5c) and chlorite. At higher temperature, wonesite formed rectangular, stubby grains up to 20 μm long and $<2 \mu\text{m}$ wide which aggregated into a layered structure, characteristic of micas (see Figure 5.5c-f). It always formed proximal to magnesiokatophorite, garnet and omphacite. Wonesite was only present in trace quantities above 700°C.

Initially, magnesiokatophorite formed fine-grained crystals intercalated with wonesite. By 660°C, large euhedral-subhedral bladed crystals formed $>30 \mu\text{m}$ in length and $<5 \mu\text{m}$ wide independent of other phases. Grain size increased with temperature (see Figure 5.5d-f) and comprised nearly one quarter of all phases at 720°C.

5.3.2.3. *Compositional analysis of SY3*

The SY3 experiments produced ten solid phases and one fluid phase as reaction products. All solid phases were analysed using FE-SEM. Table 5.4 provides representative analyses of each phase: a complete set of FE-SEM analyses can be found in the Chapter 5 Appendix. The presence of Fe^{3+} in the starting mix led to an adjustment to standard chemical ratios used. Firstly, values of Fe^{3+} were determined by stoichiometric balance. The $\text{Fe}^{3+}/\Sigma\text{Fe}$ ratio was used to show the relative proportion of Fe^{2+} to Fe^{3+} quantities in run products; the value of ΣFe was determined by the addition of the Fe^{2+} and Fe^{3+} . The revised Mg# was determined by $\text{Mg}/(\text{Mg}+\text{Fe}^{2+})$.

Run	C5127		C5138		C5127		D2036		C5159		C5114		D2021		C5143		C5127	
Mineral	CHL		EPI		ILM		OMP		TTN		GRT		KAT		WON		APA	
n	7		6		8		12		5		9		6		4		1	
T	580		540		580		640		500		680		720		660		580	
	Mean	SD	Mean	SD	Mean	SD	Mean	SD	Mean	SD	Mean	SD	Mean	SD	Mean	SD	Mean	
Wt%	H ₂ O	11.21	0.17	1.89	0.04	0.00	0.00	0.00	0.00	0.00	0.00	0.00	2.04	0.02	4.16	0.15	1.78	
	Na ₂ O	0.24	0.10	0.02	0.05	0.12	0.12	7.99	0.43	0.00	0.00	0.11	0.04	5.68	0.46	3.91	1.31	0.00
	MgO	14.78	0.57	0.20	0.33	1.22	0.30	5.97	0.32	0.02	0.04	5.71	0.39	13.82	0.55	21.07	0.99	0.00
	Al ₂ O ₃	19.01	0.38	24.28	0.82	0.12	0.25	7.34	0.53	0.89	0.13	20.43	0.23	11.05	1.01	13.09	0.57	0.00
	SiO ₂	26.11	0.42	37.85	0.73	0.23	0.23	54.81	0.57	30.67	0.44	38.52	0.57	45.57	0.86	42.48	1.24	0.00
	P ₂ O ₅	0.00	0.00	0.00	0.00	0.00	0.00	0.00	0.00	0.00	0.00	0.05	0.07	0.00	0.00	0.00	0.00	42.81
	K ₂ O	0.00	0.00	0.00	0.00	0.00	0.00	0.00	0.00	0.00	0.00	0.00	0.00	0.14	0.04	1.75	1.62	0.00
	CaO	0.06	0.06	21.46	0.44	0.28	0.07	10.48	0.49	27.35	0.22	11.89	0.73	6.63	0.98	0.12	0.07	53.45
	TiO ₂	0.06	0.10	0.22	0.20	49.54	0.95	0.11	0.08	38.47	0.47	0.57	0.13	0.62	0.14	0.09	0.09	0.00
	Cr ₂ O ₃	0.00	0.00	0.00	0.00	0.00	0.00	0.00	0.00	0.00	0.00	0.00	0.00	0.00	0.00	0.00	0.00	0.00
	MnO	0.11	0.10	0.19	0.09	0.25	0.15	0.08	0.09	0.00	0.00	0.40	0.07	0.00	0.00	0.00	0.00	0.00
	FeO	26.90	0.43	0.00	0.00	42.12	0.47	5.03	0.22	1.19	0.09	19.85	0.57	11.59	0.51	9.63	0.39	0.74
	NiO	0.00	0.00	0.00	0.00	0.00	0.00	0.00	0.00	0.00	0.00	0.00	0.00	0.00	0.00	0.00	0.00	0.00
	Fe ₂ O ₃	0.00	0.00	13.20	1.40	5.24	0.06	8.39	0.37	0.00	0.00	2.46	0.07	1.93	0.09	0.00	0.00	0.00
Total	87.28	1.10	97.41	2.45	99.13	0.66	100.20	0.95	98.60	0.91	99.97	0.96	97.03	0.96	92.14	3.29	97.00	
Cations	Na	0.05	0.02	0.01	0.01	0.01	0.01	0.57	0.03	0.00	0.00	0.02	0.01	1.61	0.13	0.54	0.17	0.00
	Mg	2.36	0.06	0.05	0.08	0.05	0.01	0.33	0.02	0.00	0.00	0.66	0.04	3.02	0.13	2.26	0.03	0.00
	Al	2.40	0.02	4.55	0.13	0.00	0.01	0.32	0.02	0.03	0.01	1.86	0.02	1.91	0.17	1.11	0.01	0.00
	Si	2.79	0.01	6.02	0.04	0.01	0.01	2.00	0.00	1.01	0.00	2.98	0.01	6.69	0.13	3.06	0.02	0.00
	P	0.00	0.00	0.00	0.00	0.00	0.00	0.00	0.00	0.00	0.00	0.00	0.00	0.00	0.00	0.00	0.00	3.08
	K	0.00	0.00	0.00	0.00	0.00	0.00	0.00	0.00	0.00	0.00	0.00	0.00	0.03	0.01	0.16	0.15	0.00
	Ca	0.01	0.01	3.65	0.05	0.01	0.00	0.41	0.02	0.97	0.01	0.99	0.06	1.04	0.15	0.01	0.01	4.86
	Ti	0.00	0.01	0.03	0.02	0.94	0.01	0.00	0.00	0.96	0.00	0.03	0.01	0.07	0.01	0.00	0.00	0.00
	Cr	0.00	0.00	0.00	0.00	0.00	0.00	0.00	0.00	0.00	0.00	0.00	0.00	0.00	0.00	0.00	0.00	0.00
	Mn	0.01	0.01	0.03	0.01	0.01	0.00	0.00	0.00	0.00	0.00	0.03	0.00	0.00	0.00	0.00	0.00	0.00
	Fe	2.41	0.06	0.00	0.00	0.89	0.01	0.15	0.01	0.03	0.00	1.28	0.04	1.42	0.06	0.58	0.02	0.05
	Ni	0.00	0.00	0.00	0.00	0.00	0.00	0.00	0.00	0.00	0.00	0.00	0.00	0.00	0.00	0.00	0.00	0.00
	Fe ₃	0.00	0.00	1.58	0.15	0.10	0.00	0.23	0.01	0.00	0.00	0.14	0.00	0.21	0.01	0.00	0.00	0.00
	Total	10.03	0.01	15.90	0.02	2.00	0.01	4.01	0.01	3.01	0.00	7.99	0.01	16.00	0.02	7.73	0.04	7.99
Mg#	0.49	0.01	0.00	0.00	0.05	0.01	0.68	0.02	0.03	0.05	0.34	0.01	0.68	0.02	0.80	0.01	0.00	
Al#	1.00	0.00	0.75	0.02	0.03	0.06	0.58	0.02	1.00	0.00	0.93	0.00	0.90	0.01	1.00	0.00	0.00	

TABLE 5.4. Table of representative phase analyses for SY3 in in Series 3

Chlorite displayed no significant compositional variation in this series – the minor changes that were evident were within one standard deviation of the mean. The mean Mg# was 0.50 but showed no correlation with temperature. Chlorite analyses consistently recorded the presence of trace Na, Ti, Ca, Mn and K. The stoichiometric formula for chlorite was described as $(\text{Mg}_{2.35}\text{Fe}_{2.37}\text{Ca}_{0.01}\text{Mn}_{0.01}\text{Na}_{0.04})\text{Al}_{2.39}(\text{Si}_{2.81}\text{Ti}_{0.01})\text{O}_{12}(\text{OH})_8$, near the mid-point of the clinochlore-chamosite solid solution.

Garnet was present in all experimental runs although grain size was too small at both 500°C and 540°C to obtain accurate analyses. This phase exhibited significant compositional variation with temperature. The Mg# varied between 0.16 at 580°C to 0.43 at 740°C (see Figure 5.6a). The large grossular component observed at lower temperature systematically diminished in favour of pyrope as observed in Figure 5.6b. The $\text{Fe}^{3+}/\Sigma\text{Fe}$ ratio also displayed some variability, between 0–0.11, evidence of the accommodation of only small amounts of Fe^{3+} in this phase.

Ilmenite was observed in all nine experimental runs. Until chlorite disappeared, the geikielite component in ilmenite increased with temperature, evidenced by the Mg# increasing from 0.01

to 0.11. However, after chlorite had reacted out, except for a single data point (D2013), the Mg# maintained a consistent 0.11 as seen in Figure 5.6d.

Omphacite appeared in all run products. The mean Mg# varied between 0.65 and 0.72 and the $\text{Fe}^{3+}/\Sigma\text{Fe}$ ratio also varied between 0.55 and 0.70. However, neither measure showed any significant correlation with temperature. The Na+Ca ratio remained very consistent at 0.98. Together, these values indicated this phase changed little from the starting mix.

Rutile was present in trace to minor amounts in each run according to mass balance calculations. Whilst rutile was observed, grains were both small and typically intercalated with ilmenite. As a result, no accurate chemical analyses were obtained.

Amphibole, close to magnesiokatophorite, formed in six experimental runs. Run products formed at 640°C contained an intercalation of amphibole, mica and chlorite which prevented the acquisition of suitable analyses. The Mg# in magnesiokatophorite displayed an interesting pattern in this experimental set. Between 640°C and 700°C, the Mg# decreased from 0.82 to 0.63. After 700°C, it demonstrated a positive correlation with temperature increasing from 0.63 to 0.73 (see Figure 5.6c). This change in relationship mirrored the stability field of wonesite. As wonesite increased its modal proportion, the Mg# of magnesiokatophorite reduced. However, as wonesite began to react-out, the Mg# of the amphibole increased. A similar trend was observed in regards the $\text{Fe}^{3+}/\Sigma\text{Fe}$ ratio. Two exchange vectors were in operation with magnesiokatophorite: $[\text{NaFe}^{2+} \leftrightarrow \square\text{Fe}^{3+}]$ operated towards barroisite and the exchange vector $[\text{SiMg}^{2+} \leftrightarrow \text{Al}^{\text{IV}}\text{Al}^{\text{VI}}]$ acted towards magnesiotaramite (Leake *et al.*, 1997).

Although it was observed in the run products of four experiments (and in trace amounts according to mass balance calculations in two others), the complex textural features of the sodic mica, close to wonesite, made the acquisition of data problematic. Accurate analyses were only achieved in two of the four runs (C5143 and C5114). Notwithstanding the lack of data, the Mg# in wonesite showed little variation with temperature, declining from 0.80 to 0.79 over a 20°C interval. Oxide totals indicated that wonesite contained no Fe^{3+} . Its stoichiometric formula was represented by $(\text{Na},\text{K}_{0.67} \square_{0.33} \text{Ca}_{0.01} \text{Mg},\text{Fe}_{2.85}) \text{Al}_{1.09} \text{Si}_{3.08} \text{O}_{10} (\text{OH})_2$, placing it in a solid-solution between the mica end-members preiswerkite and aspidolite and the theoretical end-member beyond wonesite (Rieder *et al.*, 1999).

Three phases which were constituents of the starting mix also appeared as run products in various experiments: apatite, epidote and titanite. In each instance, these phases showed little evidence of compositional change from the starting mix and so were not considered reaction products. Apatite was present in all experimental runs at 0.6wt%. The few grains for which accurate analyses were obtained did show variation but this can be attributed to interference

from proximal ilmenite grains. Epidote appeared in three experimental runs and displayed a consistent $\text{Fe}^{3+}/\Sigma\text{Fe}$ ratio of 1.0 and showed no relationship with temperature. Titanite appeared in a single experimental run (C5159) and showed no significant change from the starting mix composition.

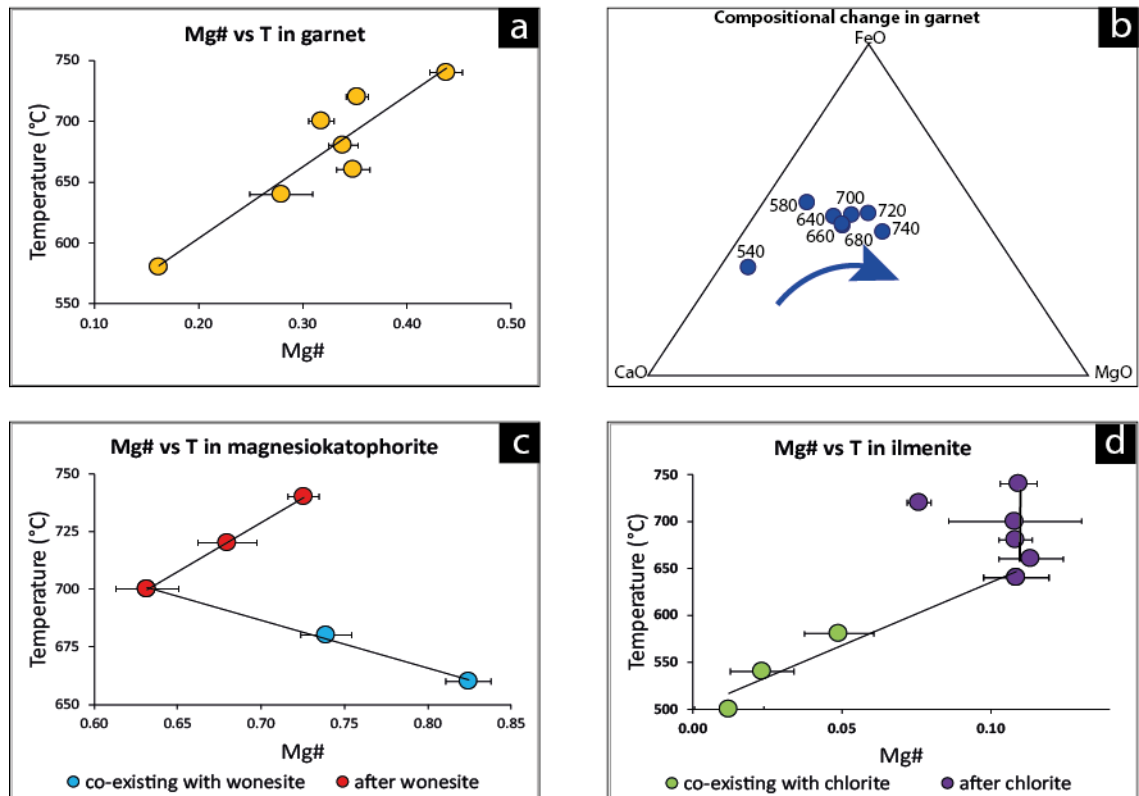


FIGURE 5.6. Relevant compositional plots for SY3 experimental set in Series 3

a) Plot of Mg# vs T in garnet which shows strong positive correlation. b) Plot of compositional change in garnet with temperature: garnet becomes increasingly Mg-rich with increasing T - from grossular-almandine composition at low T to an equi-grossular-almandine-pyrope composition at high T. c) Plot of Mg# vs T in magnesiokatophorite. This shows contrasting correlation with temperature depending upon the presence of wonesite – inverse trend when present; positive trend when absent. D) Plot of Mg# vs T in ilmenite which indicates a compositional dependency with chlorite. When both phases are present, a positive relationship between Mg# and T is observed; outside the chlorite stability field, ilmenite maintains a (generally) consistent composition.

5.3.2.4. Partitioning in SY3 set

The partitioning of Mg and Fe between co-existing phases was determined by the Mg#. This elicited a clear pattern. In the chlorite stability field, the partitioning sequence was $omp > chl > ilm$. With the appearance of garnet after epidote, the sequence was adjusted to $omp > chl > grt > ilm$. Following the disappearance of chl and its replacement with an amphibole and a mica, the partitioning sequence was again modified: $won > kat > omp > grt > ilm$. With the disappearance of the wonesite phase, the same sequence remained except at 720°C when omphacite recorded a higher Mg# than magnesiokatophorite.

Figure 5.7 displays four partitioning plots of selected co-existing phases from the SY3 experimental set. Figure 5.7a plots Mg# partitioning between omphacite and garnet, with the partitioning coefficient calculated using $K_D = (X_{Mg}^{omph})(X_{Fe}^{grt}) / (X_{Fe}^{omph})(X_{Mg}^{grt})$. Although Mg preferentially partitioned into omphacite over garnet in all instances, the moderate correlation revealed by the slope of the partitioning curve indicated that increased amounts of Mg were sequestered into garnet with increasing temperature. Figure 5.7b examined Mg# partitioning between the amphibole magnesiokatophorite and garnet. The partitioning coefficient was calculated using $K_D = (X_{Mg}^{kat})(X_{Fe}^{grt}) / (X_{Fe}^{kat})(X_{Mg}^{grt})$. A strong correlation was observed. Whilst the amphibole was the preferred repository for Mg compared with garnet at all temperature intervals, with increasing temperature Mg showed an increased affinity for garnet. Figure 5.7c examined the partitioning behaviour of Mg# in ilmenite with two co-existing phases – omphacite and chlorite using the equations $K_D = (X_{Mg}^{ilm})(X_{Fe}^{omph}) / (X_{Fe}^{ilm})(X_{Mg}^{omph})$ and $K_D = (X_{Mg}^{chl})(X_{Fe}^{ilm}) / (X_{Fe}^{chl})(X_{Mg}^{ilm})$ respectively. The dual plots revealed identical partitioning behaviours. For the ilmenite-omphacite pair, Mg partitioning always favoured omphacite over ilmenite but with increasing temperature, ilmenite accommodated increased amounts of Mg.

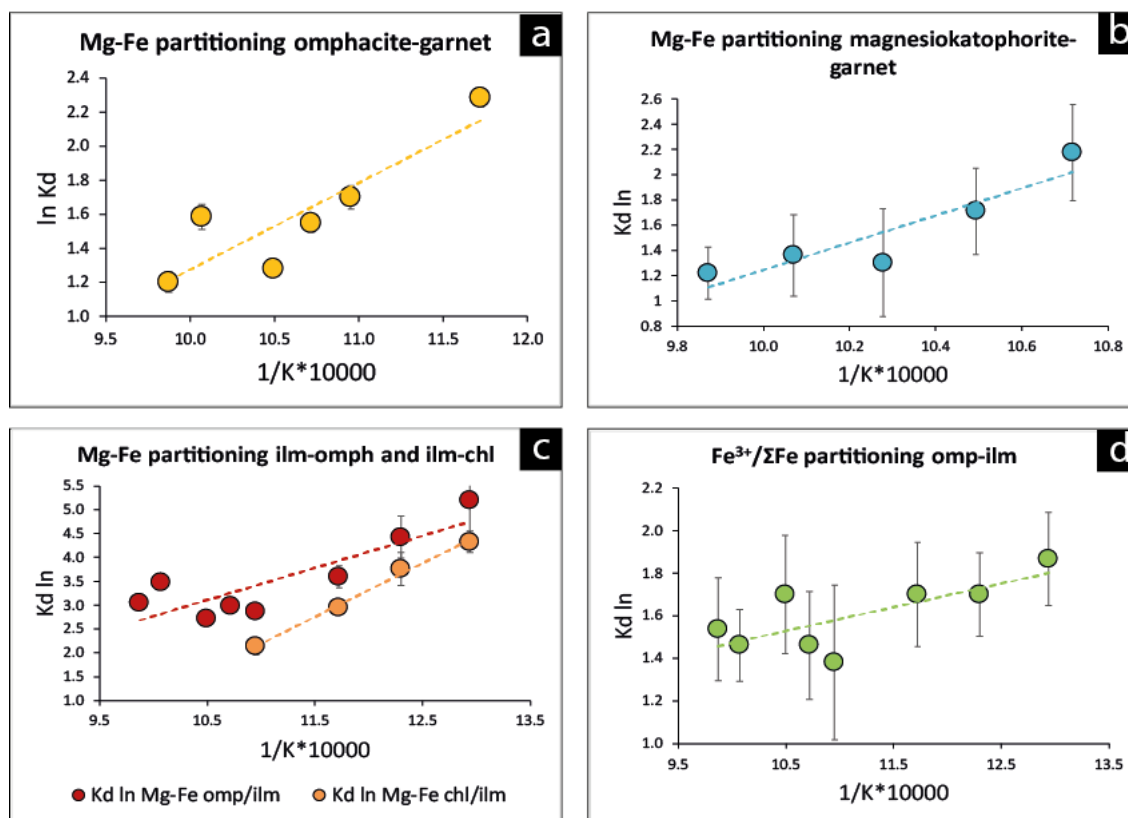


FIGURE 5.7. Relevant partitioning plots for SY3 bulk composition in Series 3 experiments

Figure 5.7a-c shows Mg# partitioning plots between selected co-existing phases in the SY3 experimental series. Each show that Mg# partitioning changes with increasing temperature. Figure 5.7d examines $Fe^{3+}/\Sigma Fe$ partitioning between omphacite and ilmenite which shows a positive correlation.

As for the ilmenite-chlorite pair, Mg partitioning strongly favoured chlorite over ilmenite, but with increasing temperature, ilmenite attracted increased quantities. Whilst Mg and Fe were identified in apatite, titanite and rutile, the quantities were insufficient to be included in partitioning comparisons.

The partitioning of Fe³⁺ was determined by the Fe³⁺/ΣFe ratio. This series displayed a consistent partitioning sequence. At low temperature, Fe³⁺ preferentially partitioned in the following order: *epi* > *omp* > *ilm*. With the disappearance of epidote, this sequence was modified to include garnet: *omp* > *ilm* > *grt*. With the introduction of amphibole following the breakdown of chlorite, the sequence at all temperatures was: *omp* > *kat* > *ilm* > *grt*, and except for the run at 700°C where garnet accommodated Fe³⁺ in preference to magnesiokatophorite, this remained the partitioning sequence to higher temperature. Figure 5.7d showed Fe³⁺ partitioning between omphacite and ilmenite with the partitioning coefficient calculated using $K_D = \frac{(X_{Fe^{3+}}^{omp})(X_{\Sigma Fe}^{ilm})}{(X_{Fe^{3+}}^{ilm})(X_{\Sigma Fe}^{omp})}$. Fe³⁺ always displayed a consistent preference for omphacite over ilmenite. However, with increasing temperature, Fe³⁺ showed an increased affinity for ilmenite.

5.3.2.5. Summary of findings from the SY3 experimental set

Phase relations and chemical composition of phases were used to determine mass balance of each phase at each temperature interval. The summary of findings is listed in Table 5.5. Figure 5.8 illustrates the changing abundance of phases with increasing temperature.

Expt	Run	C5159	C5138	C5127	D2036	C5143	C5114	C5137	D2021	D2013
Time	(hrs)	192	192	192	120	168	120	120	120	120
P	(Gpa)	3	3	3	3	3	3	3	3	3
T	(°C)	500	540	580	640	660	680	700	720	740
PHASES	APA	0.6	0.6	0.6	0.6	0.6	0.6	0.6	0.6	0.6
	CHL	47.3	43.7	42.0	9.7	0.0	0.0	0.0	0.0	0.0
	EPI	18.3	20.4	17.3	0.0	0.0	0.0	0.0	0.0	0.0
	ILM	1.9	3.9	3.0	5.8	7.6	7.2	6.2	3.1	6.9
	OMP	26.0	26.9	27.2	9.5	4.4	2.0	0.7	0.7	3.2
	TTN	3.3	0.0	0.0	0.0	0.0	0.0	0.0	0.0	0.0
	GRT	0.0	1.5	6.1	51.5	60.3	60.3	60.7	62.2	62.8
	KAT	0.0	0.0	0.0	7.3	8.3	8.5	13.8	24.3	19.7
	WON	0.0	0.0	0.0	9.9	12.8	15.4	11.7	1.0	0.2
	RUT	2.4	2.7	3.2	1.6	1.1	1.1	1.2	2.8	1.2
	H2O	0.0	0.3	0.6	4.0	4.9	4.9	5.0	5.3	5.4
	TOTAL		100.0	100.0	100.0	100.0	100.0	100.0	100.0	100.0

TABLE 5.5. Summary of results for SY3 experimental set in Series 3

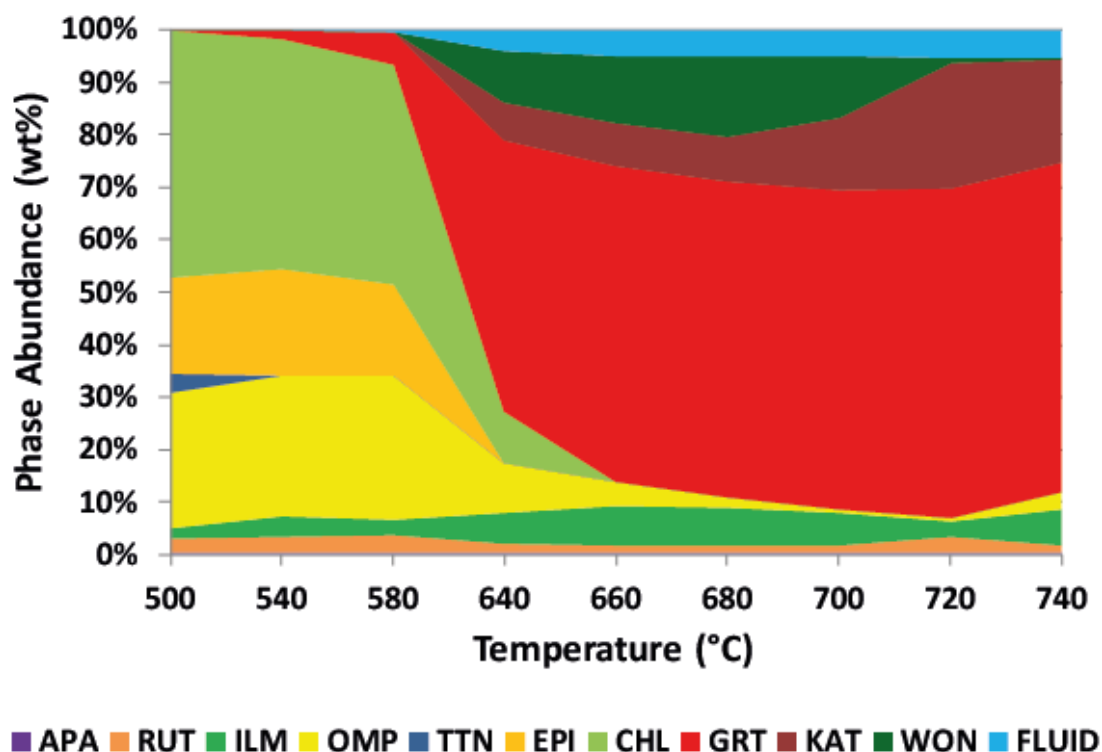


FIGURE 5.8: Phase abundance with increasing temperature in SY3 experimental set.

5.3.3. SAMPLE SY4 (MG#=0.68)

The SY4 experiments determined nine data points at 3.0 GPa encompassing a temperature range of 540°C to 800°C. Table 5.6 lists the experimental conditions and run products of these experiments.

Expt	Time	P	T	Run products
Number	(hrs)	(GPa)	(°C)	
C5142	192	3.0	540	chl, ilm, grt, ttn, cpx, rut, apa, mgt, fluid
C5139	196	3.0	580	chl, ilm, grt, cpx, rut, apa, mgt, ttn, fluid
C5124	164	3.0	620	chl, ilm, grt, cpx, rut, apa, mgt, ttn, fluid
C5110	120	3.0	660	chl, ilm, grt, cpx, rut, apa, mgt, fluid
C5107	48	3.0	700	chl, grt, ilm, rut, apa, mgt, fluid
C5150	120	3.0	720	chl, grt, ilm, rut, apa, ol, fluid, mgt, sp
C5162	120	3.0	740	chl, grt, ilm, rut, apa, ol, fluid, mgt, sp
C5136	120	3.0	760	chl, grt, ol, sp, fluid, ilm, rut, apa, mgt
D2011	120	3.0	800	grt, ol, sp, fluid, ilm, rut, apa, mgt

TABLE 5.6. Experimental conditions and run products for SY4 experimental set in Series 3

Run products – major (>5 wt%) in bold text; minor (1-5 wt%) in regular text; trace (<1 wt%) in italicized text.

5.3.3.1. *Changing phase relations with increasing temperature in SY4 set*

The bulk composition of the SY4 sample comprised predominantly chlorite with minor apatite, ilmenite and titanite as shown in Table 5.2b. The changing phase relations with increasing temperature have been illustrated with six microphotographs in Figure 5.9.

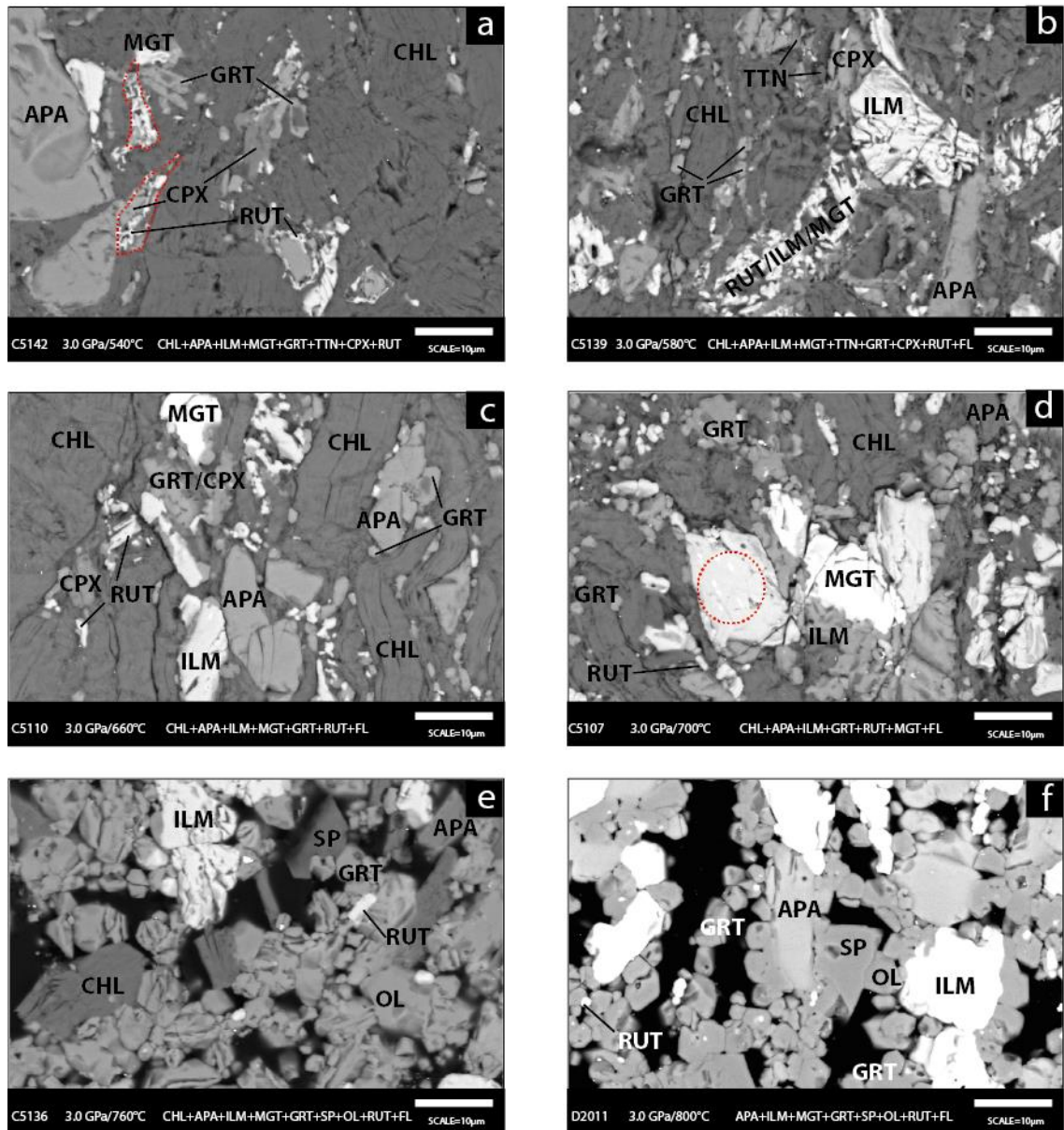


FIGURE 5.9. Changing phase relations by temperature in SY4 experiments.

a) 540°C Omphacite and epidote, present in the starting mix, have disappeared. Titanite is in the process of breakdown: b) 580°C Trace titanite remains. The Fe-Ti oxides commonly form an intercalated texture. c) 660°C Titanite has reacted out, cpx has reduced its modal abundance. In this view, cpx and grt form an intercalated texture. d) 700°C. Cpx has entirely disappeared following its reaction with chlorite. Ilm and mgt form larger grains. e) 760°C Chlorite has commenced breakdown. f) 800°C. Chlorite has disappeared.

At 540°C (Figure 5.9a), chlorite was the dominant phase, interspersed with grains of apatite. Titanite was approaching its upper thermal stability and was undergoing chemical reaction – grains appeared proximal to the newly-formed clinopyroxene and the Fe-Ti oxides ilmenite,

magnetite and rutile. These reaction products formed pseudomorphically in former titanite grains (see Figure 5.9a, marked by orange, dotted lines). Epidote and omphacite, present in the bulk composition, had disappeared by this temperature. At 580°C (Figure 5.9b), chlorite comprised >80wt% of the phases present. Only tiny grains of titanite remained, again proximal to the phases cpx and the three Fe-Ti minerals. Small crystals of garnet were present. At 660°C (Figure 5.9c), titanite had entirely reacted-out and only trace cpx remained. Ilmenite, rutile and magnetite formed as pseudomorphs in former titanite grains. Garnet crystals were larger and more plentiful. At 700°C (Figure 5.9d), cpx had entirely disappeared. Chlorite comprised <80wt% of the minerals present and apatite remained stable. Ilmenite and magnetite had formed larger grains whilst rutile still formed tiny, elongate grains. Magnetite formed exsolution lamellae within ilmenite grains (see Figure 5.9d, inside red circle). By 760°C (Figure 5.9e), chlorite was nearing its thermal maximum for this bulk composition. Garnet, olivine, spinel and fluid now became the stable phases after chlorite. The Fe-Ti oxides seemed unaffected by the temperature increase. By 800°C (Figure 5.9f), chlorite had been replaced by garnet, olivine and spinel. Ilmenite, magnetite and rutile maintained similar proportion as at lower temperature. Mass balance indicated that apatite comprised slightly reduced proportion at this temperature, possibly due to some grains forming inclusions in garnet (see Figure 5.9f).

5.3.3.2. *Textural analysis of SY4*

Experiments produced eleven run products which varied in accordance with temperature and stability fields. No melt was observed.

Chlorite (chl) was the dominant phase in the chlorite stability field and comprised large laths up to 50 µm in length and 30 µm in width which formed an agglomerated mass in run products. Chlorite textures were little affected by changes in temperature.

Three phases appeared in all run products. Garnet (grt) formed subhedral-euhedral grains which varied in size from 2-20 µm, with size increasing with increasing temperature. Smaller grains tended to be more euhedral and homogeneous in texture with larger grains increasingly poikiloblastic (see Figure 5.9f), especially following the disappearance of chlorite. Apatite (apa) ranged in appearance from subhedral elongate, bladed grains up to 50 µm in length (see Figure 5.9a) to short, anhedral-subhedral blocky grains 5-10 µm (see Figure 5.9e), consistent with relict textures from the starting material. All exhibited an homogenous appearance. Apatite co-existed with all other phases and no reaction rims were observed along grain boundaries. Ilmenite (ilm) typically possessed a blocky, subhedral appearance with a grain size between 5-

15 μm . Some grains possessed a heterogeneous texture (see Figure 5.9d) indicative of exsolution lamellae of co-existing magnetite.

At higher temperature ($>700^\circ\text{C}$), the commencement of chlorite decomposition was evidenced by the appearance of garnet, olivine and spinel as reaction products. Olivine (ol) grains varied between 2-10 μm , with grain size increasing with increasing temperature. Olivine was generally homogeneous in appearance with the occasional rim indicative of compositional variation (see Figure 5.9f). Olivine always grew proximal to the garnet and spinel phases. Spinel (sp) formed euhedral-subhedral grains of 4-16 μm with grain size strongly related to temperature. Spinel possessed an homogeneous appearance (see Figure 5.9f) indicative of the attainment of equilibrium.

Several phases occurred in only a few run products and in small quantities. Clinopyroxene was produced in four experimental runs following the breakdown of titanite. The small grain size, and proximity to garnet grains, made analysis difficult, although some larger crystals did form (see Figure 5.9b,c). Magnetite (mgt) formed anhedral grains ranging in size from 1-20 μm . This phase always occurred proximal to ilmenite, and exhibited an homogeneous texture. Titanite (ttn) was observed in two experimental runs (C1542 and C5139) where it formed subhedral, spear-like grains 5-10 μm in length (see Figure 5.9a, b). Titanite was close to its thermal maximum at 580°C and was in the process of reacting-out. Titanite co-existed with cpx, ilmenite, magnetite and rutile. Rutile (rut) was observed in two experiments (C1542 and C1539) although mass balance calculations indicated it was present in minor amounts in most runs. Rutile formed small subhedral, blocky grains ranging between 1-4 μm in length (see Figure 5.9a,c,d).

5.3.3.3. *Compositional analysis of SY4*

The SY4 experiments produced ten solid phases and one fluid phase as reaction products. All solid phases were analysed using FE-SEM. Table 5.7 provides representative analyses of each phase: a complete set of FE-SEM analyses can be found in the Chapter 5 Appendix.

Chlorite was the major phase in this experimental set. It maintained a consistent composition throughout with an Mg# a mean 0.68, described stoichiometrically as $(\text{Mg}_{3.38} \text{Fe}_{1.43} \text{Ca}_{0.01} \text{Mn}_{0.01}) \text{Al}_{2.28} \text{Si}_{2.88} \text{O}_{12} (\text{OH})_8$, near the mid-range of the clinochlore-chamosite solid solution. No significant correlation was observed between Mg# and temperature – any variation was within one standard deviation. The single exception to this pattern occurred with run C5136 (760°C) where the Mg# rose significantly to 0.84. Mass balance calculations indicated just 15.5 wt% of chlorite remained at this temperature, indicative of this phase approaching its thermal maximum. Chlorite of lower Mg# had already decomposed leaving only the high-Mg# chlorite.

With no evidence of newly-formed chlorite in this set of experiments, the high-Mg# chlorite must have been present in the starting mix.

Run	C5110		C5107		C5124		C5162		C5162		C5142		C5136		D2011		C5142		C5110	C5139
Mineral	APA		CHL		GRT		GRT		ILM		TTN		OL		SP		CPX		MGT	RUT
n	9		7		4		5		10		5		4		8		1		1	1
T	660		700		620		740		740		540		760		800		540		660	580
	Mean	SD	Mean	SD	Mean	SD	Mean	SD	Mean	SD	Mean	SD	Mean	SD	Mean	SD	Mean	Mean	Mean	
Wt%	H2O	1.71	0.01	11.71	0.12	0.00	0.00	0.00	0.00	0.00	0.00	0.00	0.00	0.00	0.00	0.00	0.00	0.00	0.00	0.00
	Na2O	0.00	0.00	0.03	0.04	0.04	0.07	0.00	0.00	0.00	0.00	0.02	0.04	0.00	0.00	0.00	0.00	0.20	0.00	0.00
	MgO	0.02	0.04	22.10	0.67	3.61	0.34	7.43	0.34	3.81	0.18	0.03	0.07	36.81	1.72	15.54	0.35	13.67	0.42	0.00
	Al2O3	0.01	0.03	18.55	0.67	19.07	0.53	20.96	0.53	0.13	0.11	0.25	0.06	0.21	0.23	60.86	1.16	1.87	0.00	0.00
	SiO2	0.15	0.06	28.03	0.59	37.86	0.81	38.95	0.69	0.07	0.08	30.65	0.29	37.40	1.14	0.35	0.21	51.78	0.00	0.00
	P2O5	42.40	0.42	0.02	0.06	0.55	0.34	0.28	0.36	0.00	0.00	0.00	0.00	0.14	0.24	0.02	0.05	0.16	0.00	0.00
	K2O	0.00	0.00	0.00	0.00	0.00	0.00	0.00	0.00	0.00	0.00	0.00	0.00	0.00	0.00	0.00	0.00	0.00	0.00	0.00
	CaO	53.68	0.36	0.14	0.05	18.74	0.86	12.48	1.47	0.30	0.11	27.02	0.36	0.11	0.06	0.08	0.07	22.61	0.34	0.00
	TiO2	0.09	0.11	0.10	0.09	1.18	0.16	0.93	0.73	49.90	0.72	39.34	0.35	0.35	0.41	0.67	0.20	0.34	0.64	97.85
	Cr2O3	0.00	0.00	0.00	0.00	0.00	0.00	0.00	0.00	0.00	0.00	0.00	0.00	0.00	0.00	0.00	0.00	0.00	0.00	0.00
	MnO	0.00	0.00	0.21	0.04	1.59	0.29	1.36	0.29	0.64	0.09	0.00	0.00	0.19	0.12	0.02	0.06	0.28	0.00	0.00
	FeO	0.73	0.12	17.05	0.57	15.29	1.04	18.03	0.84	37.17	0.41	1.32	0.28	24.74	1.55	18.93	0.50	9.01	0.00	1.31
	NiO	0.00	0.00	0.00	0.00	0.00	0.00	0.00	0.00	0.00	0.00	0.00	0.00	0.00	0.00	0.00	0.00	0.00	0.00	0.00
	Fe2O3	0.00	0.00	0.00	0.00	1.89	0.13	0.00	0.00	7.34	0.08	0.00	0.00	0.00	0.00	3.72	0.10	0.00	101.69	0.00
	Total	97.07	0.72	86.24	0.70	99.81	0.93	100.40	1.42	99.35	0.57	98.64	0.68	99.93	1.72	100.20	1.68	99.92	103.09	99.16
Cations	Na	0.00	0.00	0.01	0.01	0.01	0.01	0.00	0.00	0.00	0.00	0.00	0.00	0.00	0.00	0.00	0.01	0.00	0.00	
	Mg	0.00	0.01	3.38	0.08	0.42	0.04	0.84	0.04	0.14	0.01	0.00	0.00	1.45	0.04	0.61	0.01	0.76	0.02	
	Al	0.00	0.00	2.24	0.08	1.75	0.03	1.88	0.05	0.00	0.00	0.01	0.00	0.01	0.01	1.88	0.01	0.08	0.00	
	Si	0.01	0.01	2.87	0.04	2.95	0.04	2.97	0.04	0.00	0.00	1.01	0.01	0.99	0.01	0.01	0.01	1.94	0.00	
	P	3.15	0.01	0.00	0.01	0.04	0.02	0.02	0.02	0.00	0.00	0.00	0.00	0.00	0.01	0.00	0.00	0.01	0.00	
	K	0.00	0.00	0.00	0.00	0.00	0.00	0.00	0.00	0.00	0.00	0.00	0.00	0.00	0.00	0.00	0.00	0.00	0.00	
	Ca	5.04	0.03	0.02	0.01	1.56	0.06	1.02	0.11	0.01	0.00	0.96	0.01	0.00	0.00	0.00	0.00	0.91	0.01	
	Ti	0.01	0.01	0.01	0.01	0.07	0.01	0.05	0.04	0.93	0.01	0.98	0.01	0.01	0.01	0.01	0.00	0.01	0.01	
	Cr	0.00	0.00	0.00	0.00	0.00	0.00	0.00	0.00	0.00	0.00	0.00	0.00	0.00	0.00	0.00	0.00	0.00	0.00	
	Mn	0.00	0.00	0.02	0.00	0.10	0.02	0.09	0.02	0.01	0.00	0.00	0.00	0.00	0.00	0.00	0.00	0.01	0.00	
	Fe	0.05	0.01	1.46	0.06	1.00	0.07	1.15	0.06	0.77	0.01	0.04	0.01	0.55	0.04	0.41	0.01	0.28	0.00	
	Ni	0.00	0.00	0.00	0.00	0.00	0.00	0.00	0.00	0.00	0.00	0.00	0.00	0.00	0.00	0.00	0.00	0.00	0.00	
	Fe3	0.00	0.00	0.00	0.00	0.11	0.01	0.00	0.00	0.14	0.00	0.00	0.00	0.00	0.00	0.07	0.00	0.00	1.97	
	Total	8.26	0.02	10.00	0.01	8.00	0.01	8.01	0.01	2.00	0.01	3.00	0.00	3.00	0.01	3.00	0.00	4.01	2.00	
	Mg#	0.04	0.07	0.70	0.01	0.30	0.03	0.42	0.02	0.15	0.01	0.03	0.07	0.73	0.02	0.59	0.01	0.73	1.00	
Al#	0.00	0.00	1.00	0.00	0.94	0.00	1.00	0.00	0.03	0.02	1.00	0.00	0.00	0.00	0.96	0.00	1.00	0.00		

TABLE 5.7. Table of representative phase analyses for SY4 in in Series 3

Garnet was present in all run products and showed evidence of extensive compositional change with temperature. The Mg# ranged from 0.20 at 540°C to 0.55 at 800°C (see Figure 5.10a) which illustrated the changing composition from grossular-almandine garnet at low temperature to a pyrope-almandine rich garnet at high temperature (see Figure 5.10b). Small amounts of Fe³⁺ were accommodated by garnet at temperatures <700°C; above 700°C, however, no Fe³⁺ was required to obtain stoichiometric balance. All garnet scans contained between 0.5 and 2.0 wt% titanium, lower than stoichiometric proportions of Al and Si, and above stoichiometric

proportions of divalent cations, but a consistent total of 8.0 cations.

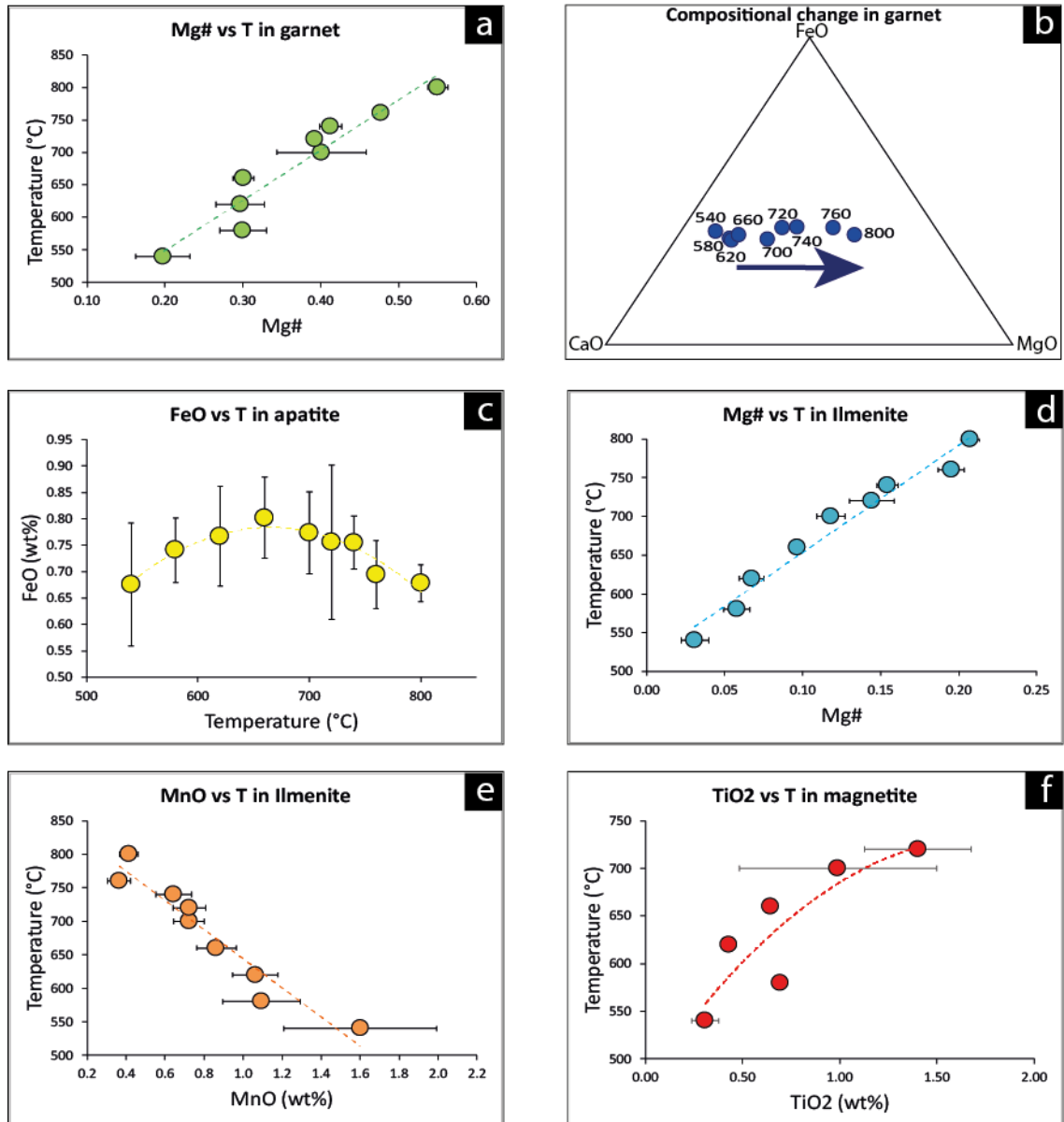


FIGURE 5.10. Relevant compositional plots for SY4 bulk composition in Series 3

a) Plot of Mg# vs T in garnet which shows a strong positive correlation. b) Plot of compositional change in garnet with temperature: garnet becomes increasingly Mg-rich with increasing temperature. c) Plot of FeO vs T in apatite which shows a strong, non-linear correlation. d) Plot of Mg# vs T in ilmenite which shows a strong positive correlation. e) Plot of MnO vs T in ilmenite which shows a strong, inverse correlation. f) Plot of TiO₂ vs T in ilmenite which shows a weak but positive, non-linear correlation.

Olivine first appeared at 720°C marking the beginning of the thermal decomposition of chlorite. The Mg# showed a strong correlation with temperature increasing from 0.68 at 720°C to 0.75 at 800°C. Spinel first appeared at 740°C in trace amounts. The Mg# displayed a significant increase with increasing temperature – from 0.49 at 760°C to 0.59 at 800°C.

The Fe-Ti oxides magnetite, ilmenite and rutile were present in trace to minor amounts in all experimental runs. Ilmenite showed an increase in Mg# with increasing temperature (see Figure 5.10d) indicating an increasing geikielite component. Several ilmenite grains showed evidence

of exsolution lamellae of magnetite (see Figure 5.9d), most pronounced at lower temperature runs. Magnetite was present in trace quantities, but analyses witnessed an increase in spinel and ulvöspinel components (see Figure 5.10f) with increasing temperature. Rutile formed minor quantities in most run products. The small grain size proved problematic for data collection purposes with only a single accurate scan obtained. It contained a little over 1.3 wt% FeO.

Apatite was present in all experimental runs. Its composition remained remarkably consistent across all experiments except for FeO and SiO₂, each of which showed a strong non-linear correlation with increasing temperature (see Figure 5.10c). Previous investigation of apatites from Syros indicate that the hydrous component was a mixture of hydroxylapatite and fluoroapatite and contained no Cl (Miller *et al.*, 2009).

Clinopyroxene formed as a run product from the breakdown of omphacite present in the bulk composition. Small grain size meant that few accurate analyses could be obtained. Nevertheless, Mg# was positively correlated with temperature: it increased from 0.73 at 540°C to 0.76 at 580°C.

Titanite was observed in a single experimental run at 540°C after which it disappeared having reached its maximum thermal stability.

5.3.3.4. Elemental partitioning in the SY4 set

A comparison of Mg# across co-existing phases in this experimental set yielded a consistent pattern of partitioning of the elements Mg and Fe. At low temperature in the cpx+ttn stability field, Mg partitioning occurred in the following sequence: *cpx* > *chl* > *grt* > *ilm*. Following the disappearance of cpx and ttn, the remaining phases followed the same partitioning order: *chl* > *grt* > *ilm*. In the chlorite stability field during the breakdown of chlorite, several new phases were included: *chl* > *ol* > *grt* > *sp* > *ilm*. At temperatures above the chlorite stability field, the sequence was modified to *ol* > *sp* > *grt* > *ilm* with Mg preferentially partitioning into spinel rather than garnet.

Whilst magnetite, rutile, titanite and apatite each contained Mg and Fe, the quantities were minute and so have been disregarded for this exercise.

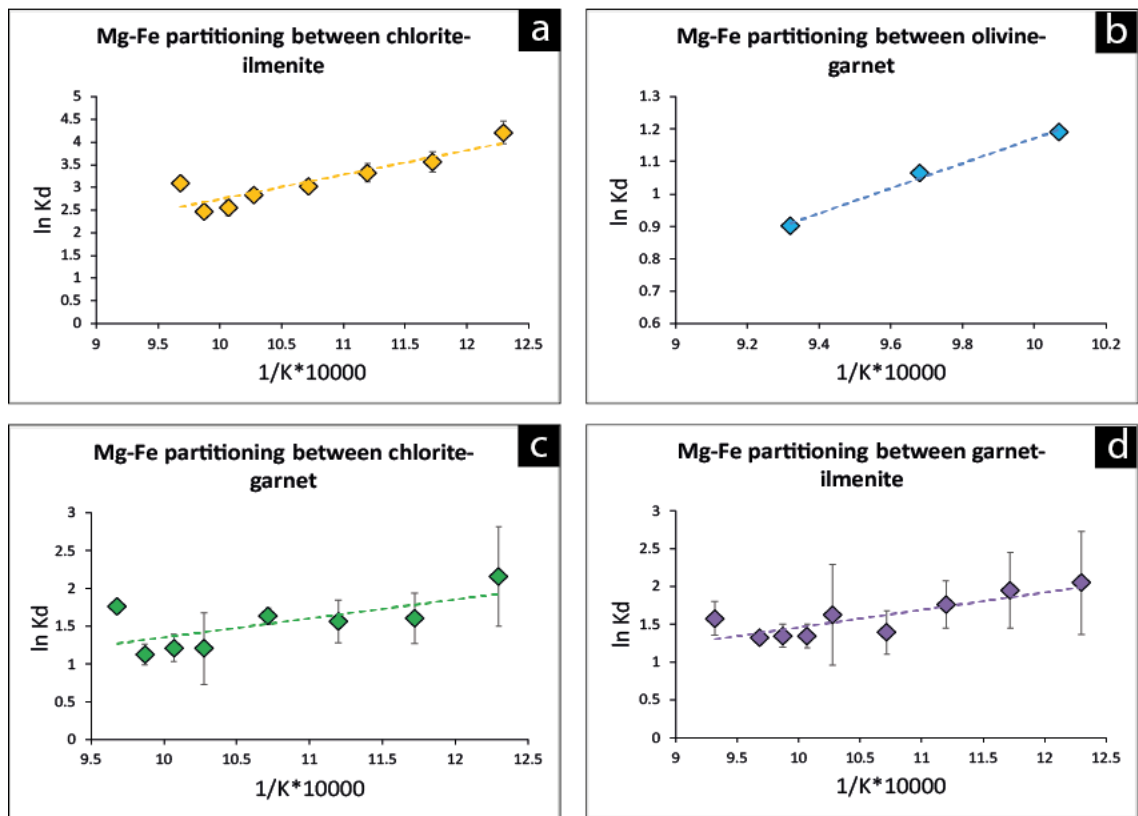


FIGURE 5.11. Relevant partitioning plots for SY4 bulk composition in Series 3 experiments

Figures a)-d) plot Mg-Fe partitioning between various coexisting phases, each showing strong correlation.

Figure 5.11 illustrated a selection of element partitioning plots arising from the SY4 experimental set.

Figures 5.11a-d plot Mg-Fe partitioning between co-existing phases, each of which show strong positive correlation. Figure 5.12a plotted Mg-Fe partitioning between chlorite and ilmenite using the $K_D = \frac{(X_{Mg}^{chl})(X_{Fe}^{ilm})}{(X_{Fe}^{chl})(X_{Mg}^{ilm})}$. It showed a strong correlation, evidence of Mg preferentially partitioning into chlorite over ilmenite but at a reduced rate with increasing temperature. Figure 5.11b explored Mg# partitioning between olivine and garnet using the coefficient $K_D = \frac{(X_{Mg}^{ol})(X_{Fe}^{grt})}{(X_{Fe}^{ol})(X_{Mg}^{grt})}$. Although only three data points were used, the trend was unmistakable: Mg preferentially partitioned into olivine over garnet but with increasing temperature, garnet sequestered increasing amounts of Mg. Mg# partitioning between chlorite and garnet was displayed in Figure 5.11c using the coefficient $K_D = \frac{(X_{Mg}^{chl})(X_{Fe}^{grt})}{(X_{Fe}^{chl})(X_{Mg}^{grt})}$. Whilst Mg always preferentially partitioned into chlorite over garnet, it was apparent that with increasing temperature increased quantities of Mg favoured the garnet phase. Figure 5.11d plotted Mg# partitioning between garnet and ilmenite using the coefficient $K_D = \frac{(X_{Mg}^{grt})(X_{Fe}^{ilm})}{(X_{Fe}^{grt})(X_{Mg}^{ilm})}$. The strong correlation shows that Mg preferentially partitioned into garnet over ilmenite but at a reduced rate with increasing temperature.

No relationship was observed with Mn-Fe partitioning between garnet and ilmenite using a recognised geothermometer (Powceby *et al.*, 1991). Two reasons are offered. Firstly, the low Mn:Fe ratio (1:11 and 1:40 respectively) meant that the geothermometer simply was not able to identify any inherent partitioning pattern. Secondly, the presence of titanium produced an unusual garnet stoichiometry which was not accommodated by this geothermometer. Experimental studies have shown (Ackerson *et al.*, 2017) that the incorporation of Ti into garnet can lead to a deficit of Al and Si cations and a surplus of divalent cations, as with the current results. This requires several unusual substitution mechanisms to achieve charge balance and this likely affects the precision of the thermometer.

5.3.3.5. Summary of findings from the SY4 experimental set

Expt	Number	C5142	C5139	C5124	C5110	C5107	C5150	C5162	C5136	D2011
Time	(hrs)	192	196	164	120	48	120	120	120	120
P	(GPa)	3.0	3.0	3.0	3.0	3.0	3.0	3.0	3.0	3.0
T	(°C)	540	580	620	660	700	720	740	760	800
PHASES	APA	4.7	4.7	4.7	4.7	4.6	4.7	4.7	3.2	3.1
	CHL	83.4	82.4	82.2	81.2	79.5	74.4	73.9	15.5	0.0
	ILM	3.9	3.2	3.0	3.6	3.7	3.7	3.6	3.6	3.5
	MGT	0.3	0.5	0.1	0.7	0.8	0.1	0.1	0.1	0.1
	TTN	1.9	0.6	0.1	0.0	0.0	0.0	0.0	0.0	0.0
	GRT	2.9	4.1	4.4	5.7	9.0	9.7	10.5	30.0	36.0
	OL	0.0	0.0	0.0	0.1	0.0	4.2	3.9	25.9	31.0
	SP	0.0	0.0	0.0	0.0	0.0	0.2	0.2	11.8	14.4
	CPX	1.8	2.4	3.3	1.8	0.0	0.0	0.0	0.0	0.0
	RUT	1.1	2.0	2.0	1.9	1.9	1.9	1.9	1.9	1.8
	H2O	0.1	0.1	0.2	0.2	0.4	1.1	1.1	8.0	10.0
	TOTAL		100.0	100.0	100.0	100.0	100.0	100.0	100.0	100.0

TABLE 5.8. Table of results for SY4 experiments in Series 3.

Table displays, for each run, the experimental conditions, run products and their modal proportions as determined by mass balance.

Phase relations and chemical composition of phases were used to determine mass balance of each phase at each temperature interval. The summary of findings is listed in Table 5.8. Figure 5.12 illustrates the changing abundance of phases with increasing temperature.

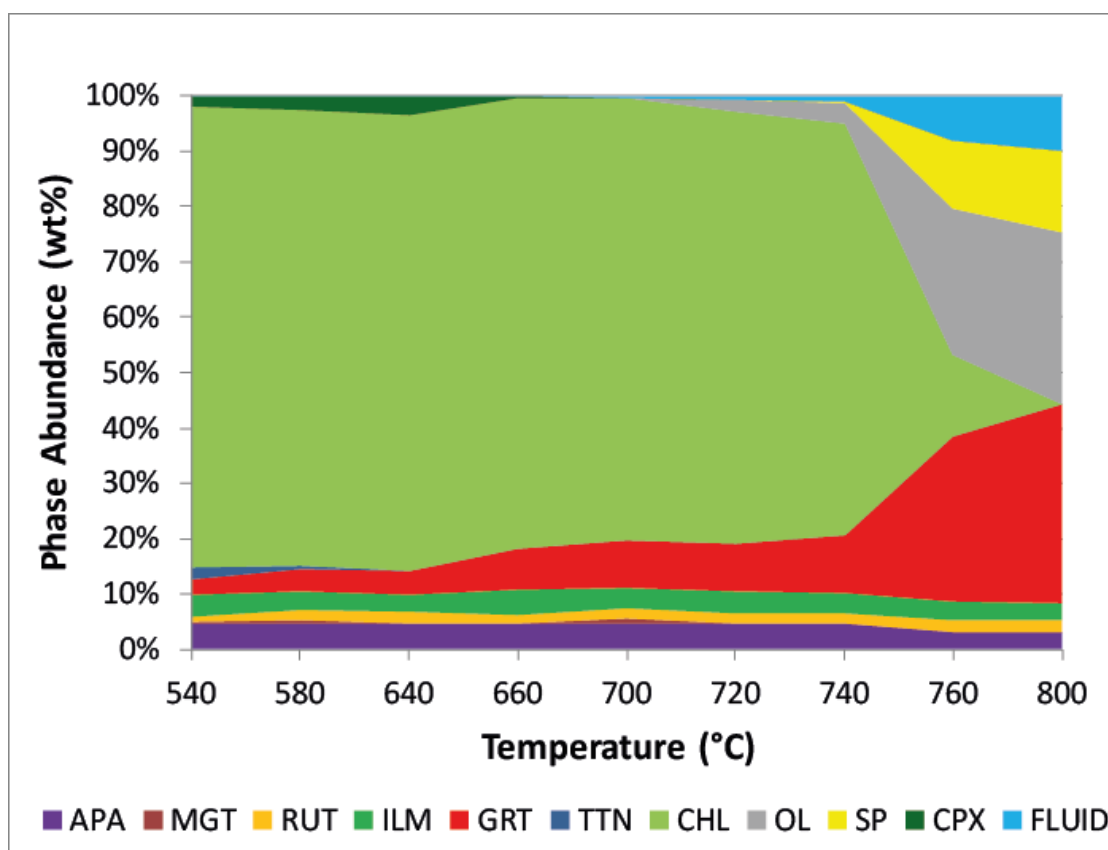


FIGURE 5.12. Changing phase relations by temperature in SY4 experiments.

5.3.4. HIGH TEMPERATURE SET (MG#=0.94)

Three isobaric (3.0 GPa) experiments were conducted between 1000°C and 1150°C to ascertain the onset of melting in an ultramafic chlorite. The starting mix was identical to that for Series 2 starting mix examined in Chapter 4. Table 5.9 lists the experimental conditions and run products of these experiments.

Time (hrs)	P (GPa)	T (°C)	Run products
69	3	1000	Grt, Ol, Fluid, Opx, Sp
120	3	1100	Grt, Ol, Fluid, Opx, Sp, melt
120	3	1150	Ol, Sp, Fluid, Melt

TABLE 5.9. Table of results for high temperature experiments in Series 3.

Run products – major (>5 wt%) in bold text; minor (1-5 wt%) in regular text; trace (<1 wt%) in italicized text.

5.3.4.1. Changing phase relations with increasing temperature in high temperature set

The bulk composition in this high temperature set comprised predominantly chlorite with pyrope garnet seeds added as nucleating agent as described in Table 4.2 (chapter 4). The changing phase relations with increasing temperature have been shown with six

microphotographs in Figure 5.13. We see unequivocal change in both phase relations and phase textures which track the development of melt.

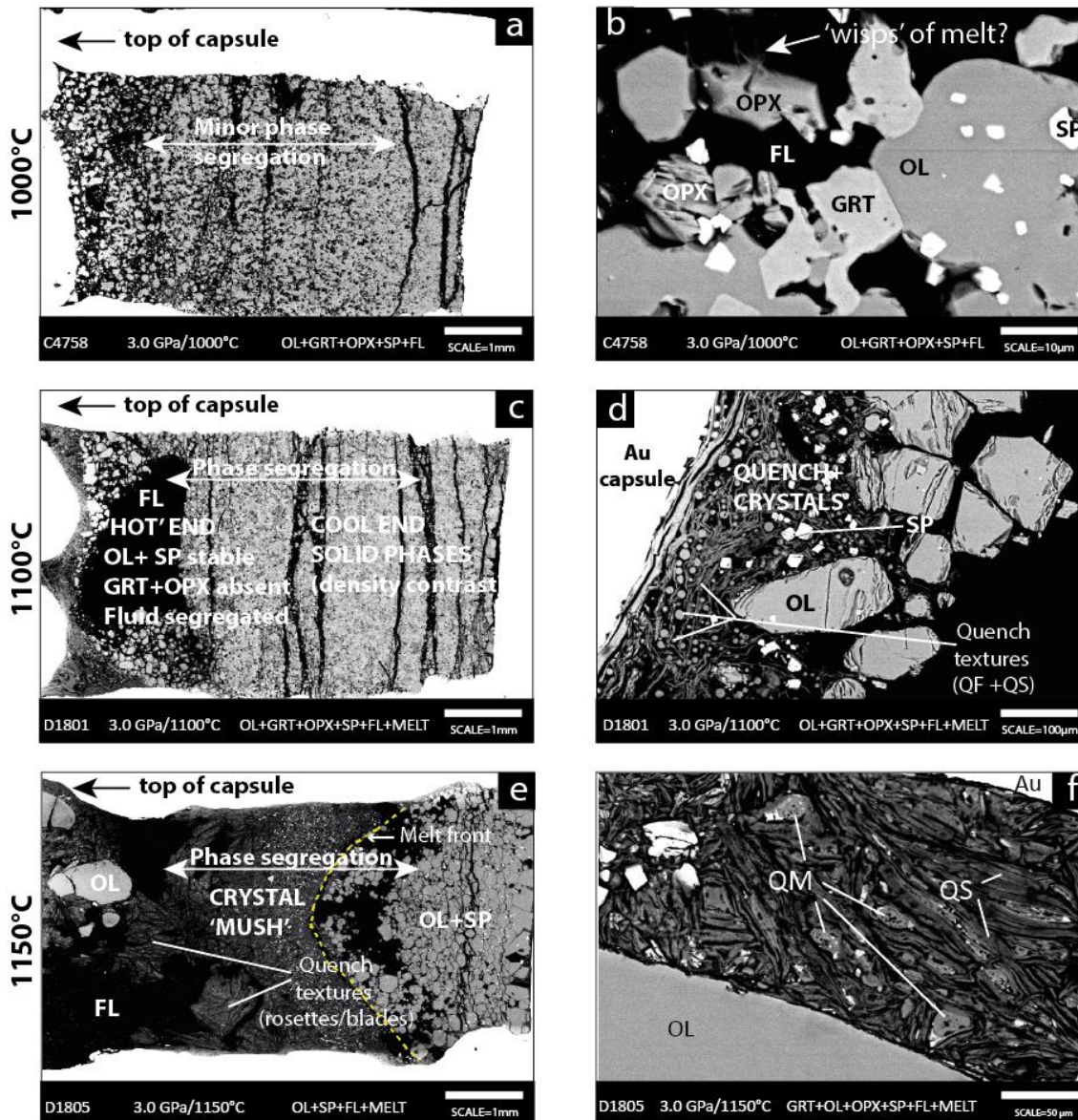


FIGURE 5.13. Changing phase relations and textures in high-temperature experiments.

1000°C. a) The capsule contents have a slight heterogeneous appearance. b) At larger scale, garnet, olivine, opx and spinel are in stable co-existence. **1100°C.** c) Capsule contents have developed a distinct heterogeneous texture. Fluid has aggregated at the hot end of the capsule. The denser phases such as garnet and spinel dominate the cold end. d) At 100 µm scale, quench textures, interpreted as both vapour quench ('fish eggs') and solute quench ('strings'), are observed at the top end. **1150°C.** e) Run products are well segregated in this view. Olivine and spinel are segregated at the cool end of the capsule. At the hot end, melt, fluid and crystals have formed a 'mush'. f) Garnet and opx have disappeared. Melt textures present in this view: QM refers to "quenched melt", identified by microvesicles throughout the anhedral shape. QS refers to "quench solute", identified by the sinuous crystalline shapes surrounding the melt.

At 1000°C, the run products of chlorite schist began to segregate within the capsule which created a slight heterogeneous appearance. The 'hot' top end of the capsule witnessed increased porosity compared with the 'cool' bottom end (see Figure 5.13a). This led to fluid aggregation in the upper capsule whilst the denser phases aggregated in the lower regions. Phase segregation is a potential precursor to the formation of melt. However, an examination

of capsule contents at large scale (Figure 5.13b, 10 μm scale bar) showed that each of the phases olivine, garnet, spinel and opx displayed equilibrated grain boundaries.

At 1100°C, a distinct transformation was apparent. At small scale (Figure 5.13c), the capsule contents developed a distinct heterogeneity, undergoing full segregation with the 'hot' end containing fluid and large crystals of olivine (Till *et al.*, 2012a) whilst the 'cool' end was the repository for the denser phases such as garnet and spinel. At larger scale (Figure 5.13d), the change in texture was unequivocal. Quench textures dominated the 'hot' end adjacent to the capsule walls. Numerous 'fish-egg' and 'string' features provided evidence of quench - the former presumed to be a solute quenched from vapour whilst the latter represents a solute quenched from either vapour or melt (Mibe *et al.*, 2011; Green *et al.*, 2012; Till *et al.*, 2012a). At the 'cool' end, none of these quench textures were observed.

At 1150°C, phase segregation was even more pronounced. The bottom section, which contained the phases olivine and spinel, comprised $\sim 1/3$ of the entire capsule. Large olivine crystals remained at the top end proximal to fluid. Most capsule contents formed in the central section which contained a mixture of fluid, melt and crystal 'mush'. Quenched melt (QM) is observed for the first time (Figure 5.13f) along with other quench textures. In addition to the 'fish egg' and 'string' textures found at lower temperature, large rosette shapes and bladed crystals added to the variety (see Figure 5.13e). At larger scale (see Figure 5.18b), melt was observed forming at an intergranular level distal from capsule walls. No opx or garnet was observed at this temperature.

5.3.4.2. Textural analysis of high temperature set

Olivine grains increased in size with temperature - typically, they were 10-30 μm at 1000°C and $>200 \mu\text{m}$ at 1150°C. Spinel inclusions provided a poikiloblastic appearance. Grains exhibited a generally subhedral appearance at all temperature intervals; however, contacts with solid phases sometimes formed euhedral edges and anhedral boundaries when contacting fluid (see Figure 5.13b).

Spinel formed subhedral-euhedral crystals 5-10 μm across at 1000°C increasing to $>30 \mu\text{m}$ by 1150°C. It displayed equilibrated textures with olivine in all views.

Garnet formed subhedral-euhedral crystals $>10 \mu\text{m}$ in diameter at 1000°C. They frequently possessed a poikiloblastic appearance. At 1100°C, the denser garnet phase was segregated to the cooler end of the capsule, as evidenced by their absence at the 'hot' top of the capsule (see Figure 5.13c). It increasingly adopted an anhedral appearance and a decrease in size. Mass balance saw a decline in modal proportion at this temperature. At 1150°C, garnet was no longer

stable; remnant grains were identified in the central 'mush' region of the capsule confirmed by FE-SEM analyses that they no longer possessed the composition of stoichiometric garnet. Mass balance confirmed the absence of garnet at 1150°C.

Opx was scarce at all temperatures in this series. When observed at temperatures <1100°C, grains possessed a subhedral appearance, were distinctly poikiloblastic but co-existed in stable form with olivine, garnet and spinel. At temperatures >1100°C, opx was segregated to the cooler end of the capsule and underwent melting. By 1150°C, no opx was observed, confirmed by mass balance which indicated this phase had entirely disappeared by this stage.

5.3.4.3. Compositional analysis of high temperature phases

The high temperature experiments produced four solid phases and two fluid phases as reaction products. All solid phases were analysed using FE-SEM. Table 5.10 provides representative analyses of each solid phase: a complete set of FE-SEM analyses can be found in the Appendix.

Each of the four phases present in the high temperature set of experiments displayed compositional change with increasing temperature, with the largest change corresponding to the commencement of melting.

Olivine maintained a consistent Mg# at 0.95 at both 1000°C and 1100°C, but increased to 0.97 by 1150°C. The increase in the forsterite component mirrored the commencement of melting (at the intergranular level) as described above.

Garnet displayed an increase in pyrope component with increasing temperature, evidenced by the Mg# rising from 0.90 to 0.91. It also showed an increase in the Cr# from 0.06 at 1000°C to 0.07 to 1100°C.

Spinel showed a marked increase in Mg# over the 150°C temperature increase, from 0.79 at 1000°C to 0.91 at 1150°C. An inverse pattern was observed with the Cr# - it decreased from 0.46 at 1000°C to 0.25 at 1150°C. The largest move occurred between 1100°C and 1150°C: Mg# 0.81-0.91, and Cr# 0.47-0.25, which corresponded with the modal decline of the garnet and opx phases.

The Mg# of opx increased from 0.95 at 1000°C to 0.96 at 1100°C. Across the same temperature interval, there was a decrease in Cr# from 0.15 to 0.11. This compositional change mirrored the disappearance of opx through melting.

	Run	C4758		D1801		D1801		D1801	
	Phase	SP		OL		EN		GRT	
	n	7		8		5		9	
	P (GPa)	3		3		3		3	
	T (°C)	1000		1100		1100		1100	
		Mean	SD	Mean	SD	Mean	SD	Mean	SD
Wt%	Na ₂ O	0.00	0.00	0.00	0.00	0.00	0.00	0.01	0.03
	MgO	18.85	0.76	53.29	0.56	35.90	0.65	25.05	0.47
	SiO ₂	0.00	0.00	41.69	0.40	56.21	0.68	43.11	0.46
	Al ₂ O ₃	31.72	1.69	0.04	0.06	2.95	0.12	22.27	0.46
	NiO	0.00	0.00	0.03	0.07	0.00	0.00	0.00	0.00
	FeO	8.83	0.25	4.66	0.13	2.99	0.10	4.26	0.13
	MnO	0.00	0.00	0.00	0.00	0.00	0.00	0.04	0.07
	Cr ₂ O ₃	40.33	2.21	0.00	0.00	0.52	0.14	2.60	0.44
	CaO	0.00	0.00	0.01	0.03	0.34	0.04	2.46	0.15
	TiO ₂	0.27	0.06	0.00	0.00	0.00	0.00	0.00	0.00
	Total	100.00	0.00	99.73	0.99	98.91	1.28	99.77	1.01
	Cations	Na	0.00	0.00	0.00	0.00	0.00	0.00	0.00
Mg		0.80	0.03	1.90	0.01	1.84	0.01	2.60	0.02
Si		0.00	0.00	1.00	0.00	1.93	0.00	3.00	0.01
Al		1.07	0.05	0.00	0.00	0.12	0.00	1.83	0.03
Ni		0.00	0.00	0.00	0.00	0.00	0.00	0.00	0.00
Fe		0.21	0.01	0.09	0.00	0.09	0.00	0.25	0.01
Mn		0.00	0.00	0.00	0.00	0.00	0.00	0.00	0.00
Cr		0.91	0.06	0.00	0.00	0.01	0.00	0.14	0.03
Ca		0.00	0.00	0.00	0.00	0.01	0.00	0.18	0.01
Ti		0.01	0.00	0.00	0.00	0.00	0.00	0.00	0.00
Total		3.00	0.01	3.00	0.00	4.00	0.00	8.01	0.01
Mg#		0.79	0.01	0.95	0.00	0.96	0.00	0.91	0.00
Cr#	0.46	0.03	0.00	0.00	0.11	0.03	0.07	0.01	

TABLE 5.10. Table of representative phase analyses for high temperature set in Series 3

5.3.4.4. Partitioning in the high temperature set

The three high temperature experiments showed a consistent pattern of Mg-Fe partitioning. At temperatures below 1100°C, the partitioning sequence was *opx* > *ol* > *grt* > *sp*. Above 1100°C following the disappearance of *opx*, Mg partitioning continued to follow the same sequential order: *ol* > *grt* > *sp*.

Figure 5.14a plotted Mg# partitioning between garnet and spinel following the breakdown of chlorite. Whilst Mg always showed an affinity for garnet over spinel, the strong correlation was evidence of spinel becoming increasingly Mg-rich with increased temperature. Figure 5.14b showed the result of Mg# partitioning between garnet and olivine. Mg preferentially partitioned into olivine over garnet in all instances. However, the absence of a significant slope in the plot indicated that Mg partitioning between these two phases did not change with increasing temperature following the disappearance of chlorite. Mg# partitioning between olivine and spinel following chlorite breakdown in the garnet stability field was displayed in Figure 5.14c.

Whilst Mg partitioning always favoured olivine over spinel, the strong correlation indicated that Mg increased its partitioning into the spinel phase with increasing temperature. Figure 5.14d examined Mg# partitioning between olivine and orthopyroxene after chlorite breakdown. Chemical analyses showed that Mg partitioning marginally favoured opx over olivine. The absence of slope indicated that Mg partitioning between the two phases underwent no significant change with increasing temperature.

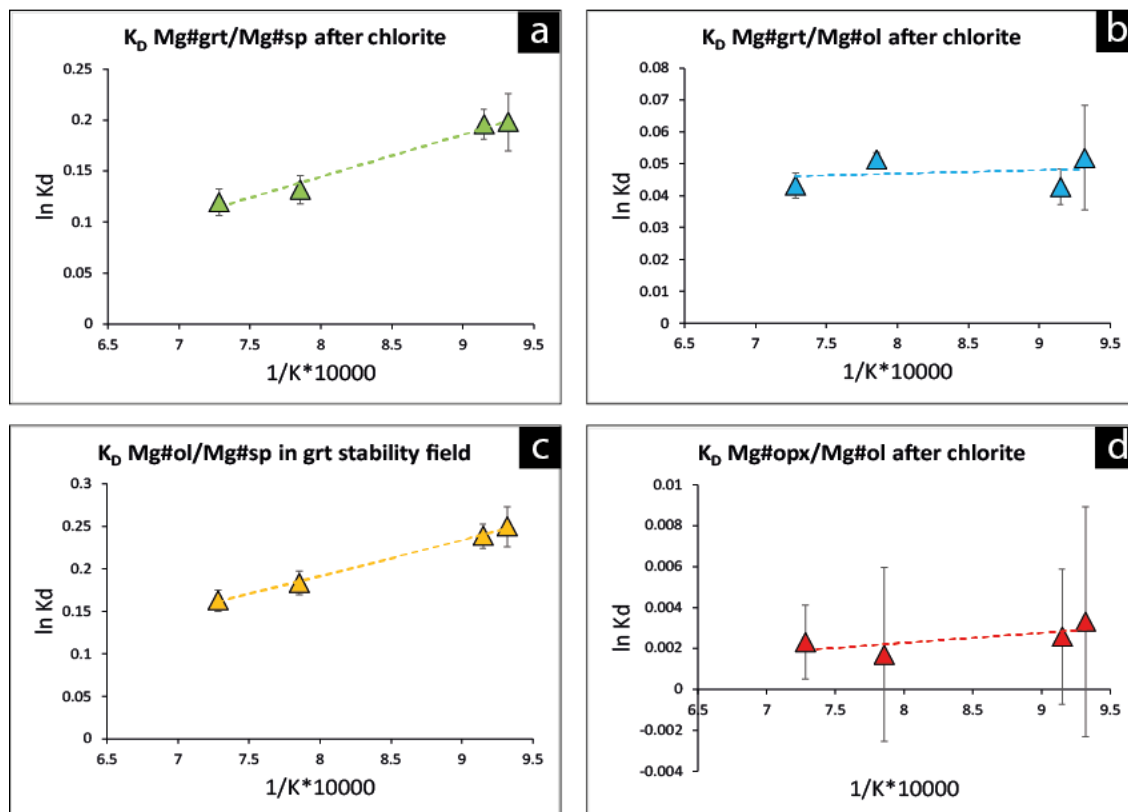


FIGURE 5.14. Relevant partitioning plots for high temperature set in Series 3 experiments

Figures 5.14a-d illustrates Mg# partitioning between various co-existing phases following the breakdown of chlorite in the high temperature experimental set. Partitioning involving spinel shows a positive correlation. Other phases show no change in partitioning behaviour with increased temperature.

Al-Cr partitioning also exhibited a consistent pattern throughout this experimental set as follows: $sp > opx > grt$. With the disappearance of the opx and garnet phases after 1100°C, spinel remained the only Al/Cr-bearing phase.

5.3.4.5. Summary of findings from the high temperature experimental set

Phase relations and chemical composition of phases were used to determine mass balance of each phase at each temperature interval. The summary of findings is listed in Table 5.11.

Figure 5.15 shows the changing phase abundance with increasing temperature.

Expt	Number	C4758	D1801	D1805
Time	(hrs)	69	120	120
P	(GPa)	3	3	3
T	(°C)	1000	1100	1150
PHASES	OL	39.7	40.1	56.9
	EN	1.8	1.5	0.0
	GRT	46.5	42.7	0.0
	SP	0.6	1.8	10.9
	FLUID	11.4	11.4	11.2
	MELT	0.0	2.4	21.0
	TOTAL	100.0	100.0	100.0

TABLE 5.11. Table of results for high temperature experiments in Series 3.

Table displays, for each run, the experimental conditions, run products and their modal proportions determined by mass balance. Note that the modal proportions for the melt phase are estimates only.

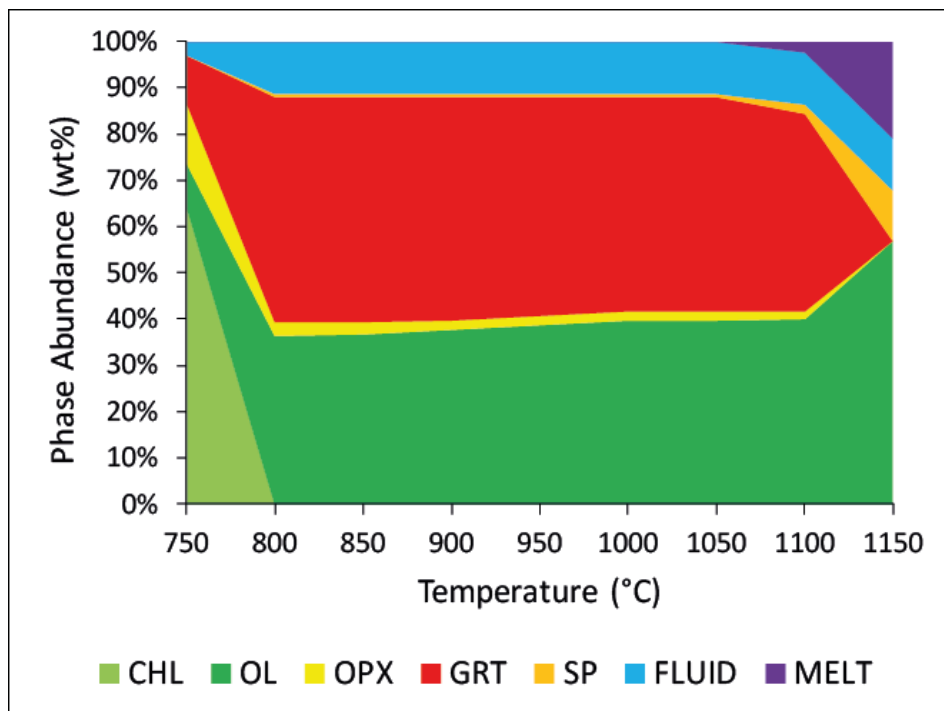


FIGURE 5.15. Changing phase abundance with temperature in high-temperature experimental set.

5.4. DISCUSSION

The discussion will comprise three parts. The first examines the approach to equilibrium. The second part delves into the details of the mélange diapir model proposed by Marschall and Schumacher (Marschall and Schumacher, 2012) investigating the stability of mafic chlorite schist from Syros and the density of these rocks to test the feasibility of their model. The third part explores the work of Till (Till *et al.*, 2012a), examining their criteria for determining melt in chlorite peridotite and the location of the wet peridotite solidus. The results of the current study will be used to test the validity of their findings.

5.4.1. APPROACH TO EQUILIBRIUM

Low temperature experiments tend to be characterised by sluggish kinetics which make reversal experiments, the classic method to prove the attainment of equilibrium, unworkable. Nevertheless, several alternative techniques were used to confirm phase equilibrium.

Textural observations in all three sets of experiments in this series revealed euhedral grain boundaries (see Figure 5.5e and 5.9c,e) and triple junction contacts (see Figure 5.14f) especially between garnet-olivine and spinel-olivine following the disappearance of chlorite. These textures provide a simple confirmation of local equilibrium. Poikiloblastic grains typically indicate that a phase is not fully equilibrated. Whilst garnet and ilmenite frequently possessed a poikiloblastic appearance, multiple scans of the region surrounding an inclusion resulted in analyses which were remarkably consistent. Small error bars in compositional plots further illustrated the limited chemical variation in point analyses (see Figures 5.6a,c and 5.10a,c,e). Garnet often forms zoned crystals reflecting either the incomplete resorption of relict pyrope cores, or the progression of garnet growth of varied composition. Either pathway produces garnet crystals which are not entirely homogeneous. Multiple analyses of the outer rims of garnet proved to be quite chemically homogeneous, marking a distinct boundary between rim and core (see Figure 5.5 e,f and 5.9d), thus showing local equilibrium had been attained.

Extensive chemical analysis of each phase showed a consistent variation in composition with increasing temperature, a pattern expected in this experimental series. Generally, experiments were separated by a narrow temperature interval (20°C-40°C) which enabled phase boundaries to be tightly bracketed. The presence of a phase at one data point and its absence at the next, or vice-versa, indicated that a chemical reaction had proceeded to completion, evidence of equilibrium having been achieved (see chlorite in Table 5.5 and olivine in Table 5.8).

A strong indication of the attainment of equilibrium is revealed by patterns of major element partitioning between co-existing phases. In each of the three sets of experiments in this series, partitioning plots showed high levels of correlation and so provided convincing evidence of equilibrated phases. In the SY3 set, Mg-Fe partitioning between omphacite, garnet, chlorite, ilmenite and magnesiokatophorite showed a strong relationship; indeed, several plots displayed almost perfect correlation (see Figure 5.7b,c), a robustness which could only occur if phases were well-equilibrated. In the SY4 set, Mg-Fe partitioning plots between chlorite-ilmenite and garnet-ilmenite were highly correlated (see Figure 5.9a,c,d). The plot which illustrated partitioning between Fe in garnet and Mn in ilmenite (see Figure 5.9f) showed an almost perfect correlation and matched well a previously published geothermometer (Powceby *et al.*, 1991). In the high temperature set, partitioning plots of the garnet-olivine and opx-olivine pairs (Figure

5.14b,d) illustrated no change in partitioning behaviour over a 200°C interval, indicative of no phase changes in that temperature range. The highly correlated trend which was observed with the garnet-spinel partitioning plot, however, was due to the growth of spinel at the expense of garnet with increasing temperature (see Figure 5.14a).

There was no evidence of Fe loss to the capsule in experimental runs, confirmed by mass balance calculations; this meant that the oxygen fugacity remained close to the Ni-NiO buffer throughout.

5.4.2. MAFIC CHLORITE SCHIST FROM SYROS, GREECE

This study will investigate two of the assumptions made by Marschall and Schumacher on the behaviour of chlorite. Firstly, what is the maximum thermal stability of chlorite mélange of varying composition? Secondly, is the density contrast between chlorite mélange and peridotite sufficient to drive diapiric rise? Each of these questions will be addressed in turn. Finally, the veracity of the mélange diapir model will be examined in light of these results.

5.4.2.1. Stability of mafic chlorite schist from Syros, Greece

Samples SY3 and SY4 were sourced from Syros in Greece, chosen as typical examples of chlorite schist from this location. As suggested by their identifiers, SY3 with an Mg# of 0.50 was characteristic of a Zone III assemblage, whilst SY4 with an Mg# of 0.68 was likely representative of a Zone IV rock type (Miller *et al.*, 2009; Pogge von Strandmann *et al.*, 2015).

SY3 and SY4 were used to experimentally determine the maximum thermal stability of the low Mg# chlorite. These results added to the experimental findings of high Mg# chlorite determined in Chapter 4.

Figure 5.16 plotted three chlorite compositions, each with different Mg#, against temperature which illustrated three key aspects of the stability of mafic chlorite schists. The first, represented by the triangle symbols, plotted the maximum thermal stability of chlorite in a bulk composition dominated by the chlorite phase. The second and third involved chlorite stability in a chlorite-rich schist which co-exists with plentiful omphacite and/or clinopyroxene, a typical bulk composition in a subducted slab. The diamond symbols marked the upper boundary of the chl+cpx reaction and thus the thermal maximum of chlorite. The square symbols marked the lower boundary of the chl+cpx reaction and the thermal minimum of chl+cpx field and the introduction of the garnet phase.

The results of experimental set SY4 (Mg#=0.68) revealed that chlorite attained a maximum thermal stability of ~780°C prior to its breakdown (blue triangle). Co-existing cpx disappeared ~680°C following its reaction with chlorite (blue diamond). Experimental set SY3 (Mg#=0.50) exhibited a slightly reduced stability field. Due to the bulk composition, chlorite disappeared near 650°C (red diamond) following its reaction with omphacite. Although the chlorite thermal maximum could not be ascertained in this set of experiments, it would be expected to occur near 765°C (red triangle). As a point of comparison, the experimental results on ultramafic chlorite stability from Series 2 were also plotted in Figure 5.16. The maximum thermal stability of chlorite (Mg#=0.94) occurred ~790°C (green triangle). The cpx-out temperature was located near 745°C.

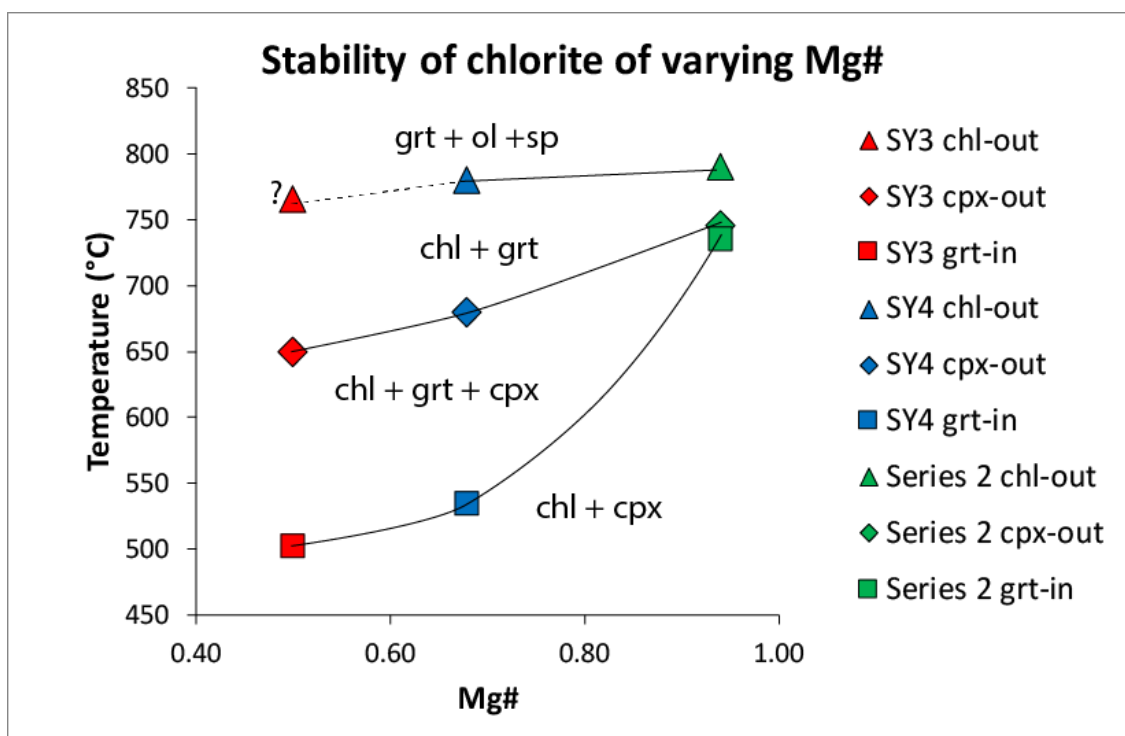


FIGURE 5.16. Maximum stability of chlorite of different Mg#

Results of three sets of chlorite experiments of differing Mg#. For each experimental set, three key locations are displayed: the maximum thermal stability of chlorite (triangular symbol), the upper boundary of the chl+cpx reaction (diamond symbol, relevant to Ca-bearing systems), and the lower boundary of the chl+cpx reaction (square symbol). The maximum chlorite point in the SY3 set is estimated since this could not be determined experimentally. Note the widening of the field between the two reactions as Mg# reduces – the classic banana-shaped plot.

These results confirm that as the quantity of Fe in chlorite increased, the thermal maximum of chlorite reduced – from 790°C (Mg#=0.94) to 765°C (Mg#=0.50). In omphacite/cpx-rich chlorite schists, this reduction was even more pronounced: from 745°C (Mg#=0.94) to 650°C (Mg#=0.50). The overall effect is clearly observed in Figure 5.16. As the Mg# of two common schist compositions decreases, the chlorite stability gap broadened.

The significance of these findings is that chlorite schist of either mafic composition would fully dehydrate at 3.0 GPa between 680°C and 780°C. This would lead to the escape of the entire fluid component from chlorite schist, along with its chemical “signature”, at temperatures below the melting of the garnet peridotite.

More broadly, these results show that monomineralic chlorite schists have greater thermal stability than veins and fissures of chlorite schist which form proximal to eclogite-rich minerals in the slab. The stability of chlorite in mafic systems stands in clear contrast to ultramafic chlorite as examined in previous chapters.

5.4.2.2. Density of mafic chlorite schist

The experimental results of sets SY3 and SY4 indicated that the breakdown of mafic chlorite schist at sub-arc depths (3.0 GPa) with increasing temperature produced a garnet peridotite of higher density than the average lherzolite or harzburgite already present in the hanging wall of the mantle wedge.

Table 5.12a and b provides the average density of chlorite schist at each experimental point in set SY3 and SY4 respectively. Density of average peridotite has been based on published data (Schmidt and Poli, 1998). Full calculations are provided in the Appendix.

Results from the SY3 set showed that the density of chlorite schist experienced a gradual increase with increasing temperature which correlated with the modal increase of the garnet and fluid phases (see Figure 5.17). At 500°C, density of the run products registered 3.22 g/cm³. This was lower than the average density of the harzburgite (3.29 g/cm³) or lherzolite (3.30 g/cm³) in the hanging wall of the mantle wedge. Between 580°C and 640°C, however, a large jump in density was registered. As the proportion of garnet rose from 6.1 wt% to 51.5 wt% and free fluid from 0.6 g/cm³ to 4.0 g/cm³ over this temperature interval, so too did the density of the bulk composition rise from 3.27 g/cm³ to 3.54 g/cm³. At this temperature, although ~10 wt% of chlorite remained, the products already registered significantly higher density than the overhanging peridotite. With the disappearance of chlorite, the density of the former schist remained high, varying between 3.59 – 3.63 g/cm³.

Expt Time	Run (hrs) (GPa) (°C)	MW	Mean density (p)	C5159 Rel. density 192 wt% p	C5138 Rel. density 192 wt% p	C5127 Rel. density 192 wt% p	D2036 Rel. density 120 wt% p	C5143 Rel. density 168 wt% p	C5114 Rel. density 120 wt% p	C5137 Rel. density 120 wt% p	D2021 Rel. density 120 wt% p	D2013 Rel. density 120 wt% p
	APA	502.30	3.19	0.6 0.02	0.6 0.02	0.6 0.02	0.6 0.02	0.6 0.02	0.6 0.02	0.6 0.02	0.6 0.02	0.6 0.02
*	CHL	634.66	2.93	47.3 1.38	43.7 1.28	42.0 1.23	9.7 0.28	0.0 0.00	0.0 0.00	0.0 0.00	0.0 0.00	0.0 0.00
	EPI	519.59	3.45	18.3 0.63	20.4 0.70	17.3 0.60	0.0 0.00	0.0 0.00	0.0 0.00	0.0 0.00	0.0 0.00	0.0 0.00
	ILM	151.71	4.72	1.9 0.09	3.9 0.19	3.0 0.14	5.8 0.28	7.6 0.36	7.2 0.34	6.2 0.29	3.1 0.14	6.9 0.33
	OMP	209.78	3.34	26.0 0.87	26.9 0.90	27.2 0.91	9.5 0.32	4.4 0.15	2.0 0.07	0.7 0.02	0.7 0.02	3.2 0.11
	TTN	196.03	3.48	3.3 0.12	0.0 0.00	0.0 0.00	0.0 0.00	0.0 0.00	0.0 0.00	0.0 0.00	0.0 0.00	0.0 0.00
*	GRT	403.14	3.74	0.0 0.00	1.5 0.06	6.1 0.24	51.5 2.00	60.3 2.34	60.3 2.34	60.7 2.37	62.2 2.44	62.8 2.46
	KAT	819.86	3.35	0.0 0.00	0.0 0.00	0.0 0.00	7.3 0.24	8.3 0.28	8.5 0.28	13.8 0.46	24.3 0.81	19.7 0.66
	WON	857.26	3.35	0.0 0.00	0.0 0.00	0.0 0.00	9.9 0.33	12.8 0.43	15.4 0.52	11.7 0.39	1.0 0.03	0.2 0.01
	RUT	79.87	4.25	2.4 0.10	2.7 0.11	3.2 0.14	1.6 0.07	1.1 0.05	1.1 0.05	1.2 0.05	2.8 0.12	1.2 0.05
	H2O	18.02	1.00	0.0 0.00	0.3 0.00	0.6 0.01	4.0 0.04	4.9 0.05	4.9 0.05	5.0 0.05	5.3 0.05	5.4 0.05
TOTAL				100.0 3.22	100.0 3.26	100.0 3.27	100.0 3.54	100.0 3.62	100.0 3.61	100.0 3.61	100.0 3.59	100.0 3.63
*	Lherzolite - av. density			3.30 3.30	3.30 3.30	3.30 3.30	3.30 3.30	3.30 3.30	3.30 3.30	3.30 3.30	3.30 3.30	3.30 3.30
*	Harzburgite - av. density			3.29 3.29	3.29 3.29	3.29 3.29	3.29 3.29	3.29 3.29	3.29 3.29	3.29 3.29	3.29 3.29	3.29 3.29

a

SY3

Expt Time	Run (hrs) (GPa) (°C)	MW	density	C5142 Rel. density 192 wt% p	C5139 Rel. density 196 wt% p	C5124 Rel. density 164 wt% p	C5110 Rel. density 120 wt% p	C5107 Rel. density 48 wt% p	C5150 Rel. density 120 wt% p	C5162 Rel. density 120 wt% p	C5136 Rel. density 120 wt% p	D2011 Rel. density 120 wt% p
	APA	502.30	3.19	4.7 0.15	4.7 0.15	4.7 0.15	4.7 0.15	4.6 0.15	4.7 0.15	4.7 0.15	3.2 0.10	3.1 0.10
*	CHL	606.27	2.83	83.4 2.36	82.4 2.33	82.2 2.32	81.2 2.29	79.5 2.25	74.4 2.10	73.9 2.09	15.5 0.44	0.0 0.00
	ILM	151.71	4.72	3.9 0.18	3.2 0.15	3.0 0.14	3.6 0.17	3.7 0.17	3.7 0.17	3.6 0.17	3.6 0.17	3.5 0.17
	MGT	391.22	5.15	0.3 0.01	0.5 0.02	0.1 0.01	0.7 0.04	0.8 0.04	0.1 0.01	0.1 0.01	0.1 0.01	0.1 0.01
	TTN	196.03	3.48	1.9 0.07	0.6 0.02	0.1 0.00	0.0 0.00	0.0 0.00	0.0 0.00	0.0 0.00	0.0 0.00	0.0 0.00
*	GRT	140.70	3.27	0.0 0.00	4.1 0.16	4.4 0.17	5.8 0.22	9.0 0.35	9.7 0.37	10.5 0.40	30.0 1.16	36.0 1.39
	OL	142.27	3.64	0.0 0.00	0.0 0.00	0.0 0.00	0.0 0.00	0.0 0.00	4.2 0.15	3.9 0.14	25.9 0.93	31.0 1.10
*	SP	216.55	3.40	1.8 0.06	2.4 0.08	3.3 0.11	1.8 0.06	0.0 0.00	0.2 0.01	0.2 0.01	11.8 0.45	14.4 0.54
	CPX	79.87	4.25	1.1 0.04	2.0 0.09	2.0 0.09	1.9 0.08	1.9 0.08	1.9 0.08	1.9 0.08	1.9 0.08	1.8 0.08
	RUT	79.87	4.25	1.1 0.04	2.0 0.09	2.0 0.09	1.9 0.08	1.9 0.08	1.9 0.08	1.9 0.08	1.9 0.08	1.8 0.08
	H2O	18.02	1.00	0.1 0.00	0.1 0.00	0.2 0.00	0.2 0.00	0.4 0.00	1.1 0.01	1.1 0.01	8.0 0.08	10.0 0.10
TOTAL				100.0 2.99	100.0 3.00	100.0 2.99	100.0 3.01	100.0 3.04	100.0 3.05	100.0 3.05	100.0 3.05	100.0 3.38
*	Lherzolite- av. density			3.30 3.30	3.30 3.30	3.30 3.30	3.30 3.30	3.30 3.30	3.30 3.30	3.30 3.30	3.30 3.30	3.30 3.30
*	Harzburgite - av. density			3.29 3.29	3.29 3.29	3.29 3.29	3.29 3.29	3.29 3.29	3.29 3.29	3.29 3.29	3.29 3.29	3.29 3.29

b

SY4

TABLE 5.12. Density comparison of mafic chlorite schist and average peridotite at 3.0 GPa.

a) Density of each experimental point in set SY3. b) Density of each experimental point in set SY4. Mass of each phase is taken from mass balance calculations for this study. Phases marked with an asterisk denote that density is calculated using the phase composition for that experiment. H₂O densities are removed from total density figures listed. Shaded column indicates the P,T location at which schist density exceeds that of average peridotite. Refer to the Appendix for full set of calculations.

A similar pattern emerged with the experimental results in SY4. At 540°C, the density of run products registered 2.99 g/cm³, considerably lower than the overriding peridotite. Density registered a gradual increase with increasing temperature, again corresponding to the increased proportion of garnet and fluid. Between 740°C and 760°C, as chlorite breakdown was in progress, density of run products jumped from 3.05 g/cm³ to 3.33 g/cm³. The final experimental data point at 800°C, with no chlorite remaining, had the garnet peridotite registering 3.38 g/cm³.

The presence of Fe in the chemical system is known to expand the garnet stability field to lower pressure which impacts the location of the spinel to garnet transition. An established spinel-garnet geobarometer (O'Neill, 1981) shows that for each 0.1 reduction in the X_{Mg}^{ol} , the position of the spinel-garnet transition is reduced by ~0.2 GPa. Olivine formed in the SY4 experimental set possessed a X_{Mg}^{ol} value of 0.75 at 800°C which would place the garnet-spinel transition near 1.0 GPa. We have seen in Table 5.12 that as chlorite approached its thermal maximum at sub-arc depths, the density of the breakdown product phases increased dramatically in accordance with the modal increase of garnet. The geobarometer informs us that this effect commences near 35 kms depth in the upper fore-arc. This would dramatically affect the buoyancy of mafic chlorite schists with the transformation of spinel peridotite to garnet peridotite occurring at much shallower conditions.

The low-temperature density contrast which exists between chlorite schist and the over-riding peridotite in the mantle wedge, which may initiate diapiric upwelling, will entirely disappear prior to the complete breakdown of chlorite. Indeed, at the point of complete transformation, garnet peridotite is denser than the mantle peridotite. This would cause the newly-formed garnet peridotite to sink back through the mantle peridotite due to the changed density contrast. Based on the experimental evidence determined in this study, Syros rocks would not be able to form diapirs able to penetrate the mantle wedge.

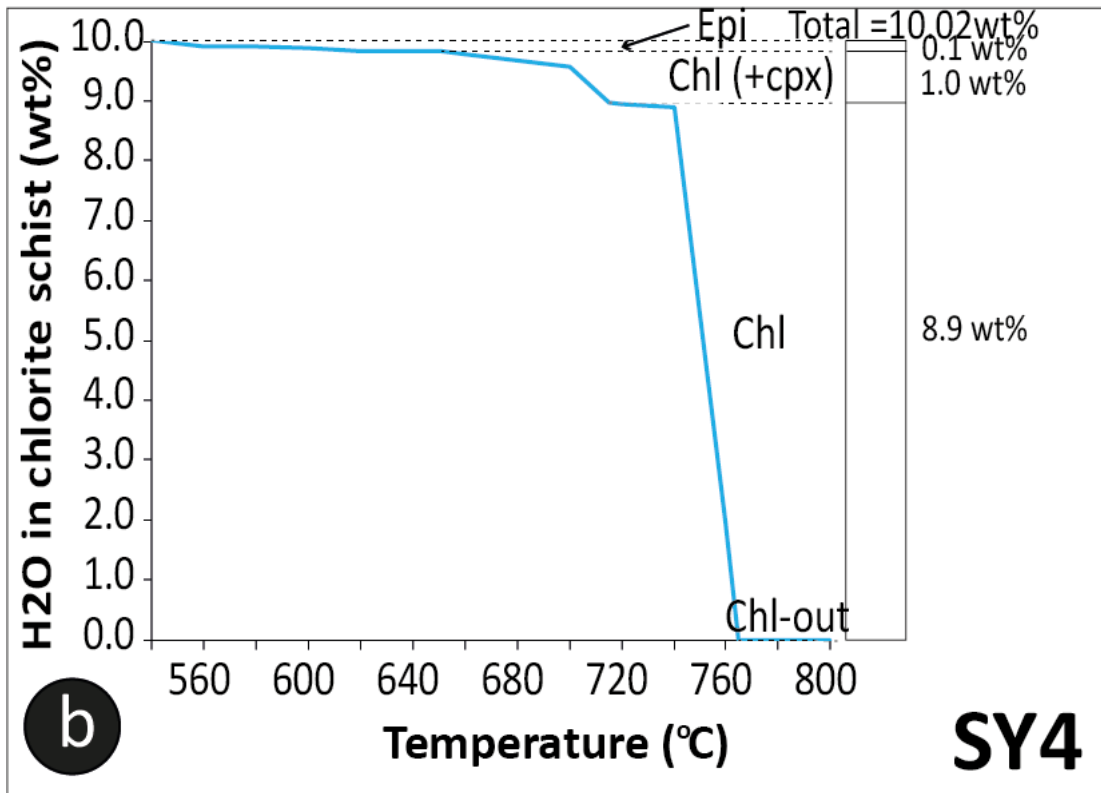
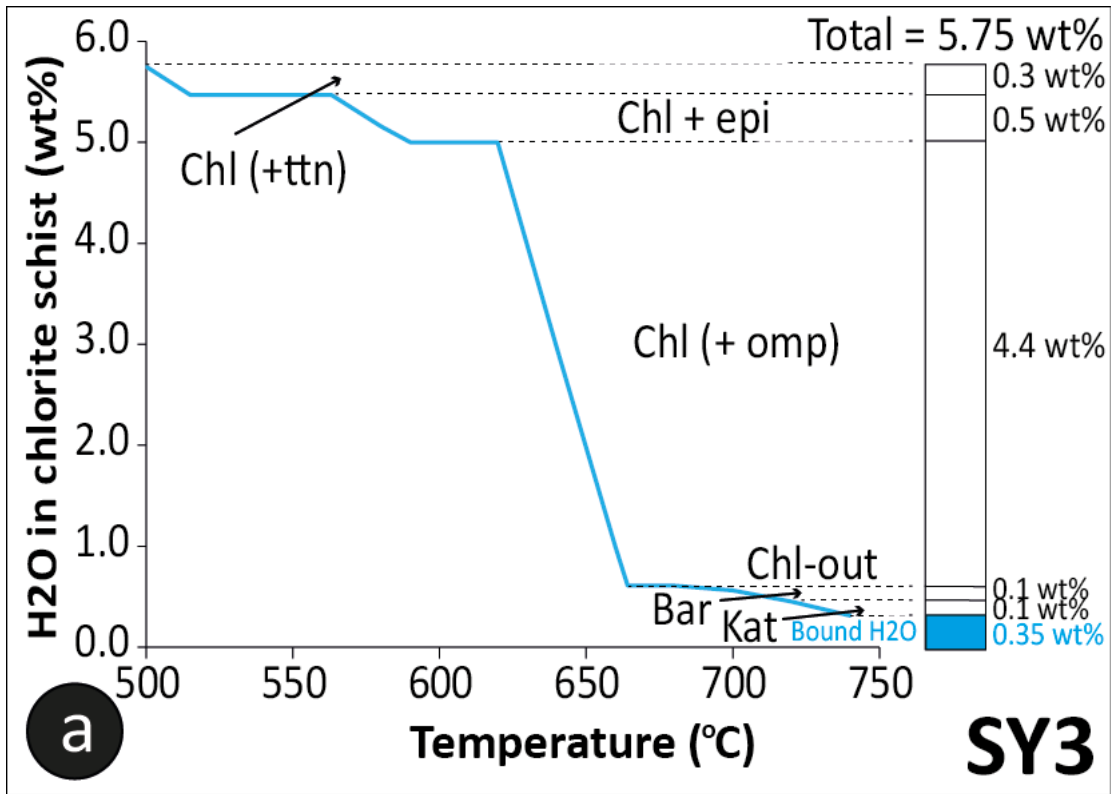


FIGURE 5.17. Water release from mafic chlorite schist by temperature.

a) Quantity of water released with increasing temperature at 3.0 GPa in SY3 composition. Phase in brackets denotes the phase-in reaction with chlorite which releases the corresponding quantity of water. Bulk of water release occurs with chlorite breakdown. Note that ~6 wt% of the original water is retained in the amphibole phase beyond 740°C.

b) Quantity of water released with increasing temperature at 3.0 GPa in SY4 composition. Around 1 wt% water is released following chl+cpx reaction; the remaining 8.9 wt% is released upon chlorite breakdown.

5.4.2.3. Further implications for the *mélange* diapir model

Marschall and Schumacher have intentionally applied their *mélange* diapir model to the fore-arc section of the subduction channel at pressures below 2.5 GPa. This is within the spinel stability field, which they confirm with several key measures: chlorite is stable to ~900°C, chlorite breakdown products are ol, opx and spinel; their Figure 2 provides a P,T plot with a scale advancing only to 2.5 GPa. Chlorite *mélange* at P<2.5 GPa is more buoyant than average lherzolite or harzburgite, and following the dehydration of chlorite, the product spinel peridotite also remains less-dense than the overlying peridotite. Therefore, the buoyant upwelling of chlorite *mélange* at P<2.5 GPa is both possible and internally consistent with their model. However, there are two potential problems which arise concerning the mechanism of diapiric flow. The first concerns the ability of diapirs to transport *mélange* through the mantle wedge. The second concerns the total reliance upon corner flow to drag the rising *mélange* at an oblique angle into the mantle such that it is positioned below sub-arc volcanoes.

A density contrast requires that as the less-dense, buoyant chlorite *mélange* rises, the denser peridotite must descend to fill the volume formerly occupied by the schist. If we assume the subduction channel is entirely filled with chlorite *mélange* prior to the start of any upwelling, then the channel itself would quickly be filled with peridotite and the subduction channel would cease to exist. This is not what has been viewed in exhumed subduction channels (Angiboust *et al.*, 2012) and not what geophysical investigations have shown (Hacker *et al.*, 2003; Abers, 2005). However, a density contrast may, of itself, be insufficient to transport cold, chlorite *mélange* through dense peridotite. This can be illustrated with a simple analogy. A helium-filled balloon is less-dense than the air surrounding it. Due to the density contrast, it will therefore rise upward of its own accord. If the same balloon is released inside a room, it will quickly rise to the ceiling but is prevented from further rise due to the intervention of the ceiling. The balloon will remain at that point, unable to penetrate the denser ceiling. Or will it? If we accord with the Marschall and Schumacher model, and continue to fill the balloon with helium, it could become sufficiently large and buoyant to cause the ceiling to bulge, fracture and then it would be free to continue its upward journey. Returning to their actual model, such a vast 'bulge' of chlorite schist would be required to achieve the buoyancy needed to penetrate a peridotite 'ceiling' up to 70 kms thick that the concept lacks plausibility.

Diapirs require normal faults and fractures to act as conduits through dense overhead rocks. Seamounts and serpentinite diapirs can penetrate the crust courtesy of normal faults and fractures found in the fore-arc region (Tatsumi, 2003; Osada *et al.*, 2004; Schuiling, 2011). Diapirs are commonly a shallow geological feature rising only a few kilometres. The Marschall

and Schumacher model, by contrast, suggests that cold diapirs could form at much deeper levels and rise buoyantly, intercepting large volumes of dense peridotite without the advantage of faults to enable passage.

Cool, ascending diapirs disrupt corner flow. As the diapir moves upward through the mantle wedge, it disrupts the downward progression of corner flow, the broader convective process which mixes rocks in the mantle wedge (Kelemen *et al.*, 2002; Hasenclever *et al.*, 2011). As the cooler ascending material passes upward through the mantle, the temperature reduction re-directs corner flow into a much-reduced convective cell on each side of the diapir. Experimental work has shown this to be a permanent disruption (Hasenclever *et al.*, 2011). Consequently, whilst the initial diapir may be dragged inwards at an angle oblique to the subduction channel due to the action of corner flow, this cannot be the case with any subsequent plumes as that flow has been stemmed. Therefore, any subsequent diapiric upwellings would rise vertically, not inwardly towards the hottest part of the mantle. In this way, chlorite within the diapir would entirely dehydrate, not melt, and this would change the chemical 'signature' of the buoyant parcel. In addition, with a vertical rise, the diapir would not be spatially associated with the location of arc volcanoes but be much closer to the fore-arc trench.

Application of the H₂O/Ce thermometer to fluids in arc magmas reveals that the intrusion of cold mantle diapirs rising from the subduction channel would cool the mantle wedge too much, leading to the cessation of convective corner flow (Cooper *et al.*, 2012). The Marschall and Schumacher model offers a neat method for bringing together fluid sources from sediment, slab and mantle sources, where they are mechanically mixed in the subduction channel. However, the H₂O/Ce thermometer negates the possibility that diapirs could transport this mix of fluids to arc magma chambers.

Marschall and Schumacher offer no explanation as to why they restrict their model to fore-arc pressures. They acknowledge that numerous geophysical studies show buoyancy contrasts extending beyond 150 kms depth along a subduction channel (Marschall and Schumacher, 2012, p. 863 and references therein). So why refer only to the upper section? It may well concern the changes which occur beyond 2.5 GPa.

From ~2.0 GPa, garnet begins to replace spinel as the main Al-bearing mineral with increasing pressure - the spinel-garnet transition. In the case of chlorite mélangé, the breakdown of chlorite means the product rock progressively changes from a spinel peridotite to a garnet peridotite with increasing pressure. Garnet peridotite has a significantly greater density than spinel peridotite due to changed phase relations. Therefore, at pressures >2.5 GPa, a chlorite mélangé has sufficient buoyancy to permit a diapiric upwelling to form. With the progressive

breakdown of chlorite with increasing temperature, garnet peridotite forms which has a greater density than the average lherzolite and harzburgite in the overriding mantle wedge. Its buoyancy would stall even before all chlorite had disappeared, and upon exceeding the chlorite thermal boundary, garnet peridotite, being denser, would begin to sink back through the original mantle rocks.

Marschall and Schumacher further claim that Syros chlorite is stable to near 900°C and the wet peridotite solidus occurs near 810°C (Marschall and Schumacher, 2012 - see Figure 2, panel 4). This temperature interval is important to the working of their model. Chlorite contacting the mantle rocks on the outer layer of the diapir will begin to melt prior to dehydration. The partial melt provides thermal protection for the inner parts, delaying chlorite dehydration. Once the inner melange reaches 900°C, the diapir has ascended well into the hot mantle wedge such that upon full dehydration, the released fluids intermingle with the surrounding melt and not as free water. In this way, the water contents of chlorite go immediately from bound form to melt with no 'free' water released upon chlorite breakdown. The experimental results from the current study indicate this is not the case. Syros chlorite, at best, possesses a thermal maximum near 3.0 GPa, 780°C (SY4 - Mg#=0.68). At 760°C, just 15.5 wt% chlorite remains meaning that over 80% of the original chlorite has already dehydrated. Even if one accepts that the wet peridotite solidus is located near 810°C (this question is addressed in the next section of this chapter), then a >30°C gap remains between chlorite dehydration and the onset of melting where free water has completely dispersed. This substantially lower temperature means that chlorite will have commenced thermal breakdown prior to being encased in a diapir. Since the model requires chlorite dehydration and chlorite melting to occur within the confines of the diapir, this is a substantial weakness and means that at pressures above 2.5 GPa, the Marschall and Schumacher model has no application.

5.4.3. THE ONSET OF MELTING IN GARNET PERIDOTITE

The results of the high temperature experimental set determined that the onset of melting in garnet peridotite, the product following chlorite breakdown in chlorite schist, was bracketed between at 3.0 GPa between 1100°C and 1150°C. Evidence will be provided by an examination of two key points: changing phase textures and changing phase composition, both of which will follow a short section defining the characteristics of quench textures. This section will conclude with a short critique of the work of Till (Till *et al.*, 2012a) regarding their positioning of the wet peridotite solidus due to incorrect interpretation of their own experimental results.

5.4.3.1. Quench textures

Fortunately, the high-temperature experiments conducted in this series were conducted in the P,T region below the SCEP and therefore a simple classification is possible. Three main types of quench textures have been identified, labelled in short by QF, QM and QS after Mibe (Mibe *et al.*, 2011). Quench textures which assume a smooth, spherulous habit or have a fish-egg appearance are considered to be solute quenched from a fluid (QF) (Adam *et al.*, 1997; Carter *et al.*, 2015). In contrast, anhedral-spherulous shapes containing multiple voids, microvesicles (Carter *et al.*, 2015) or bubbles are considered to be melt, the bubbles indicating fluid exsolved from the melt at quench (QM) (Spandler *et al.*, 2007; Klimm *et al.*, 2008; Mibe *et al.*, 2011). The third quench type - elongate sinuous, crystalline 'strings' and 'wisps' (QS) - indicate exsolved solute (Stalder, 2012) but it is indeterminate as to whether or not they have derived from fluid or melt or both. Consequently, the presence of QS is not a distinguishing characteristic of the presence of melt.

5.4.3.2. The appearance of melt textures

This set of high-temperature experiments successfully bracketed the wet solidus in garnet peridotite at 3.0 GPa between 1100°C and 1150°C.

Figure 5.18a-c provides a series of microphotographs at 820°C, 1100°C and 1150°C respectively which tracked the changes in phase texture with increasing temperature to illustrate the first appearance of melt. Since the starting material used in this set was identical to that used in Series 2 experiments (Chapter 4), it has been possible to provide visual evidence of these changes over a wider temperature interval.

At 820°C (Figure 5.18a), some 30°C above the experimentally-determined chlorite-out boundary, no melt was visible within the capsule contents. Olivine and poikiloblastic garnet, the dominant phases present, generally formed large grains (>10 µm) and possessed subhedral-euhedral grain boundaries. Smaller garnet and olivine grains (<5 µm) were randomly distributed throughout the field-of-view along with minor spinel and opx. There was no evidence of phase segregation at this temperature. Porosity (vapour) did not show a gradation towards the hot end of the capsule. Taken together, these textures indicated a complete absence of melt at this temperature.

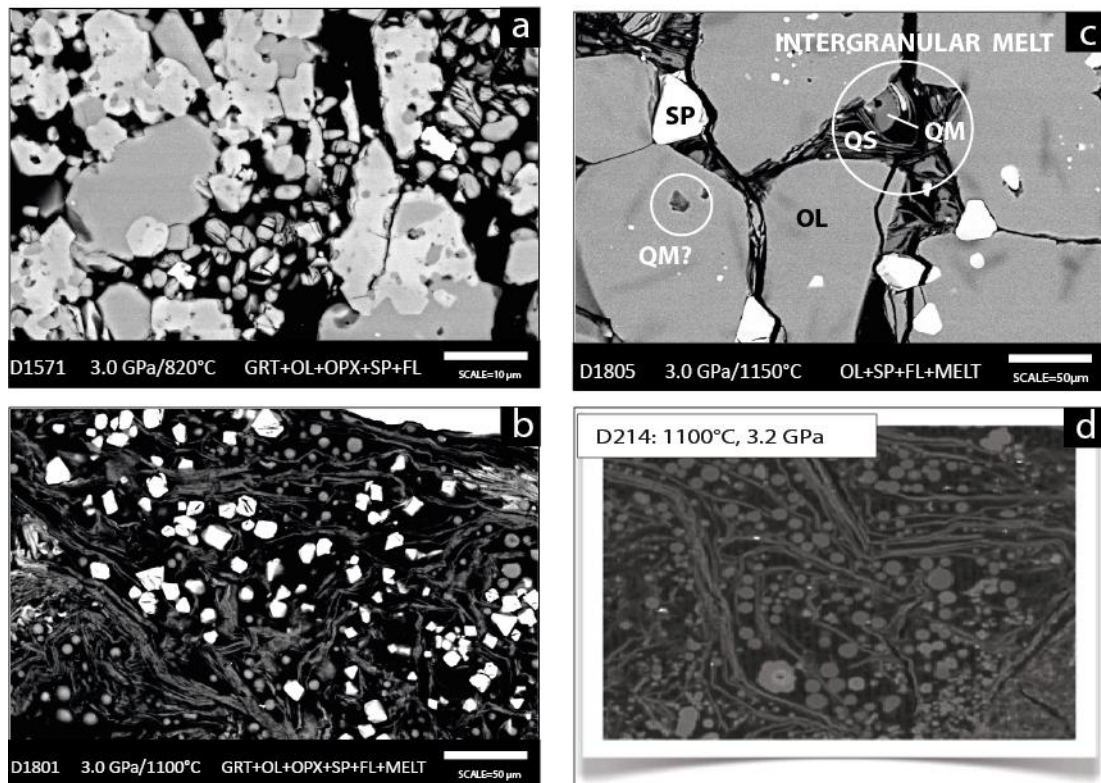


FIGURE 5.18. *The onset of melting in chlorite peridotite illustrated by phase textures.*

a) Capsule contents at 820°C in current study. No evidence of melt textures. b) Capsule contents at 1100°C in current study. Plentiful spinel, QF (quench fluid) spherules, and QS. c) Melt forms at a triple junction at the cooler end of the capsule. d) Reproduction of microphotograph from Figure 2 in Till (Till et al., 2012a) of capsule contents at 3.2 GPa, 1100°C. A comparison of images in b) and d) reveal good agreement between phase textures in both studies.

At 1000°C, some slight textural changes were detected. Olivine and garnet formed slightly larger grains (>15 μm) and appeared a little more homogeneous although garnet remained poikiloblastic. At larger scale, a density contrast had begun to form (see Figure 5.13a) as well as a porosity gradient, both of which favoured the hot end of the capsule. However, no melt textures were observed anywhere within the capsule.

At 1100°C, an unmistakable change in appearance was observed. Phase segregation had created a distinct density contrast with fluid and large olivine grains restricted to the hot end of the capsule and the denser phases compacted at the cooler end (see Figure 5.18b). The presence of multiple spherules (QF) and sinuous shapes (QS) adjacent to the hot end of the capsule wall signalled newly-formed quench products (see Figure 5.13d). Importantly, no melt quench (QM) was observed anywhere in the capsule contents. Mass balance indicated a slight reduction in phase abundance of both garnet and opx at this temperature and its replacement by an estimated 2wt% melt although none was observed.

At 1150°C, melt textures were confirmed with the presence of all three types of quench – QF, QS and QM. At small scale (see Figure 5.13f), vesicular, anhedral blobs of melt quench were observed surrounded by strings of melt quench. At large scale (see Figure 5.18c), the same

textures were observed forming in triple junctions between olivine grains in cooler parts of the capsule. Garnet and opx had entirely disappeared at this temperature with an estimated >20wt% melt present in capsule contents.

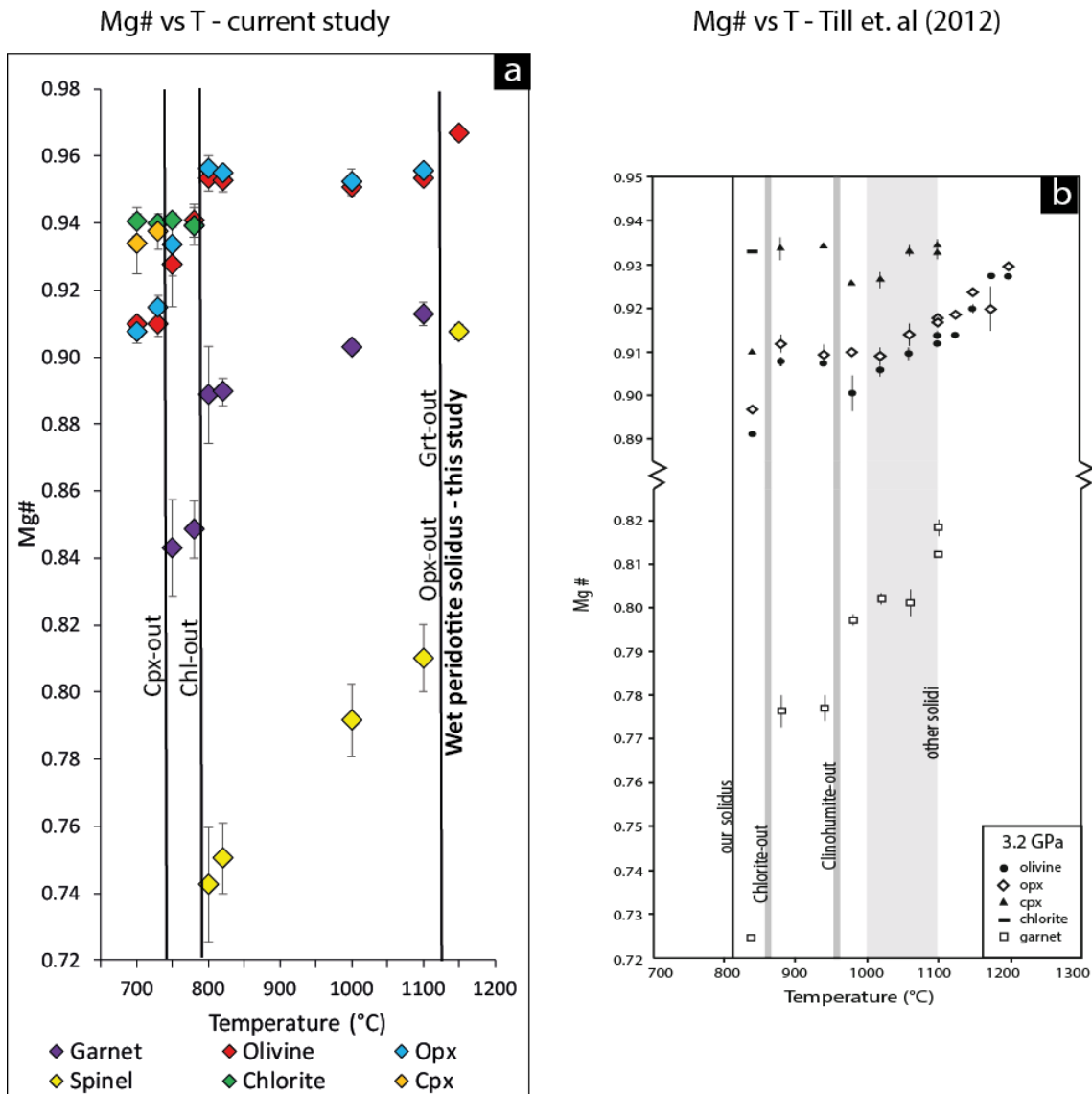


FIGURE 5.19. Mg# vs temperature - current study compared with Till et. al.

a) **Current study.** Mg# for six phases plotted against temperature. Three solid black lines mark location of sudden rise in Mg# indicating a phase change. The last of these, near 1125°C, indicates the wet peridotite solidus. b) **Till et. al. study.** Mg# vs temperature showing key phase changes as well as the location of the wet peridotite solidus near 810°C – over 300° lower than in this study.

5.4.3.3. Changes in phase composition signal the location of the wet solidus

This set of high-temperature experiments showed the onset of melting in garnet peridotite occurred at 3.0 GPa between 1100°C and 1150°C which indicates the location of the wet peridotite solidus. Since sudden changes in Mg# over a small temperature interval typically indicate a phase boundary, the Mg# of each phase in this experimental set was plotted against temperature, shown graphically in Figure 5.19a.

The Mg# of all six solid phases were plotted against temperature between 700°C and 1150°C, integrating the results from Series 2 (chapter 4) with the high-temperature set. The solid vertical lines marked the location of sudden jumps in Mg#. The first jump, near 740°C, marked the disappearance of the cpx phase and the appearance of garnet. At this point, the Mg# of both olivine and opx rose by 0.02. The next sudden rise in Mg# was registered near 790°C. This coincided with chlorite breakdown and the introduction of the spinel phase. Co-existing phases olivine, opx and garnet registered corresponding rises of 0.1, 0.2 and 0.4 respectively. The next major jump occurred after a large temperature interval of ~300°C. Between 1100°C and 1150°C, the Mg# of the two remaining phases olivine and spinel rose by 0.02 and 0.10 respectively. This interval saw the disappearance of both garnet and opx and the appearance of melt, thereby marking the location of the wet peridotite solidus.

Figure 5.19b is a reproduction of Fig.3 from the Till *et al.* article. Its inclusion here enables a direct comparison of compositional data from both sets of experiments. At first glance, they appear quite similar.

5.4.3.4. The location of the wet solidus

The location of the wet peridotite solidus at 3.0 GPa between 1100°C and 1150°C is in good agreement with previous experimental work into the partial melting of saturated peridotite (Green, 1973, 1976; Millhollen *et al.*, 1974; Kessel *et al.*, 2005) and of saturated, amphibole-bearing peridotite (Niida and Green, 1999; Fumagalli *et al.*, 2009; Pirard and Hermann, 2015b), when adjusted for differences in bulk compositions. However, these results contrast significantly with another group of experimental researchers who claim the wet peridotite solidus occurs some 300°C lower (Mysen and Boettcher, 1975; Gaetani and Grove, 1998; Grove *et al.*, 2006).

The most recent experimental study published by this group (Till *et al.*, 2012a) argued that melt was observed at 3.2 GPa, 810°C in experiments using a chlorite peridotite bulk composition. Unfortunately, no photographic evidence and limited data was supplied to support this claim at these P,T conditions (Green *et al.*, 2012; Stalder, 2012). The Supplementary datafile accompanying the published article contained sparse information in general and no data on experimentation below 880°C (at 3.2 GPa) making it impossible to verify this interpretation. With the aid of a microphotograph from the current study, shown in Figure 5.18a, capsule contents at 3.0 GPa, 820°C were examined for signs of melt. According to Till *et al.*, melt textures should be present. As already discussed above, there was no evidence, either texturally or chemically, of melt contained in capsule contents at these P,T conditions.

A photograph of capsule contents at 3.2 GPa, 1100°C, however, was provided in the Till study, reproduced here in Figure 5.18d. The similar P,T conditions and bulk composition of both studies allowed a photographic comparison of phase textures to be made. Two microphotographs from the current study, therefore, have been included showing capsule contents at 3.0 GPa, 1100°C (Figures 5.13d and 5.18c). All three images possessed strikingly similar phase textures which suggested strong agreement between both sets of experimental results. However, textural and compositional data have been interpreted in significantly different ways in each study, and in the case of the Till study, this has led to the incorrect placement of the wet peridotite solidus.

5.4.3.5. Further implications for the location of the wet peridotite solidus

Till, Grove and Withers (Till *et al.*, 2012a) claimed to have experimentally determined the wet peridotite solidus at 3.2 GPa, 810°C, some 300°C lower than determined in most previous studies. Two commentaries soon followed (Green *et al.*, 2012; Stalder, 2012) along with replies from the authors (Till *et al.*, 2012b, 2012c). Each reviewer responded to numerous issues arising from the original paper and each produced a comprehensive critique, making it unnecessary for me to repeat these points here. Neither reviewer seemed especially concerned with the study's methodology or the results obtained. Instead, their concerns involved the interpretation of the results, and the sparsity of evidence provided in support of their claims.

The key finding of their study regarded the changed location of the wet peridotite solidus. This should have been easy to support. Firstly, the textural evidence. How simple would it have been to provide two microphotographs – one at 3.2 GPa, 780°C which showed the absence of melt, and a second at 3.2 GPa, 840°C which showed the presence of melt? Secondly, the compositional evidence. How easy would it have been to include compositional data on each co-existing phase at these same P,T locations to show the sudden jump in Mg# corresponding to the phase change incurred by the appearance of melt? This evidence was not presented in the text of the article, nor in the Supplementary material. Indeed, what is most interesting about this article is not what **was** included as supporting evidence but rather what was **not**. There appears to have been some serious inverse cherry-picking involved. By their own admission (Till *et al.*, 2012a, p. 1084-5), their desire to produce research of "...great importance...", irrespective of what the actual results showed, seems to have compromised their ability to draw sound, scientific interpretations of their findings.

Stalder concludes his commentary stating that even with the scant data Till *et. al.* made available, their results point to the actual location of the wet peridotite solidus being nearer 1100°C than 810°C, and their interpretation that it is at lower temperature does not accord with

their own data or the bulk of previous experimental studies (Stalder, 2012), a view with which I wholeheartedly agree.

5.5. CONCLUSIONS AND IMPLICATIONS

The three sets of experiments in this study provided new findings on the stability of chlorite of mafic composition, as well as the melting behaviour of chlorite schist at high temperatures.

Eighteen experiments were conducted at sub-arc pressure (3.0 GPa) using two samples of mafic chlorite schist from Syros, Greece, SY3 (Mg#=0.50) and SY4 (Mg#=0.68). The results showed, in the SY3 set, the maximum thermal stability of chlorite was determined at 765°C. In more cpx-rich compositions, chlorite stability was reduced to 650°C. In the SY4 set, the maximum stability of chlorite occurred ~780°C whilst in omphacite-dominant compositions, it was reduced to 680°C.

As chlorite became increasingly Fe-rich, its stability field reduced and the gap between the cpx+chl reaction and the terminal chlorite reaction widened.

The phase composition from the same two sets of experiments showed the changes in density with increasing temperature. In SY3, a major jump in density occurred between 580°C and 640°C which corresponded to the disappearance of chlorite. In SY4, a similar jump in density occurred between 740°C and 760°C which also corresponded to chlorite disappearance.

At low temperatures, experiments revealed that mafic chlorite schists were buoyant and could form diapiric upwellings through the overhanging mantle peridotite. In both instances, however, even before the complete disappearance of chlorite, the transformed garnet peridotite was denser than the mantle rocks and as such buoyancy would cease.

These results show that although the Marschall and Schumacher model had application at fore-arc pressures, albeit with several weaknesses, density and stability data from the current study showed that it had no function at sub-arc depths.

The third experimental set determined the wet peridotite solidus in ultramafic chlorite schists (Mg#=0.94). The results showed the onset of melt occurred between 1100°C and 1150°C. This was confirmed by the presence of all three types of quench textures, the absence of garnet and opx phases, and by a jump in Mg# in ol and sp, the only remaining solid phases at that temperature.

These experimental results dispute those of Till et. al. who insist that the wet peridotite solidus was located ~810°C.

CHAPTER 6 : SUMMARY, IMPLICATIONS AND FUTURE RESEARCH

This program of research was directed by three inter-related aims surrounding the stability of chlorite in the subduction zone. This chapter revisits these aims in turn: each provides a summary of research findings, the implications of these results and the identification of possible future research directions.

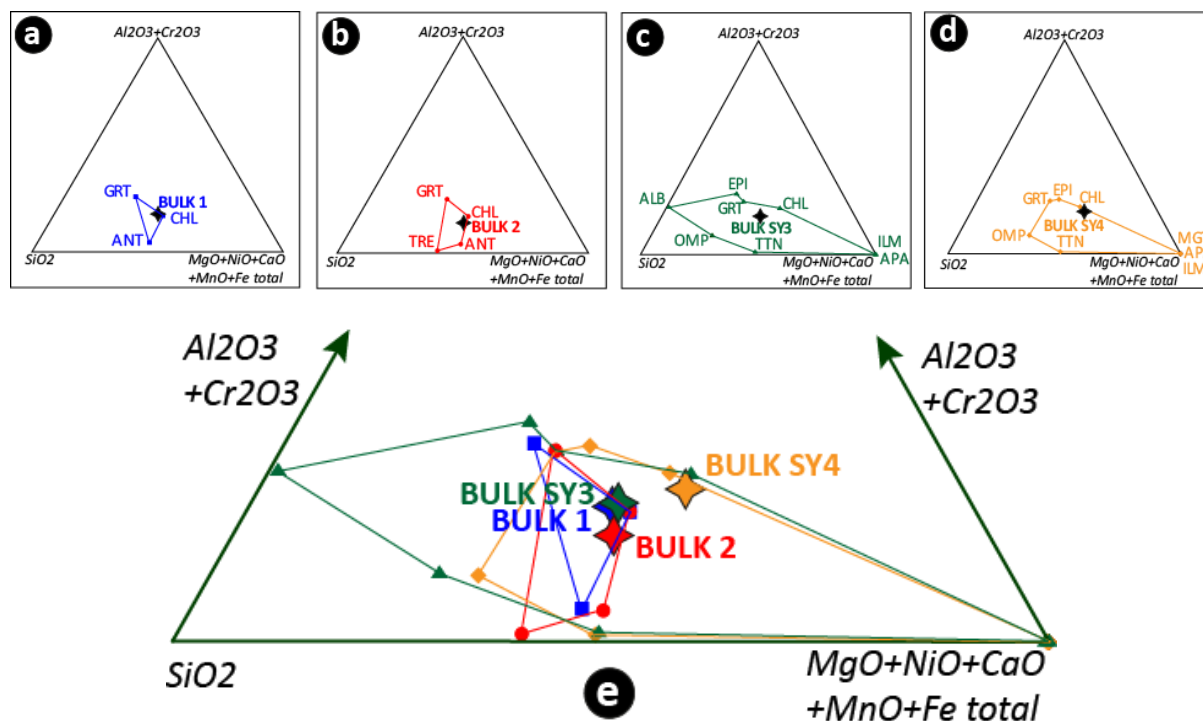


FIGURE 6.1: Comparison of bulk compositions used in this study

a-d) Chemographs of each of the bulk compositions used in this study: Bulk 1 (blue), Bulk 2 (red), Bulk SY3 (green) and Bulk SY4 (orange) respectively. Coloured tie-lines link each of the phases included in each starting mix. **e)** A compilation of all four bulk compositions in the same compositional space enabling ease of comparison. Phase abbreviations as previously denoted.

Three separate series of experiments were undertaken, using contrasting chlorite compositions from natural samples, to constrain the stability field of chlorite within a subduction setting. The varied compositions have been shown in Figure 6.1. In three-component compositional space, Figure 6.1a-d shows the location of each bulk composition and the minerals comprising each starting mix. Figure 6.1e shows all four bulk compositions as an overlay to enable comparison of starting mixes.

Series 1 experiments (Chapter 3) studied chlorite in an ultramafic chlorite mélangé schist (chlorite $Mg\#=0.94$), typically formed in the subduction channel between the downgoing slab and the hanging wall of the mantle wedge. This series examined the two dehydration reactions relevant to this lithology: $chl = ol + opx + sp + H_2O$ (Reaction 1), applicable at low pressure, and at high-pressure: $chl =$

ol+grt+sp+H₂O (Reaction 2). This study is the first to examine these reactions relevant to a chlorite mélange schist.

Series 2 experiments (Chapter 4) studied chlorite peridotite (chlorite Mg#=0.94) typically formed from metasomatic action in the mantle wedge. A fertile chlorite lherzolite was examined using the model reaction for this lithology: chl+cpx = ol+grt+H₂O (Reaction 3), whilst chlorite harzburgite was studied using the model reaction chl+opx = ol+grt+H₂O (Reaction 4). Reactions 3 and 4 were studied together here for the first time. Series 3 (Chapter 5) examined two samples of mafic chlorite schist (chlorite Mg#=0.50 and 0.68) typically formed metasomatically within the downgoing slab. Reactions 2 and 3 were used to guide the relevant chemical reactions.

Ninety-five (n= 29, 45, 9, 9 and 3 respectively) piston cylinder experiments were conducted at a range of pressures (1.0 GPa to 6.2 GPa) and temperatures (500°C to 1150°C). The resulting data was used to explore the three aims upon which this thesis was based.

6.1 SUMMARY OF FINDINGS

6.1.1 AIM 1: TO CONSTRAIN THE STABILITY FIELD OF CHLORITE IN CHLORITE SCHIST, CHLORITE LHERZOLITE AND CHLORITE HARZBURGITE

Experimental results enabled the stability field of chlorite to be closely constrained in three contrasting chlorite lithologies. The maximum pressure stability of chlorite schist and chlorite peridotite was determined at 6.2 GPa, some 40 kms deeper than determined by previous research. A phase diagram combining results from Series 1 and 2 is displayed in Figure 6.2. Each of the high-pressure Reactions 2-4 possessed similar gradients but were thermally separate.

Series 1 results determined the location of the terminal chlorite Reactions 1 and 2 relevant to chlorite mélange schist. A plot of those results, shown in green in Figure 6.1, produced a curve described as follows: a steep positive Clapeyron slope to 2.3 GPa, 850°C, then a near-vertical rise to ~3.4 GPa, 840°C, a slight backbend dipping steeply negative to near 5.7 GPa, 735°C, a further moderate backbend to 6.2 GPa, 675°C, then a sharp backbend to 6.3 GPa, 610°C. Up to ~3.5 GPa, this curve closely resembled numerous previous studies of chlorite stability. In this study, however, the chlorite stability boundary rose more steeply which created a chlorite stability field at least 0.8 GPa higher than determined in any previous study.

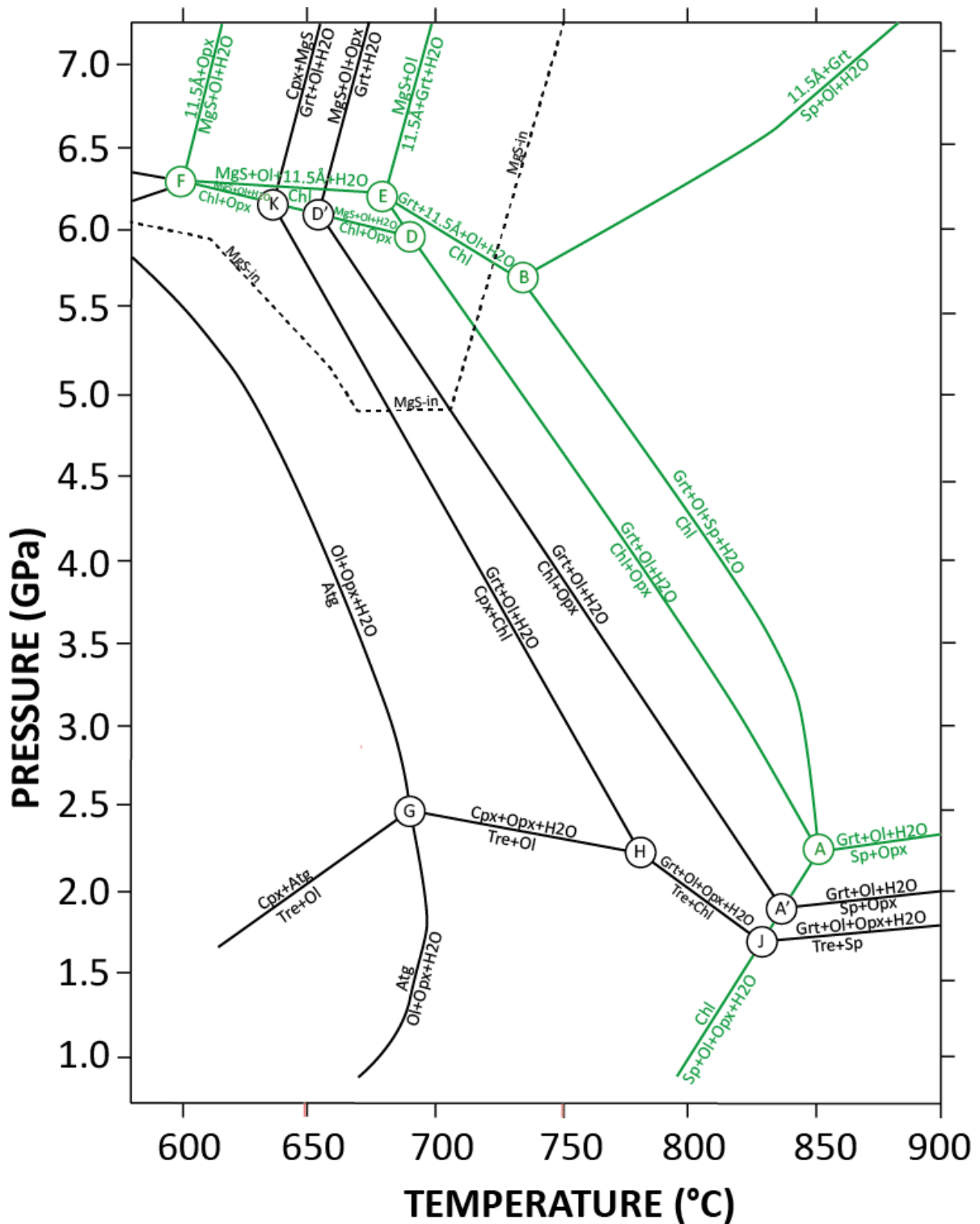


FIGURE 6.2: Comparison of phase relations in chlorite peridotite and chlorite schist

Phase relations for Series 5 (chlorite peridotite) shown in black; Series 1 (chlorite schist) shown in green. The dotted line indicates the low P-T boundary of the MgS phase due to solid solution. The chlorite stability field in chlorite schist is shifted to higher temperature compared to chlorite peridotite due to contrasting compositions. Phase abbreviations as previously denoted.

Series 2 results marked the curves of Reactions 3 and 4 relevant to chlorite Iherzolite and chlorite harzburgite respectively, shown in black in Figure 6.1. Reaction 3 possessed a slightly steeper gradient

compared with Reaction 4 and the thermal separation between both reactions diminished with increasing pressure: from ~50°C at 2.5 GPa to zero where they converged at Invariant Point K near 6.2 GPa, 635°C. Reaction 4 was explored in both Series 1 and 2. The slope of each curve was very similar, however compositional differences meant that in chlorite peridotite, Invariant Points A and D were shifted such that the chlorite stability field was slightly reduced. The resulting Invariant Point A' was located some 0.4 GPa and 20°C lower than Invariant Point A, and Invariant Point D' located some 0.2 GPa higher and 35°C lower. This meant that Reaction 4 commenced at lower pressure and terminated at higher pressure compared with chlorite schist compositions, but its thermal stability was always at lower temperature.

Series 3 experiments determined constraints only at 3.0 GPa with thermal maxima recorded at 780°C (Mg#=0.68) and 765°C (Mg#=0.50), a further 15-30°C lower than in Series 2. Overall, these results showed that the stability field of chlorite extends to higher pressures and temperatures than shown in any previous chlorite study. Furthermore, chlorite mélange has a considerably higher thermal stability than other ultramafic and mafic chlorite lithologies.

Two key observations can be made regarding chlorite stability.

Chlorite possessing the same Mg# had contrasting thermal stability in differing compositions. The terminal Reaction 2 (Mg#=0.94), studied in chlorite schist, showed a maximum thermal chlorite stability at 3.0 GPa of ~850°C. Reaction 4 (Mg#=0.94), as occurs in depleted harzburgite, showed that in the presence of opx, chlorite recorded a thermal maximum at 3.0 GPa of ~790°C. Reaction 3 (Mg#=0.94), relevant to fertile lherzolite, revealed that chlorite attained a thermal maximum of ~750°C at 3.0 GPa. Therefore, chlorite in chlorite lherzolite breaks down a full 100°C lower temperature than does chlorite of the same Mg# in a chlorite schist.

High Mg# chlorite had a higher thermal stability than compositions with a lower Mg#. In Series 3, two contrasting mafic chlorite schists were examined. Sample SY4 (Mg#=0.68) had a thermal maximum at 3.0 GPa of ~780°C whilst the SY3 sample (Mg#=0.50) reacted out at 3.0 GPa by 765°C. Therefore, increasing quantities of Fe in chlorite can result in an 85°C difference in the maximum stability of chlorite.

Chlorite stability was affected by the elements present in the bulk composition. The Series 1 bulk composition contained minor chromium and iron which enabled their impact upon chlorite stability to be determined. The addition of Cr enhanced the chlorite stability field to higher pressure and higher temperature. This effect was maximised at high-pressure, low-temperature locations. The inclusion of Fe, however, had different effects depending upon the P,T conditions. Under low-pressure, high-

temperature conditions, the chlorite stability field was reduced to lower temperature. Conversely, under high-pressure, low-temperature conditions, the chlorite stability field was expanded to higher pressure. The resultant effect was to significantly steepen the Clapeyron slope of the chlorite-out boundary which increased its thermal stability with increasing pressure. The Series 2 bulk composition contained minor calcium in addition to Fe and Cr. The effect was to shift the chlorite stability field to lower temperature by a consistent 35°C regardless of the pressure.

6.1.2 AIM 2: TO INVESTIGATE IF CHLORITE BREAKS DOWN INTO ANHYDROUS OR HYDROUS MINERAL ASSEMBLAGES

Perhaps the most significant finding from these experimental studies was the appearance of unexpected hydrous phases which formed as a breakdown product of chlorite.

The breakdown of chlorite in chlorite mélange schist accorded with Reaction 2 at pressures below 5.7 GPa. At higher pressures, chlorite breakdown produced the 11.5Å-phase (~12.1 wt% H₂O). This phase has an extensive stability field to at least 12 GPa, 1000°C (Cai *et al.*, 2015) but has never before been found in experiments using natural minerals as starting materials. Due to the presence of a small amount of opx, Mg-sursassite (~7.1 wt% H₂O) also appeared above 6.0 GPa, 700°C. It possessed a narrower stability field but it did extend to higher pressures and temperatures.

In chlorite lherzolite, chlorite breakdown followed the Reaction 3. However, in chlorite harzburgite, the breakdown of chlorite followed Reaction 4 only to 4.9 GPa. At higher pressures, Mg-sursassite replaced garnet as the stable Al-bearing phase. Its stability field was extended to lower pressure and higher temperature likely due to the presence of calcium in the system.

In mafic chlorite schist, the disappearance of chlorite witnessed the appearance of the amphibole magnesiokatophorite (~2.04 wt% H₂O) and the mica wonesite (~4.2 wt% H₂O), the former thermally stable beyond 740°C at 3.0 GPa.

The formation of these hydrous minerals after chlorite breakdown provides potential for large volumes of water to be sequestered beyond sub-arc depths and released into the deeper mantle upon thermal breakdown. Up to 25 % of the total water repository in chlorite can be retained in the 11.5Å-phase following chlorite breakdown whilst up to 8 % could be retained in the MgS phase.

6.1.3 AIM 3: TO EXAMINE THE IMPLICATIONS OF CHLORITE STABILITY UPON SLAB DIAPIR AND MANTLE MELTING MODELS

In unaltered mafic lithosphere, lawsonite is the dominant stable hydrous mineral, hosting bound water to very high pressure. As the slab continues its downward journey, though, metasomatism acts to chloritize large swathes of mafic rocks, sequestering large volumes of water which vastly increases their capacity to transport water to greater depth. However, as experimental findings in this study showed, the stability of chlorite in mafic lithologies varied according to Mg# and furthermore, mafic chlorite always liberated water before ultramafic chlorite schists.

Experimental results in Series 3 showed that the stability field of mafic chlorite is shifted to lower temperatures compared to ultramafic lithologies. In the SY3 set, the maximum thermal stability of chlorite at 3.0 GPa was determined at 765°C. In cpx-dominant compositions, chlorite stability was reduced to 650°C. In the SY4 set, the maximum stability of chlorite occurred at 3.0 GPa near 780°C whilst in omphacite-dominant compositions, it was reduced to 680°C. As chlorite became increasingly Fe-rich, its stability field reduced and the gap between the Reaction 3 and Reaction 2 widened.

Experimental data enabled the density of mafic chlorite schist to be determined. Within the chlorite stability field, chlorite schist of any composition was less dense than the proximal peridotite situated in the mantle wedge indicating that chlorite mélangé diapirs could form. However, as chlorite began to breakdown, the more buoyant chlorite schist began its transformation into dense garnet peridotite and any buoyancy contrast was lost. In SY3, a major jump in density occurred between 580°C and 640°C which corresponded to the disappearance of chlorite. In SY4, a similar jump in density occurred between 740°C and 760°C which also corresponded to chlorite disappearance. These results indicated that whilst mélangé diapirs could form, subsequent density changes meant they could not operate as fluid transport vehicles through the mantle wedge.

The high-temperature experiments determined that the wet peridotite solidus in chlorite peridotite occurred at 3.0 GPa between 1100°C and 1150°C. This was confirmed by observation of phase textures, the presence of varied quench textures, and the sudden increase in Mg# of solid mineral phases. No evidence of the onset of melting was observed near 810°C (Till, Grove and Withers, 2012) thereby disputing the existence of chlorite melting in hydrous peridotites.

6.2 IMPLICATIONS OF INCREASED CHLORITE STABILITY FIELD AND WATER TRANSPORT

This was the first comprehensive experimental study of chlorite stability at high pressure. It was the first study to show a clear delineation between Reaction 3 and Reaction 4, relating to fertile and

depleted peridotite respectively, and the chlorite terminal reactions, Reactions 1 and 2, relevant to chlorite schists.

Numerous implications arose from these results:

Increased stability field of chlorite. Chlorite has a more extensive stability field than recognised in previous studies. These results confirm chlorite stability to at least 6.2 GPa, 675°C in chlorite mélange schist and 6.2 GPa, 735°C in chlorite peridotite, equivalent to ~190 kms depth.

Complex phase relations at high pressure. The presence of the hydrous minerals chlorite, 11.5Å phase and MgS to high pressures and temperatures indicated a significant change to phase relations than expected by the model formulae (Reactions 1-4). This could alter future experimental undertakings.

Reactions 2 and 4 more important than Reaction 3. At high pressure, chlorite breakdown in fertile peridotite follows Reaction 3 ($\text{chl} + \text{cpx} = \text{ol} + \text{grt} + \text{H}_2\text{O}$). In contrast, chlorite breakdown in depleted peridotite does not follow Reaction 4 ($\text{chl} + \text{opx} = \text{ol} + \text{grt} + \text{H}_2\text{O}$), producing instead the hydrous phase MgS in lieu of garnet. Similarly, chlorite dehydration in chlorite mélange does not accord with the terminal Reaction 2 ($\text{chl} = \text{ol} + \text{grt} + \text{sp} + \text{H}_2\text{O}$) producing instead the 11.5Å-phase in lieu of spinel. The overall effect is that Reactions 2 and 4 extend the hydrous stability field. Therefore, Reaction 3 is less important than Reactions 2 and 4 regarding water transport.

Bulk composition affects chlorite stability. These results confirmed that high Mg# chlorite has higher thermal stability than low Mg# chlorite. The presence of Ca reduces thermal stability, Cr increases chlorite stability to higher pressure and temperature, and Fe reduces thermal stability at low pressure but increases it at high pressure.

Naturally-occurring minerals. This study was the first to use only naturally-occurring minerals. The appearance of the uncommon, hydrous minerals 11.5Å-phase and MgS at high pressure suggests that they could be found in naturally-occurring rocks. Furthermore, the absence of 10Å-phase in any experimental run may be related to the use of natural minerals in the starting materials.

Up-temperature shift in the hydrous-anhydrous boundary at sub-arc depths. The elevated stability field of chlorite, 11.5Å-phase and MgS shifted the hydrous-anhydrous boundary to higher temperature. At 6.2 GPa, this led to a significant increase of 150°C in chlorite peridotite and 200°C in chlorite schists.

The location of the 'anhydrous nose' related to bulk composition. The change to the chlorite stability field leads to a shift in the location of the 'anhydrous nose'. In chlorite peridotites, it is located near

4.9 GPa, 710°C, which indicates a down-pressure change of 1.3 GPa but an up-temperature shift of 130°C. The shift is even more significant in chlorite schists. In this lithology, the 'anhydrous nose' is located near 5.7 GPa, 735°C, a down-pressure shift of 0.5 GPa and a thermal increase of 155°C.

Patterns of water release. These experimental results demonstrated that chlorite breakdown produced free water over a small temperature interval. In contrast, the breakdown of 11.5Å-phase, MgS and magnesiokatophorite liberated water over a wider temperature range.

Water transport to the deep mantle. With each of the hydrous phases chlorite, 11.5Å-phase and MgS shown to be stable above 6.0 GPa, bound water can be transported beyond sub-arc depths to the deep mantle. Around 8 % of the water contained in chlorite is sequestered in MgS following chlorite breakdown whilst ~25% of water contained in chlorite is retained in the 11.5Å-phase.

Quantity of water transport dependent upon location of hydrous phases. Where the hydrous phases chlorite, 11.5Å-phase and MgS form impacts their capacity to transport water to the deeper mantle. Chlorite mélange schist forms on the slab surface. Geophysical modelling (Arcay, Tric and Doin, 2007; Syracuse, van Keken and Abers, 2010) indicated that chlorite in this lithology can feasibly survive subduction but only on the coolest of slabs since the 'anhydrous nose' at 5.7 GPa, 735°C forces chlorite dehydration prior to the formation of 11.5Å-phase in warmer slabs. In contrast, chlorite peridotite forms in the interior of the down-going hydrated oceanic lithosphere, where the thermal profile remains much cooler than the slab surface. Geophysical modelling (Arcay, Tric and Doin, 2007; Syracuse, van Keken and Abers, 2010) showed that chlorite and MgS formed within the slab would remain stable at all P,T conditions experienced in the sub-arc, thus ensuring the successful transport of sequestered water into the deeper mantle.

Recalibration of the water budget. With bound water able to be subducted beyond sub-arc depths, a recalibration of the water budget is required to accommodate the additional water sequestered in these hydrous minerals within the deep mantle. It follows that the sub-arc water budget also needs to be adjusted as chlorite does not necessarily dehydrate at sub-arc depths which leads to a reduction of water volume at these depths.

Peridotite composition determines the quantity of water liberation. Fertile lherzolites can contain twice the quantity of chlorite compared with depleted harzburgites (Schmidt and Poli, 1998) and therefore twice the volume of sequestered water. This is due to the higher levels of Al in lherzolite required to form chlorite in the first instance. However, lherzolites also contain Ca and experimental results in Series 2 showed that bound water in lherzolites is liberated along Reaction 3 whilst water liberation in harzburgites occurs with Reaction 4. Reaction 3 is shown to have lower P,T stability than

Reaction 4 and so lherzolites will liberate twice the volume of water compared to harzburgites but at lower P,T conditions. Furthermore, this means that harzburgites are more successful water transport repositories than lherzolites, but they only transport half the quantity. Chlorite mélange schists still have the highest P,T stability of any of the chlorite lithologies studied therefore they will be able to transport water to greater depth where water liberation occurs.

Mantle rheology. Small amounts of water added to high-pressure, high-temperature mantle rocks have a profound impact upon rheology, phase relations and their geophysical responses. This research highlights the need to assess the impact of additional hydrous minerals at depth and to more fully understand the process of water liberation in the deep mantle. In turn, this would require the recalibration of existing geophysical models to account for these changes.

Chlorite schist is more buoyant than peridotite. The results showed that chlorite schist of any composition is more buoyant than peridotite. Therefore, it is theoretically possible that they could form diapiric structures in the subduction channel.

Mafic chlorite schist dehydrates prior to melting. These results show that the maximum stability of chlorite in a mafic chlorite schist is $\sim 780^{\circ}\text{C}$ which is $\sim 300^{\circ}\text{C}$ lower than the onset of melting in this lithology. This means that a large thermal gap exists between the liberation of water from chlorite and the onset of melting of the protolith. Therefore, bound water in chlorite schist would be released long before being incorporated into melt.

Corner flow is disrupted by diapiric rise. According to the Marschall and Schumacher model (Marschall and Schumacher, 2012), corner flow acts to drag a rising diapir obliquely into the hottest part of the mantle wedge positioning it directly underneath arc volcanoes. However, the rise of cool diapirs through the mantle wedge has been shown experimentally to permanently disrupt corner flow. This means that any subsequent diapir would rise vertically into the cooler fore-arc region with no spatial association with arc volcanism. Consequently, corner flow is not the key mechanism in mass transport through the mantle wedge.

The Marschall and Schumacher model has no application at sub-arc depths. Due to the density of garnet peridotite, the disruption to corner flow and the lower stability field of mafic chlorite, it is apparent that the mélange diapir model proposed by Marschall and Schumacher (Marschall and Schumacher, 2012) has no application at sub-arc conditions.

Wet peridotite solidus determined at 3.0 GPa between 1100°C and 1150°C . This indicates that the initial transport of fluid bound in hydrous minerals from sediments, slab or mantle rocks must occur in ways other than as melt. These results confirm the bulk of previous research on this theme and

serve to dispel the research of Till (Till, Grove and Withers, 2012) who argued that the wet peridotite solidus was located at a considerably lower temperature.

6.3 FUTURE RESEARCH DIRECTIONS

Whilst numerous data points were determined in this suite of experiments, there remain several avenues of research to establish a fully constrained chlorite stability field.

Additional high-pressure chlorite experiments. Further experiments need to be conducted at pressures above 6.2 GPa and temperatures below 675°C to fully constrain the upper stability boundary of chlorite. Prime among these is Reaction F2/E6 ($\text{chl}=\text{MgS}+\text{ol}+11.5\text{\AA}$) which currently has no high-pressure constraints. Although several data points were experimentally determined for Reaction B6/E2 ($\text{chl}=\text{grt}+11.5\text{\AA}+\text{ol}+\text{H}_2\text{O}$), more precise constraints are required.

Any future experimentation planned at higher pressures would need to be conducted on a multi-anvil device as these pressures are very near the maximum possible on the UHP apparatus.

Low-pressure constraints on 11.5Å-phase. Further experiments are required to determine more precise constraints on the stability field of the hydrous 11.5Å-phase and MgS, including their delineation from each other in P,T space. Schreinemakers analysis identified several important reactions involving these phases to higher pressure: Reaction F1 ($\text{opx}+11.5\text{\AA}=\text{MgS}+\text{ol}+\text{H}_2\text{O}$), Reaction K1 ($\text{MgS}+\text{cpx}+\text{ol}=\text{grt}+\text{opx}+\text{H}_2\text{O}$), Reaction E1 ($\text{ol}+\text{MgS}=\text{grt}+11.5\text{\AA}+\text{H}_2\text{O}$), Reaction B1 ($\text{ol}+\text{sp}+\text{H}_2\text{O}=11.5\text{\AA}+\text{grt}$).

Experiments at high pressure using SY3 and SY4. According to the findings from Series 1 experiments, an increase of iron in the bulk composition should substantially increase the chlorite stability field at high pressure. It would be interesting to see if that did occur by undertaking further piston cylinder experiments using this bulk composition.

Al in chlorite. The addition of aluminium to (normally Al-free) minerals is known to alter their stability fields. Does chlorite of varied Al-concentration impact the chlorite stability field? Piston cylinder experimentation would provide insight into this phenomenon.

Role of minor elements in Mg-sursassite. Experimental results revealed two trends in MgS composition: a strong inverse correlation between Ca and Fe cations and increasing pressure, and a positive correlation between Cr cations and increasing pressure. This trend may be the result of using natural minerals in the starting material, but the role of minor elements seems not to have been studied by other researchers and warrants further investigation.

Melt experiments using varied chlorite composition. It is envisaged that the location of the wet solidus would change if chlorite of different Mg# or chlorite-bearing schists of varied mineral composition were used in experimentation. Whilst it is anticipated that the results would have limited impact upon the veracity of the Marschall and Schumacher model, or of the work of Till et al., this would be an interesting exercise in more fully understanding the behaviour of natural chlorite schists.

Recalibration of chlorite values in thermodynamic databases. The experimental results from this study reveal chlorite of different compositions have varied stability fields, particularly at high pressure. Commonly-used thermodynamic databases (Holland and Powell, 2011) accommodate high-pressure chlorite, but do not account for the presence of chromium in chlorite. This study shows the need to recalibrate thermodynamic databases using chlorite of varied composition.

CHAPTER 7 : REFERENCE LIST

Abers, G. A. (2005) 'Seismic low-velocity layer at the top of subducting slabs: observations, predictions, and systematics', *Physics of the Earth and Planetary Interiors*, 149(1–2), pp. 7–29.

Ackerson, M. R., Watson, E. B., Tailby, N. D. and Spear, F. S. (2017) 'Experimental investigation into the substitution mechanisms and solubility of Ti in garnet', *American Mineralogist*, 102(1), pp. 158–172.

Adam, J., Green, T. H., Sie, S. H. and Ryan, C. (1997) 'Trace element partitioning between aqueous fluids, silicate melts and minerals', *European Journal of Mineralogy*, 9, pp. 569–584.

Angiboust, S., Langdon, R., Agard, P., Waters, D. and Chopin, C. (2012) 'Eclogitization of the Monviso ophiolite (W. Alps) and implications on subduction dynamics', *Journal of Metamorphic Geology*, 30(1), pp. 37–61.

Angiboust, S., Pettke, T., de Hoog, J. C. M., Caron, B. and Oncken, O. (2014) 'Channelized Fluid Flow and Eclogite-facies Metasomatism along the Subduction Shear Zone', *Journal of Petrology*, 55(5), pp. 883–916.

Arcay, D., Tric, E. and Doin, M.-P. (2007) 'Slab surface temperature in subduction zones: Influence of the interplate decoupling depth and upper plate thinning processes', *Earth and Planetary Science Letters*, 255(3–4), pp. 324–338.

Arculus, R. J. and Johnson, R. W. (1978) 'Criticism of Generalised models for the magmatic evolution of arc-trench systems', *Earth and Planetary Science Letters*, 39(3), pp. 118–126.

Artioli, G., Fumagalli, P. and Poli, S. (1999) 'The crystal structure of Mg₈ (Mg₂Al₂) Al₈Si₁₂ (O, OH) 56 pumpellyite and its relevance in ultramafic systems at high pressure', *American Mineralogist*, 84, pp. 1906–1914.

Bailey, S. W. (1988) 'Chlorites: structures and crystal chemistry', in Bailey, S. W. (ed.) *Hydrous phyllosilicates*. Chelsea, Michigan: Mineralogical Society of America, pp. 347–405.

Bauer, J. F. and Sclar, C. B. (1981) 'The "10A phase" in the system MgO-SiO₂-H₂O', *American Mineralogist*, 66(1971), pp. 576–585.

Bebout, G. E. (1991) 'Field-based evidence for devolatilization in subduction zones: implications for arc magmatism.', *Science (New York, N.Y.)*, 251(4992), pp. 413–6.

- Bebout, G. E. and Barton, M. D. (2002) 'Tectonic and metasomatic mixing in a high- T , subduction-zone melange — insights into the geochemical evolution of the me slab – mantle interface', *Chemical Geology*, 187, pp. 79–106.
- Bebout, G. E. and Penniston-Dorland, S. C. (2016) 'Fluid and mass transfer at subduction interfaces- The field metamorphic record', *Lithos*. Elsevier B.V., 240–243(March 2016), pp. 228–258.
- Behn, M. D., Kelemen, P. B., Hirth, G., Hacker, B. R. and Massonne, H.-J. (2011) 'Diapirs as the source of the sediment signature in arc lavas', *Nature Geoscience*. Nature Publishing Group, 4(9), pp. 641–646.
- Blanco-Quintero, I. F., Garcia-Casco, A. and Gerya, T. V. (2010) 'Tectonic blocks in serpentinite melange (eastern Cuba) reveal large-scale convective flow of the subduction channel', *Geology*, 39(1), pp. 79–82.
- Brey, G. P., Kohler, T. and Nickel, K. G. (1990) 'Geothermobarometry in Four-phase Lherzolites I . Experimental Results from 10 to 60 kb', *Journal of Petrology*, 31(6), pp. 1313–1352.
- Bromiley, G. D. and Pawley, A. R. (2002) 'The high-pressure stability of Mg-sursassite in a model hydrous peridotite: a possible mechanism for the deep subduction of significant volumes of H₂O', *Contributions to Mineralogy and Petrology*, 142(6), pp. 714–723.
- Bromiley, G. D. and Pawley, A. R. (2003) 'The stability of antigorite in the systems MgO-SiO₂-H₂O (MSH) and MgO-Al₂O₃-SiO₂-H₂O (MASH): The effects of Al³⁺ substitution on high-pressure stability', *American Mineralogist*, 88(1987), pp. 99–108.
- Bulle, F., Bröcker, M., Gärtner, C. and Keasling, A. (2010) 'Geochemistry and geochronology of HP mélanges from Tinos and Andros, cycladic blueschist belt, Greece', *Lithos*. Elsevier B.V., 117(1–4), pp. 61–81.
- Cagnioncle, A. M., Parmentier, E. M. and Elkins-Tanton, L. T. (2007) 'Effect of solid flow above a subducting slab on water distribution and melting at convergent plate boundaries', *Journal of Geophysical Research*, 112(B9), pp. 1–19.
- Cannat, M. (1993) 'Emplacement of mantle rocks in the seafloor at mid-ocean ridges', *Journal of Geophysical Research*, 98(B3), p. 4163.
- Cai, N., Inoue, T., Fujino, K., Ohfuji, H. and Yurimoto, H. (2015) 'A Possible New Al-bearing Hydrous Mg-silicate (23 Å phase) in the Deep Upper Mantle', *American Mineralogist*, 100, pp. 2330–2335.

Carter, L. B., Skora, S., Blundy, J. D., De Hoog, J. C. M. and Elliott, T. (2015) 'An Experimental Study of Trace Element Fluxes from Subducted Oceanic Crust', *Journal of Petrology*, 56(8), pp. 1585–1606.

Castro, A. and Gerya, T. V. (2008) 'Magmatic implications of mantle wedge plumes: Experimental study', *Lithos*, 103(1–2), pp. 138–148.

Castro, A., Gerya, T., García-Casco, A., Fernández, C., Díaz-Alvarado, J., Moreno-Ventas, I. and Löw, I. (2010) 'Melting relations of MORB-sediment mélanges in underplated mantle wedge plumes; Implications for the origin of Cordilleran-type batholiths', *Journal of Petrology*, 51(6), pp. 1267–1295.

Chantel, J., Mookherjee, M. and Frost, D. J. (2012) 'The elasticity of lawsonite at high pressure and the origin of low velocity layers in subduction zones', *Earth and Planetary Science Letters*. Elsevier, 349–350, pp. 116–125.

Cloos, M. and Shreve, R. L. (1988) 'Subduction-channel model of prism accretion, melange formation, sediment subduction, and subduction erosion at convergent plate margins: 2. Implications and discussion', *Pure and Applied Geophysics PAGEOPH*, 128(3–4), pp. 501–545.

Connolly, J. A. D. (1990) 'Multivariable phase-diagrams — an algorithm based on generalized thermodynamics.', *American Journal of Science*, 290, pp. 666–718.

Cooper, L. B., Ruscitto, D. M., Plank, T., Wallace, P. J., Syracuse, E. M. and Manning, C. E. (2012) 'Global variations in H₂O/Ce: 1. Slab surface temperatures beneath volcanic arcs', *Geochemistry, Geophysics, Geosystems*, 13(3), pp. 1-27.

Dalou, C., Koga, K. T., Shimizu, N., Boulon, J. and Devidal, J. L. (2012) 'Experimental determination of F and Cl partitioning between lherzolite and basaltic melt', *Contributions to Mineralogy and Petrology*, 163(4), pp. 591–609.

Deer, W. A., Howie, R. A. and Zussman, J. (1992) *Introduction to the rock-forming minerals*. 2nd edn. Harlow, UK: Pearson Education Limited.

Delany, J. and Helgeson, H. (1978) 'Calculation of the Thermodynamic Consequences of Dehydration in Subducting Oceanic Crust to 100 KB and > 800°C', *American Journal of Science*, 278(May), pp. 638–686.

Deschamps, F., Godard, M., Guillot, S. and Hattori, K. (2013) 'Geochemistry of subduction zone serpentinites: A review', *Lithos*. Elsevier B.V., 178, pp. 96–127.

Dilek, Y., Festa, A., Ogawa, Y. and Pini, G. A. (2012) 'Chaos and geodynamics: Mélanges, mélange-forming processes and their significance in the geological record', *Tectonophysics*, 568–569, pp. 1–6.

- Dvir, O., Pettke, T., Fumagalli, P. and Kessel, R. (2011) 'Fluids in the peridotite–water system up to 6 GPa and 800°C: new experimental constraints on dehydration reactions', *Contributions to Mineralogy and Petrology*, 161(6), pp. 829–844.
- England, P. C. and Katz, R. F. (2010) 'Melting above the anhydrous solidus controls the location of volcanic arcs.', *Nature*. Nature Publishing Group, 467(7316), pp. 700–3.
- Evans, B. W. and Trommsdorff, V. (1978) 'Petrogenesis of garnet lherzolite, Cima di Gagnone, Lepontine Alps', *Earth and Planetary Science Letters*, 40(3), pp. 333–348.
- Fawcett, J. and Yoder, H. (1966) 'Phase relationships of chlorites in the system MgO–Al₂O₃–SiO₂–H₂O', *The American Mineralogist*, 51(March–April), pp. 353–380.
- Fischer, J. K., Gemmi, M., Merlini, M., Fumagalli, P. and Poli, S. (2010) 'The effect of Cr on chlorite stability and the appearance of a new Al-rich silicate', *Geophysical Research Abstracts*, 12, p. 7294.
- Fockenberg, T. (1995) 'New experimental constraints up to 100 kbar in the system MgO–Al₂O₃–SiO₂–H₂O (MASH): Preliminary stability fields of chlorite, chloritoid, staurolite, MgMgAl-pumpellyite, and pyrope.', *Bochumer Geologische und Geotechnische Arbeiten*, 44, pp. 39–44.
- Fockenberg, T. (1998) 'An experimental study of the pressure-temperature stability of MgMgAl-pumpellyite in the system MgO–Al₂O₃–SiO₂–H₂O', *American Mineralogist*, 83, pp. 220–227.
- Fumagalli, P., Stixrude, L., Poli, S. and Snyder, D. (2001) 'The 10A phase: A high-pressure expandable sheet silicate stable during subduction of hydrated lithosphere', *Earth and Planetary Science Letters*, 186(2), pp. 125–141.
- Fumagalli, P. and Poli, S. (2005) 'Experimentally Determined Phase Relations in Hydrous Peridotites to 6.5 GPa and their Consequences on the Dynamics of Subduction Zones', *Journal of Petrology*, 46(3), pp. 555–578.
- Fumagalli, P., Zanchetta, S. and Poli, S. (2009) 'Alkali in phlogopite and amphibole and their effects on phase relations in metasomatized peridotites: a high-pressure study', *Contributions to Mineralogy and Petrology*, 158(6), pp. 723–737.
- Fumagalli, P., Poli, S., Fischer, J., Merlini, M. and Gemmi, M. (2014) 'The high-pressure stability of chlorite and other hydrates in subduction mélanges: experiments in the system Cr₂O₃–MgO–Al₂O₃–SiO₂–H₂O', *Contributions to Mineralogy and Petrology*, 167(2), p. 979.
- Fyfe, W. S. and Mackenzie, W. S. (1969) 'Some aspects of experimental petrology', *Earth Science Reviews*, 5(3), pp. 185–215.

- Gaetani, G. and Grove, T. (1998) 'The influence of water on melting of mantle peridotite', *Contributions to Mineralogy and Petrology*, (April 1997).
- Gemmi, M., Fischer, J., Merlini, M., Poli, S., Fumagalli, P., Mugnaioli, E. and Kolb, U. (2011) 'A new hydrous Al-bearing pyroxene as a water carrier in subduction zones', *Earth and Planetary Science Letters*. Elsevier B.V., 310(3–4), pp. 422–428.
- Gemmi, M., Merlini, M., Palatinus, L., Fumagalli, P. and Hanfland, M. (2016) 'Electron diffraction determination of $11 \cdot 5 \text{ \AA}$ and HySo structures: Candidate water carriers to the Upper Mantle', *American Mineralogist*, 101, pp. 2645–2654.
- Gerya, T. V., Connolly, J. A. D., Yuen, D. A., Górczyk, W. and Capel, A. M. (2006) 'Seismic implications of mantle wedge plumes', *Physics of the Earth and Planetary Interiors*, 156(1–2), pp. 59–74.
- Gerya, T. V. and Yuen, D. A. (2003) 'Rayleigh–Taylor instabilities from hydration and melting propel “cold plumes” at subduction zones', *Earth and Planetary Science Letters*, 212(1–2), pp. 47–62.
- Goto, A. and Tatsumi, Y. (1990) 'Stability of chlorite in the upper mantle', *American Mineralogist*, 75, pp. 105–108.
- Gottschalk, M., Fockenberg, T., Grevel, K., Under, B., Wirth, R., Schreyer, W. and Maresch, W. (2000) 'Crystal Structure of the high-pressure phase $\text{Mg}_4(\text{MgAl})\text{Al}_4[\text{Si}_6\text{O}_{21}/(\text{OH})_7]$: An analogue of sursassite', *European Journal of Mineralogy*, 12(5), pp. 935–945.
- Green, D. H. (1973) 'Experimental melting studies in a model upper mantle composition at high pressure under water-saturated and water-undersaturated conditions.', *Earth and Planetary Science Letters*, 19, pp. 37–53.
- Green, D. H. (1976) 'Experimental testing of “equilibrium” partial melting of peridotite under water-saturated, high-pressure conditions.', *Canadian Mineralogist*, 14, pp. 255–268.
- Green, D. H., Rosenthal, A. and Kovács, I. (2012) 'Comment on “The beginnings of hydrous mantle wedge melting”', CB Till, TL Grove, AC Withers, *Contributions to Mineralogy and Petrology*, DOI 10.1007/s00410-011-0692-6', *Contributions to Mineralogy and Petrology*, 164(6), pp. 1077–1081.
- Green, D. H., Hibberson, W. O., Rosenthal, A., Kovacs, I., Yaxley, G. M., Falloon, T. J. and Brink, F. (2014) 'Experimental Study of the Influence of Water on Melting and Phase Assemblages in the Upper Mantle', *Journal of Petrology*, 55(10), pp. 2067–2096.
- Green, D. H. (2015) 'Experimental petrology of peridotites, including effects of water and carbon on melting in the Earth's upper mantle', *Physics and Chemistry of Minerals*, 42(2), pp. 95–122.

Grove, T., Chatterjee, N., Parman, S. and Medard, E. (2006) 'The influence of H₂O on mantle wedge melting', *Earth and Planetary Science Letters*, 249(1–2), pp. 74–89.

Grove, T. L., Till, C. B. and Krawczynski, M. J. (2012) 'The Role of H₂O in Subduction Zone Magmatism', *Annual Review of Earth and Planetary Sciences*, 40(1), pp. 413–439.

Guillot, S., Hattori, K. H. and Sigoyer, J. D. (2001) 'Evidence of hydration of the mantle wedge and its role in the exhumation of eclogites', *Earth and Planetary ...*, 193.

Hacker, B. R., Abers, G. A. and Peacock, S. M. (2003) 'Subduction factory 1. Theoretical mineralogy, densities, seismic wave speeds, and H₂O contents', *Journal of Geophysical Research*, 108(B1), p. 2029.

Hall, P. S. and Kincaid, C. (2001) 'Diapiric flow at subduction zones: a recipe for rapid transport.', *Science (New York, N.Y.)*, 292(5526), pp. 2472–5.

Hasenclever, J., Morgan, J. P., Hort, M. and Rüpke, L. H. (2011) '2D and 3D numerical models on compositionally buoyant diapirs in the mantle wedge', *Earth and Planetary Science Letters*. Elsevier B.V., 311(1–2), pp. 53–68.

Hebert, L. B., Antoshechkina, P., Asimow, P. and Gurnis, M. (2009) 'Emergence of a low-viscosity channel in subduction zones through the coupling of mantle flow and thermodynamics', *Earth and Planetary Science Letters*. Elsevier B.V., 278(3–4), pp. 243–256.

Hermann, J. and Spandler, C. J. (2008) 'Sediment Melts at Sub-arc Depths: an Experimental Study', *Journal of Petrology*, 49(4), pp. 717–740.

Hermann, J., Spandler, C. J., Hack, A. and Korsakov, A. V. (2006) 'Aqueous fluids and hydrous melts in high-pressure and ultra-high pressure rocks: Implications for element transfer in subduction zones', *Lithos*, 92(3–4), pp. 399–417.

Hermann, J., Troitzsch, U. and Scott, D. (2016) 'Experimental subsolidus phase relations in the system CaCO₃-CaMg(CO₃)₂ up to 6.5 GPa and implications for subducted marbles', *Contributions to Mineralogy and Petrology*. Springer Berlin Heidelberg, 171(10), pp. 1–17.

Herrmann, W. and Berry, R. F. (2002) 'MINSQ - a least squares spreadsheet method for calculating mineral proportions from whole rock major element analyses', *Geochemistry: Exploration, Environment, Analysis*, 2(4), pp. 361–368.

Holland, T. J. B. and Powell, R. (2011) 'An improved and extended internally consistent thermodynamic dataset for phases of petrological interest, involving a new equation of state for solids', *Journal of Metamorphic Geology*, 29, pp. 333–383.

- Hunziker, P. (2003) *The stability of tri-octahedral Fe²⁺-Mg-Al chlorite: a combined experimental and theoretical study*.
- Hyndman, R. D. and Peacock, S. M. (2003) 'Serpentinization of the forearc mantle', *Earth and Planetary Science Letters*, 212(3–4), pp. 417–432.
- Jenkins, D. (1981) 'Experimental phase relations of hydrous peridotites modelled in the system H₂O-CaO-MgO-Al₂O₃-SiO₂', *Contributions to Mineralogy and Petrology*, 77, pp. 166–176.
- Jenkins, D. M. and Chernosky, J. V. (1986) 'Phase equilibria and crystallochemical properties of Mg-chlorite', *American Mineralogist*, 71, pp. 924–936.
- John, T., Scambelluri, M., Frische, M., Barnes, J. D. and Bach, W. (2011) 'Dehydration of subducting serpentinite: Implications for halogen mobility in subduction zones and the deep halogen cycle', *Earth and Planetary Science Letters*. Elsevier B.V., 308(1–2), pp. 65–76.
- van Keken, P. E. (2003) 'The structure and dynamics of the mantle wedge', *Earth and Planetary Science Letters*, 215(3–4), pp. 323–338.
- Kelemen, P. B., Rilling, J. L., Parmentier, E. M., Mehl, L. and Hacker, B. R. (2002) 'Thermal Structure due to Solid-State Flow in the Mantle Wedge Beneath Arcs', in *Subduction Factory, Geophys. Monogr. Series*, pp. 293–311.
- Keppler, H. (2017) 'Fluids and trace element transport in subduction zones', *American Mineralogist*, 102(1), pp. 5–20.
- Kessel, R., Schmidt, M. W., Ulmer, P. and Pettke, T. (2005a) 'Trace element signature of subduction-zone fluids, melts and supercritical liquids at 120–180 km depth', *Nature*, 437(7059), pp. 724–727.
- Kessel, R., Ulmer, P., Pettke, T., Schmidt, M. W. and Thompson, A. B. (2005b) 'The water-basalt system at 4 to 6 GPa: Phase relations and second critical endpoint in a K-free eclogite at 700 to 1400 °C', *Earth and Planetary Science Letters*, 237(3–4), pp. 873–892.
- Khisina, N. R. and Wirth, R. (2008) 'Nano-inclusions of high-pressure hydrous silicate, Mg₃Si₄O₁₀(OH)₂ · nH₂O (10 Å-phase), in mantle olivine: Mechanisms of formation and transformation', *Geochemistry International*, 46(4), pp. 319–327.
- King, R. L., Bebout, G. E., Moriguti, T. and Nakamura, E. (2006) 'Elemental mixing systematics and Sr–Nd isotope geochemistry of mélange formation: Obstacles to identification of fluid sources to arc volcanics', *Earth and Planetary Science Letters*, 246(3–4), pp. 288–304.
- Kleppe, A. K., Jephcoat, A. P. and Welch, M. D. (2003) 'The effect of pressure upon hydrogen bonding

in chlorite : A Raman spectroscopic study of clinocllore to 26 . 5 GPa', *American Mineralogist*, 88(1995), pp. 567–573.

Klimm, K., Blundy, J. D. and Green, T. H. (2008) 'Trace element partitioning and accessory phase saturation during H₂O-saturated melting of basalt with implications for subduction zone chemical fluxes', *Journal of Petrology*, 49(3), pp. 523–553.

Koyama, T., Shimizu, H., Utada, H., Ohtani, E. and Hae, R. (2004) 'Water contents in the mantle transition zone beneath the north Pacific derived from the electrical conductivity anomaly [abs.]', *Eos, Transactions, American Geophysical Union supp.*, v. 85(47), p. abs. no. T31F-05.

Lafuente, B., Downs, R. T., Yang, H. and Stone, N. (2015) 'The power of databases: the RRUFF project', in *Highlights in Mineralogical Crystallography*, pp. 1–30.

Lanari, P., Wagner, T. and Vidal, O. (2014) 'A thermodynamic model for di-trioctahedral chlorite from experimental and natural data in the system MgO–FeO–Al₂O₃–SiO₂–H₂O: applications to P–T sections and geothermometry', *Contributions to Mineralogy and Petrology*, 167(2), p. 968.

Leake, B. E., Wooley, A. R., Arps, C. E., Birch, W. D., Gilbert, M. C., Grice, J. D., Hawthorne, F. C., Kisch, H. J., Krivovichev, V. G., Lintout, K., Laird, J., Mandarino, J. A., Maresch, W. V., Nickel, E. H., Rock, N. M., Schumacher, J. C., Smith, D. C., Stephenson, N., Ungaretti, L., Whittaker, E. J. and Youzhi, G. (1997) 'Nomenclature of amphiboles: Report of the sub-committee on amphiboles of the International Mineralogical Association, Commission on new minerals and mineral names.', *The Canadian Mineralogist*, 35, pp. 219–246.

Li, H. and Hermann, J. (2017) 'The effect of fluorine and chlorine on trace element partitioning between apatite and sediment melt at subduction zone conditions', *Chemical Geology*. Elsevier, 473(September), pp. 55–73.

Louvel, M., Sanchez-Valle, C., Malfait, W. J., Cardon, H., Testemale, D. and Hazemann, J. L. (2014) 'Fluids in the crust. Constraints on the mobilization of Zr in magmatic-hydrothermal processes in subduction zones from in situ fluid-melt partitioning experiments', *American Mineralogist*, 99(8–9), pp. 1616–1625.

Luth, R. W. (2014) 'Volatiles in Earth's Mantle', *Treatise on Geochemistry*. 2nd edn. Edited by H. Holland and K. Turekian. Elsevier Ltd., 4(2002), pp. 355–391.

Manning, C. E. (2004) 'The chemistry of subduction-zone fluids', *Earth and Planetary Science Letters*, 223(1–2), pp. 1–16.

Manthilake, G., Mookherjee, M., Bolfan-Casanova, N. and Andrault, D. (2015) 'Electrical conductivity

of lawsonite and dehydrating fluids at high pressures and temperatures', *Geophysical Research Letters*, 42(18), pp. 7398–7405.

Marocchi, M., Hermann, J. and Morten, L. (2007) 'Evidence for multi-stage metasomatism of chlorite-amphibole peridotites (Ulten Zone, Italy): Constraints from trace element compositions of hydrous phases', *Lithos*, 99(1–2), pp. 85–104.

Marschall, H. R. (2006) 'Syros Metasomatic Tourmaline: Evidence for Very High- 11B Fluids in Subduction Zones', *Journal of Petrology*, 47(10), pp. 1915–1942.

Marschall, H. R., Altherr, R. and Rupke, L. H. (2007) 'Squeezing out the slab — modelling the release of Li, Be and B during progressive high-pressure metamorphism', *Chemical Geology*, 239(3–4), pp. 323–335.

Marschall, H. R. and Schumacher, J. C. (2012) 'Arc magmas sourced from mélange diapirs in subduction zones', *Nature Geoscience*. Nature Publishing Group, 5(12), pp. 862–867.

Martin, L., Hermann, J., Gauthiez-Putallaz, L., Whitney, D. L., Vitale Brovarone, A., Fornash, K. F. and Evans, N. J. (2014) 'Lawsonite geochemistry and stability - implication for trace element and water cycles in subduction zones', *Journal of Metamorphic Geology*, 32(5), pp. 455–478.

Mibe, K., Kawamoto, T., Matsukage, K. N., Fei, Y. and Ono, S. (2011) 'Slab melting versus slab dehydration in subduction-zone magmatism.', *Proceedings of the National Academy of Sciences of the United States of America*, 108(20), pp. 8177–82.

Miller, D. P., Marschall, H. R. and Schumacher, J. C. (2009) 'Metasomatic formation and petrology of blueschist-facies hybrid rocks from Syros (Greece): Implications for reactions at the slab–mantle interface', *Lithos*. Elsevier B.V., 107(1–2), pp. 53–67.

Miller, N. C. and Behn, M. D. (2012) 'Timescales for the growth of sediment diapirs in subduction zones', *Geophysical Journal International*, 190(3), pp. 1361–1377.

Millhollen, G. L., Irving, A. J. and Wyllie, P. J. (1974) 'Melting Interval of Peridotite with 5.7 per cent Water to 30 Kilobars.', *Journal of Geology*, 82(5), pp. 575–587.

Mori, Y., Shigeno, M. and Nishiyama, T. (2014) 'Fluid-metapelite interaction in an ultramafic mélange: implications for mass transfer along the slab-mantle interface in subduction zones', *Earth, Planets and Space*. Springer, 66(1), p. 47.

Mysen, B. and Boettcher, A. (1975) 'Melting of a Hydrous Mantle : I . Phase Relations of Natural Peridotite at High Pressures and Temperatures with Controlled Activities of Water , Carbon Dioxide , and Hydrogen', *Journal of Petrology*, 16(3), pp. 520–548.

Nielsen, S. G. and Marschall, H. R. (2017) 'Geochemical evidence for mélangé melting in global arcs', *Science Advances*, 3(4), pp. 1–6.

Niida, K. and Green, D. H. (1999) 'Stability and chemical composition of pargasitic amphibole in MORB pyrolite under upper mantle conditions', *Contributions to Mineralogy and Petrology*, 135(1), pp. 18–40.

Omega Engineering (2011) *Revised Thermocouple Reference Tables*, Omega.

O'Neill, H. S. (1981) 'The transition between spinel lherzolite and garnet lherzolite, and its use as a geobarometer', *Contribution to Mineralogy and Petrology*, 77(2), pp. 185–194.

Osada, Y., Yamamoto, K., Ueno, T., Maekawa, H. and Nogami, N. (2004) 'Significance of Serpentinites and Related Rocks in the High-Pressure Metamorphic Terranes, Circum-Pacific Regions', *International Geology Review*, 46(5), pp. 426–444.

Padron-Navarta, J. A., Lopez Sanchez-Vizcaino, V., Garrido, C. J., Gomez-Pugnaire, M. T., Jabaloy, A., Capitani, G. C. and Mellini, M. (2008) 'Highly ordered antigorite from Cerro del Almiraz HP–HT serpentinites, SE Spain', *Contributions to Mineralogy and Petrology*, 156(5), pp. 679–688.

Padron-Navarta, J. A., Hermann, J., Garrido, C. J., Lopez, S.-J. V. and Gomez-Pugnaire, M. T. (2010a) 'An experimental investigation of antigorite dehydration in natural silica-enriched serpentinite', *Contributions to Mineralogy and Petrology*, 159, pp. 25–42.

Padrón-Navarta, J. A., Tommasi, A., Garrido, C. J., Sánchez-Vizcaíno, V. L., Gómez-Pugnaire, M. T., Jabaloy, A. and Vauchez, A. (2010b) 'Fluid transfer into the wedge controlled by high-pressure hydrofracturing in the cold top-slab mantle', *Earth and Planetary Science Letters*. Elsevier B.V., 297(1–2), pp. 271–286.

Padron-Navarta, J. A., Lopez Sanchez-Vizcaino, V., Garrido, C. J. and Gomez-Pugnaire, M. T. (2011) 'Metamorphic Record of High-pressure Dehydration of Antigorite Serpentinite to Chlorite Harzburgite in a Subduction Setting (Cerro del Almiraz, Nevado-Filabride Complex, Southern Spain)', *Journal of Petrology*, 52(10), pp. 2047–2078.

Padron-Navarta, J. A., Sanchez-Vizcaino, V. L., Hermann, J., Connolly, J. A. D., Garrido, C. J., Gomez-Pugnaire, M. T. and Marchesi, C. (2013) 'Tschermak's substitution in antigorite and consequences for

phase relations and water liberation in high-grade serpentinites', *Lithos*. Elsevier B.V., 178, pp. 186–196.

Parra, T. (2005) 'Experimental data on the Tschermak substitution in Fe-chlorite', *American Mineralogist*, 90(2–3), pp. 359–370.

Pawley, A. R. and Holloway, J. R. (1993) 'Water sources for subduction zone volcanism: new experimental constraints.', *Science*, 260(5108), pp. 664–7.

Pawley, A. R. (2003) 'Chlorite stability in mantle peridotite: the reaction clinocllore+enstatite = forsterite+pyrope+H₂O', *Contributions to Mineralogy and Petrology*, 144(4), pp. 449–456.

Pawley, A. R., Chinnery, N. J., Clark, S. M. and Walter, M. J. (2011) 'Experimental study of the dehydration of 10-Å phase, with implications for its H₂O content and stability in subducted lithosphere', *Contributions to Mineralogy and Petrology*, 162(6), pp. 1279–1289.

Pawley, A. and Wood, B. (1995a) 'The high-pressure stability of talc and 10 Å phase: potential storage sites for H₂O in subduction zones', *American Mineralogist*, 80, pp. 998–1003.

Pawley, A. R. and Wood, B. J. (1995b) 'The low pressure stability of Phase A Mg₇Si₂O₈(OH)₆', *Contributions to Mineralogy and Petrology*, 124(December 1995), pp. 90–97.

Peacock, S. M. (1987) 'Serpentinization and infiltration metasomatism in the Trinity peridotite, Klamath province, northern California: implications for subduction zones', *Contributions to Mineralogy and Petrology*, 95(1), pp. 55–70.

Peacock, S. M. (1993) 'Large-scale hydration of the lithosphere above subducting slabs', *Chemical Geology*, 108(1–4), pp. 49–59.

Peacock, S. M. (2004) 'Thermal Structure and Metamorphic Evolution of Subducting Slabs', in *Inside the Subduction Factory*, pp. 7–22.

Penniston-Dorland, S. C., Gorman, J. K., Bebout, G. E., Piccoli, P. M. and Walker, R. J. (2014) 'Reaction rind formation in the Catalina Schist: Deciphering a history of mechanical mixing and metasomatic alteration', *Chemical Geology*. Elsevier B.V., 384, pp. 47–61.

Penniston-Dorland, S. C., Kohn, M. J. and Manning, C. E. (2015) 'The global range of subduction zone thermal structures from exhumed blueschists and eclogites: Rocks are hotter than models', *Earth and Planetary Science Letters*. Elsevier B.V., 428, pp. 243–254.

Pirard, C. and Hermann, J. (2015a) 'Focused fluid transfer through the mantle above subduction zones', *Geology*, 43(10), pp. 915–918.

- Pirard, C. and Hermann, J. (2015b) 'Experimentally determined stability of alkali amphibole in metasomatised dunite at sub-arc pressures', *Contributions to Mineralogy and Petrology*, 169(1).
- Plank, T. (2014) 'The Chemical Composition of Subducting Sediments', in Holland, H. and Turekian, K. (eds) *Treatise on Geochemistry*. 2nd edn. Elsevier Ltd., 4, pp. 607–629.
- Pogge von Strandmann, P. A. E., Dohmen, R., Marschall, H. R., Schumacher, J. C. and Elliott, T. (2015) 'Extreme magnesium isotope fractionation at outcrop scale records the mechanism and rate at which reaction fronts advance', *Journal of Petrology*, 56(1), pp. 33–58.
- Poli, S. and Schmidt, M. W. (2002) 'Petrology of Subducted Slabs', *Annual Review of Earth and Planetary Sciences*, 30(1), pp. 207–235.
- Poli, S., Franzolin, E., Fumagalli, P. and Crottini, A. (2009) 'The transport of carbon and hydrogen in subducted oceanic crust: An experimental study to 5 GPa', *Earth and Planetary Science Letters*, 278(3–4), pp. 350–360.
- Powceby, M. Y., Wall, V. J. and O'Neill, H. (1991) 'An experimental study of the effect of Ca upon garnet Ilmenite Fe-Mn exchange equilibria', *American Mineralogist*, 76(9–10), pp. 1580–1588.
- Rashchenko, S. V., Likhacheva, A. Y., Goryainov, S. V., Krylov, A. S. and Konstantin, D. L. (2016) 'In situ spectroscopic study of water intercalation into talc : New features of 10 Å phase formation', *American Mineralogist*, 101, pp. 431–436.
- Reynard, B., Mibe, K. and de Moortèle, B. Van (2011) 'Electrical conductivity of the serpentinised mantle and fluid flow in subduction zones', *Earth and Planetary Science Letters*. Elsevier B.V., 307(3–4), pp. 387–394.
- Richard, G. C., Iwamori, H., Suetsugu, D., Bina, C., Inoue, T., Wiens, D. A. and Jellinek, M. (2010) 'Stagnant slab, wet plumes and Cenozoic volcanism in East Asia', *Physics of the Earth and Planetary Interiors*, 183(1–2), pp. 280–287.
- Rieder, M., Cavazzini, G., D'Yakonov, Y., Frank-Kamenetskii, V., Gottardi, G., Guggenheim, S., Koval, P., Muller, G., Neiva, A., Radoslovich, E., Robert, J., Sassi, F., Takeda, H., Weiss, Z. and Wones, D. (1999) 'Nomenclature of the Micas', *Mineralogical Magazine*, 63(2), pp. 267–279.
- Rupke, L. (2004) 'Serpentine and the subduction zone water cycle', *Earth and Planetary Science Letters*, 223(1–2), pp. 17–34.
- Scambelluri, M., Muntener, O., Hermann, J., Piccardi, G. B. and Trommsdorff, V. (1995) 'Subduction of water into the mantle: history of an Alpine peridotite', *Geology*, 23, pp. 459–462.

- Scambelluri, M., Müntener, O., Ottolini, L., Pettke, T. T. and Vannucci, R. (2004) 'The fate of B, Cl and Li in the subducted oceanic mantle and in the antigorite breakdown fluids', *Earth and Planetary Science Letters*, 222(1), pp. 217–234.
- Scambelluri, M., Pettke, T., Rampone, E., Godard, M. and Reusser, E. (2014) 'Petrology and Trace Element Budgets of High-pressure Peridotites Indicate Subduction Dehydration of Serpentinized Mantle (Cima di Gagnone, Central Alps, Switzerland)', *Journal of Petrology*, 55(3), pp. 459–498.
- Schmadicke, E. (2000) 'Phase relations in peridotitic and pyroxenitic rocks in the model systems CMASH and NCMASH', *Journal of Petrology*, 41(1), pp. 69–86.
- Schmidt, M. W. and Poli, S. (1994) 'The stability of lawsonite and zoisite at high pressures: Experiments in CASH to 92 kbar and implications for the presence of hydrous phases in subducted lithosphere', *Earth and Planetary Science Letters*, 124(1–4), pp. 105–118.
- Schmidt, M. W. and Poli, S. (1998) 'Experimentally based water budgets for dehydrating slabs and consequences for arc magma generation', *Earth and Planetary Science Letters*, 163(1–4), pp. 361–379.
- Schmidt, M. W. and Poli, S. (2014) 'Devolatilization During Subduction', in Holland, H. and Turekian, K. (eds) *Treatise on Geochemistry*. 2nd edn. Elsevier Ltd., 4, pp. 669–701.
- Schreyer, W., Maresch, W. V., Medenbach, O. and Baller, T. (1986) 'Calcium-free pumpellyite, a new synthetic hydrous Mg-Al-silicate formed at high pressures', *Nature*, 321(6069), pp. 510–511.
- Schuling, R. D. (2011) 'Troodos: A Giant Serpentinite Diapir', *International Journal of Geosciences*, 2(2), pp. 98–101.
- Segnit, E. R. (1963) 'Synthesis of clinocllore at high pressures', *American Mineralogist*, 48(9 & 10), pp. 1080–1089.
- Smith, D. (1995) 'Chlorite-rich ultramafic reaction zones in Colorado Plateau xenoliths: recorders of sub-Moho hydration', *Contributions to Mineralogy and Petrology*, 121(2), pp. 185–200.
- Sorensen, S. S. and Barton, M. D. (1987) 'Metasomatism and partial melting in a subduction complex Catalina Schist, southern California', *Geology*, 15(2), p. 115.
- Sorensen, S. S. and Grossman, J. N. (1993) 'Accessory minerals and subduction zone metasomatism: a geochemical comparison of two melanges (Washington and California, USA)', *Chemical Geology*, 110, pp. 269–297.

- Spandler, C., Mavrogenes, J. and Hermann, J. (2007) 'Experimental constraints on element mobility from subducted sediments using high-P synthetic fluid/melt inclusions', *Chemical Geology*, 239(3–4), pp. 228–249.
- Spandler, C., Hermann, J., Faure, K., Mavrogenes, J. A. and Arculus, R. J. (2008) 'The importance of talc and chlorite “hybrid” rocks for volatile recycling through subduction zones ; evidence from the high-pressure subduction melange of New Caledonia', *Contributions to Mineralogy and Petrology*, 155, pp. 181–198.
- Spandler, C., Yaxley, G., Green, D. H. and Scott, D. (2010) 'Experimental phase and melting relations of metapelite in the upper mantle: Implications for the petrogenesis of intraplate magmas', *Contributions to Mineralogy and Petrology*, 160, pp. 569–589.
- Spandler, C. J. and Pirard, C. (2013) 'Element recycling from subducting slabs to arc crust: A review', *Lithos*. Elsevier B.V., 170–171, pp. 208–223.
- Spandler, C., Pettke, T. and Hermann, J. (2014) 'Experimental study of trace element release during ultrahigh-pressure serpentinite dehydration', *Earth and Planetary Science Letters*. Elsevier B.V., 391, pp. 296–306.
- Stalder, R. (2012) 'Comment on “The beginnings of hydrous mantle wedge melting”, CB Till, TL Grove, AC Withers, Contributions to Mineralogy and Petrology, DOI 10.1007/s00410-011-0692-6', *Contributions to Mineralogy and Petrology*, 164(6), pp. 1069–1071.
- Staudigel, H. and Schreyer, W. (1977) 'The Upper Thermal Stability of Clinocllore, Mg₅Al(AlSi₃O₁₀)(OH)₈, at 10-35 kb PH₂O', *Contributions to Mineralogy and Petrology*, 61, pp. 187–198.
- Syracuse, E. M., van Keken, P. E. and Abers, G. A. (2010) 'The global range of subduction zone thermal models', *Physics of the Earth and Planetary Interiors*, 183(1–2), pp. 73–90.
- Tamura, Y. (2003) 'Some geochemical constraints on hot fingers in the mantle wedge: evidence from NE Japan', *Geological Society, London, Special Publications*, 219(1), pp. 221–237.
- Tatsumi, Y. (1986) 'Formation of the volcanic front in subduction zones', *Geophysical Research Letters*, 13(8), pp. 717–720.
- Tatsumi, Y. (1989) 'Migration of Fluid Phases and Genesis of Basalt Magmas in Subduction Zones', *Journal of Geophysical Research*, 94(B4), pp. 4697–4707.

- Tatsumi, Y. (2003) 'Some constraints on arc magma genesis', in Eiler, J. (ed.) *Inside the subduction Factory*, pp. 277–292.
- Till, C. B., Grove, T. L. and Withers, A. C. (2012a) 'The beginnings of hydrous mantle wedge melting', *Contributions to Mineralogy and Petrology*, 163(4), pp. 669–688.
- Till, C. B., Grove, T. L. and Withers, A. C. (2012b) 'Reply to "Comment on 'The beginnings of hydrous mantle wedge melting' by Till et al." by Green, Rosenthal and Kovacs', *Contributions to Mineralogy and Petrology*, 164(6), pp. 1083–1085.
- Till, C. B., Grove, T. L. and Withers, A. C. (2012c) 'Reply to "Comment on 'The beginnings of hydrous mantle wedge melting' by Till et al." by Stalder', *Contributions to Mineralogy and Petrology*, 164(6), pp. 1073–1076.
- Torres-Roldan, R. L., Garcia-Casco, A. and Garcia-Sanchez, P. A. (2000) 'Cspace: An integrated workplace for the graphical and algebraic analysis of phase assemblages on 32-bit wintel platforms', *Computers and Geosciences*, 26(7), pp. 779–793.
- Truckenbrodt, J. and Johannes, W. (1999) 'H₂O loss during piston-cylinder experiments', *American Mineralogist*, 84, pp. 1333–1335.
- Tsuno, K. and Dasgupta, R. (2012) 'The effect of carbonates on near-solidus melting of pelite at 3GPa: Relative efficiency of H₂O and CO₂ subduction', *Earth and Planetary Science Letters*, 319–320, pp. 185–196.
- Turner, S. J. and Langmuir, C. H. (2015) 'What processes control the chemical compositions of arc front stratovolcanoes?', *Geochemistry, Geophysics, Geosystems*, 16, pp. 1865–1893.
- Ulmer, P. and Trommsdorff, V. (1999) 'Phase relations of hydrous mantle subducting to 300 km', in Fei, Y., Bertka, C. M., and Mysen, B. O. (eds) *Mantle petrology: field observations and high pressure experimentation: a tribute to Francis R. (Joe) Boyd*. Special Pu. The Geochemical Society, pp. 259–281.
- Ulmer, P. (2001) 'Partial melting in the mantle wedge — the role of H₂O in the genesis of mantle-derived "arc-related" magmas', *Physics of the Earth and Planetary Interiors*, 127(1–4), pp. 215–232.
- Veblen, D. R. (1983) 'Exsolution and Crystal-Chemistry of the Sodium Mica Wonesite', *American Mineralogist*, 68(5–6), pp. 554–565.
- Vidal, O., Parra, T. and Trotet, F. (2001) 'A thermodynamic model for Fe-Mg aluminous chlorite using data from phase equilibrium experiments and natural pelitic assemblages in the 100°C to 600°C, 1 to 25 kb range', *American Journal of Science*, 301, pp. 557–592.

- Vidal, O., Parra, T. and Vieillard, P. (2005) 'Thermodynamic properties of the Tschermak solid solution in Fe-chlorite: Application to natural examples and possible role of oxidation', *American Mineralogist*, 90(2–3), pp. 347–358.
- Wada, I., Behn, M. D. and Shaw, A. M. (2012) 'Effects of heterogeneous hydration in the incoming plate, slab rehydration, and mantle wedge hydration on slab-derived H₂O flux in subduction zones', *Earth and Planetary Science Letters*. Elsevier, 353–354, pp. 60–71.
- Wang, A., Freeman, J. and Kuebler, K. E. (2002) 'Raman Spectroscopic Characterization of Phyllosilicates', *Lunar and Planetary Science XXXIII*, 63130, pp. 1–2.
- Webb, S. A. C. and Wood, B. J. (1986) 'Spinel-pyroxene-garnet relationships and their dependence on Cr/Al ratio', *Contributions to Mineralogy and Petrology*, 92(4), pp. 471–480.
- Welch, M. D., Pawley, A. R., Ashbrook, S. E., Mason, H. E. and Phillips, B. L. (2006) 'Si vacancies in the 10-Å phase', *American Mineralogist*, 91(10), pp. 1707–1710.
- Wiens, D. A., Conder, J. A. and Faul, U. H. (2008) 'The Seismic Structure and Dynamics of the Mantle Wedge', *Annual Review of Earth and Planetary Sciences*, 36(1), pp. 421–455.
- Wunder, B. and Schreyer, W. (1992) 'Metastability of the 10-A phase in the system MgO-SiO₂-H₂O (MSH). what about hydrous MSH phases in subduction zones?', *Journal of Petrology*, 33(4), pp. 877–889.
- Wunder, B. and Gottschalk, M. (2002) 'Fe-Mg solid solution of sursassite, (Fe,Mg)₄(Mg,Fe,Al)₂Al[Si₆O₂₁(OH)₇]', *European Journal of Mineralogy*, 14(3), pp. 575–580.
- Yoder, F. (1952) 'The MgO-Al₂O₃-SiO₂-H₂O system and the related metamorphic facies', *American Journal of Science*, Bowen Vol., pp. 569–627.
- Zack, T. and John, T. (2007) 'An evaluation of reactive fluid flow and trace element mobility in subducting slabs', *Chemical Geology*, 239(3–4), pp. 199–216.
- Zanazzi, P. F., Comodi, P., Nazzareni, S. and Andreozzi, G. B. (2009) 'Thermal behaviour of chlorite: an in-situ single-crystal and powder diffraction study', *European Journal of Mineralogy*, 21(3), pp. 581–589.
- Zheng, Y. F. (2009) 'Fluid regime in continental subduction zones: petrological insights from ultrahigh-pressure metamorphic rocks', *Journal of the Geological Society*, 166, pp. 763–782.
- Zibera, L., Klemme, S. and Nimis, P. (2013) 'Garnet and spinel in fertile and depleted mantle: Insights from thermodynamic modelling', *Contributions to Mineralogy and Petrology*, 166(2), pp. 411–421.

